2002

Overpressuring, diagenesis, and fluid flow at the Matagorda Island 519 field, offshore Texas, Gulf of Mexico

Kera Gautreau Spears
Louisiana State University and Agricultural and Mechanical College

OVERPRESSURING, DIAGENESIS, AND FLUID FLOW AT THE MATAGORDA ISLAND 519 FIELD, OFFSHORE TEXAS, GULF OF MEXICO

A Thesis

Submitted to the Graduate Faculty of the
Louisiana State University and
Agricultural and Mechanical College
in partial fulfillment of the
requirements for the degree of
Master of Science

In

The Department of Geology and Geophysics

by
Kera Gautreau Spears
B.S., Louisiana State University, 2000
August 2002

ACKNOWLEDGEMENTS

I would like to thank Dr. Jeff Hanor for his wisdom and guidance in serving as my major advisor. I also wish to thank Dr. Darrell Henry and Dr. Phil Bart for serving as my committee members. I am grateful to Charlie Brewster for providing the data that initially sparked my interest in this study, and for his extensive knowledge of the regional and field geology of Matagorda Island 519, and his willingness to share such knowledge.

NSF grant number EAR-9805446 provided the funding for my research assistantship, and GSA, Sigma Xi, GCAGS, and SPWLA awarded grants to me for this study. In addition to these financial contributions, I wish to thank the MMS Gulf of Mexico regional office in New Orleans, Louisiana, for providing public well log and paleontologic data.

The LSU Department of Geology and Geophysics faculty and staff has been supportive of me in various ways during the course of my graduate studies. I also appreciate the support that I have received from my fellow graduate students, especially Scott Szalkowski, Robert Little, and Juan Chow.

My parents, Kirk and Lori Gautreau, have continuosly supported and encouraged me in everything that I have ever strived for. My mother- and father-in law, Glenda and Jack Spears, have welcomed me into their family as their own, and I am grateful to them for their love and support in all of my endeavors over the past few years.

I would especially like to thank my husband, Russell Spears, for his love, devotion, and faith in me. He has been a soucre of motivation and inspiration to me, which will always be cherished.

TABLE OF CONTENTS

LIST OF TABLES

LIST OF FIGURES

ABSTRACT

The relations between overpressuring, diagenesis, and fluid flow in sedimentary basins are complex and multifaceted. The Matagorda Island 519 field (MI 519), offshore Texas, provides an excellent area for investigating some of these relations. The top of overpressure at MI 519 occurs at a depth of 3.5 to 3.8 km in a Lower Miocene deltaic sequence. On the basis of log-derived lithostratigraphy, the pressure seal does not appear to be lithologic in origin. Geochemical, mineralogical, and cuttings information indicate instead that the precipitation of diagenetic calcite and possibly quartz cements has been the major factor in seal development. Stratigraphic variation in mudstone chemistry indicates diagenesis has been an open-system process, with significant loss of Ca, Si, Mg, and Fe and gain of K in sediments below the pressure seal. Fluid pressures calculated from shale resistivities provide evidence for several vertically-stacked overpressured compartments at MI 519. Lateral sealing within the overpressured section may be provided by faults and precipitation of diagenetic cements within faults.

In contrast to other areas of the Gulf of Mexico Basin, overpressure development at MI 519 does not appear to be due to compaction disequilibrium because of the lack of significant post-Miocene deposition and a lack of a reversal in mudstone porosity below the top of overpressure. More likely causes of overpressuring are clay mineral dewatering, petroleum generation, and the presence of a large column of natural gas.

At least six stages of fluid flow and/or diagenetic development have occurred at the field: 1) calcite cementation within preferred intervals from fluids that originated by dissolution of updip salt domes, 2) deep overpressure development and upward focused flow of underlying Mesozoic brines and the development of secondary porosity in reservoir beds by carbonate

dissolution, 3) precipitation of a seal by mixing of deeply-sourced and updip-sourced fluids, 4) hydrocarbon generation and shallow overpressure development, with hydrocarbons filling in porosity created by calcite dissolution, 5) “hard” overpressure development from smectite dehydration, and 6) development of a shallow freshwater lens during the Pleistocene lowstand.

CHAPTER 1. INTRODUCTION

The relations between overpressuring, diagenesis, and fluid flow are important aspects of understanding the hydrogeology of sedimentary basins. Although there has been extensive research conducted to understand the nature of each of these processes within the Gulf of Mexico sedimentary basin, important problems remain, including the role of fluid flow in driving sediment diagenesis and the potential role of diagenesis in creating fluid pressure seals. In order to describe the potential interaction between these three phenomena, it is first necessary to briefly explain the significance of each individual process.

Fine-grained sediments composed of clay size grains have played an important role in the overpressuring, diagenesis, and hydrogeology of the Gulf of Mexico basin. Following common usage, these sediments will be referred to variously as mudstones, mudrocks, and shales in this thesis.

1.1. Overpressuring

Overpressuring refers to fluid pressures that significantly exceed the hydrostatic gradient, the pressure at a given depth due to the weight of the overlying fluid, typically 10 MPa/km (0.465 psi/ft). Fluid pressures in sedimentary basins like the Gulf of Mexico generally track along a profile with increasing depth that initially follows a hydrostatic pressure gradient. Fluid pressures then transition into a zone of overpressure with increasing depth (Figure 1.1). Lithostatic pressure is the pressure at a given depth due to the weight of the overburden or overlying column of rock (fluid plus matrix), and the lithostatic gradient is typically 23 MPa/km (1.0 psi/ft). In general, fluid pressures can not exceed the lithostatic gradient because rocks will fracture at pressures slightly below lithostatic pressure (Nunn and Sassen, 1986).

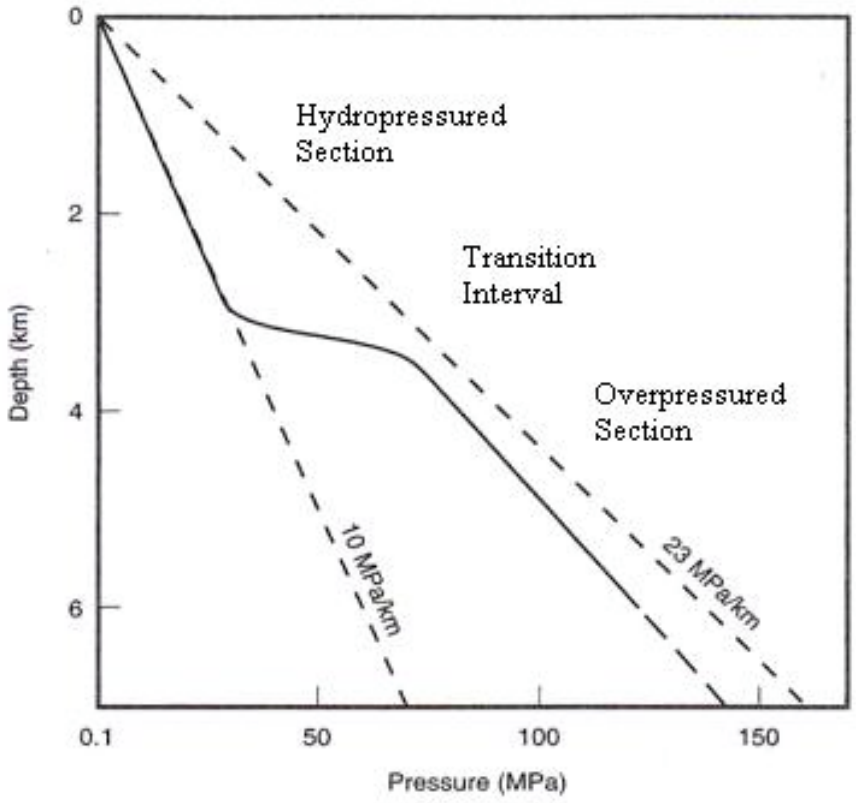

Figure 1.1. Schematic plot of fluid pressure (solid line) versus depth for the Gulf of Mexico. Dashed lines show the hydrostatic (10 MPa/km) and lithostatic (23 MPa/km) pressure gradients (from Bethke, 1986 in Deming, 2001).

Considerable research has focused on understanding the nature of overpressuring and the geologic consequences associated with overpressuring, such as entrapment of hydrocarbons, structural deformation, and environmental hazards. Reviews of the subject are given by authors such as Bredehoft and Hanshaw (1968), Bradley (1975), Fertl (1982), Hunt (1990), Al-Shaieb et al. (1994), Bradley and Powley (1994), He and Corrigan (1995), Neuzil (1995), Osborne and Swarbrick (1997), Spears (2000), Cathles (2001), Deming (1994, 1995, 2001), and Deming et al. (in press).

Two conditions are required in order for overpressuring to occur. The first condition is that some force must raise fluid pressure above hydrostatic. The second condition is the formation or existence of a seal or a geologic barrier or barriers of sufficiently low permeability that allow fluid pressures to be increased and maintained over extended periods of time. These two features must coexist to sustain overpressuring within a given area over significant periods of time.

1.1.1. Causes of Increased Fluid Pressure

Mechanisms believed to be responsible for generating overpressuring in sedimentary basins such as the Gulf of Mexico are one of the major points of debate among researchers. Many researchers believe that rapid deposition and associated compaction disequilibrium are the primary causes of overpressuring in sediments (Osborne and Swarbick, 1997; Hubbert and Rubey, 1959 *in* Hanor, 1987). Overpressuring can result when pore fluids are not able to escape from low permeability shales quickly enough to maintain a normal porosity versus depth compaction curve (Deming, 2001). Thus, shales can play a key role in the understanding of overpressuring in sedimentary basins, and the hydrologic properties of shales thus must be determined in order to understand the original overpressuring.

Aquathermal pressuring, the thermal expansion of aqueous fluid with progressive burial of entrapped water (Barker, 1972 *in* Hanor,1987), has also been proposed as a mechanism for overpressuring. Osmotic diffusion of water through semipermeable strata into sediments containing more saline fluids has been shown to influence overpressuring as well (Hanor, 1987). Dewatering of clay minerals during burial diagenesis in sediments with low permeability has also been proposed as a major contributor to overpressuring in sedimentary basins (Hanshaw and Bredehoft, 1968; Al-Shaieb et al., 1994; Awwiller, 1993; Land et al., 1997; Lynch, 1997). Petroleum generation, with its conversion of hydrocarbons into liquids and gases, has been proposed as a mechanism that generates overpressuring in sediments (Barker, 1990; Neuzil, 1995).

1.1.2. Pressure Seals

Much of the debate surrounding the study of overpressuring centers around the concept of pressure seals in sedimentary basins. A pressure seal was first defined by Hunt (1990, p. 2) as:

> "…a zone of rocks capable of hydraulic sealing, that is, preventing the flow of oil, gas, and water….the term refers to seals that prevent essentially all pore fluid movement over substantial intervals of geologic time."

Figure 1.2 illustrates how an inferred pressure seal exists on a fluid pressure versus depth graph as the region of high fluid pressure gradient (Deming, 2001). Associated with pressure seals, a pressure compartment is defined by Deming (2001, p. 220) as:

> "…a three-dimensional hydraulically isolated volume of the Earth's crust that has a fluid pressure different from the ambient

surroundings. The role of the pressure seal is to maintain anomalous pressures in the lower system by preventing the movement of fluid across compartment boundaries. "

A conceptual model of a generic pressure compartment is shown in Figure 1.3. In this model the interior of the compartment is hydrostatically pressured and of relatively high permeability, and is separated from the surrounding environment by a pressure seal (Deming, 2002). The concept of pressure seals and pressure compartments in sedimentary basins can be expressed on different levels (Figure 1.4).

The most widely proposed mechanisms for forming pressure seals are the depositional loading of fine-grained sediments, diagenesis, and capillary forces. Depositional loading is the rapid deposition of a thick shale sequence followed by deposition of a capping layer of sand. Rapid deposition of sediments can often cause abnormal compaction within the sediments, which causes elevated fluid pressures due to the rapid decrease in pore volumes (Osborne and Swarbick, 1997). Diagenesis contributes to pressure sealing when precipitates from diagenetic reactions occlude the pore spaces within sediments, thus reducing permeability. Al-Shaieb et al. (1994) claim that pressure seals exhibit distinct diagenetic bands, and suggest that diagenetic processes such as calcite precipitation in pore spaces may be an effective sealing mechanism.

Capillary seals are created when pore spaces effectively act as water-saturated capillary tubes that other fluids, such as oil or gas, can not migrate through unless the capillary force is overcome (Deming, 2002). The entrapment of a hydrocarbon phase thus has the potential for generating a seal that permits the accumulation of excess fluid pressure. Hunt (1990), however, explicitly states in the definition of a pressure seal that "…the

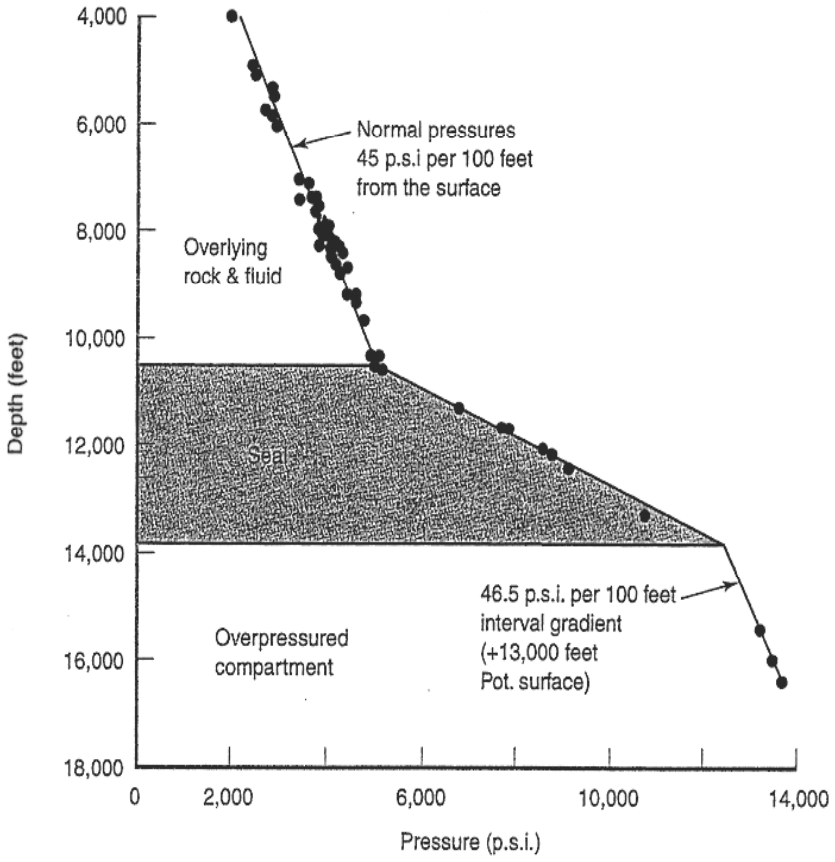

Figure 1.2. A pressure seal is inferred to exist in the region of high fluid pressure gradient shaded on this plot of fluid pressure as a function of depth from Cook Inlet fields, Alaska (Deming, 2002; from Hunt, 1990, after Powley, 1980).

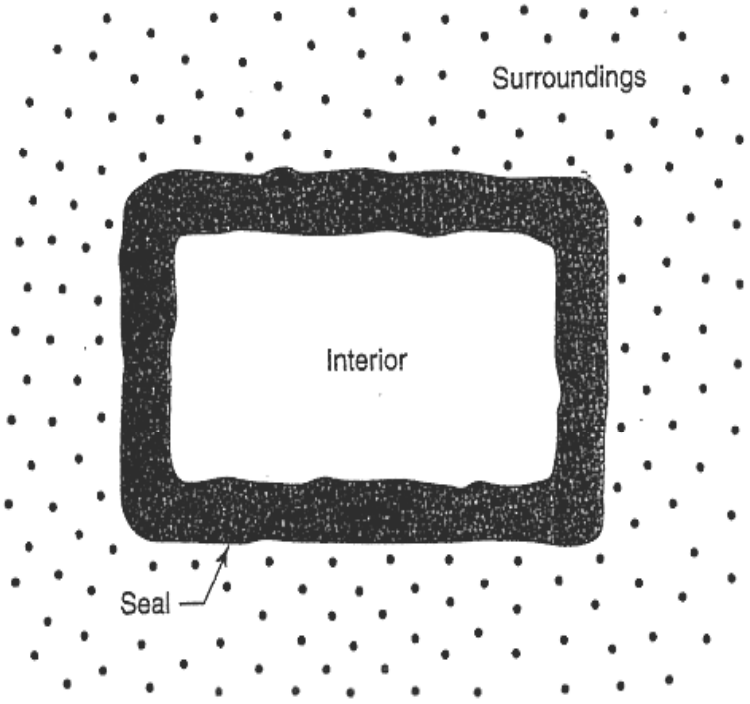

Figure 1.3. Conceptual model of a generic pressure compartment (from Ortoleva, 1994 *in* Deming, 2002).

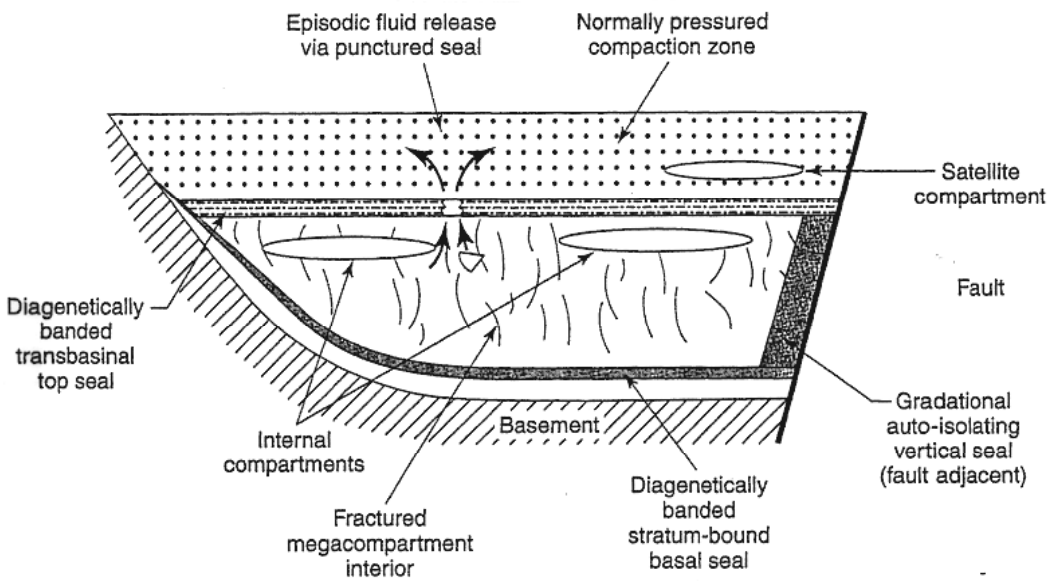

Figure 1.4. Pressure compartment/seal paradigm of sedimentary basin hydrogeology showing different levels of compartmentalization (Ortoleva, 1994 *in* Deming, 2002).

term [pressure seal] does not refer to capillary seals…" while other authors, such as Revil et al. (1998), propose that pressure seals could form in sedimentary basins through the formation of capillary gas seals.

1.1.3. Debate Over the Permeability of Pressure Seals

Bredehoft et al. (1994) claim that two schools of thought have developed in the debate over pressure seals. The static school considers that abnormally high pressures can be maintained over geologic time by pressure seals (Bradley, 1975; Hunt, 1990; Bradley and Powley, 1994; Ortoleva, 1994; Cathles, 2001). Proponents of the static school believe that pressure seals can function as effective permeability barriers over geologic time, and thus can trap large quantities of petroleum.

The dynamic school considers that pressure seals are not effective over geologic time scales as fluid flow barriers and that "there are no totally impermeable geologic materials" (Bredehoft et al., 1982, p. 297). Chamberlin (1885) claimed that "no stratum is entirely impervious", and he is considered by many to be one of the patriarchs of the dynamic school (Deming et al., in press). Data from the dynamic school suggests that average permeabilities in the continental and oceanic crusts are sufficiently high to sustain fluid circulation in a constant manner throughout the earth's crust (Huenges et al., 1997; Fisher, 1998; Ingebritsen and Manning, 1999; Fisher and Becker, 2000).

1.1.4. Hydraulics of Sealing

Deming (1994) quantified the conditions under which pressure seals may retain abnormal pressures by calculating the time a seal of a specified thickness and permeability can confine excess pressures (Deming, 2001). To maintain a pressure seal with an average thickness of 100 to 1000 meters over geologic time (approximately 1 Ma or 10^6 years), Deming concluded that required seal permeabilities would be in the range of 10^{-23} to

10^{-25} m^2, as illustrated in Figure 1.5. Deming further stated that this range of permeabilities is too high to maintain abnormal fluid pressures over geologic time, and "…if pressure seals exist, …some type of active geochemical or capillary mechanism is necessary" to "…offset the natural tendency for pressure equalization."

According to calculations performed by Bethke (1986) anomalous formation pressures in sedimentary sequences that contain more than 85% shale and shaly sediment could be maintained at sedimentation rates of 0.1-10 mm (0.004-0.4 in) per year if average shale permeabilities were in the range of 10^{-18} to 10^{-20} m^2 (10^{-14} to 10^{-16} cm^2) or 10^{-5} to 10^{-7} darcies. Results from Bethke (1986) are consistent with laboratory measurements of shale permeabilities from sediments in the Gulf of Mexico (Neglia, 1979), as illustrated in Figure 1.6.

In contrast, He and Corrigan (1995) state that for a seal layer having a given thickness of 100-1000 m (328-3280 ft) excess pressures (head) can be maintained over geologic time scales of 1 to 10 million years for a higher range of permeabilities than those inferred by Deming (Figure 1.7). He and Corrigan (1995) suggest a better quantitative description of a pressure seal is:

> "…the time required for the base of a layer of given permeability and thickness to dissipate excess pressure (head) to some fraction of the initial head (e.g., 0.1 Δh)."

These authors claim that shale bulk compressibilities must also be considered when describing pressure seals. These authors also cite the research of other authors, such as Bredehoeft and Hanshaw (1968) and Carslaw and Jaeger (1959). Bredehoft and Hanshaw (1968) addressed the dissipation of excess pressure in a semi-infinite media after imposing a stepwise change in excess pressure (head) across the media while applying a zero-head

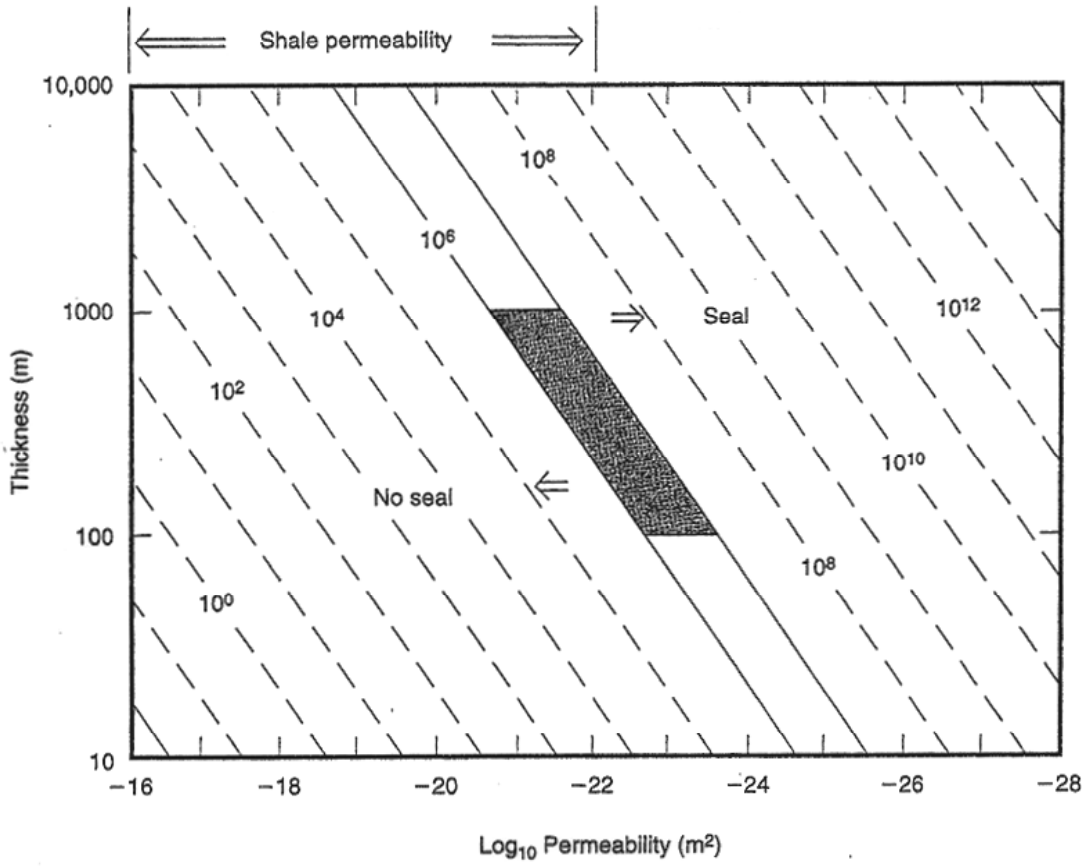

Figure 1.5. Maximum time in years over which a layer of a given thickness and permeability can confine excess pressures, according to calculations by Deming (1994). Shaded area indicates approximate permeability required to sustain a 100 to 1000 meter thick seal over a geologic time of 10^6 to 10^7 years (from Deming, 1994 *in* Deming, 2002).

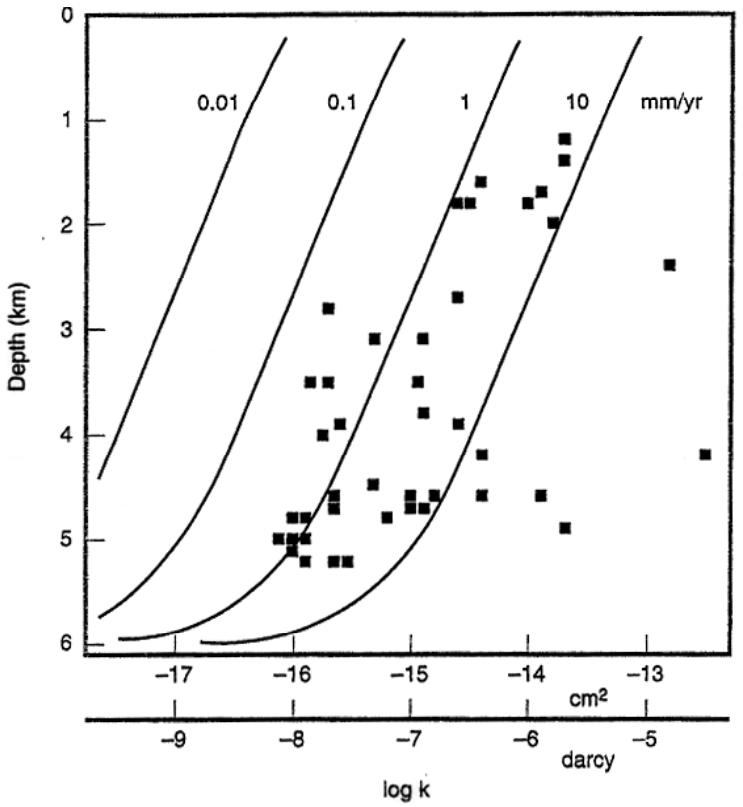

Figure 1.6. Permeability profiles required for generating and maintaining overpressuring in a 6-km deep sedimentary basin as a function of sedimentation rate in millimeters per year. Solid squares represent Gulf Coast shale permeability measurements reported by Neglia (1979) (from Bethke, 1986 *in* Deming, 2001).

(hydrostatic pressure) upper boundary (He and Corrigan, 1995). Carslaw and Jaeger (1959) provide an analytical solution to the problem of energy dissipation in a finite layer for the same initial and upper boundary condition used by Bredehoft and Hanshaw (1968), but with a no-flow lower boundary condition (He and Corrigan, 1995). Figure 1.8 illustrates the various pressure profiles produced from (A) Deming (1994), (B) Bredehoft and Hanshaw (1968), (C) Carslaw and Jaeger (1959), and (D) He and Corrigan (1995).

He and Corrigan (1995) suggest that Deming cannot constrain the evolution of excess pressure (head) in a temporal sense because he uses a constant-head lower boundary. These authors also suggest that, in terms of calculating the time required for head at the base of a sealing layer to dissipate to 0.1 Δh for equivalent parameters of diffusivity and thickness of the sealing layer, Deming has also underestimated time of excess pressure maintenance by a factor of four.

1.1.5. Overpressuring in the Gulf of Mexico Basin

Within most of the Cenozoic portion of the Gulf of Mexico basin, shale-dominated sequences are overlain by deltaic systems containing alternating series of sands and shales which grade vertically upward into massive fluvial-deltaic sand sequences (Mello, 1994 *in* Deming, 2001). The massive sands are typically hydrostatically pressured. Overpressuring occurs either in the mixed sands and shales or in the underlying shale sequences (Deming, 2001).

In the Gulf of Mexico overpressuring is common throughout the entire basin, yet there are different mechanisms believed to be responsible for overpressuring in different regions of the basin. Along the coast of Louisiana overpressuring within Cenozoic sediments is believed to be due to rapid deposition of fine-grained sediments and subsequent rapid

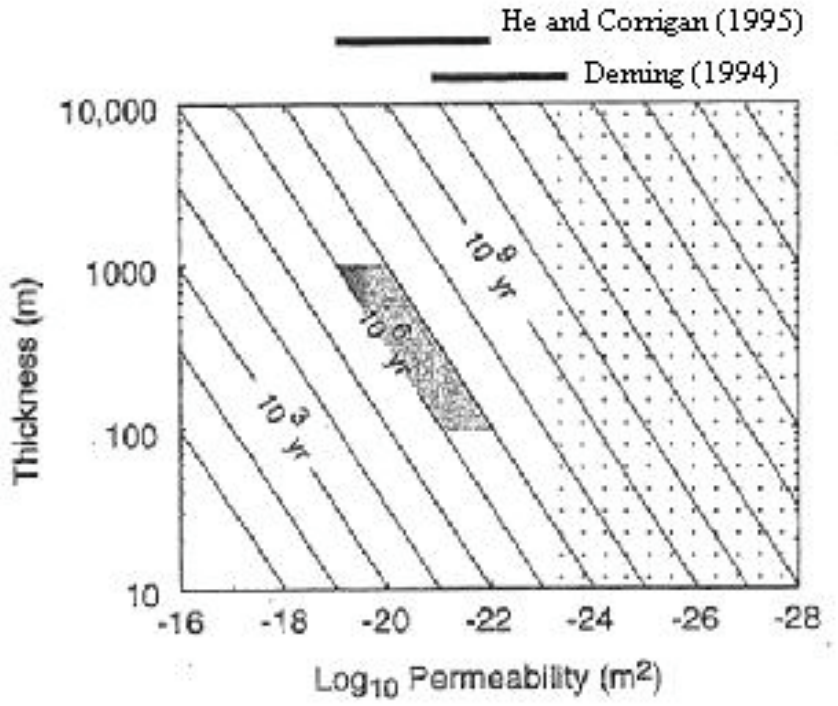

Figure 1.7. Time in years required for the base of a layer of given thickness and permeability to dissipate excess pressures (head) to 10% of initial value for a bulk compressibility of 10^{-8} Pa^{-1}. For comparison with Deming (1994) the shaded area of a 100-1000 meter thick layer over geologic time scales of 1-10 m.y. is shown; excess pressures are maintained for a higher range of permeabilities (upper solid bar above graph) than inferred by Deming (lower solid bar above graph). Stippled region refers to shale permeabilities that are probably unrealistically low (Neuzil, 1994) (from He and Corrigan, 1995).

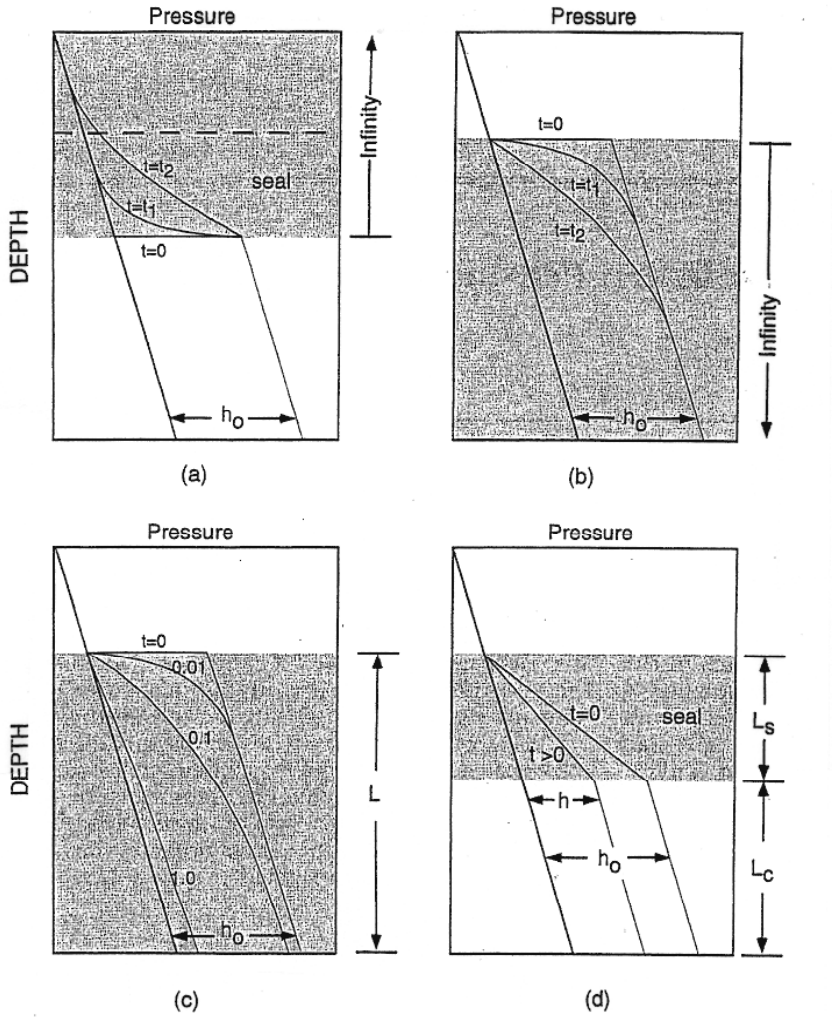

Figure 1.8. Pressure profiles as a function of time. t represents time, h_0 represents change in head, and L represents thickness. (a) Deming (1994); shaded region indicates a semi-infinite upper boundary and a constant head lower boundary. (b) Bredehoeft and Hanshaw (1968); shaded region indicates a semi-infinite lower boundary and a zero-head upper boundary. (c) Carslaw and Jaeger (1959); shaded region indicates a shale unit of finite thickness (L) and numbers on curve indicate values of Dt/L^2. (d) Idealized pressure compartment where excess head is constant everywhere within the compartment but decreases with time; shaded region indicates seal of given thickness (Ls) and underlying unshaded region indicates pressure compartment of given thickness (Lc). (after He and Corrigan, 1995).

burial of these sediments (Bray, 1989; Nikiel, 1998; Spears, 2000). Cenozoic sediment supply was not as plentiful along the western margin of the Gulf of Mexico as along the Louisiana coast (Galloway et al., 2000), however, and overpressuring in the western Gulf of Mexico is less influenced by rapid deposition of fine-grained sediments and rapid burial. Overpressuring along the Texas gulf coast is believed to be due to other factors, such as diagenesis (Lynch, 1997; Brewster et al., 1998; Klein et al., 1998).

1.2. Diagenesis

1.2.1. Review of Diagenesis in Sedimentary Basins

Recent research on sedimentary diagenesis in the Gulf of Mexico basin has focused on topics related to diagenetic reactions and the influence that these reactions have on fluid flow, mass transfer, overpressuring, and elemental mobility. Diagenesis related to fluid flow and to overpressuring in the north-central Gulf of Mexico has been extensively studied (Hanor, 1987; Bray, 1989; Funayama, 1990; Wintsch and Kvale, 1994). Wilcoxin (19xx) reviewed diagenesis in the Wilcox group of South Louisiana as both depth-dependent and facies-dependent. Nikiel (1998) and Nikiel and Hanor (1999) propose that variations in fluid density and the development of overpressuring at depth in the south Louisiana Gulf Coast are potential driving forces for large-scale fluid flow.

Other researchers have focused on diagenesis and related processes of overpressuring and fluid flow in the western Gulf of Mexico (Taylor, 1990; Awwiller, 1993; Lynch et al., 1997; Bloch et al., 1999; Lynch et al., 1999). Lynch and Land (1996) propose that diagenesis of calcite cement in Frio formation sandstones is reflected in formation water chemistry, and imply that mass exchange of diagenetic calcite cement is controlled by fault block compartmentalization. Taylor and Land (1996) suggest that allochthonous Miocene formation waters provide evidence for a potential link between deep sources of fluids and

carbonate dissolution in the Corsair Trend of the Texas Gulf Coast, and that fluid flow occurs in an episodic fashion, driven by periodic buildup and release of geopressures.

Lynch (1997) describes the relations between illite-smectite diagenesis and fluid flow from shales into sandstones, generation of abnormal formation-water fluid pressures, onset of sandstone diagenesis and distribution of authigenic phases in sandstones. Brewster et al. (1998) and Klein et al. (1998) propose that diagenetic processes in geopressured Lower Miocene sandstones in the offshore Texas Gulf Coast are related to fluid flow and pressure cell formation. According to these authors, the observed conditions reflect complicated sequences of diagenetic events that generate secondary porosity, and thus enhance reservoir quality by creating pressure compartments. Al-Shaieb et al. (1994) cites evidence of distinct bands of diagenetically precipitated calcite that occur in connection with pressure seals.

The influence of diagenesis on reservoir quality has been studied both in North America (Dutton et al., 2000) and in the North Sea (Barclay and Worden, 2000; Conybeare and Shaw, 2000; Durand et al., 2000; Jeans, 2000; Macaulay et al., 2000; Marchand et al., 2000; Midtbo et al., 2000; Nadeau, 2000; Osborne and Swarbick, 1997; Pay et al., 2000; Stewart et al., 2000; Syrowski, 2001; Worden et al., 2000), as well as the Niigata Basin of Japan (Niu and Ishida, 2000). Research involving the influence of diagenesis on reservoir quality has mainly focused on the North Sea, although recent research has also focused on the Gulf of Mexico basin.

Driving forces for burial diagenesis cover a wide range of mechanisms and conditions. According to Hanor (1996), changes in pressure and temperature, introduction and loss of CO_2, introduction of organic acids, redox reactions, and mixing of fluids of diverse composition can all contribute to burial diagenesis.

Debate on shale diagenesis has focused on whether shales behave as open or closed diagenetic systems, and, therefore, whether or not mass is exchanged across shale layers. Many authors propose that there is significant evidence to support the claim of shales as open chemical systems (Boles and Franks, 1979; Howard, 1979; Altaner et al., 1984; Moncure et al., 1984; Hower, 1983; Land et al., 1997; Lynch, 1996; Lynch, 1997; Land and Milliken, 2000). Other authors feel that there is equally sufficient evidence to consider shales closed systems (Hower et al., 1976; Eslinger et al., 1979; Pollastro, 1985; Jennings and Thompson, 1986; Pearson and Small, 1988). In this study shales will be referred to as both sources and sinks of diagenetically reactive components.

Sandstone diagenesis has not been the subject of such intense debate as shale diagenesis. However, the possibility of mass transfer between sandstones and adjacent shales is also contentious. Diagenetic reactions that occur within sandstones have been proposed to be responsible for being the sources of cements, such as quartz, calcite, and feldspars, that are found in adjacent shales (Land and Milliken, 2000).

1.3. Fluid Flow

1.3.1. Gulf of Mexico Regional Flow Regimes

Fluid flow within sedimentary basins is an important topic that has been extensively studied by many authors for different reasons. Understanding fluid flow regimes in the Gulf of Mexico has significance in several ways, such as in the enhanced recovery of oil and gas reserves, the utilization of water resources, and in developing a regional understanding of the complex hydrogeologic framework throughout the basin. Defining the mechanisms that drive fluid flow is an important means by which sedimentary diagenesis can be linked to overpressuring.

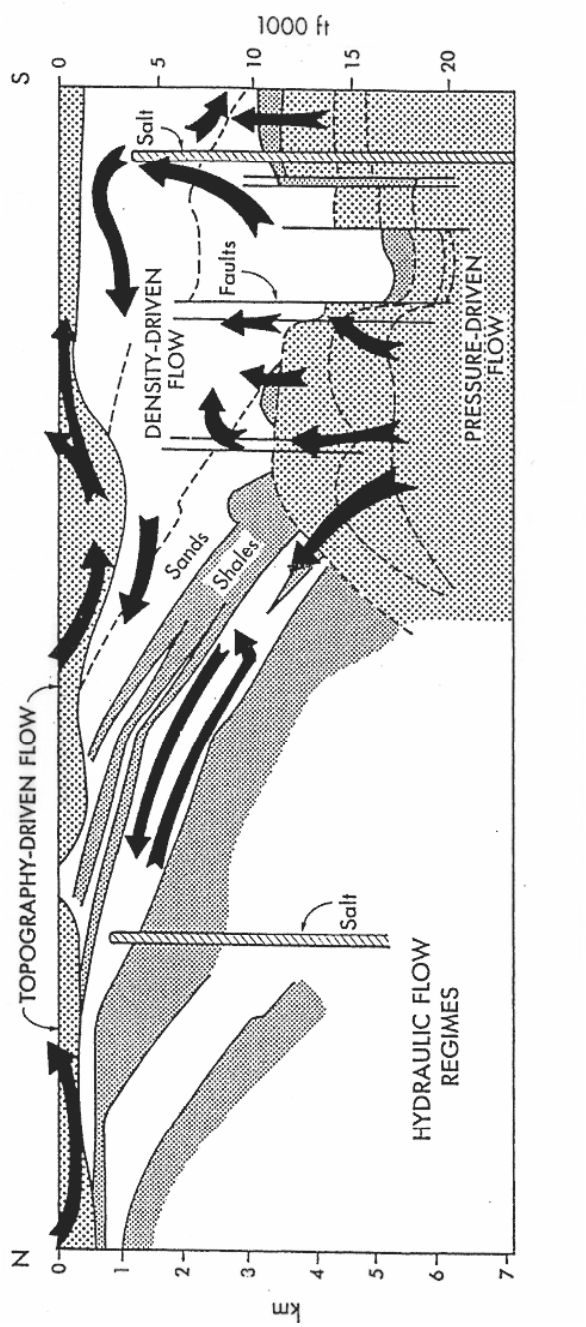

Figure 1.9. Regional flow regimes that dominate the Louisiana Gulf Coast (from Hanor and Sassen, 1990).

According to Hanor and Sassen (1990) regional flow regimes within the Gulf of Mexico basin are considered to be dominantly topographically-driven, pressure-driven, and density-driven (Figure 1.9). Local flow regimes are often associated with one or more of the regional flow regimes, and these can vary depending on the factors within a specific system. Shallow, topography-driven flow of meteoric water is common within the onshore Gulf of Mexico, both along the Louisiana and the Texas coasts (Dutton, 1994; Nikiel, 1998). The deepest part of the section is dominated by pressure-driven flow related to overpressuring. In areas such as south Louisiana where salt domes are dominant, density-driven thermohaline circulation associated with salt dome dissolution and the elevated temperatures of salt has been proposed as a fluid flow mechanism responsible for transporting dissolved solids over large distances (Bennett and Hanor, 1987; Hanor and Sassen, 1990; Bray, 1989).

1.3.2 Fluid Flow and Diagenesis

The relation between fluid flow and diagenesis has been a focus of many studies (Awwiller, 1993; Brewster et al., 1998; Hanor, 2001; Land and Milliken, 2000; Land et al., 1997; Lynch, 1997; Lynch, 1996; Lynch and Land, 1996; Lynch et al., 1999; Lynch et al., 1997; Taylor, 1990; Taylor and Land, 1996; Wintsch and Kvale, 1994). Observed mineralogy and present salinity values can be indicative of current and past fluid flow regimes, both locally and regionally.

Hanor (2001) extended the concept of mixing of fluids of varying composition as a driving force for diagenesis. Calculations by Hanor (2001) show that considerable volumes of minerals could be dissolved and precipitated as the result of episodic mixing of rock-buffered formation waters of varying salinity (Figure 1.10). Calcite and quartz are among the mineral phases that could be precipitated. Both of these mineral phases have been suggested

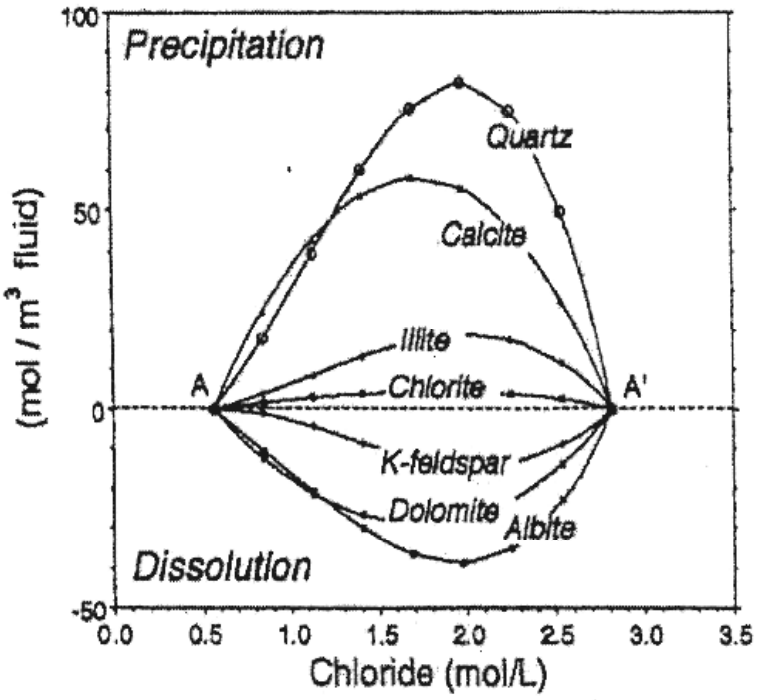

Figure 1.10. Theoretical precipitation and dissolution of various minerals from pore fluids resulting from mixing of two end-member fluids of differing chlorinity (from Hanor, 2001).

as diagenetic cements responsible for forming some pressure seals (Al-Shaieb et al., 1994; Brewster et al., 1998; Klein et al., 1998).

1.4. Purpose of This Study

Despite the interest in overpressuring, diagenesis, and fluid flow, there have been relatively few published field studies documenting the potential relations between these three processes. The purpose of this study was to investigate the relations among overpressuring, diagenesis, and fluid flow at the Matagorda Island 519 field (MI 519) in the offshore Texas shelf of the Northwestern Gulf of Mexico. Published studies of previous Amoco research at this field by Brewster et al. (1998) and Klein et al. (1998) determined that gas accumulations occur in off-structure, overpressured sandstones. Compartmentalized hydrocarbon reservoirs are thought to have formed as a result of diagenetic processes that generated secondary porosity within the sandstones. These authors proposed that the diagenetic processes are related to fluid flow and pressure cell formation, and their proposed geologic model of reservoir development involves several periods of pressure formation and diagenetic mineral assemblages that are consistent with alteration resulting from fluid flow.

The focus of this study is on the nature of the pressure seal at Matagorda Island 519. Brewster et al. (1998) published pressure-depth curves for six wells in the field which show an abrupt transition from hydrostatic to overpressured conditions at a depth of approximately 3600-4200 m. A wide variety of geophysical borehole logs for the field, including spontaneous potential (SP), resistivity, conductivity, neutron, density, sonic, formation evaluation, Rwa, temperature, and porosity, are available in the public domain, and permit correlation of trends in fluid pressures with sediment and fluid properties over a large depth interval. Although few formation water analyses are available for the field, abundant information on formation water salinity can be derived from the geophysical logs. Spatial

variations in salinity can be used in turn to help constrain the interpretation of the hydrogeology of the field. In addition, Brewster (personal communication) has provided information on sediment bulk chemistry and sediment mineralogy, which can be used to examine sediment diagenesis.

Specific questions addressed in this study include the following. What is the nature of the pressure seal at Matagorda Island 519? Is it depositional, diagenetic, and/or capillary? Has overpressuring been caused by rapid sediment loading, or is some other mechanism required? How has the formation of a pressure seal affected fluid flow within the field? Is there evidence for fluid mixing? Has diagenesis been largely a closed-system process or is there evidence for exchange between sands and shales and/or transport of potentially diagenetically-reactive components from distances far outside of the field?

The nature of the pressure seal and overpressuring will be determined through analysis of lithostratigraphy, sediment chemical properties, and fluid properties. If lithology controls overpressuring and the formation of a pressure seal at Matagorda Island 519, then an extremely thick shale sequence should correspond to the top of overpressure. Analysis of enrichment and depletion trends with depth for diagenetic cements can determine if diagenesis controls overpressuring and pressure seal development, and the implications for mass exchange and fluid flow associated with diagenesis. Fluid flow regimes within the study area will be determined from analysis of chemical properties and fluid properties, especially salinity. Variability in salinity with depth and spatial variations in salinty are indicative of hydrodynamic flow regimes.

CHAPTER 2. GEOLOGIC SETTING OF MATAGORDA ISLAND 519

2.1. Introduction

Matagorda Island 519 field is located adjacent to the State-Federal lease boundary, offshore of Matagorda Bay along the Texas Gulf Coast (Figure 2.1). The field is actually comprised of wells located in three adjacent blocks, Matagorda Island 519, 518, and 487. Figure 2.2 illustrates the relative location of each well used in this study, and Table 2.1 lists the well numbers and location for each of the wells, in order from southwest to northeast. Miocene and younger intervals are analyzed in this research, with most of the focus on the Lower Miocene section.

2.2. Tectonic and Structural Setting

2.2.1. Gulf of Mexico Growth Faulting

Large-scale growth faults are common in much of the shallow Gulf of Mexico. These features are observed throughout the Texas Gulf Coast, and they generally follow the orientation of the coastline. Development of growth faults, such as those found within the Gulf of Mexico, is illustrated in Figure 2.3.

2.2.2. Overview of Structural Development of the Texas Gulf Coast

The regional tectonic framework of the Texas Gulf Coast is related to zones of crustal weakness formed during Mesozoic rifting in the Gulf of Mexico (Martin, 1978, and Hall et al., 1983, *in* Morton et al., 1985). There was a significant interaction between sedimentation and tectonics in the Gulf of Mexico, and basement block faulting determinined the distribution and thickness of the Jurassic Louann Salt and the axes of major depocenters as well (Morton et al., 1985).

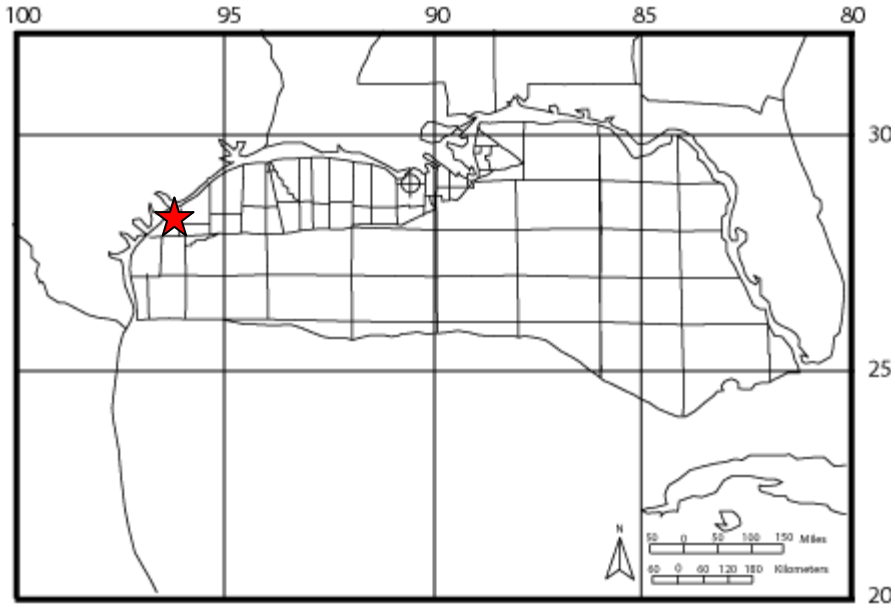

Figure 2.1(a). Relative location of the Matagorda Island 519 field within the Gulf of Mexico basin, indicated by star.

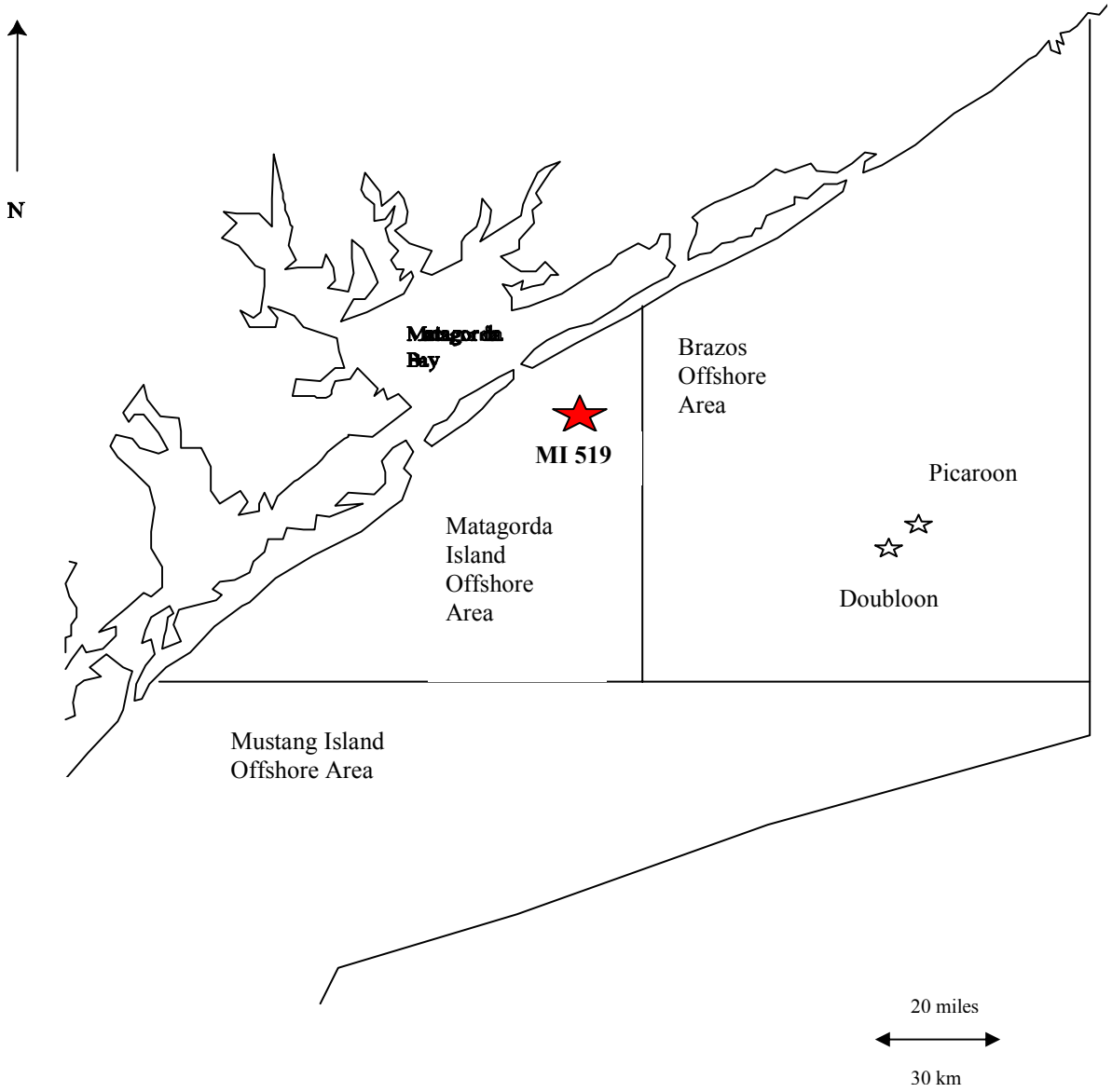

Figure 2.1(b). Location map illustrating the relative location of the Matagorda Island 519 field along the Texas Gulf Coast, as well as the locations of Picaroon and Doubloon fields in the Brazos offshore area.

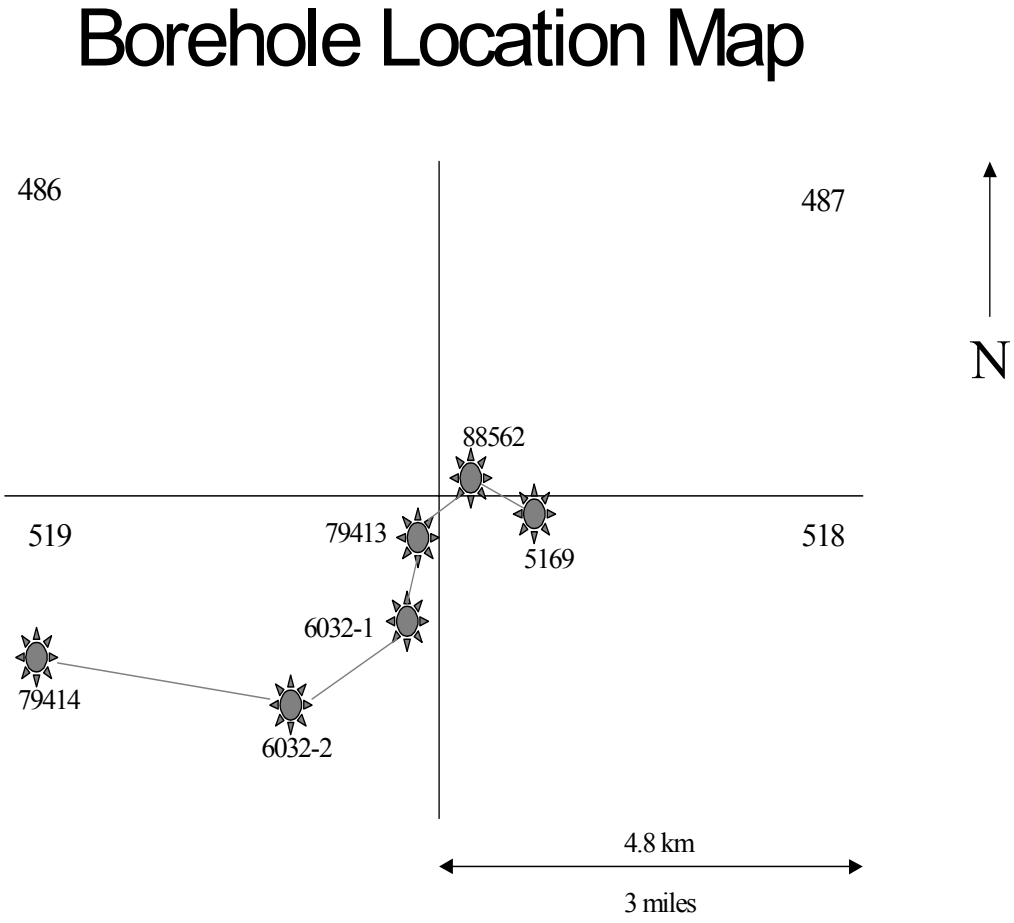

Figure 2.2. Location map illustrating the relative locations of wells used in this study.

Table 2.1. Wells included in Matagorda Island 519 field study area, listed in order from southwest to northeast.

Well Number	API Number	Location
State Lease 79414 #1	42-703-30312	Matagorda Island Block 519
OCS 6032 #2	42-703-40432	Matagorda Island Block 519
OCS 6032 #1	42-703-40294	Matagorda Island Block 519
State Lease 79413 #1	42-703-30300	Matagorda Island Block 519
State Lease 88562 #	42-703-30340	Matagorda Island Block 487
OCS 5169 #1	42-703-40318	Matagorda Island Block 518

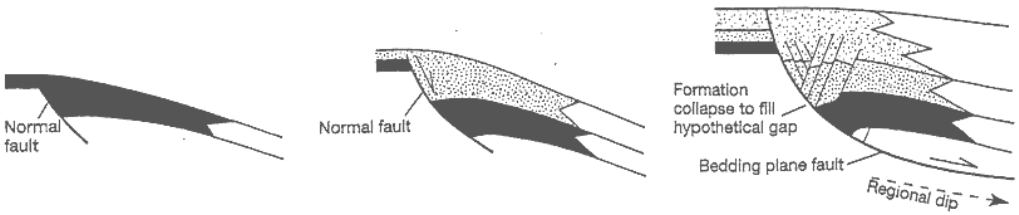

Figure 2.3. Development of growth faults. Displacement on a listric normal fault occurs during sedimentation, resulting in equivalent beds being thicker in the hanging wall block, relative to the footwall block. The fault passes into a bedding-plane fault at depth (from Twiss and Moores, 1992).

The formation of secondary structural features, such as growth faults, salt and shale diapirs and ridges, local unconformities, and withdrawl synclines, is controlled by the positions of contemporaneous and former shelf margins, the presence of deformed salt or undercompacted shale, and changes in sedimentation rate (Morton et al., 1985). Salt diapirs are limited in their distribution along the Texas Gulf Coast, but shale ridges and associated listric normal faults are ubiquitous (Morton et al., 1985). Figure 2.4 illustrates the locations of principal tectonic and salt structures beneath the offshore areas and Coastal Plain of Texas.

Regional growth faults, which occur as long, subparallel, down-to-basin faults along the Texas coast were formed in response to gravity-induced extensional stresses near former shelf margins (Morton et al., 1985). These growth faults caused substantial thickening on their downthrown side, and displaced stratigraphically equivalent beds by as much as 10,000 feet (3000 meters) (Morton et al., 1985). In general, fault surfaces flatten with increasing depth and become broad bedding-plane faults within the overpressured section of massive marine shale (Bally, 1983 and Bruce, 1984 in Morton et al., 1985).

Figure 2.5 shows a structural cross-section extending from the Llano Uplift in southwest Texas to the Gulf of Mexico abyssal plain (Worrall and Snelson, 1989). The Matagorda Island 519 field is located approximately halfway between the shoreline and the edge of the continental shelf, shoreward of the Corsair fault zone. Miocene sediments and regional growth faulting dominate this region. The nearest underlying source of salt to Matagorda Island 519 is Jurassic, located at depths of approximately 30,000 feet (10 kilometers).

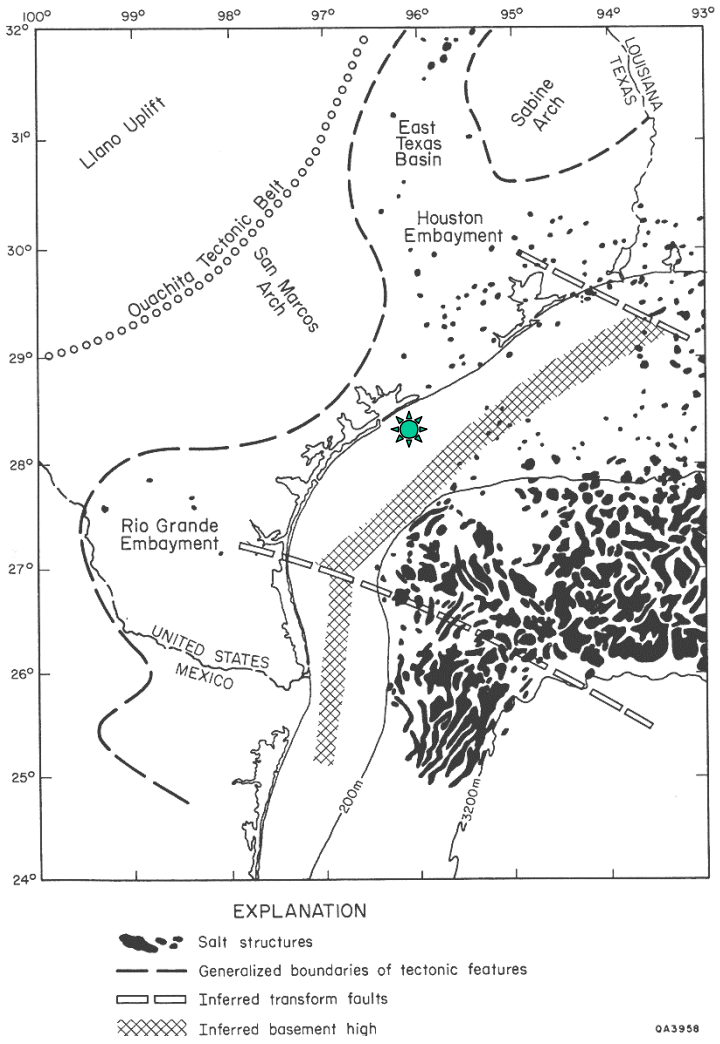

Figure 2.4. Locations of principal tectonic and salt structures beneath the offshore areas and Coastal Plain of Texas. Asterisk marks location of Matagorda Island 519. (modified from Morton et al., 1985).

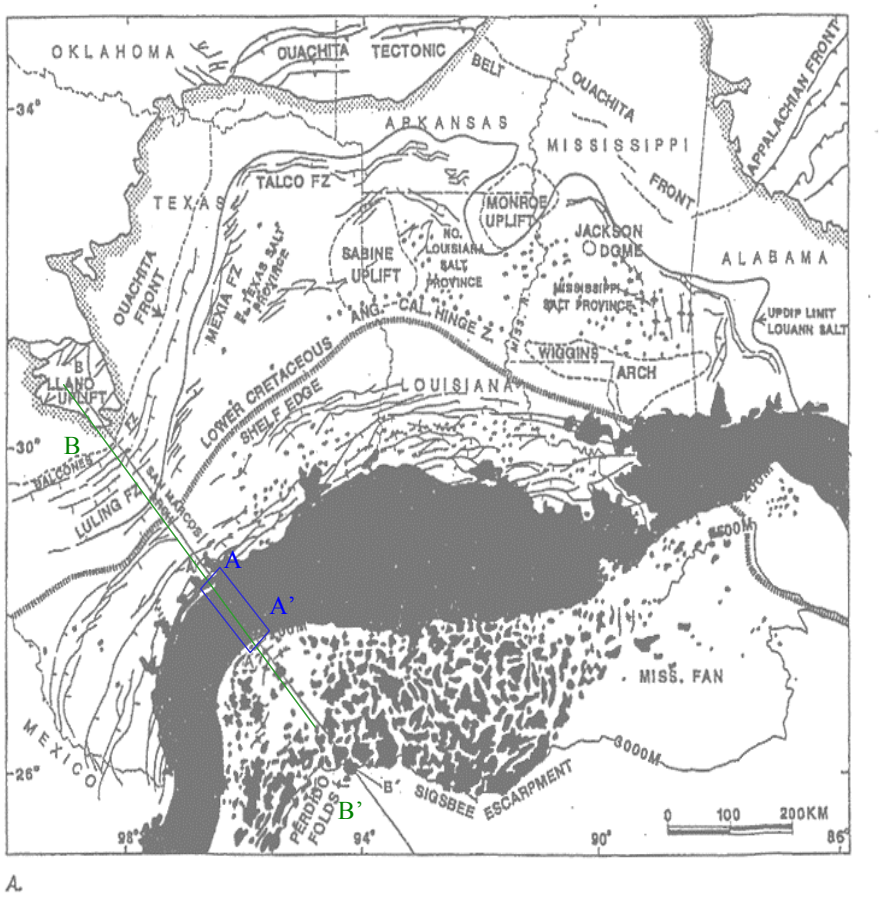

A.

Figure 2.5(a). Map view of the normal fault province in the Gulf Coast area. The location of cross-section B-B' is shown in green, and cross-section A-A' is shown in blue. Matagorda Island 519 is located along cross section A-A' (after Worrall and Snelson, 1989).

2.2.3. Overview of Structural Geology Local to the Matagorda Island Offshore Area

Figure 2.6 illustrates the manifestation of structural features at the surface in the onshore region of Matagorda County, Texas. The locations of onshore salt domes can be observed in this figure, and it is important to note that the location of the nearest salt dome to the Matagorda Island 519 field in this figure is approximately 30 to 40 miles (50 to 65 km). In the Matagorda Island offshore area, the Corsair fault zone is the dominant structural feature (Figure 2.5b), and Corsair Type A faulting is the typical structural style associated with this area (Figure 2.7).

The Bureau of Economic Geology at the University of Texas at Austin has produced well log structural cross sections for the Miocene intervals in the vicinity of Matagorda Island (Morton et al., 1985). Figure 2.8 is a base map showing the locations of each of the portions of cross-sections shown here, and the relative location of the Matagorda Island 519 field to these cross-sections. The dip section profile (Morton et al., 1985 Plate 12) shown here extends from onshore Matagorda Bay to offshore Matagorda Island 572, and the strike section profile (Morton et al., 1985 Plate E'-E'') shown here extends along the Texas coast from Matagorda Island Block 481 to Matagorda Island Block 369. The strike and dip sections tie to one another at Matagorda Island Block 481, which is adjacent to the portion of the Matagorda Island 519 field in Block 487. Thus, due to the proximity of the profiles to the Matagorda Island 519 field, the assertion that these profiles provide an accurate estimate of the structural geology at Matagorda Island 519 is made with relative confidence.

Figure 2.9 is a dip-oriented structural profile, extending from onshore Matagorda Bay to offshore Matagorda Island Block 572, approximately 10 miles (16 km) basinward of Matagorda Island 519. Plio-Pleistocene sediments are found in the upper portion of

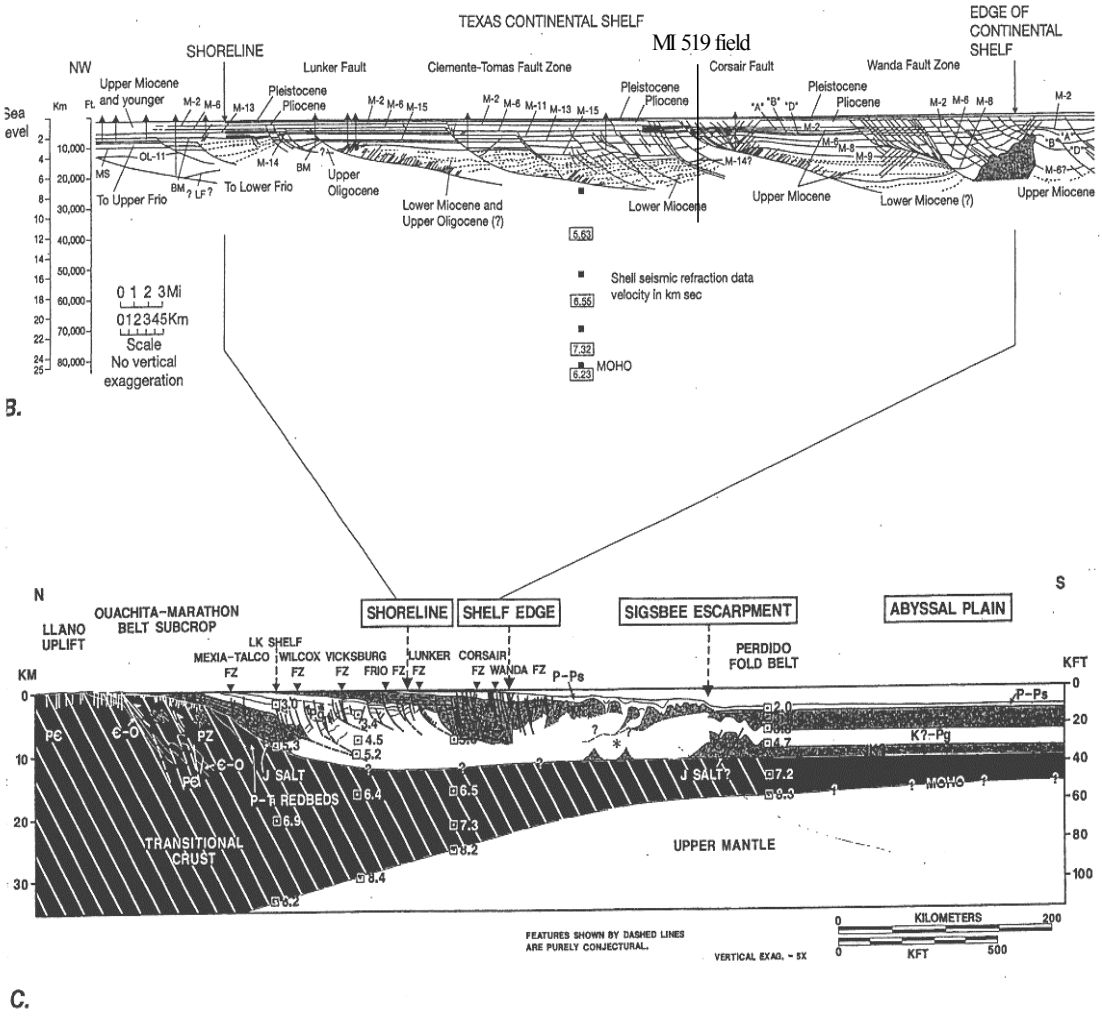

Figure 2.5(b). Cross-section A-A’ in part A across the continental shelf offshore of south Texas, which is a segment of cross-section B-B’. Asterisk indicates the location of Matagorda Island 519 on cross-section A-A’. (c) Cross-section B-B’ in part A extending from the Llano Uplift in the northwest to the Gulf of Mexico abyssal plain in the southeast (after Worrall and Snelson, 1989).

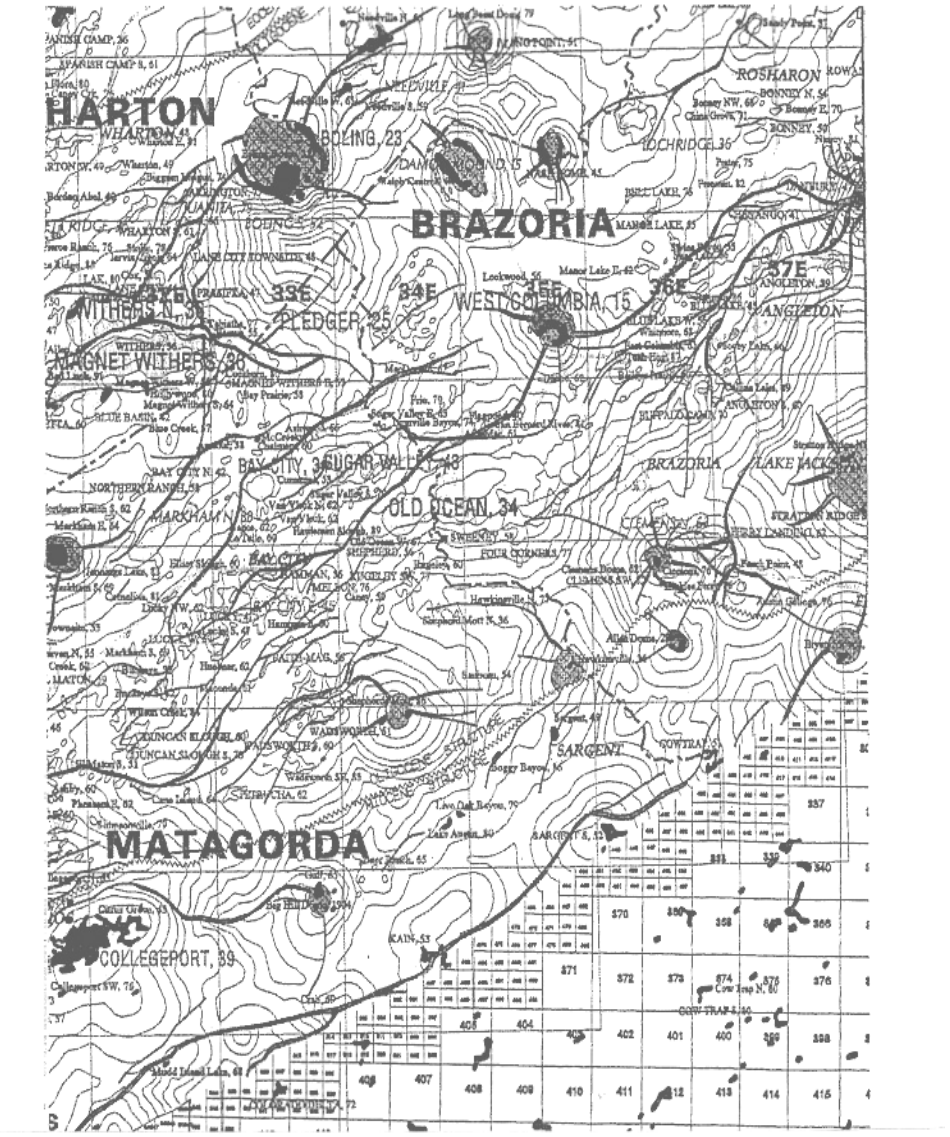

Figure 2.6. Observed structural geology in onshore Matagorda County, Texas. The Matagorda Island 519 field is located approximately 25 miles to the southwest of the area shown in this map (courtesy GeoMap, 1997). Closed contours represent the locations of present salt domes.

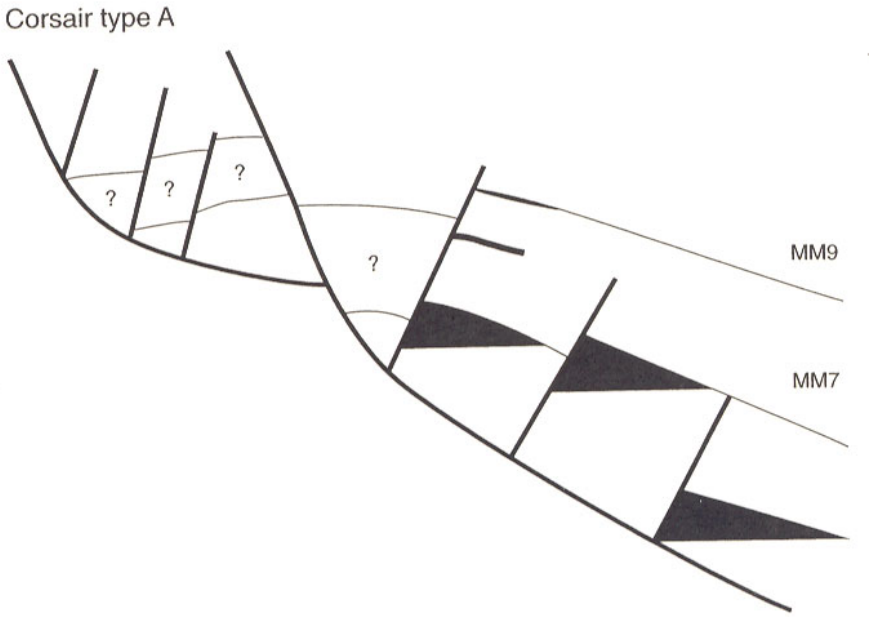

Figure 2.7. Cross-section illustrating style of Corsair Type A faulting, which is dominant at Matagorda Island 519 (from Seni et al., 1997). Darkened areas represent hydrocarbon reservoirs.

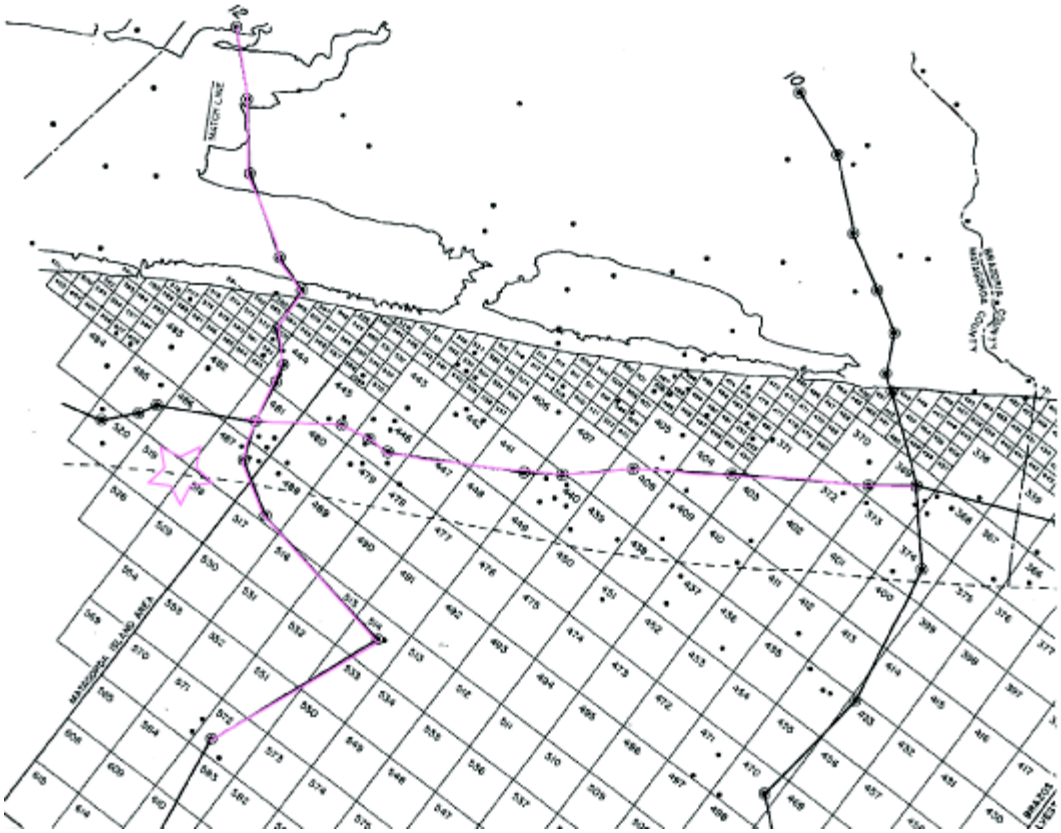

Figure 2.8. Base map showing locations of dip-section and strike-section structural profiles obtained from BEG highlighted in pink, and location of Matagorda Island 519, shown with the pink star (after Morton et al., 1985).

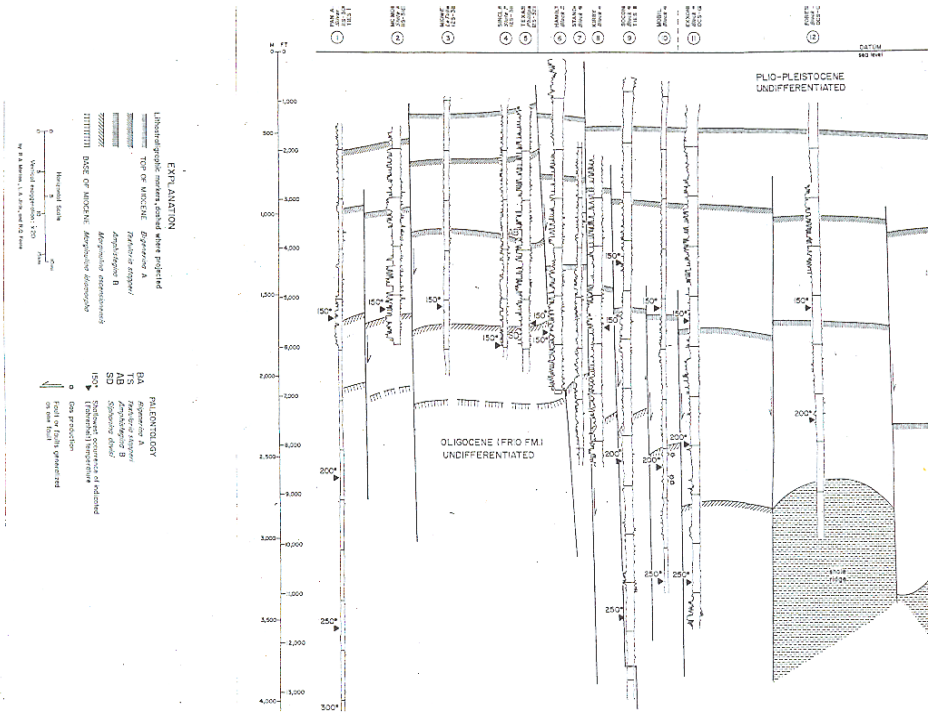

Figure 2.9. Dip-oriented structural cross-section extending from onshore Matagorda Bay to offshore Matagorda Island Block 572, approximately 10 miles basinward of Matagorda Island 519. Note projection of Matagorda Island 519 marked by asterisk, locations of highly compartmentalized region bounded by lateral faulting and shale ridges, and thickening of Miocene section basinward (after Morton et al., 1985).

this cross-section, from depths of near 1,000 feet (300 meters) upward. For most of this cross-section, Miocene sediments dominate the section, covering a depth range from approximately 1,000 feet (300 meters) down to the base of the section, which penetrates to a depth of 13,000 feet (4000 meters) basinward.

A highly compartmentalized section bounded by numerous lateral faults occurs in the region near the State-Federal lease boundary, which is located within Matagorda Island Block 487. Just updip from this region the Oligocene Frio Formation is found at depths of approximately 7,000 feet (2200 meters). Oligocene sediments are missing as the Miocene section thickens from the highly compartmentalized section basinward. Two large shale ridges are located in the offshore portion of the section, basinward from the highly compartmentalized region.

Figure 2.10 is a strike-oriented profile, extending from offshore Matagorda Island Block 481 to offshore Matagorda Island Block 369. This strike section shows that there are numerous fault-bounded blocks, similar to graben and horst types of structures, found throughout the section. In proximity to the Matagorda Island 519 field, an upthrown fault block surrounded by downthrown fault blocks on either side is located adjacent to Block 481. Similar to the dip section, the strike section is also dominated by Miocene sediments, with the top of the Miocene located at depths near 2,000 feet (600 meters) and the base of the Miocene not shown in this section, which extends down to 13,000 feet (4,000 meters).

2.2.4. Structural Geology of the Matagorda Island 519 Field

Figure 2.11 shows the manifestation of major structural features at Matagorda Island 519 on a strike-oriented seismic profile obtained for this thesis research (Brewster, personal communication). On this seismic section the relative locations of a large regional growth fault, along with associated synthetic faulting and a rollover anticline, can be seen. In

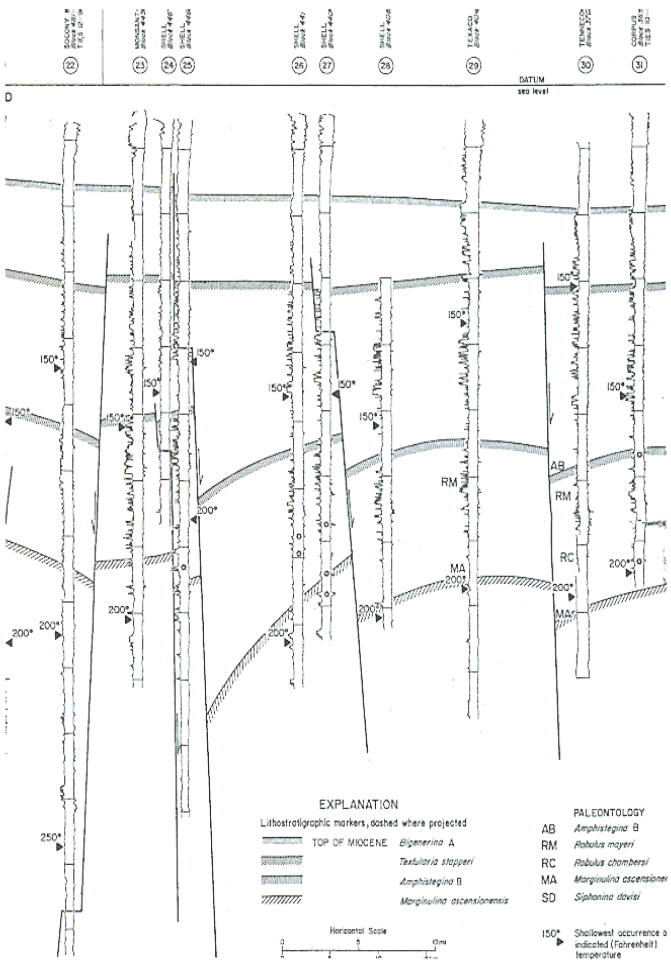

Figure 2.10. Strike-oriented structural cross-section extending from offshore Matagorda Island Block 481 to offshore Matagorda Island Block 369. Note projection of Matagorda Island 519 marked by asterisk, and locations of individual fault blocks throughout the section (from Morton et al., 1985).

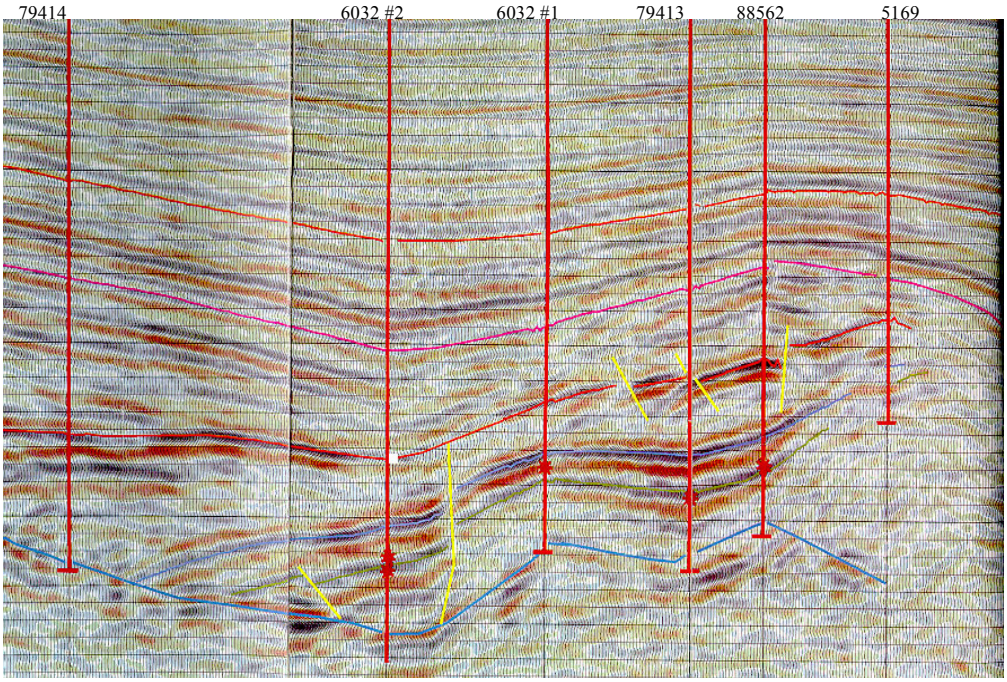

Figure 2.11. Seismic profile through Matagorda Island 519 field (Brewster, unpublished). Note locations of wells marked by red vertical straight lines, the trace of the regional growth fault near the base of the profile, marked with the light blue line, and several smaller, near-vertical faults marked in yellow. Chaotic region near the NE edge of the profile indicates the shale ridge. Stratigraphy is represented with subhorizontal colored lines, with sands shown by red lines and shales shown by blue lines. Bright red regions potentially indicate hydrocarbon reservoirs.

addition, the locations of other smaller lateral faults and a prominent shale ridge can be identified.

2.3. Depositional Setting

2.3.1. Overview of Gulf of Mexico Depositional History

Figure 2.12 shows an overview of the structural and depositional history of the Gulf of Mexico. Gulf of Mexico depositional history began with the initial rift stage of the basin, which occurred from the Triassic to the Early Jurassic (Buffler, 1991 *in* Spears, 2000). Horst and graben structures, and deposition of alternating carbonates, evaporites, and siliciclastics characterized this rift stage. During this rift stage the Eagle Mills Formation was deposited over igneous and metamorphic basement rocks as sediments from horsts began to fill in grabens, and hypersaline brines began to form in the long, deep, narrow trenches formed during rifting (Buffler, 1991).

Deposition of the massive Louann salt sheet into topographic lows (Salvador, 1991) overlying the Eagle Mills Formation and basement rock occurred basinwide during the Middle Jurassic. Salt basins, cooling, and subsidence dominated the Late Jurassic, and a gentle, shallow basin was filled primarily with Smackover Formation carbonates and deep-water shales (Buffler, 1991) during the Late Jurassic. Rifting ended and a marine transgression began in the Late Jurassic, with a sea level highstand continuing into the Early Cretaceous (Buffler, 1991) and continued deposition of thick carbonate reef accumulations.

The Middle Cretaceous marked a period when depositional style shifted from carbonates to siliciclastics within the Gulf of Mexico (Salvador, 1991) due to a rapid drop in sea level exposing shelf edge deltas (Buffler, 1991). This was the first time that significant amounts of terrigenous siliciclastics were introduced to the Northern Gulf of Mexico (Salvador, 1991). Deposition of terrigenous siliciclastics has persisted since the Cretaceous,

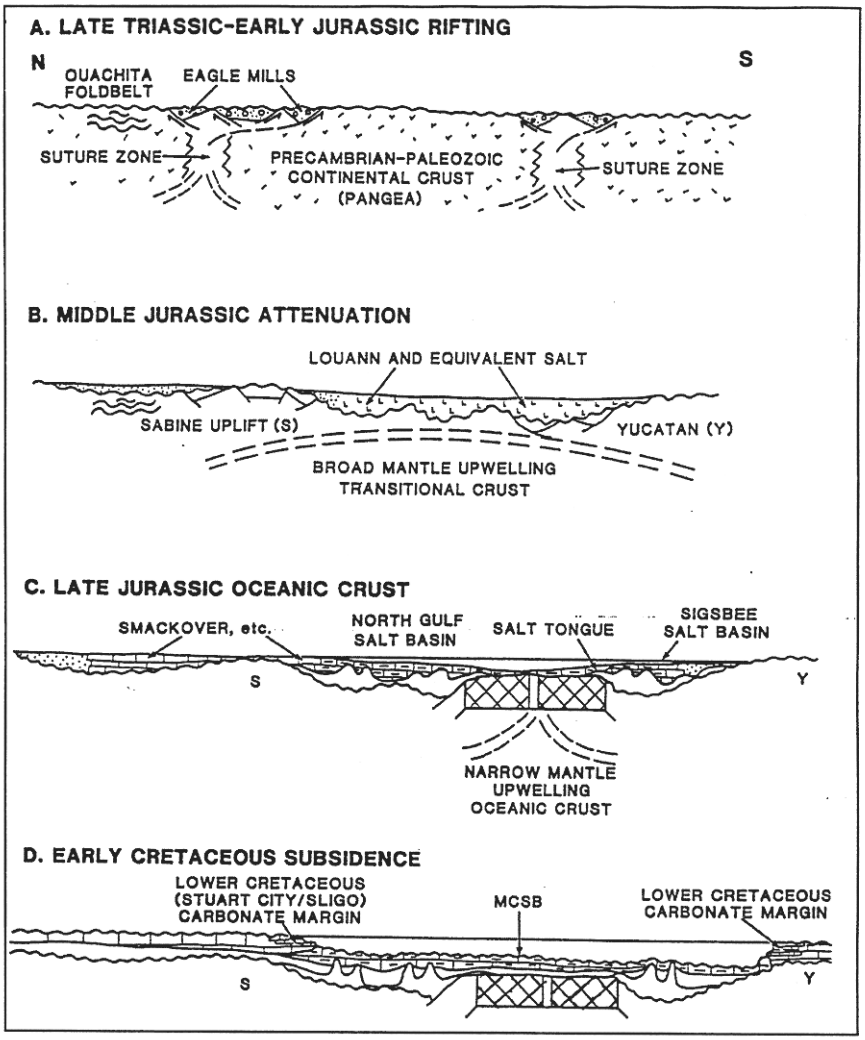

Figure 2.12. Structural and depositional history of the Gulf of Mexico basin, with N-S cross sections showing major periods of activity from the Jurassic to recent. (from Buffler, 1991 *in* Spears, 2000).

and Late Cretaceous to recent sediment loading within the Gulf of Mexico (Salvador, 1991) has caused deformation of significant volumes of salt and shale throughout the basin.

2.3.2. Cenozoic Depositional Setting of the Gulf of Mexico

Cenozoic sediment dispersal axes of the Gulf of Mexico basin and the location of basin-margin structural features are shown in Figure 2.13. Principal sediment dispersal axes that have been active during the Cenozoic Gulf of Mexico are the Rio Grande, Houston, Red River, Central Mississippi, and East Mississippi systems. Secondary sediment dispersal axes active during the Cenozoic are the Norias, Carrizo, and Corsair systems (Galloway et al., 2000). The San Marcos Arch and Edwards Plateau appear to be sources of sediment for the Carrizo and Corsair sediment dispersal axes, and the Sabine Uplift appears to be a source of sediment for the Red River sediment dispersal axis.

Principal depositional systems tracts active in the Gulf of Mexico throughout the Cenozoic are shown in Figure 2.14. In this figure, I shows fluvial→ delta→ delta-fed apron systems tract, II shows coastal plain→ shore zone→ shelf→ shelf-fed apron systems tract, and III shows delta flank→ submarine fan systems tract. Figure 2.15 illustrates the chronology of Cenozoic depositional sequences of the Gulf of Mexico, as described by Galloway et al. (2000). The term 'depisode' is used by Galloway et al. (2000) to refer to "genetic sequences that record principal basin-filling depositional episodes." The relative age and genetic sequence associated with each depisode identified by Galloway et al. (2000) is shown in Table 2.2.

2.3.3. Paleogeographic Reconstructions of Selected Depisodes

A paleogeographic reconstruction map was made by Galloway et al. for each of the major depisodes for the northern Gulf of Mexico from the Paleogene through the Pleistocene.

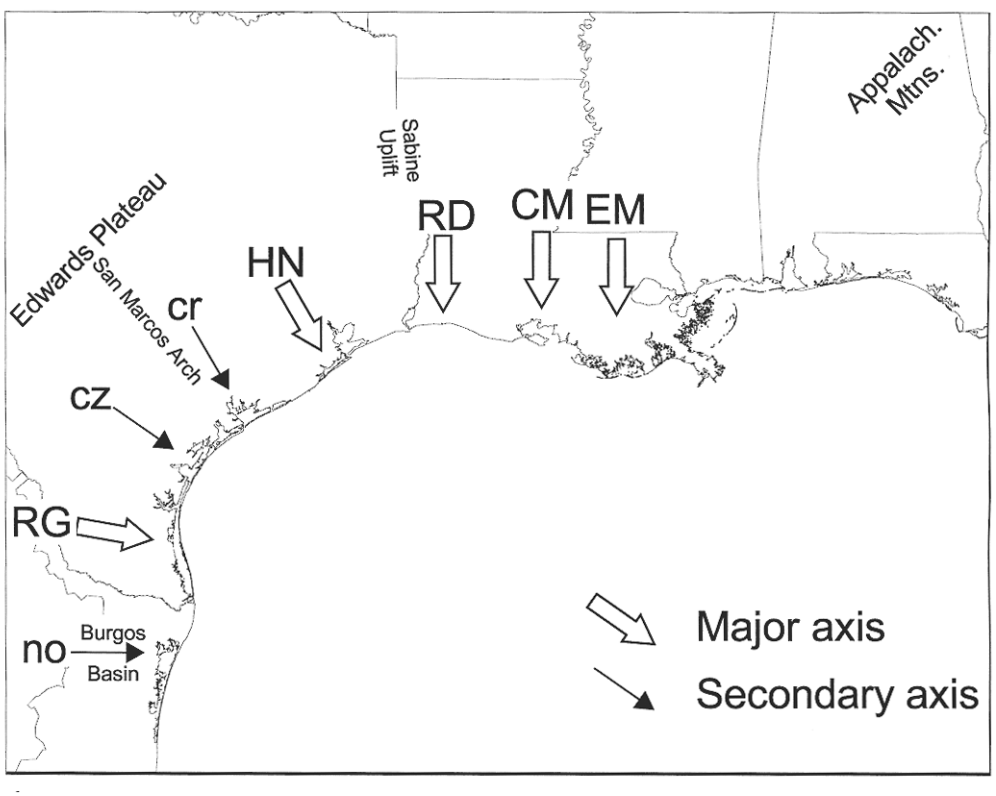

Figure 2.13. Principal (caps) and secondary (lower case) Cenozoic sediment dispersal axes of the Gulf of Mexico and location of basin-margin structural features. Note identification of symbols: no=Norias; RG=Rio Grande; cz=Carrizo; cr=Corsair; HN=Houston; RD=Red River; CM=Central Mississippi; EM=East Mississippi (from Galloway et al., 2000).

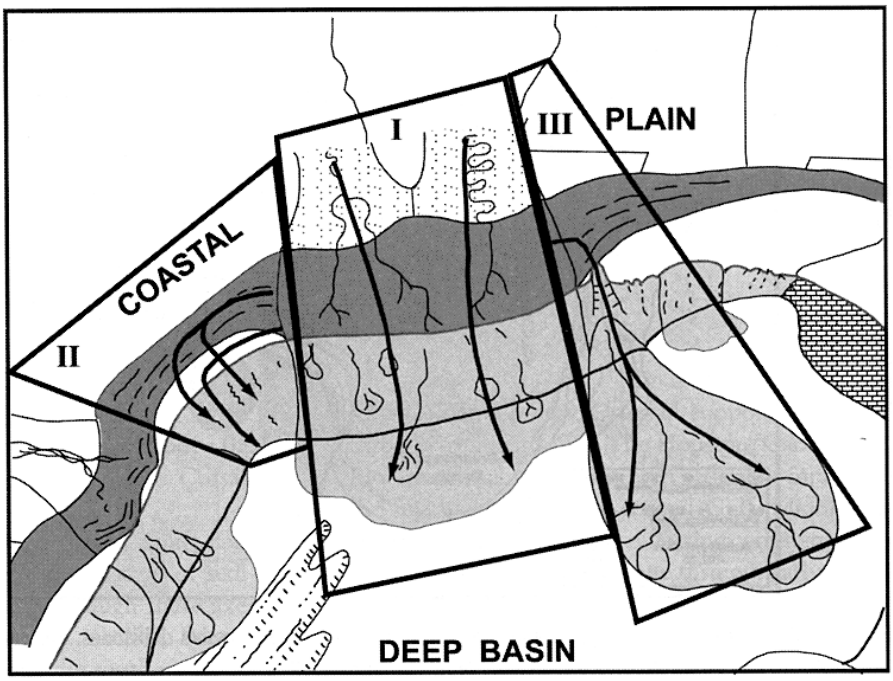

Figure 2.14. Depositional systems tracts active during the Cenozoic in the Gulf of Mexico (from Galloway et al., 2000). I refers to fluvial→ delta→ delta-fed apron systems tract, II shows coastal plain→ shore zone→ shelf→ shelf-fed apron systems tract, and III shows delta flank→ submarine fan systems tract.

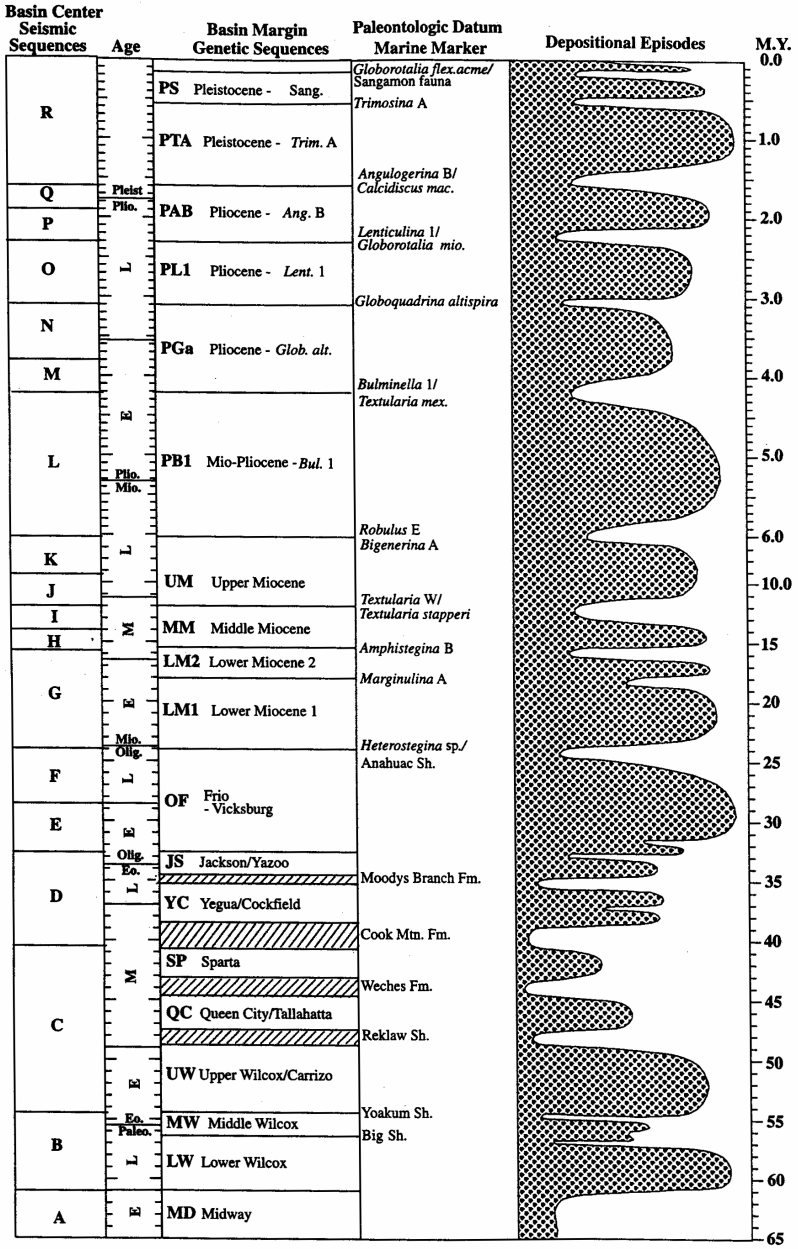

Figure 2.15. Chronology of Gulf of Mexico Cenozoic genetic sequences and their bounding marine shale units and paleontologic markers by Galloway et al. (2000). Genetic sequences record principal basin-filling depositional episodes, referred to as depisodes. Changes in amplitude of depositional episode curve reflect relative volumetric significance (Galloway et al., 2000).

Table 2.2. Basin-Margin Depositional Episodes of the Northern Gulf of Mexico, as defined by Galloway et al., 2000.

Abbreviation	Basin-Margin Sequence
PS	Sangamonian
PTA	*Trimosina* A
PAB	*Angulogerina* B
PL1	*Lenticulina* 1
PGa	*Globoquadrina* a
PB1	*Bulminella* 1
UM	Upper Miocene
MM	Middle Miocene
LM2	Second Lower Miocene
LM1	First Lower Miocene
OF	Frio-Vicksburg
JS	Jackson
YC	Yegua/Cockfield
SP	Sparta
QC	Queen City
UW	Upper Wilcox/Carrizo
MW	Middle Wilcox
LW	Lower Wilcox
MD	Midway
UK	Upper Cretaceous

The evolution of different depositional environments that have occupied the Texas Gulf Coast region throughout the Cenozoic can be traced on these maps. Only those paleogeographic reconstruction maps for selected Miocene and younger depisodes will be shown here.

According to the paleogeographic reconstructions of Galloway et al. (2000), the Matagorda Island offshore area was draped by the West Gulf Basin Floor Apron during most of the Lower and Upper Wilcox depisodes (61-48.5 Ma). Influences from the Carrizo fluvial complex and the Rosita deltaic complex, as well as the nearby Yoakum Canyon/Fan Complex contributed a high sediment load in the Upper Wilcox. The Middle Eocene Queen City depisode marks a period of weak wave-dominated deltas and extensive wave-dominated barrier/strandplain complexes along much of the Texas Gulf Coast that delivered little to no clastic sediment to the Matagorda Island offshore area. During the Late Eocene Yegua depisode the Falcon delta formed a minor axis of sediment supply that was later transformed into a broad barrier/strandplain complex with decreased sediment supply.

The Oligocene represented a period of both increased tectonic activity and sediment supply within the Gulf of Mexico, especially along the Texas Gulf Coast. The Early Frio/Vicksburg depisode is characterized by a reactivated clastic sediment source from the west as a result of active volcanism in the Sierra Madre Occidental combined with uplift of the Lower Cretaceous El Abra carbonates. Numerous major and minor deltas appeared within the Frio/Vicksburg depisode along the Texas gulf coast.

Early Miocene depisodes within the Gulf of Mexico represented the beginning of a shift in major sediment supply axes from the western margin of the Gulf toward the central Gulf as the Mississippi system began to develop. Sediment supply during the Early Miocene at Matagorda Island was relatively low (Figure 2.16), along with most of the Texas coast,

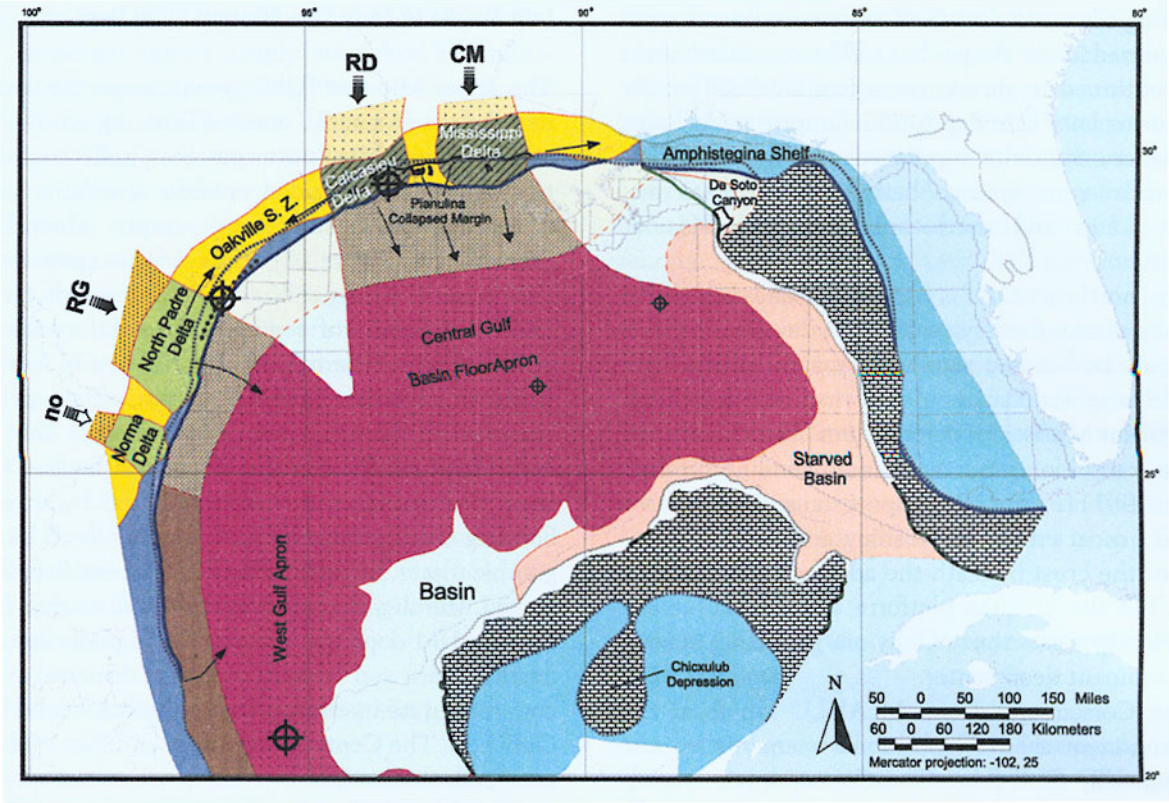

Figure 2.16. Paleogeography of the Early Miocene depisode (from Galloway et al., 2000). Sediment supply began to move away from the Texas Gulf Coast as the Mississippi system began to develop, with the exception of the *Marginulina* A marine shale tongue. Cross-hatchured circles represent active depositional axes, with brief descriptions given for each of the differently colored regions in the figure.

with the notable exception that this depisode contained the prominent *Marginulina A* fauna deposited as a marine shale tongue. The Middle Miocene depisode represents an increase in sediment supply to the Texas Gulf Coast as the Corsair delta and Corsair slope apron prograde basinward (Figure 2.17) of the prominent Corsair fault zone. Late Miocene depisodes of the Texas Gulf Coast are dominated by a broad sandy strand plain as the central Gulf accumulates large deltas and fans. During the Late Miocene depisodes small, wave-dominated, platform systems are common along the Texas coast, and the Corsair delta remained a minor sediment dispersal axis in the Matagorda Island offshore area (Figure 2.18).

The Texas Gulf Coast was sediment starved in the Matagorda Island offshore area during the Pliocene and Pleistocene relative to previous depisodes (Figure 2.19), and contained only a few minor sediment dispersal pathways sporadically throughout most of the Plio-Pleistocene intervals. This reflects the shift in major sediment dispersal axes completely away from the western Gulf and toward the central Gulf. Positions of Cenozoic shelf edge margins at the end of each successive depisode are illustrated in Figure 2.20.

2.3.4. Cenozoic Depositional Setting of the Texas Continental Shelf

Morton et al. (1985) described sedimentation of the Texas continental shelf, and a review is presented here. A generalized stratigraphic section that illustrates relations between onshore formations, principal offshore lithofacies, biostratigraphic zones, and depositional cycles of the Oligocene and Miocene Series, Texas continental shelf is shown in Figure 2.21 (Morton et al., 1985). A series of major and minor regressive and transgressive events are recorded in the sediments beneath the Texas continental shelf (Rainwater, 1964 *in* Morton et al., 1985). Facies associated with Oligocene-Miocene depositional cycles include

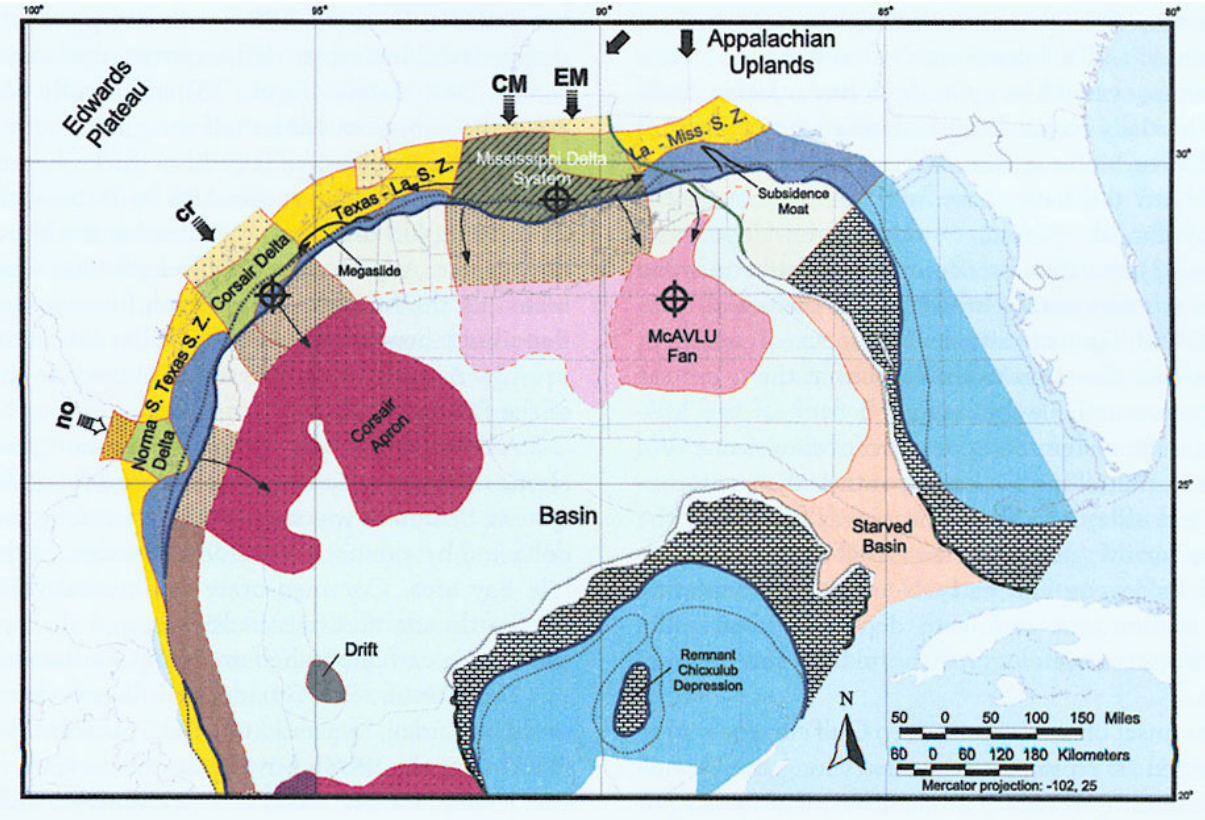

Figure 2.17. Paleogeography of the Middle Miocene depisode (from Galloway et al., 2000). Sediment supply returned to the Texas Gulf Coast with progradation of the Corsair Delta and Corsair Slope Apron basinward of the Corsair fault zone. Cross-hatchured circles represent active depositional axes, with brief descriptions given for each of the differently colored regions in the figure.

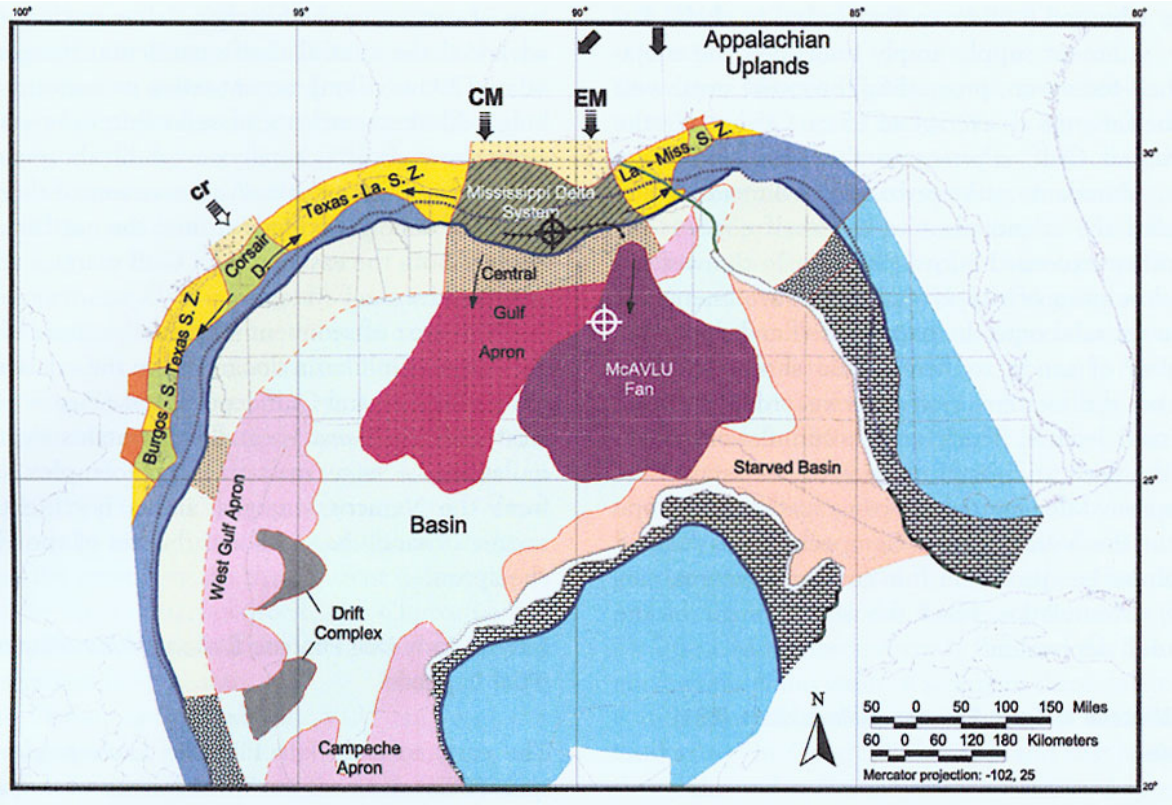

Figure 2.18. Paleogeography of the Late Miocene depisode (from Galloway et al., 2000). The Texas Gulf Coast was dominated by a broad sandy strandplain as large deltas and fans accumulated in the central Gulf. Cross-hatchured circles represent active depositional axes, with brief descriptions given for each of the differently colored regions in the figure.

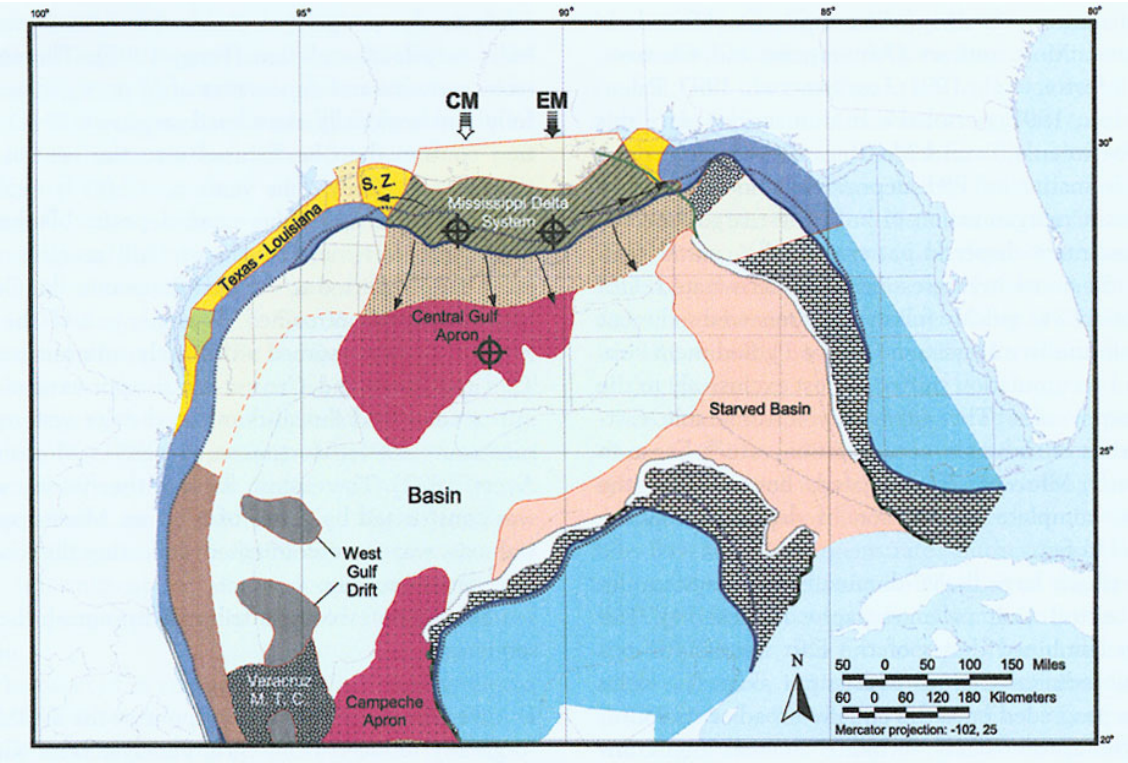

Figure 2.19. Paleogeography of the *Buliminella* 1 depisode (from Galloway et al., 2000). The Texas Gulf Coast was sediment starved for most of the Plio-Pleistocene, reflecting a shift in major sediment dispersal axes away from the western Gulf and into the central Gulf. Cross-hatchured circles represent active depositional axes, with brief descriptions given for each of the differently colored regions in the figure.

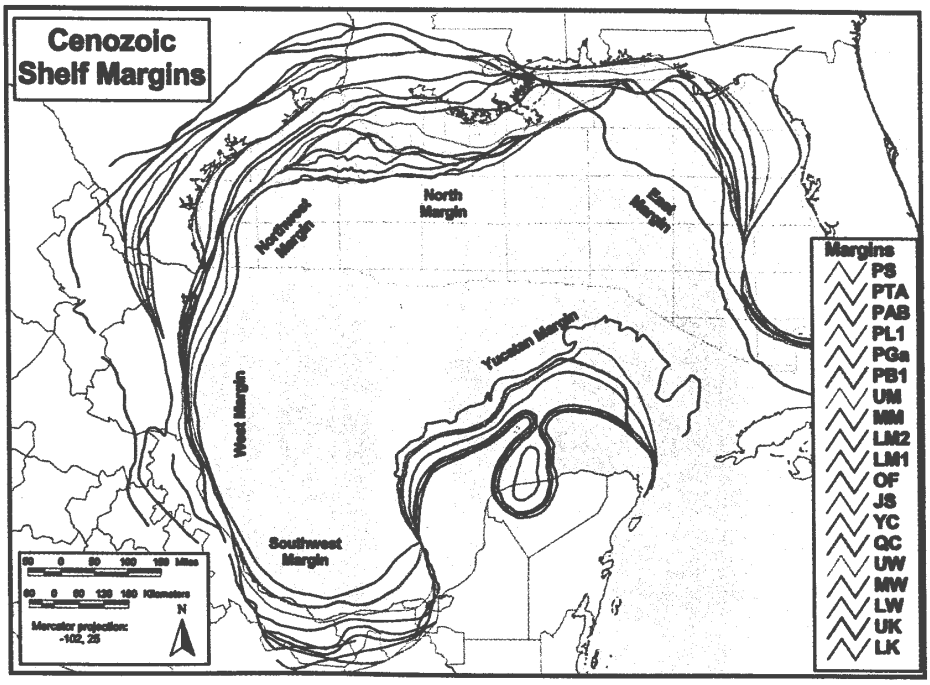

Figure 2.20. Relative positions of Cenozoic shelf edge margins at the end of each successive depisode (from Galloway et al., 2000).

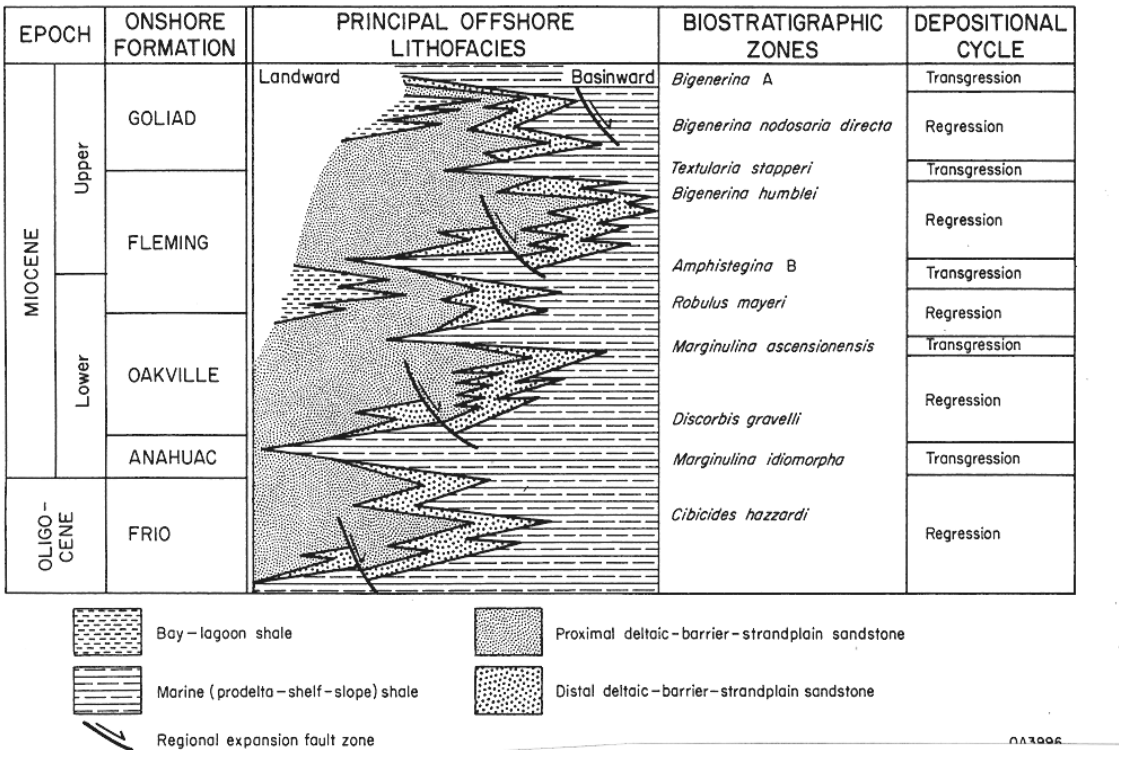

Figure 2.21. Generalized stratigraphic section showing relationships between onshore formations, offshore lithofacies, biostratigraphic zones, and depositional cycles of the Oligocene and Miocene on the Texas continental shelf (from Morton et al., 1985).

bay-lagoon shales, marine (prodelta-shelf-slope) shales, proximal deltaic-barrier-strandplain sandstones, and distal deltaic-barrier-strandplain sandstones. These depositional and erosional events are due to both extrabasinal forces, such as sea-level fluctuations and stream piracy, and variations in intrabasinal forces, such as sediment supply and subsidence.

According to the discussion presented in Morton et al. (1985) the following sequence of events is responsible for Oligocene-Miocene deposition along the Texas continental shelf. Deltas that occupied the Houston and Rio Grande embayments during the Oligocene were responsible for depositing sediments of the Frio Formation. These deltas then retreated landward during a regional marine transgression, and were subsequently buried by the Anahuac Shale. Lower Miocene deposits came from deltas and strandplains that occupied positions similar to and inherited from ancestral Frio deltas, yet these Lower Miocene deltas prograded well beyond the Frio shelf margin. Later transgression buried the Lower Miocene deltas, which were overlain by a thick marine shale containing the *Amphistegina* B foraminiferal zone (Morton et al., 1985).

With continual rise in relative sea level during the Lower Miocene, the deltas retreated landward and a broad barrier-lagoon system developed along the central Texas coast. In the Late Miocene a single large delta occupied the former interdeltaic embayment and prograded far beyond the Lower Miocene shelf margin, changing the paleogeographic setting of the Texas coast markedly. This large delta was also abandoned, transgressed, and buried by a thick marine shale containing the *Bigenerina* A foraminiferal zone. During this terminal transgression a broad barrier-lagoon system developed along the central Texas coast (Morton et al., 1985).

Lower Miocene depositional systems are reported in Seni et al. (1997) for the Texas Gulf Coast. Figure 2.22 shows the range of depositional systems that were active during the

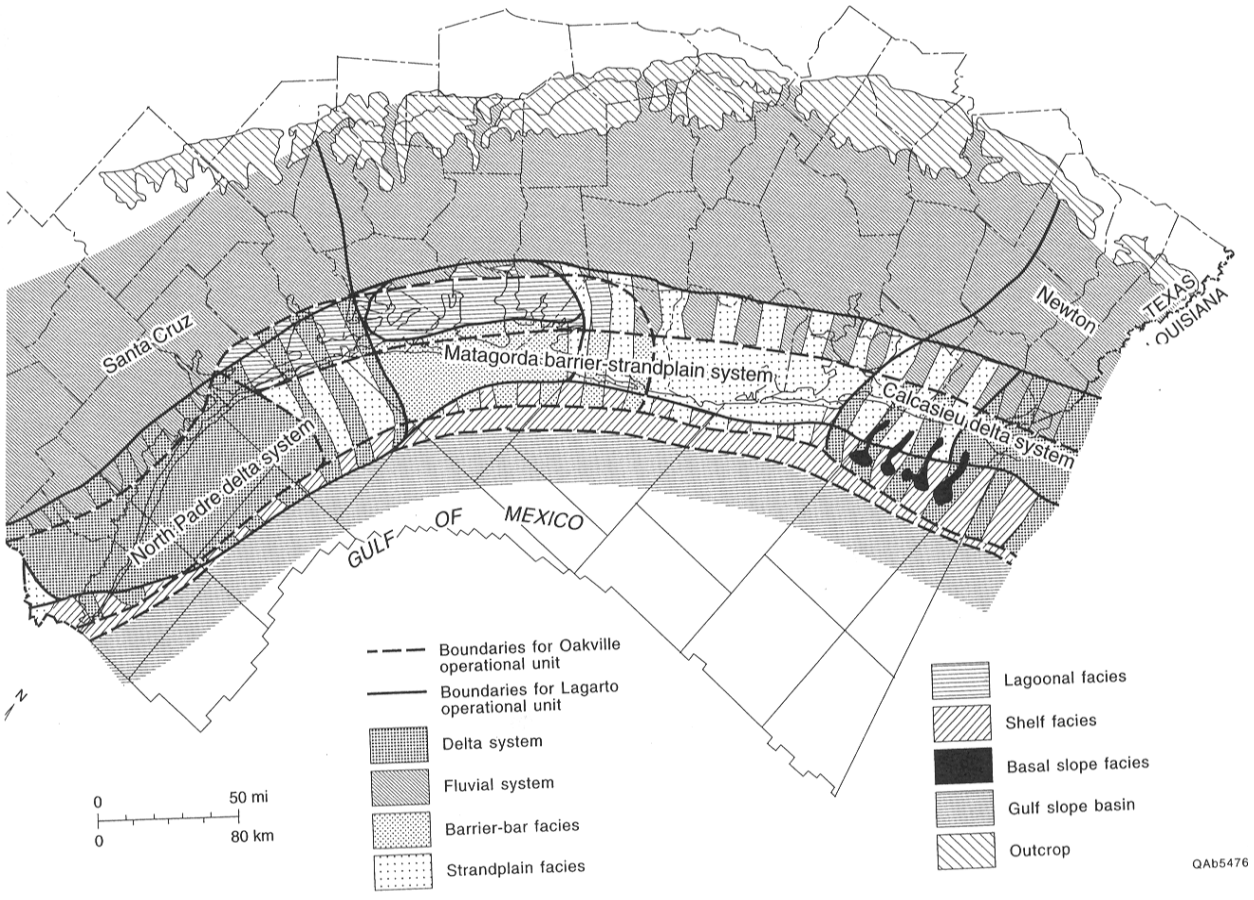

Figure 2.22. Lower Miocene depositional systems of the Texas Gulf Coast. Three major systems were active during this period, the North Padre delta system in the south, the Matagorda barrier-strandplain in the central portion of the coast, and the Calcasieu delta system in the northern portion of the coast (from Seni et al., 1997, after Galloway et al., 1986).

Lower Miocene in Texas. The Matagorda barrier-strandplain system consisted of strandplain facies, barrier-bar facies, fluvial systems, lagoonal facies, and shelf facies. The North Padre delta system was active to the south of the Matagorda barrier-strandplain system, and the Calcasieu delta system was active to the north of the Matagorda barrier-strandplain system during the Lower Miocene (Seni et al., 1997).

2.3.5. Miocene Depositional Environment of the Matagorda Island Offshore Area

In Figure 2.23 a well-log cross-section represents Miocene sections along strike for the Texas Gulf Coast in the Matagorda Island offshore area. Note identification of both submarine fan and progradational depositional environments in this figure, as well as the locations of the Lower Miocene 1 Chronozone boundary and the reservoir interval. Facies represented in the Miocene and younger intervals of the Matagorda Island offshore area typically included fully marine facies, transitional marine facies, and fresh-brackish deltaic facies (Seni et al., 1997).

2.4. Sediment Diagenesis

Only two studies on sediment diagenesis specific to the Matagorda Island area have been published (Brewster, 1998; Klein, 1998). Because there are few studies specific to the Matagorda Island area, previous studies on regional diagenesis are useful for comparison. Research on diagenetic reactions occurring within sediments of the Texas Gulf Coast performed by Land, Lynch, and Milliken are of particular interest in this study. A brief review of previous research on diagenesis of sediments from the Texas Gulf is presented here.

2.4.1. Previous Research on Sediment Diagenesis along the Texas Gulf Coast

Previous research on diagenesis and clay mineralogy of the Texas Gulf Coast has been extensive (Taylor, 1990; Jiang et al., 1995; Lynch et al., 1995; Lynch, 1996; Lynch and

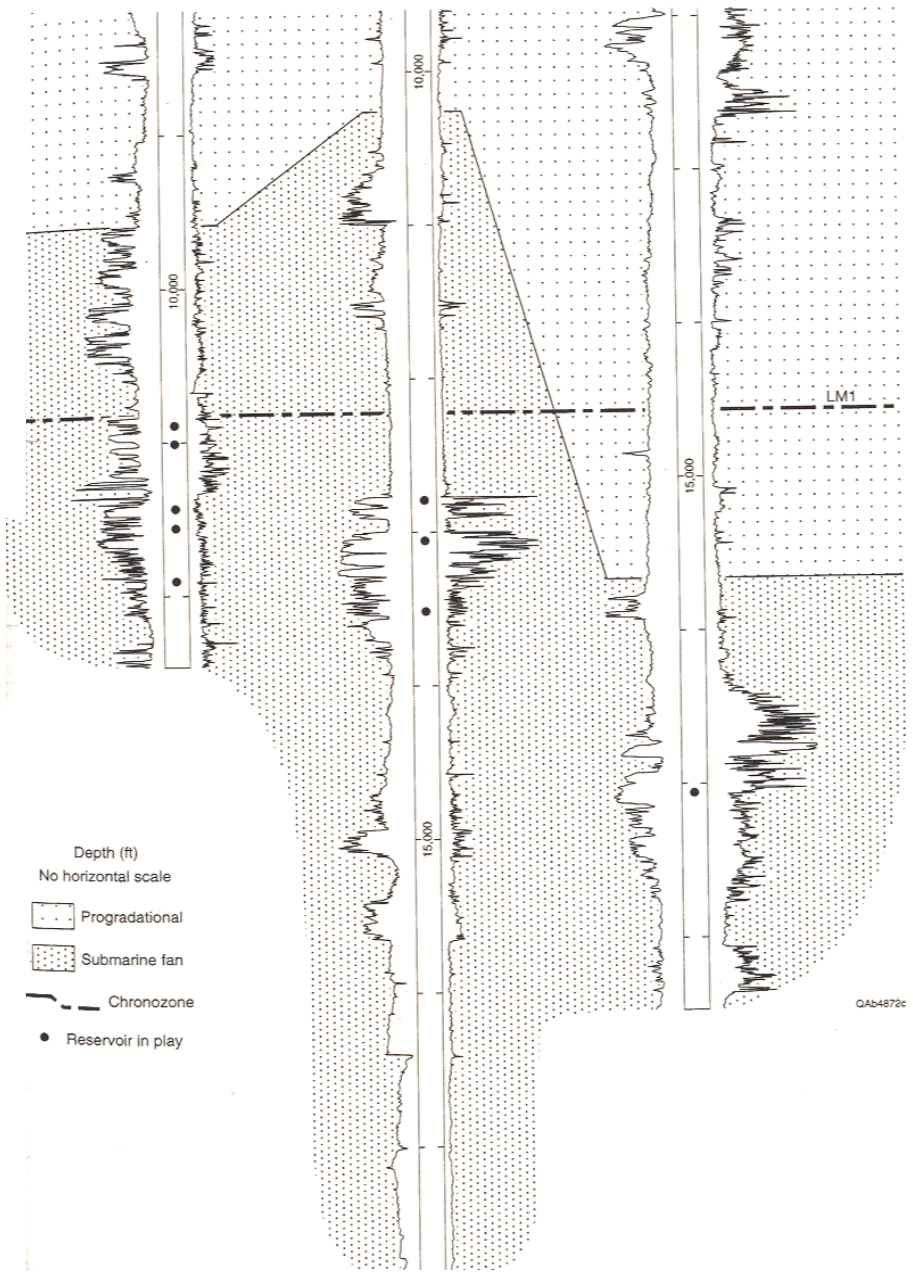

Figure 2.23. Regional Miocene SP-resistivity well log cross-section along strike of the Texas Gulf Coast across the Matagorda Island offshore area (after Seni et al., 1997). LM1 represents a regional marker within the Lower Miocene.

Land, 1996; Taylor and Land, 1996; Land et al., 1997; Lynch, 1997; Lynch et al., 1997; Land and Milliken, 2000). Burial diagenesis in the Texas Gulf Coast has been the subject of debate for a considerable amount of time. A major focus of this debate involves the nature of the relation between sandstone diagenesis and shale diagenesis.

2.4.2. Debate over Shales as Open versus Closed Geochemical Systems

Many researchers, such as Hower et al. (1976), Eslinger et al., (1979), Pollastro (1985), Jennings and Thompson (1986), and Pearson and Small (1988), concluded that shale diagenesis is a closed system. A closed system implies that there is no exchange of mass with adjacent sandstones. Other researchers, however, disagree with the notion that shale diagenesis is a closed system. Boles and Franks (1979), Howard (1979), Altaner et al. (1984), Moncure et al. (1984), Hower (1983), Land et al. (1997), Lynch (1996, 1997), and Land and Milliken (2000) all suggest that Gulf of Mexico siliciclastic sediments are open chemical systems, where mass is exchanged between shales and adjacent sandstones.

The principal diagenetic reaction that occurs within deeply buried Gulf Coast mudrocks is the clay mineral transformation from smectitic illite-smectite (I-S) to more illitic illite-smectite (Awwiller, 1993). This reaction is at the center of the debate over burial diagenesis. Many diagenetically-reactive components are mobilized during the smectite-illite transformation, including CaO, K_2O, SiO_2, MgO, B, and Fe_2O_3. These components play a key role in defining diagenesis at the Matagorda Island 519 field and in describing the potential relation between diagenesis and the other primary processes of interest in this thesis, overpressuring and fluid flow.

Lynch performed several studies along the entire span of the Texas Gulf Coast that concentrate on burial diagenesis of both sands and shales within the Oligocene Frio Formation of south Texas (Lynch, 1996; Lynch and Land, 1996; Lynch, 1997; Lynch et al.,

1997; Lynch et al., 1999). Results from studies performed by Lynch and colleagues suggest that an open system of mass exchange exists between sands and shales along the Texas Gulf Coast. Lynch's results also suggest that overpressuring is influenced by diagenesis, especially the conversion of smectite to illite, along with quantifying both reaction rates and mineral chemistry associated with the smectite-to-illite transition.

2.4.3. Research on Texas Gulf Coast Sediment Diagenesis Relevant to This Study

Studies conducted by Lynch and colleagues provide the most reasonable proxy for subsurface conditions within the reservoir interval at Matagorda Island 519, because they have been conducted on sediments of approximately the same age and geographic location. Clay mineralogy determined from XRD analysis performed by Lynch (1997) is especially useful in this study because it provides initial mineral chemistry from which to calculate normative mineralogy at Matagorda Island 519. Section 5.2 of this thesis provides detailed description of the results from this technique.

2.4.4. Research on Sediment Diagenesis at MI 519 Relevant to This Study

The Amoco Production Company has conducted previous research at the Matagorda Island 519 field, as described by Brewster et al. (1998) and Klein et al (1998). In order to understand the reservoir quality of the field, research at Amoco was focused on assessing the geochemical nature of sediments in the reservoir interval. As part of that research, whole-rock core samples were used to determine weight percent values for numerous oxides, rare earth elements (REE), and trace elements. Whole-rock and clay fraction samples were used to determine mineralogy by X-ray diffraction (XRD). Thin sections were also made for selected intervals from these core samples. Results from the oxide weight percent determination and XRD determination were made available for this thesis research.

Appendix A of this thesis contains spreadsheets of bulk chemistry and XRD mineralogy results.

Results and conclusions from the Amoco research project have explicit implications for flow regimes, pressure regimes, and diagenesis at the Matagorda Island 519 field. Amoco researchers (Brewster et al., 1998; Klein et al., 1998) have identified four distinct vertical compartments or intervals at the Matagorda Island 519 field, based on resistivity, mudweights, and diagenetic changes. These are labeled compartments A, B, C, and D in Figure 2.24. According to Brewster et al. (1998), compartment A represents a zone of high-resistivity sandstones (1.5-4 ohms) that act as a "…classic caprock formed by calcite mineral precipitation from fluids periodically expulsed from the pressurized zone." The overpressure transition zone is believed by Amoco to occur at the boundary between compartments A and B, and is approximately 300-ft (100-m) thick (Brewster et al., 1998). At this transition resistivity decreases from 1.5 ohms to 0.9-1.0 ohms, and drilling mudweight increases from 13 to 17 lbs/gal (Brewster et al., 1998).

Compartment B, which is approximately 800-ft (240 m) thick, is the first zone identified as overpressured by Amoco. In compartment B the conversion of smectite to illite is observed, with percent smectite decreasing from 50 to 25 % within this depth interval. The second overpressured zone is compartment C, which is approximately 1700-ft (500 m) thick and shows increasing resistivity at the base. Shale resistivity ranges from 0.3-0.5 ohms in compartment C, and drilling mudweights are 18 lbs/gal and higher (Brewster et al., 1998).

Compartment D is identified as the reservoir zone. At the top of compartment D resistivity increases to 1-2 ohms, drilling mudweights decrease from 18 lbs/gal and higher to 17 lbs/gal. The upper 200 feet (60 m) of compartment D is identified as tightly ferroan-

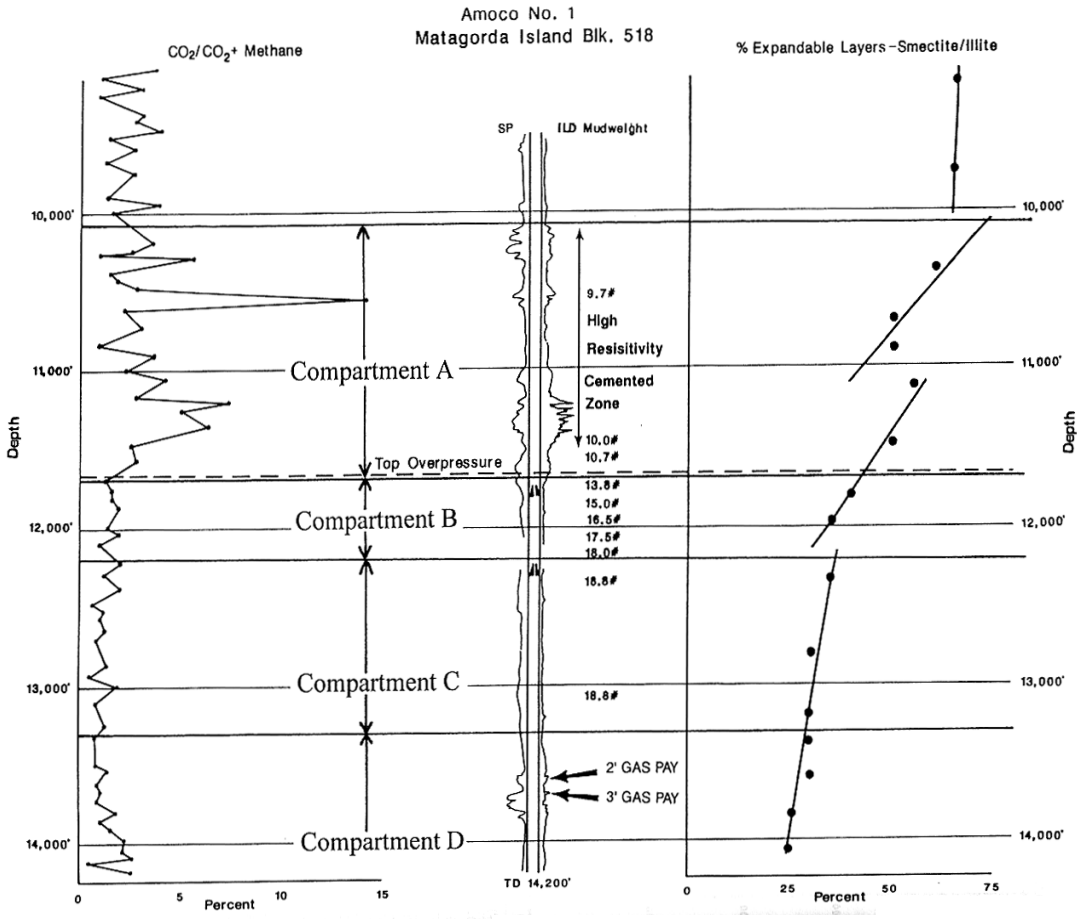

Figure 2.24. Four distinct pressure compartments have been identified by Amoco to exist at Matagorda Island 519, based on conductivity log response (from Klein et al., 1998). Data shown is from well 5169.

calcite cemented sandstones having 20-23 percent cemented intergranular pore space (Brewster et al., 1998). This intergranular pore space becomes hydrocarbon saturated within the deeper section of compartment D, which contains the productive reservoir (Brewster et al., 1998).

Production at the Matagorda Island 519 field is from overpressured Lower Miocene deltaic sandstones at depths of between 13,500 to 16,000 ft (Brewster et al., 1998). The reservoir sands have porosities of 20 to 25 percent and permeabilities of 0.02 to 300 md. The high porosities and permeabilities are the result of dissolution of calcite cements. As will be discussed, the field has had a diagenetic history similar to that of the nearby Picaroon field, Corsair trend (Taylor, 1990; Taylor and Land, 1996). Brewster et al. (1998) concluded that these compartmentalized reservoirs were formed as a result of episodic fluid flow events. Reservoir quality was enhanced by diagenetic reactions occurring within the overpressured zone, as exemplified by secondary porosity generated by dissolution of calcite (Brewster et al., 1998; Klein et al., 1998).

Figure 2.25 shows a photomicrograph taken by Amoco from a thin section of core samples from well 88562 at a depth of 14,971 feet (4569 meters) (Brewster, personal communication). Petrographic observations made from photomicrographs such as the one seen here are useful in providing direct evidence of diagenetic reactions in pore spaces of sediments. In this figure blue areas represent void spaces created from carbonate dissolution. Petrographic observations led Klein et al. (1998) to propose the following sequence of diagenetic events for the Matagorda Island 519 field. First, mechanical compaction, which was followed by local precipitation of chlorite grain coats on detrital grains. Next, calcite cementation occurred. This was followed by partial to complete dissolution of detrital grains

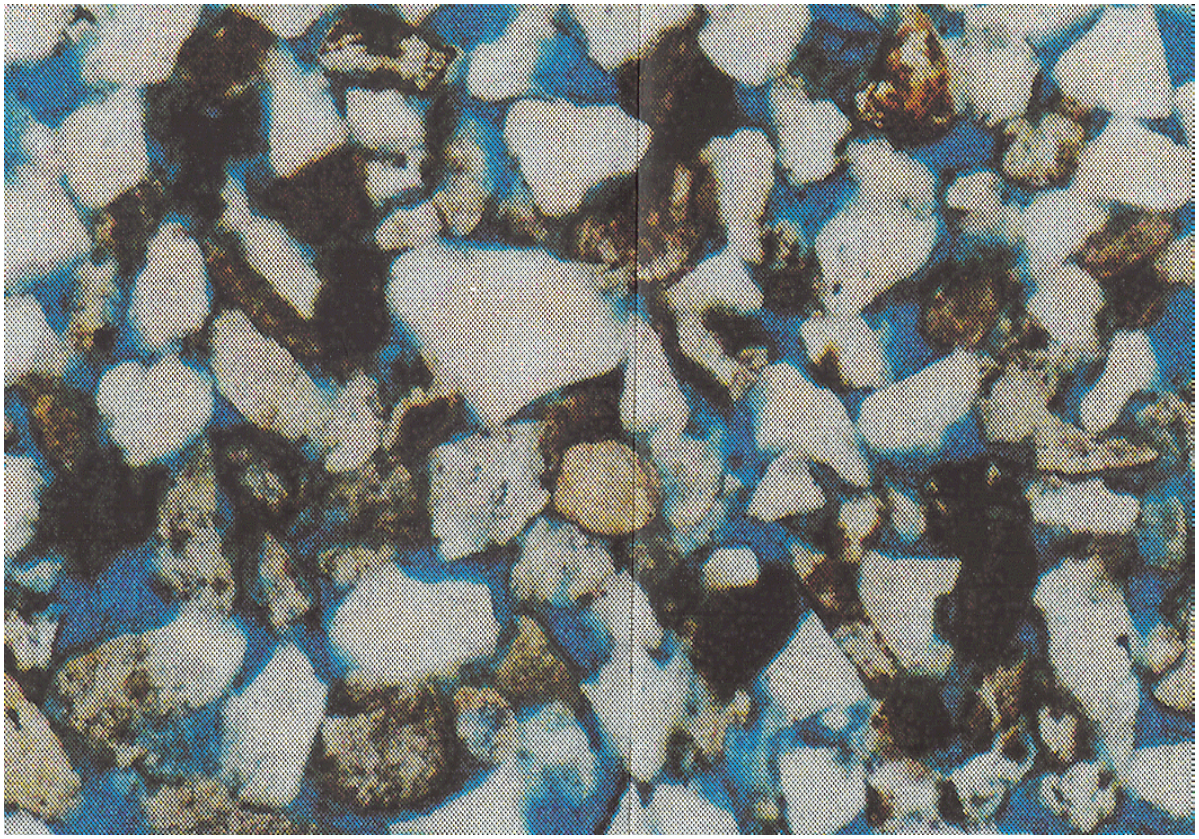

Figure 2.25. Photomicrograph taken from thin section of core sample from well 88562 (Brewster, personal communication).

and calcite cement. Finally, local recementation by ankerite, pyrite, Fe-calcite, barite, and polycrystalline quartz (Klein et al., 1998).

Klein et al. (1998) also concluded that calcite cementation occurred shallow at the Matagorda Island 519, at depths less than 8000 ft (2670 m), based on their data on intergranular volumes, burial history, and sandstone compaction models. Calcite cementation is believed to be the result of episodic fluid flow events that brought hot fluids from depth upward, migrating along the Siph D expansion fault into the Discorbis III sandstone (Brewster et al., 1998). Late-stage mineralization associated with this fluid migration event is responsible for the diagenetic seal at Matagorda Island 519, and this seal is the primary reason that hydrocarbons have accumulated "off-structure" at this field, according to Klein. Figure 2.26 shows the sequence of events leading to the formation of the Matagorda Island 519 field proposed by Amoco (Klein et al., 1998).

2.5. Aqueous Fluids of the Texas Gulf Coast

The composition of aqueous fluids is often directly or indirectly related to diagenetic processes and fluid flow. Taylor and Land (1996) studied the association of allochthonous waters and reservoir quality enhancement in deeply buried Miocene sandstones at the Picaroon Field, Corsair Trend, Offshore Texas. The location of this study area, along with its proximity to the Matagorda Island 519 field, is shown in Figure 2.27. Porosity enhancement, and thus, reservoir quality enhancement, is accomplished via dissolution of calcite cement at the Picaroon Field (Taylor and Land, 1996).

The Picaroon field is located within Brazos area Blocks A-19 and A-20 (Taylor, 1990). It is one of a number of deep overpressured gas fields that occurs along the Corsair trend. Reservoir sands are of middle Miocene age and occur within the Bigeneria humblei

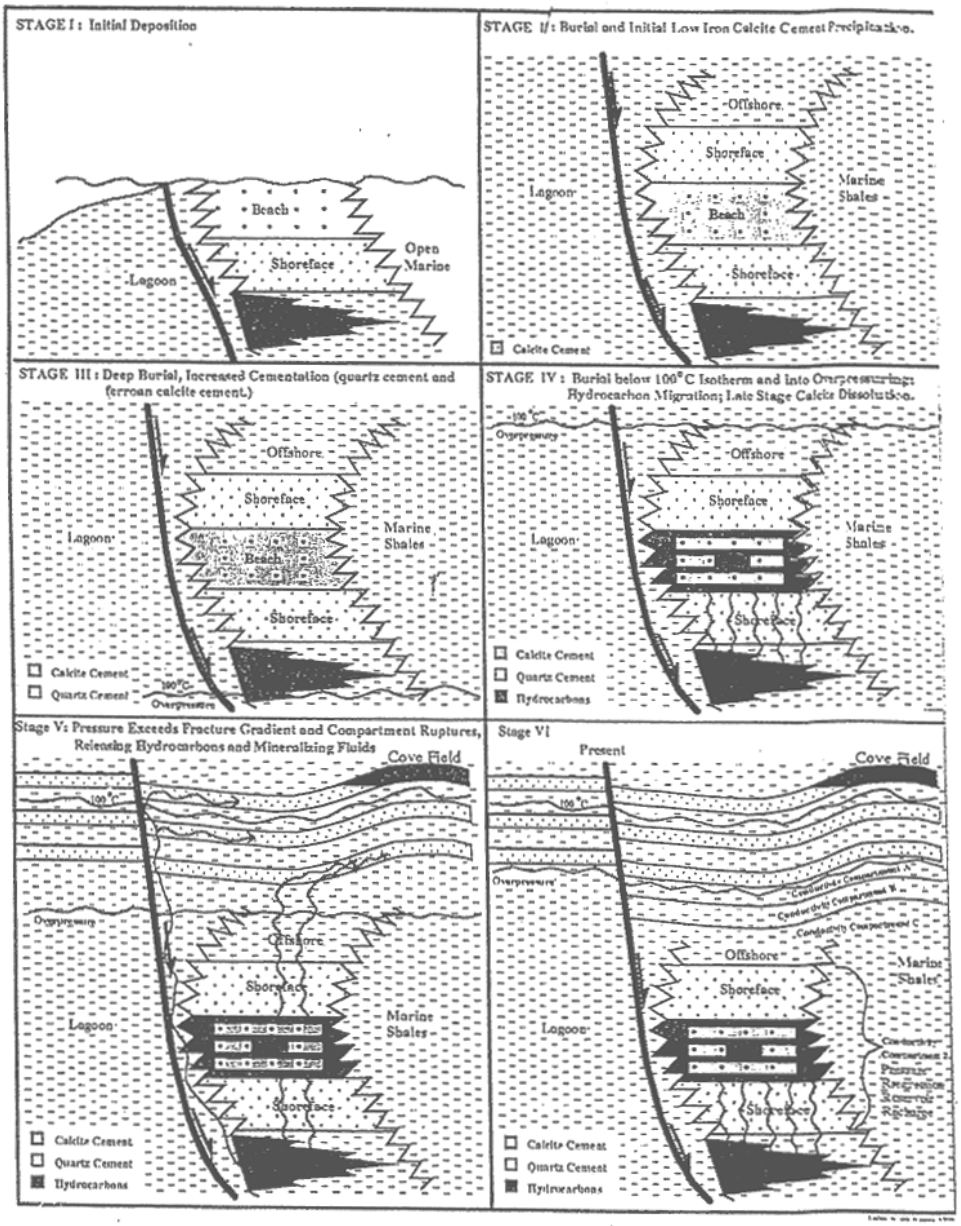

Figure 2.26. Hypothetical sequence of events proposed by Amoco that formed the Matagorda Island 519 field (after Klein et al., 1998).

foraminiferal zones at depths of 4940 to 5180 m (16,200 to 17,000 ft.) The reservoir temperature is approximately 190^{o}C (375F), and the section is highly overpressured with a geostatic ratio of 0.02MPa/m (0.94 psit/ft). The Corsair trend includes the Picaroon and Doubloon fields and Plank prospect. Reservoir sands interpreted as deltaic deposits, primarily from distributary mouth bar and delta front environments. The sands contain substantial amounts of detrital feldspar, carbonate, and lithic fragments and are classified as subarkoses, lithic arkoses, and feldspathic litharenites. Picaroon reservoir sandstones have significantly higher porosities as a result of the development of secondary porosity than do those at Doubloon and Plank (Taylor and Land, 1996).

2.5.1. Paragenetic Histories of MI 519 and Picaroon

Klein et al. (1998) have determined the following sequence of chemical diagenetic events in reservoir sands at MI 519 from petrographic observation: 1) early precipitation of chlorite grain coatings, 2) calcite cementation, 3) dissolution of feldspar, detrital calcite, and calcite cements, and 4) late stage precipitation of ferroan calcite (Ca,Fe)CO_3, ankerite (Ca(Mg,Fe)$(CO_3)_2$), pyrite, barite, sphalerite, and polycrystalline quartz. There is a lateral zoning of the late stage mineral precipitates. From downdip to updip the late cements are dominated ferroan calcite, then ankerite, and finally polycrystalline quartz, barite, and sulfides. The volume of quartz cement is sufficient to signficantly reduce secondary porosity in the updip part of the field.

According to Taylor (1990) the following similar diagenetic sequence occurred at Picaroon: 1) early diagenetic chlorite detrital coatings of detrital grains, 2) dissolution of plagioclase and K-feldspars and the formation of quartz cement, 3) abundant poikilotopic calcite cement, 4) dissolution of both ferroan calcite cements and detrital calcite grains, 5)

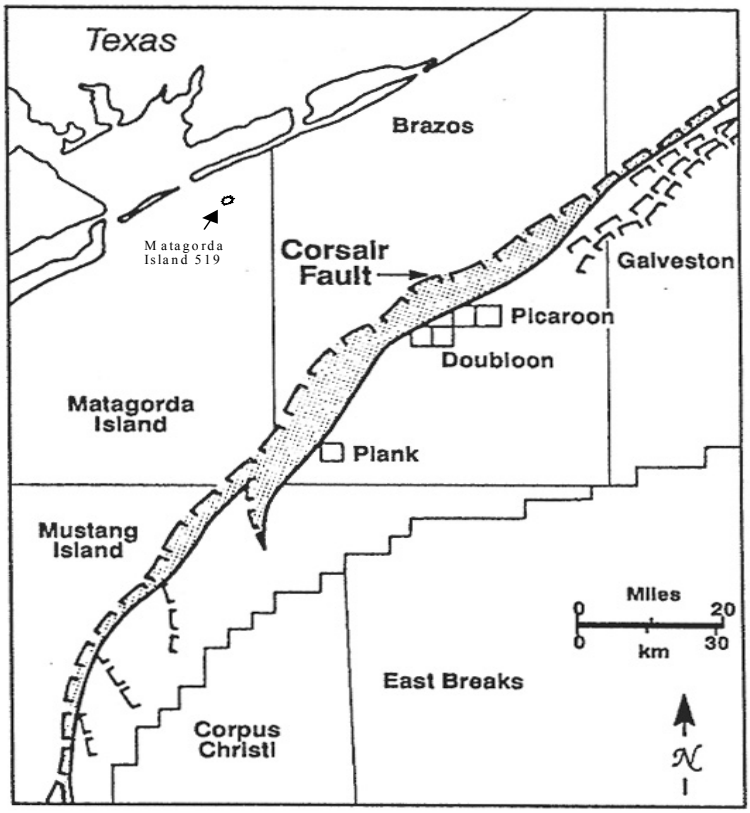

Figure 2.27. Location of the Picaroon field studied by Taylor and Land (1996), along with other fields and prospects in the vicinity of Picaroon, and the Corsair Fault. Matagorda Island 519 is indicated with an asterisk. Note the relative location of this study area to the Matagorda Island 519 study area (modified from Taylor and Land, 1996).

precipitation of ankerite cement containing 12 to 16 mole percent $FeCO_3$. Small amounts of low-Fe sphalerite and barite occur in association with ankerite. There is extensive dissolution of both K-feldspar and plagioclase in the most porous Picaroon sands, suggesting a second stage of feldspar dissolution.

2.5.2. Sr Isotopic Composition of Calcites

Calcite analyzed at MI 519 has $^{87}Sr/^{86}Sr$ values of 0.70805 to 0.71011, and most values are either less or more radiogenic than coeval lower Miocene seawater values of between 0.7083 and 0.7086. The most radiogenic calcite values are found in up dip well 5169 #1 and are attributed by Klein et al. (1998) to the effects of the late stage fluid which precipitated ankerite.

The total range in Sr isotopic composition of calcite is 0.70860 to 0.70839 at Picaroon. An attempt was made by Taylor (1990) to calculate end-member Sr isotopic values for cements and detrital grains. Cements have values of 0.7083 to 0.7086 and the detrital carbonates have Cretaceous values of 0.7066 to 0.7076. The cements are less radiogenic than coeval marine values of 0.7086 to 0.7088, and were most likely derived from older marine carbonates or seawater. The late stage ankerites are more radiogenic and have $^{87}Sr/^{86}Sr$ of 0.70963 - 0.70970. The ankerite is petrographically and chemically similar to late diagenetic ankerites from Eocene Wilcox ss of the Gulf Coast (Boles et al., 19xx). According to Taylor, the fact that the ankerite is much more radiogenic than the calcite indicates that it was not a direct replacement.

2.5.3. Oxygen and Carbon Isotopic Composition of Calcites

Klein et al. (1998) show that there is a linear correlation between $\delta^{18}O$ and $\delta^{13}C$ values of calcite samples analyzed from MI 519, which reflects a mix of detrital and

authigenic carbonate in the samples analyzed. These authors estimate that the endmember authigenic carbonate has a $\delta^{18}O$ of -10 to -8 per mil PDB and a $\delta^{13}C$ value of -4.80 to -2.60 per mil PDB.

Taylor (1996) calculated endmember isotopic compostions for calcite cements at Picaroon, which range from $\delta^{18}O$ of -10.74 to -4.52 and $\delta^{13}C$ of -4.80 to 1.50. The MI 519 and Picaroon cement compositions are thus similar. Late stage ankerite cements at Picaroon fall within this range with an average $\delta^{18}O$ of - 8.0 and an average $\delta^{13}C$ of -2.5. Detrital carbonates have an average $\delta^{18}O$ of -6.5 and a $\delta^{13}C$ of -1.75. Taylor concludes that the $\delta^{13}C$ value reflects dominantly marine carbon source. The more negative values may reflect a minor input of organic C.

2.5.4. Temperature, Depth and Timing of Calcite Cementation

Based on intergranular volumes of approximately 25-35% and calculated mechnical compaction curves, Klein et al. (1998) estimate that the calcite cements in the reservoir sands at MI 519 were emplaced at depths of approximately 1000 to < 8000 ft and that cementation occured prior to 17 ma ago. Klein et al. (1998) estimate calcite cementation temperatures of 205 to 256°F based on precipitation of formation waters having $\delta^{18}O$ value of 4.9 to 5.6 per mil PDB. Klein et al. (1998) note that temperatures this high are inconsistent with shallow depths of cementation, but may reflect precipitation from hot, ascending hydrothermal fluids.

Similar intergranular porosities occur in reservoir sands at Picaroon, and pervasive calcite cementation was thus early and at shallow depths. Taylor (1990), however, presumes the calcite cements at Picaroon were precipitated from formation waters having a $\delta^{18}O = 2$ per mil SMOW and calculates a temperature range of precpitation of 47 to 93^{o}C (Taylor,

1990). The establishment of hard overpressure after calcite may have helped preserve high porosities by inhibiting further compaction.

2.5.5. Quartz Cements

The estimated $\delta^{18}O$ of quartz cement at Picaroon is 28.8 per mil SMOW (Taylor, 1990). This value is consistent with precpitation of quartz from formation waters having a $\delta^{18}O$ composition of 0 to +3 per mil at tenperatures of 50 to 67°C.

2.5.6. Picaroon Field Model

Formation waters in the Picaroon field exhibited elevated salinities of 151 to 243 g/l TDS, with elevated Ca concentrations of 13 to 22 g/l, and heavy $\delta^{18}O$ values, and less radiogenic Sr values relative to formation waters commonly found throughout the Gulf of Mexico Tertiary section. In addition, Picaroon water samples contained unusually high concentrations of other cations, such as Sr, Ba, Fe, Pb, and Zn, and Picaroon sandstones contained late diagenetic fracture-filling ankerite, barite, and sphalerite (Taylor and Land, 1996). Ankerite was found by Taylor and Land to be in oxygen isotopic equilibrium with formation water at temperatures of greater than 147 degrees Celsius indicated by fluid inclusions. Figure 2.28 illustrates the relative timing of diagenetic events observed in Middle Miocene sandstones of the Corsair Trend, Brazos OCS area, offshore Texas, with shading indicating the relative effect of each event on sandstone porosity.

Taylor and Land (1996) propose that Picaroon brines are allochthonous to the Miocene section because they have elemental and isotopic compositions similar to waters produced from Mesozoic reservoirs in south Texas and central Mississippi. Evidence of high quality reservoirs found in association with waters of such unique composition at Picaroon caused Taylor and Land to suggest that a potential link existed between deep sources of

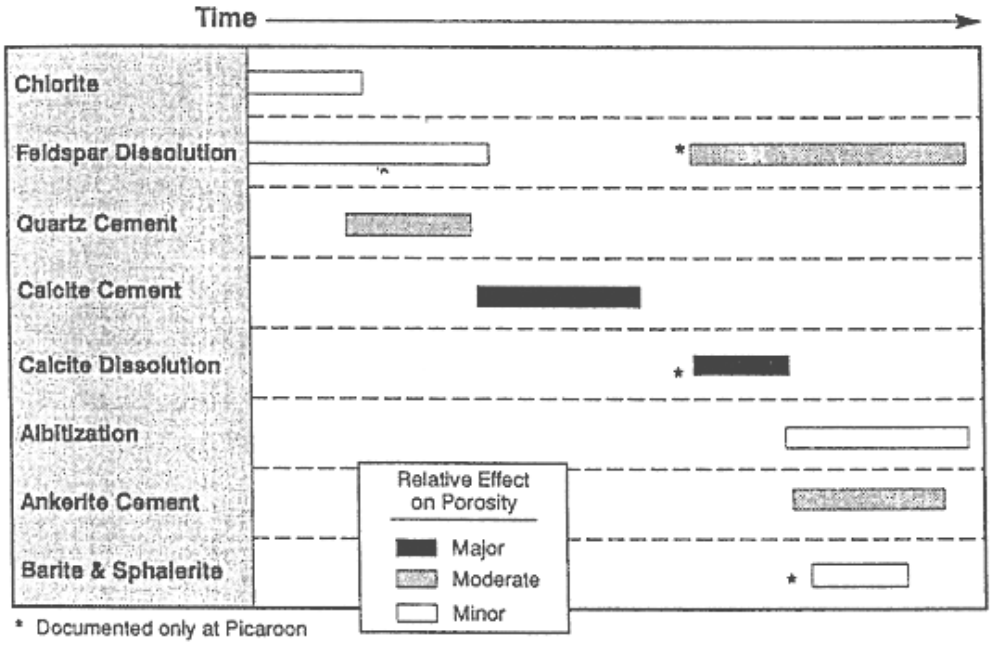

Figure 2.28. Relative timing of diagenetic events observed in middle Miocene sandstones of the Corsair Trend, Brazos OCS area, offshore Texas by Taylor and Land (1996). Note that shading reflects the relative effect of each event on sandstone porosity, and events marked with an asterik were observed only at Picaroon field (from Taylor and Land, 1996).

fluids and carbonate dissolution. The model proposed by Taylor and Land (1996) implies that hot, acidic waters from the underlying Mesozoic section were injected into Picaroon sands along major faults, resulting in significant porosity enhancement (Figure 2.29). According to this model, fluid flow was likely episodic, and driven by periodic buildup and release of geopressures (Taylor and Land, 1996).

2.5.2. Analysis of Groundwater Flow Regimes in Matagorda County, Texas

Compositions of aqueous fluids can often be indicative of fluid flow regimes within a region. Studies such as Dutton (1994) have analyzed groundwater flow in the Gulf Coast aquifer of Matagorda and Wharton Counties, Texas. Dutton (1994) proposed that groundwater flow within this aquifer is responsible for emplacement of a shallow freshwater lense within the youngest marine sediments of offshore at Matagorda Island offshore area.

2.6.Hydrocarbons

2.6.1. Overview of Hydrocarbons in the Gulf of Mexico

Hydrocarbon exploration and production in the Gulf of Mexico has proven to be economically successful, and approximately 9 percent of the world's oil and approximately 11 percent of the world's gas is believed to be located here (Nehring, 1991 *in* Seni et al., 1997). Fields within the offshore Northern Gulf of Mexico contain original proven reserves of approximately 11 billion barrels of oil and condensate and approximately 129 trillion cubic feet (TCF) of gas (Gautier et al., 1995 *in* Seni et al., 1997).

The distribution of hydrocarbon plays in the Northern Gulf of Mexico is shown in Figure 2.30. Play boundaries for the Mesozoic, Oligocene, Miocene, Pliocene, and Pleistocene are marked, as well as the state-federal lease boundary for offshore Texas, Louisiana, and Alabama. Siliciclastic depositional sequences that host hydrocarbons in the Gulf of Mexico are illustrated in Figure 2.31. Depositional styles associated with oil and gas

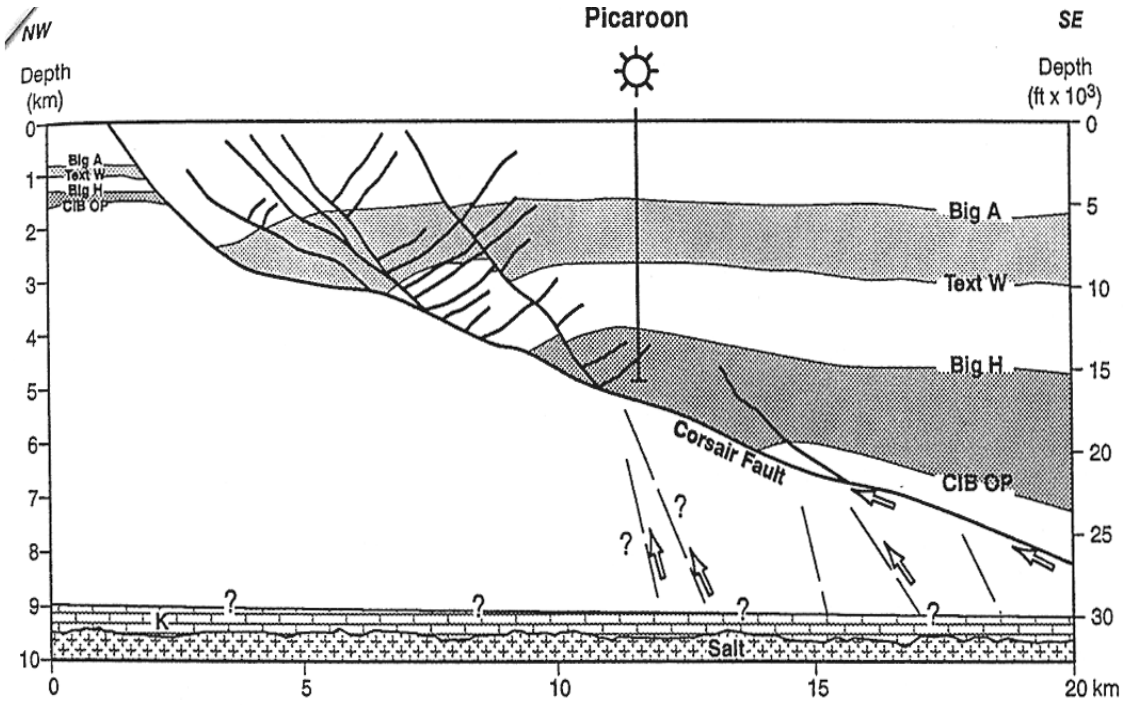

Figure 2.29. Model proposed by Taylor and Land (1996) showing large-scale structural features and regional foraminiferal zones at Picaroon field. According to the model, emplacement of brines from Mesozoic strata into Miocene sands occurred presumably with the main Corsair Fault and other faults serving as conduits (from Taylor and Land, 1996).

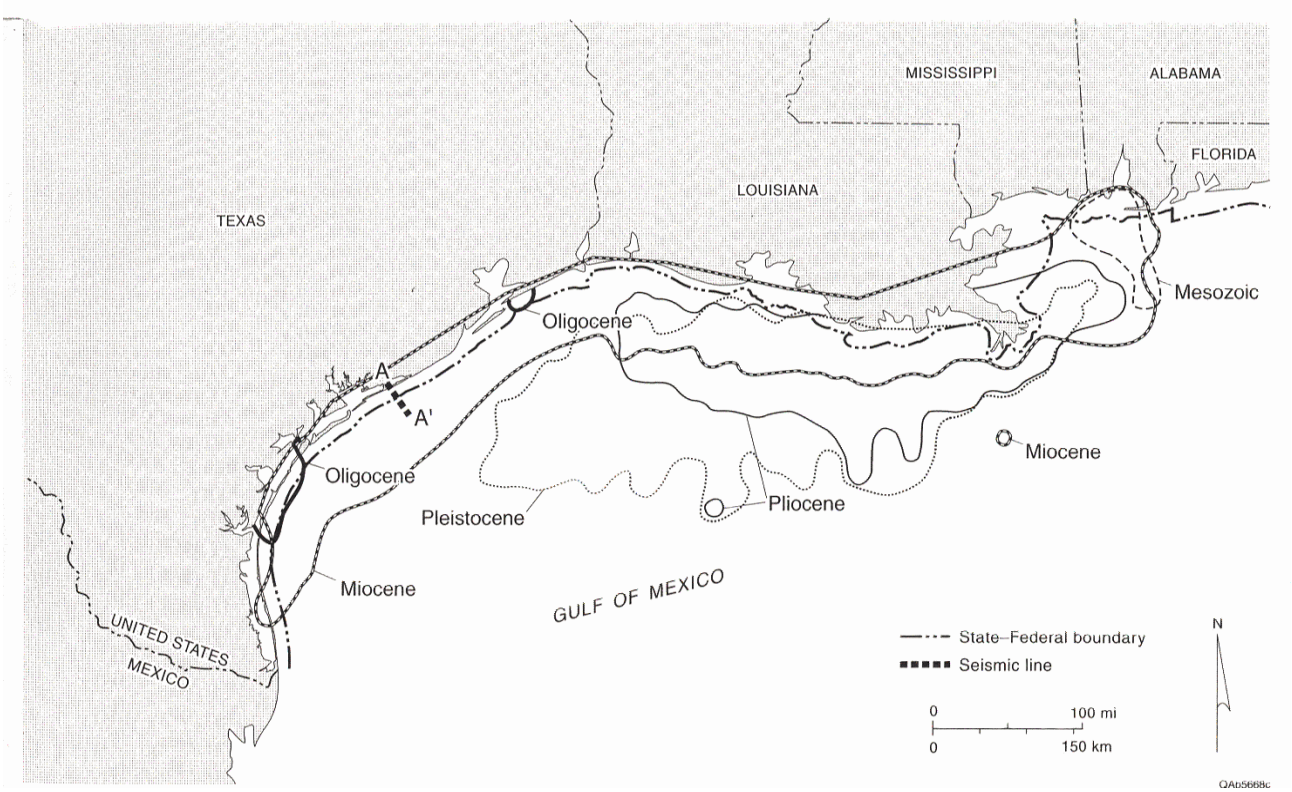

Figure 2.30. The distribution of Mesozoic to Pleistocene hydrocarbon plays in the Northern Gulf of Mexico, with the extent of each play indicated by the respective dashed line for the Mesozoic, Oligocene, Miocene, Pliocene, and Pleistocene (from Seni et al., 1997).

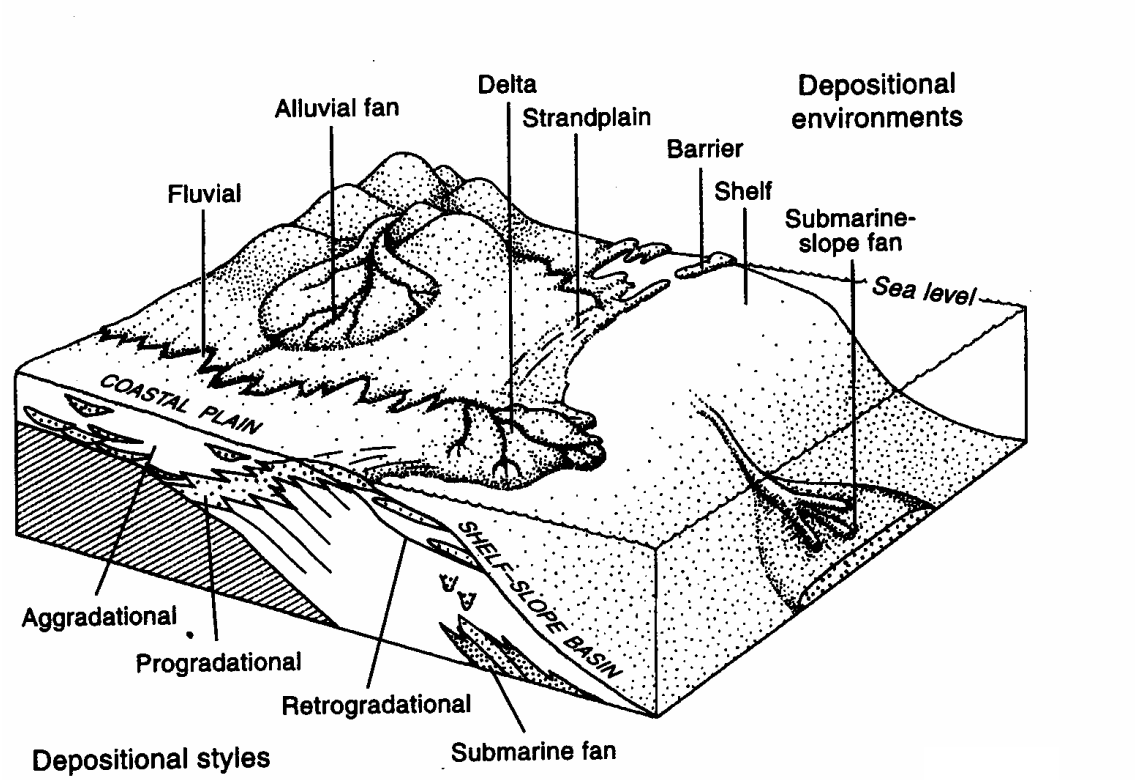

Figure 2.31. Siliciclastic depositional environments that host hydrocarbons in the Gulf of Mexico (from Seni et al., 1997).

reservoirs in the Gulf of Mexico include aggradational, progradational, retrogradational, and submarine fan (Seni et al., 1997). Depositional environments associated with oil and gas reservoirs in the Gulf of Mexico include fluvial, alluvial fan, delta, strandplain, barrier, shelf, and submarine-slope fan (Seni et al., 1997).

Figure 2.32 shows stratigraphic nomenclature, chronozones, and biozones of Mesozoic to Quaternary sections within the offshore Gulf of Mexico. Relative volumes of hydrocarbons associated with each corresponding chronozone and biozone are indicated by the size of the darkened circle found under either the 'Gas' or 'Oil' column in Figure 2.29. Gas appears to be more volumetrically significant than oil throughout the Tertiary in the Gulf of Mexico, with the largest accumulations found within the Pleistocene and significant volumes present from the Miocene through the Pleistocene. Oil appears to be most volumetrically significant in the Gulf of Mexico within the Upper Miocene, Pliocene, and Lower Pleistocene. A schematic cross section of a typical hydrocarbon-producing field is shown in Figure 2.33. There are 12 fault-block reservoirs, 7 sandstone-body reservoirs, 4 pools, 4 plays, and 4 depositional styles associated with this field. Reservoirs are indicated in black, with sandstones, muds, and faults also indicated on the cross section.

2.6.2. Texas Gulf Coast Hydrocarbons

Major oil and gas producing trends of offshore Texas and adjacent Federal waters are illustrated in Figure 2.34. A summary of oil and gas production within the Tertiary section of the Texas continental shelf is provided in Morton et al. (1985). According to Morton et al. offshore sandstone reservoirs were deposited in a variety of environments ranging from nearshore (fluvial channels, delta fronts, barrier strandplains) to deep water (submarine channels and fans). Major rivers provided coarse clastic sediments to large, high-

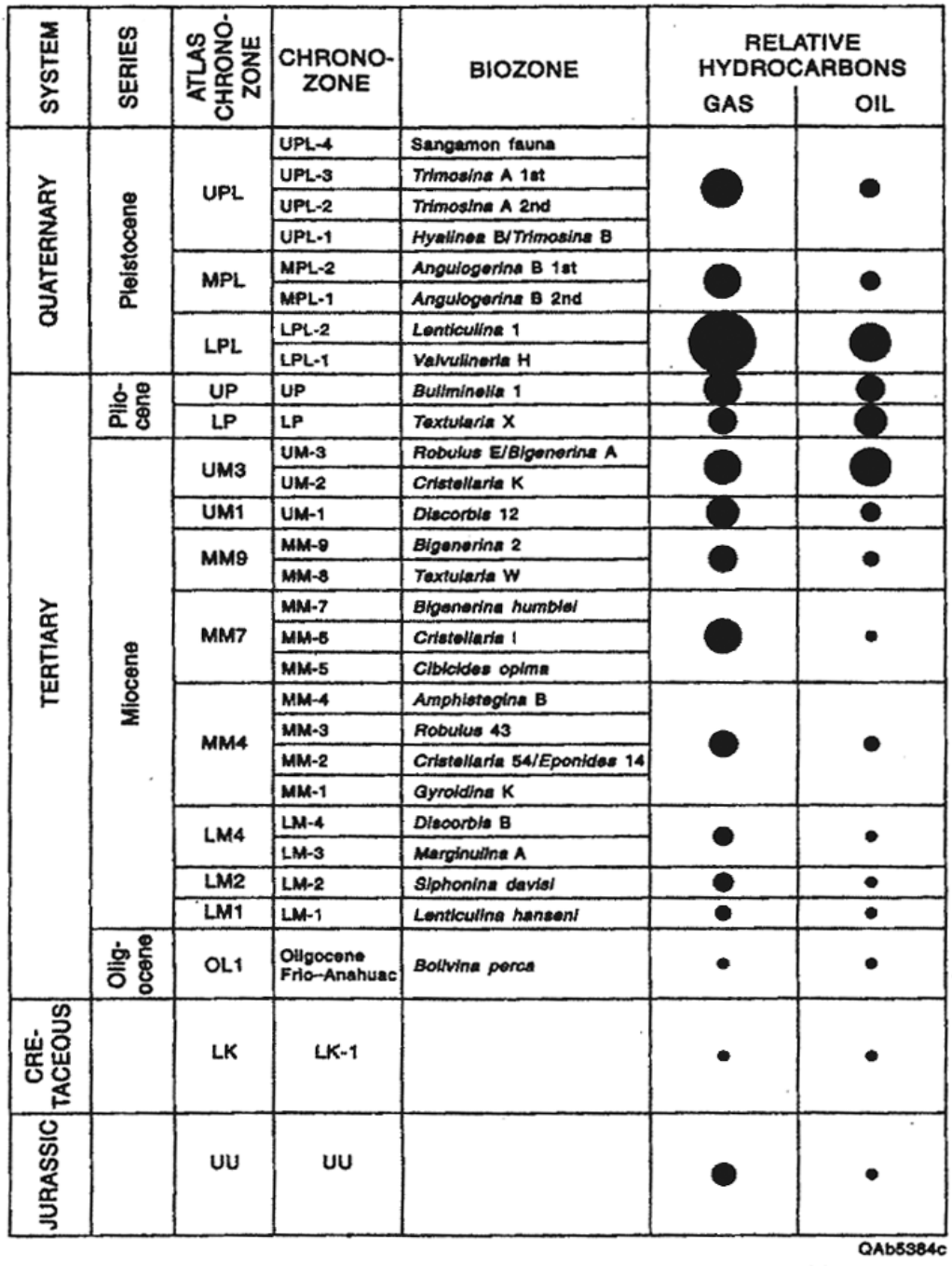

Figure 2.32. Stratigraphic nomenclature, chronozones, and biozones of Jurassic to Quaternary sections of offshore Gulf of Mexico. Relative volumes of hydrocarbons are shown in the size of individual shaded circles that correspond to each chronozone and biozone (from Seni et al., 1997).

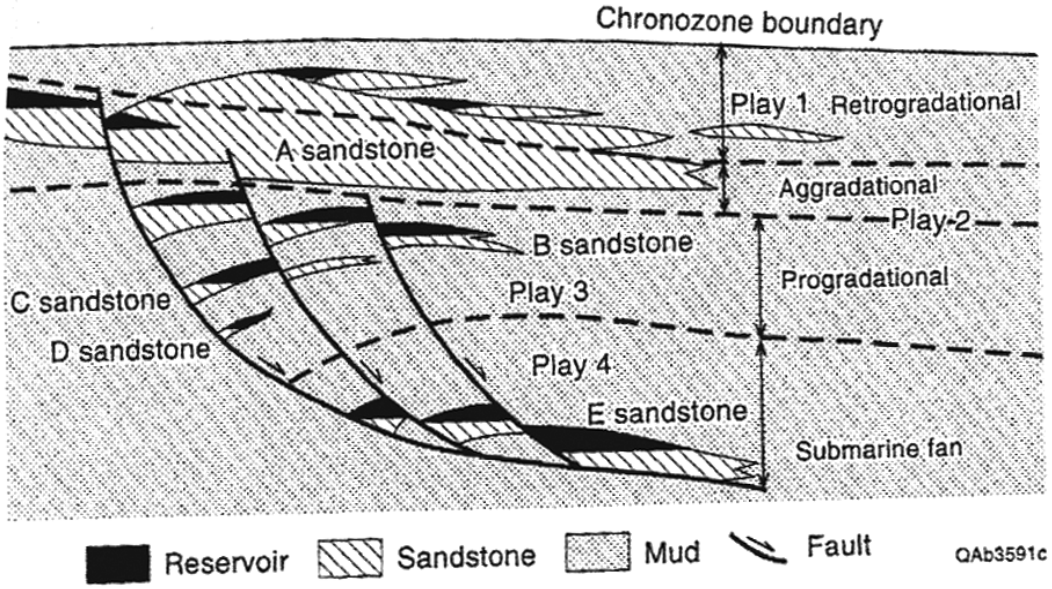

Figure 2.33. Schematic cross section of a typical hydrocarbon-producing field along the Texas Gulf Coast. 12 fault-block reservoirs, 7 sandstone body reservoirs, 4 pools, 4 plays, and 4 depositional styles are represented in this cross section. Reservoirs are shaded black (from Seni et al., 1997).

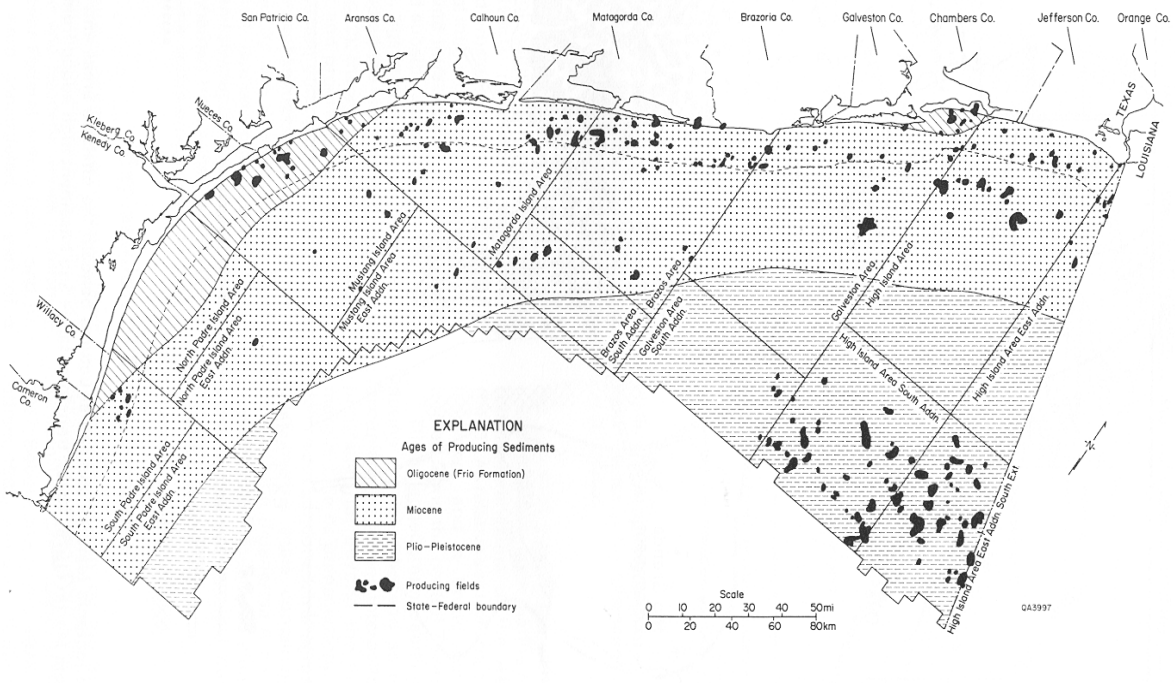

Figure 2.34. The locations of major oil and gas producing fields show the major producing trends of offshore Texas and adjacent Federal waters (from Morton et al., 1985).

constructive, wave-dominated deltas and intervening sand-rich barrier strandplains. Fine-grained sediments, or marine mud, accumulated in prodelta, shelf, and slope environments or in bays and lagoons landward of the barriers. These types of depositional systems persisted throughout the Tertiary and Quaternary (Morton et al., 1985).

Morton et al. (1985) stated that Tertiary deltaic sandstones deposited on the outer shelf and upper slope account for the greatest volume of hydrocarbon reserves. Reservoirs of barrier-strandplain and submarine-channel origin are also important producers in some downdip Frio, Lower Miocene, and Plio-Pleistocene plays (Morton et al., 1985). Structural hydrocarbon traps that are dominant in the offshore Texas continental shelf include salt domes, shale ridges, and growth faults (Morton et al., 1985). In addition, Fertl and Leach (1990) conclude that the highest concentrations of hydrocarbons are found near the top of overpressuring in Gulf Coast Tertiary rocks.

2.6.3. MI 519 Field Hydrocarbons

Matagorda Island offshore area, as well as the entire Texas Gulf Coast, is an important study area because of its economically significant large reservoirs of oil and gas. Tables 2.3 and 2.4 show cumulative oil and gas production from two state lease wells in Matagorda Island 519 that are used in this thesis. Lower Miocene reservoirs of oil and gas have been found at the Matagorda Island 519 field as off-structure, geopressured accumulations that occur along the flanks of diapiric shale ridges (Brewster et al., 1998; Klein et al., 1998). Compartmentalized reservoirs at Matagorda Island 519 are believed to have formed from diagenetic processes related to fluid flow and pressure cell formation that generated secondary porosity (Brewster et al., 1998). This field is significant economically, with over 500 billion cubic feet of gas recovered to date, and more reserves expected in the future (Brewster, personal communication).

Table 2.3. Cumulative oil and gas production from 1993 to 2001 for well SL 88562. Data obtained from the Railroad Commission of Texas Production Report Lease Production Detail for State Tract 519L (GOM) Lease 88562 – (03-119123).

Field: **Matagorda Island 519-L**

Well: **State Lease 88562 #2**

Year	Gas Production (MCF)	Condensate Production (BBL)
2001	0	0
2000	593,194	0
1999	1,989,293	4,319
1998	6,733,482	10,500
1997	7,981,597	12,290
1996	6,761,756	6,679
1995	6,666,799	12,098
1994	8,585,488	13,017
1993	8,547,276	15,633
CUMULATIVE:	**47,858,885**	**74,536**

Table 2.4. Cumulative oil and gas production from 1993 to 2001 for well SL 79413. Data obtained from the Railroad Commission of Texas Production Report Lease Production Detail for State Tract 519L (GOM) Lease 79413 – (03-109101).

Field: **Matagorda Island 519-L**

Well: **State Lease 79413 #1**

Year	Gas Production (MCF)	Condensate Production (BBL)
2001	3,333,443	2,812
2000	7,062,145	7,868
1999	5,821,418	7,977
1998	5,597,742	5,389
1997	5,756,871	6,223
1996	5,668,914	4,517
1995	5,359,180	4,553
1994	2,477,716	2,462
1993	1,097,439	1,194
CUMULATIVE:	**42,174,868**	**42,995**

Production from compartmentalized reservoirs at Matagorda Island 519 has occurred from depths of 13,500-17,300 feet (4100-5300 m) (Brewster et al., 1998; Klein et al., 1998) downthrown to a Lower Miocene expansion fault and flanking a diapiric shale ridge (Brewster et al., 1998). Sandstones at this field display excellent reservoir quality, with porosity typically between 20% and 25% and permeability typically between 0.02 to 300 millidarcies.

According to Brewster et al. (1998) and Klein et al. (1998) Matagorda Island 519 field is significant because it represents an exploration target and trap style that can become an analog for future exploration and production activities in geologic settings similar to this one. The model proposed by Klein et al. (1998) suggested that gas-condensate accumulation at Matagorda Island 519 resulted from episodic fluid flow events and a complex sequence of diagenetic events that formed the observed pressure cells. Klein et al. (1998) concluded that geochemical data were consistent with the hypothesis that deep, basinal fluids were responsible for the initial calcite cementation of the reservoir unit and its inferred subsequent dissolution.

Klein et al. (1998) also proposed that late stage mineral zonation of ankerite, Fe-calcite, pyrite, and polycrystalline quartz in the updip, and most fault proximal position were interpreted by them to be a direct hydrocarbon indicator for that type of field. According to Klein et al. (1998) this late stage mineral assemblage acts as a pore-throat seal for hydrocarbons reservoired downdip. A very high degree of water-rock interaction was inferred from the radiogenic Sr isotope composition of core samples, and was proposed to be another criterion by which to recognize fields of the Matagorda Island 519 type (Klein et al., 1998).

CHAPTER 3. TECHNIQUES

Most of the physical and chemical data obtained in this study are from borehole samples and well logs. The boreholes used here are located along a strike-oriented transect within the Matagorda Island 519 field area (Figure 2.2). For analysis of both physical and chemical properties, an accordion-fold cross section was constructed in which six wells were used as primary data sources. Figure 3.1 shows a cross-sectional view of the boreholes, including the total depth of each well. Table 3.1 is an inventory of the various types of well logs and other data available for each of the wells used in this thesis research. Note that no two wells within this study area have exactly the same suite of available data and information.

A variety of important geologic information can be derived from well logs, such as lithostratigraphy, fluid pressure, formation temperature, salinity, porosity, and depositional setting (Kehle et al., 1971; Bateman and Konen, 1977; Bateman, 1985). Typical responses of several sediment properties to the onset of overpressure are illustrated in Figures 3.2 and 3.3. Figure 3.2 illustrates how an overpressured zone correlates with a decrease in bulk density and a reversal in the normal compaction curve, while the adjacent gamma ray log shows that the corresponding depth interval is shale. Shale conductivity typically increases at the top of overpressure (Figure 3.3), and shale porosity also shows a large increase at the top of overpressure.

In addition to the abundant borehole data and sample analyses used in this study, geologic information was also collected from several other sources. Information on chronostratigraphy was obtained from MMS and Amoco paleontology reports, the structural geology of the study area was based on limited seismic data (Brewster, personal

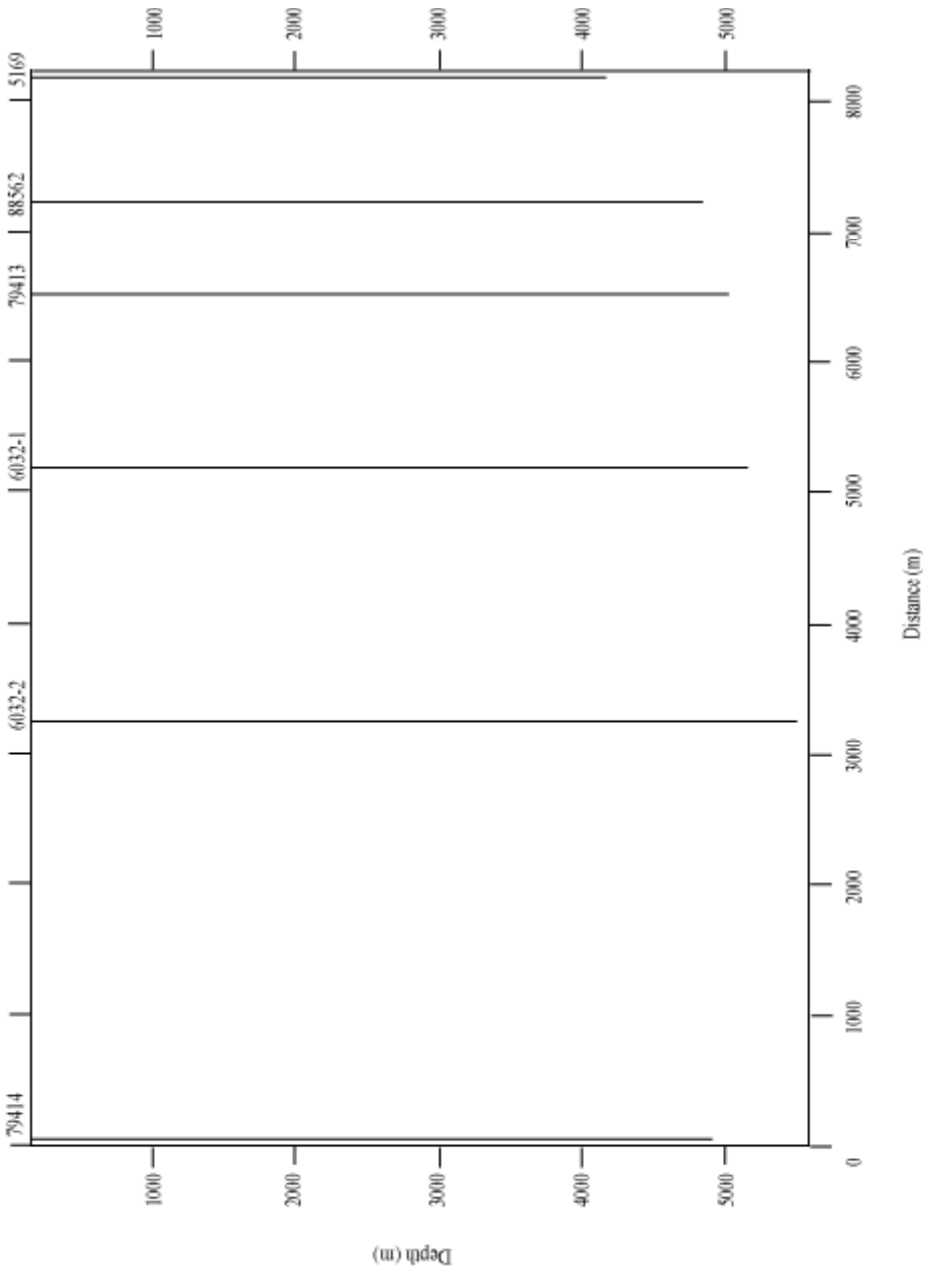

Figure 3.1. Cross-section view showing total depths of wells in Matagorda Island 519 used in this study. Depth for each well was determined from the kelly bushing.

Table 3.1. Inventory of the various types of well logs and other available data for each of the wells used in this study.

	SL 79414 #1	OCS 6032 #2	OCS 6032 #1	SL 79413 #1	SL 88562 #2	OCS 5169 #1
Whole rock chemical analysis			***	***	***	***
XRD Mineralogy	***			***	***	
Thin sections					***	***
MMS paleontological data			***			***
SP-derived salinity	***	***	***	***	***	***
Conventional SP-Res. logs	***	***	***	***	***	***
Rwa log		***				***
Porosity log (neutron and spectral density)		***	***			***
Temperature log		***				
Mudweights (logs and spreadsheets)	***	***	***	***	***	***
Pressure evaluation profile		***				
Petrophysical logs		***	***			

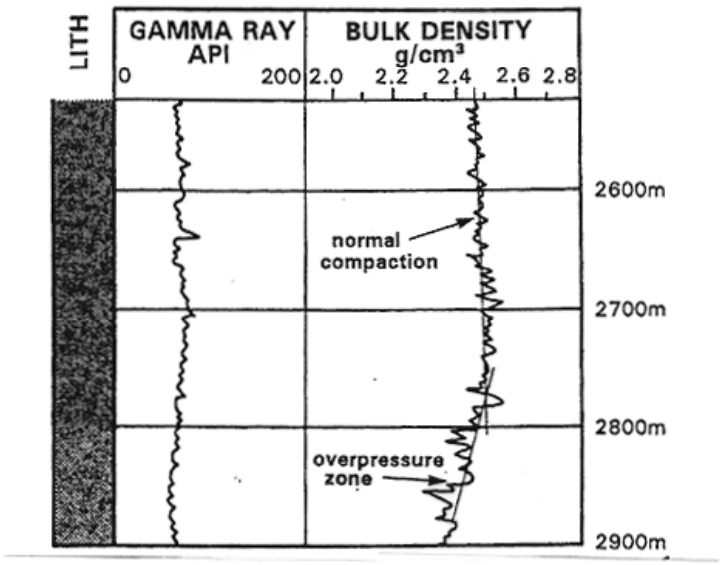

Figure 3.2. Overpressure is typically observed as a drop in bulk density that corresponds to a shaly interval on the gamma ray log (from Fertl and Rieke, 1980 in Rider, 1996).

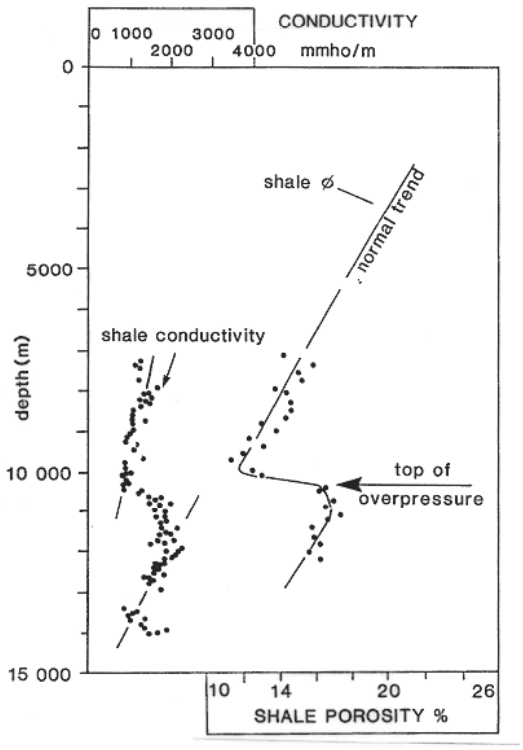

Figure 3.3. Overpressure is indicated on a plot of shale conductivity and shale porosity for deep Gulf Coast shales (from Schmidt, 1973 in Rider, 1996).

communication), and some reports within the data set of this study contain information on other properties, such as temperature.

The wells drilled at Matagorda Island 519 field were analyzed by Amoco for geochemical properties that may have enhanced reservoir quality and performance. As a result, data on whole-rock chemistry obtained from cuttings, thin sections obtained from core samples, and mineralogy obtained from X-ray diffraction analyses of both whole-rock and clay-fraction core samples were made available for this thesis research (Table 3.1). Techniques used in data analysis, interpretation, and manipulation of geochemical input data available for this study are presented in this chapter after the discussion of techniques for determining physical properties.

3.1. Structural Geology

Information regarding the structural geology of the Matagorda Island 519 field was based on the limited seismic data available for this research, and also on well log data and previous publications by Amoco geologists on this field (Brewster, 1998; Klein, 1998). The location of both major and minor faults, as well as other structural features, can be identified from the seismic data and from log data and previous publications. Identification of prominent faults is extremely important in characterizing fluid flow at the Matagorda Island 519 field, because faults can act as both conduits and barriers to flow, as well as affect hydrocarbon seal integrity.

3.2. Chronostratigraphy

Age control for the Matagorda Island 519 wells studied in this thesis relies heavily on paleontological data in the public domain (MMS, 2000) and on published regional studies (Morton et al., 1985; Seni et al., 1997). Public paleontological data was obtained for this study from the Paleo for Public Release reports compiled by the Minerals Management

Service (MMS) for two wells, OCS 6032#1 and OCS 5169 (MMS, 2000). According to the MMS, the operator (Amoco) released these reports because, although the leases were still active, ten years had passed since the reports were submitted. Also, an Amoco in-house report for well OCS 6032#1 was released by MMS because two years had passed since it was submitted to MMS. In addition to the available public paleontological data for Matagorda Island 519, paleontology reports were also available from Amoco research for well OCS 5169 (Brewster, personal communication).

Fossil data throughout the study area are sparse, and mainly consists of foraminiferal biomarkers, with limited local markers. Even limited paleontologic data is useful in establishing age control at Matagorda Island 519, which ultimately aids in understanding the development of overpressuring. Foraminifera often serve as excellent index fossils because of their limited range of habitat and chronologic range (Rosen et al., 1999). Thus, the appearance of such fossils in a well constrains the time of deposition and, possibly, depositional environment. Table 3.2 summarizes the species of foraminifera used to identify specific depositional environments and establish age control at the Matagorda Island 519 field.

Chronostratigraphy established at the Matagorda Island 519 field in this study is validated by the fact that paleontologic data from this research is consistent with previously-established chronostratigraphic models. Paleontology used in this study at Matagorda Island 519 supports the Texas Gulf Coast regional chronostratigraphy established by Morton et al. (1985) and chronostratigraphy of the Matagorda Island offshore area, including the immediate vicinity of Matagorda Island 519, reported in Seni et al. (1997).

Table 3.2. Summary of foraminiferal and nannofossil species used to identify key intervals at Matagorda Island 519 (Brewster, unpublished).

Well No.	Measured Depth (ft)	Foraminifera Observed	Nannofossils Observed
5169	13,572.50	Bigenerina cf. humblei Eponides antillarum	Dictyococcites productus Discoaster deflandrei
	13,575.50	Textularia sp.	None
	13,592.30	Bigenerina humblei Textularia sp.	Braarudosphaera bigelowii Dictyococcites productus Discoaster deflandrei Discoaster divaricatus

3.3. Lithostratigraphy

3.3.1. Vertical Distribution of Sandy and Shaly Intervals

The distribution of sands and shales within the Matagorda Island 519 field establishes a first-order control on potential fluid flow within the field. Fluids will preferentially flow through sands, and thus a determination of the distribution of sand and shale throughout the study area can provide insight into the preferred intervals through which fluid could flow.

The sedimentary sequence at Matagorda Island 519 consists of numerous interbedded sands and shales. Rather than attempt to correlate individual thin beds across the field, sand-rich and shale-rich intervals, or packages of sediment, were correlated. A visual estimate of the cumulative thickness of sand beds within 100-foot (30-m) vertical intervals was made from spontaneous potential (SP) log response, following a procedure developed by Bray and Hanor (1990), Funayama (1990), and Nikiel and Hanor (1999). Figure 3.4 illustrates SP, SSP, and shale baseline, and the typical SP for both sand and shale. Cumulative thickness was recorded as percent sand beds within each 100-foot (30-m) interval and used to construct bar graphs showing the vertical distribution of sandy and shaly intervals.

Due to the small spatial scale of this study, only three of the six wells were chosen to represent the entire section in the percent sand determination. Bar graphs of percent sand versus depth were constructed for all of the three wells studied. Correlations between bar graphs for individual wells were made to identify trends in percent sand distribution throughout the study area.

The procedure developed by Bray and Hanor (1990), Funayama (1990) and Nikiel and Hanor (1999) showed that the best stratigraphic correlations could be made based upon percent sand trends at 300-foot (100-m) vertical intervals, due to the increased complexity of

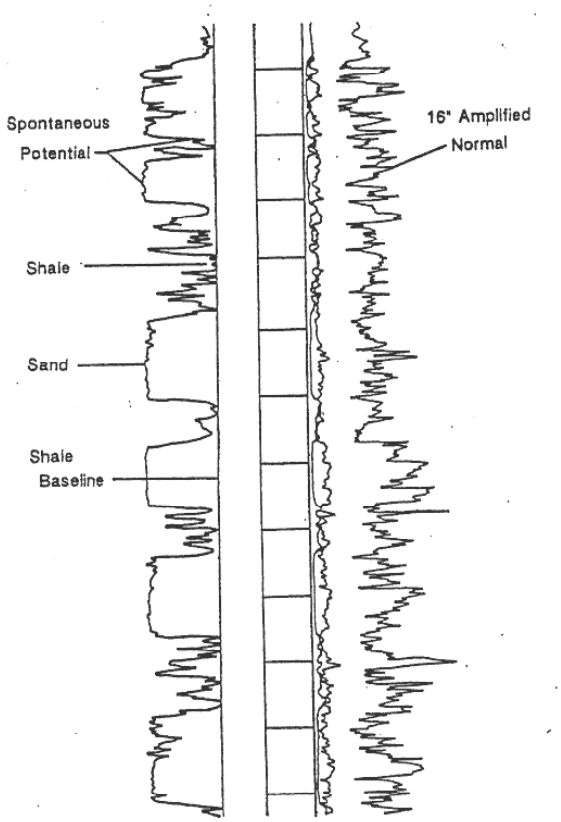

Figure 3.4. Typical SP log response, illustrating SP, SSP, and shale baseline (from Bray, 1989).

sand-shale interbedding present within 100-ft (30-m) vertical intervals. This procedure has worked well in large-scale study areas, such as those of Bray and Hanor (1990), Funayama (1990), and Nikiel and Hanor (1999), but a more detailed analysis was necessary for the Matagorda Island 519 field, due to the smaller scale of the study area.

Initial measurements were made at 100-ft (30-m) depth intervals, and these measurements were then averaged to represent percent sand distribution at 300 ft (100-m) depth intervals in order to determine which representation would best model lithostratigraphy within the study area. In order to facilitate precise, detailed lithologic and stratigraphic correlation between wells, 100-ft (30-m) depth intervals were finally chosen as the best representation of lithostratigraphy for this study. Data from each of the three bar graphs were then used in constructing a two-dimensional representation of the distribution of sandy and shaly intervals within the Matagorda Island 519 field.

3.3.2. Interpretation of Depositional Setting from SP Log

Spontaneous potential (SP) logs can be useful in determining depositional environment. Sedimentary facies that represent different depositional environments can be observed in the response of the SP log. The technique for interpreting depositional setting from well log character used in this study was based on techniques presented by Seni et al. (1997) for northern Gulf of Mexico oil and gas reservoirs.

Depositional setting is important because establishing the original, or connate, salinity of pore fluids is based on the assumed salinity of the sediments at the time of deposition. Figure 3.5 shows the relation between SP log response and inferred depositional environment (Seni et al., 1997). Characterization of generic depositional environments present at the Matagorda Island 519 field was made based on this technique. Results are presented in the following chapter.

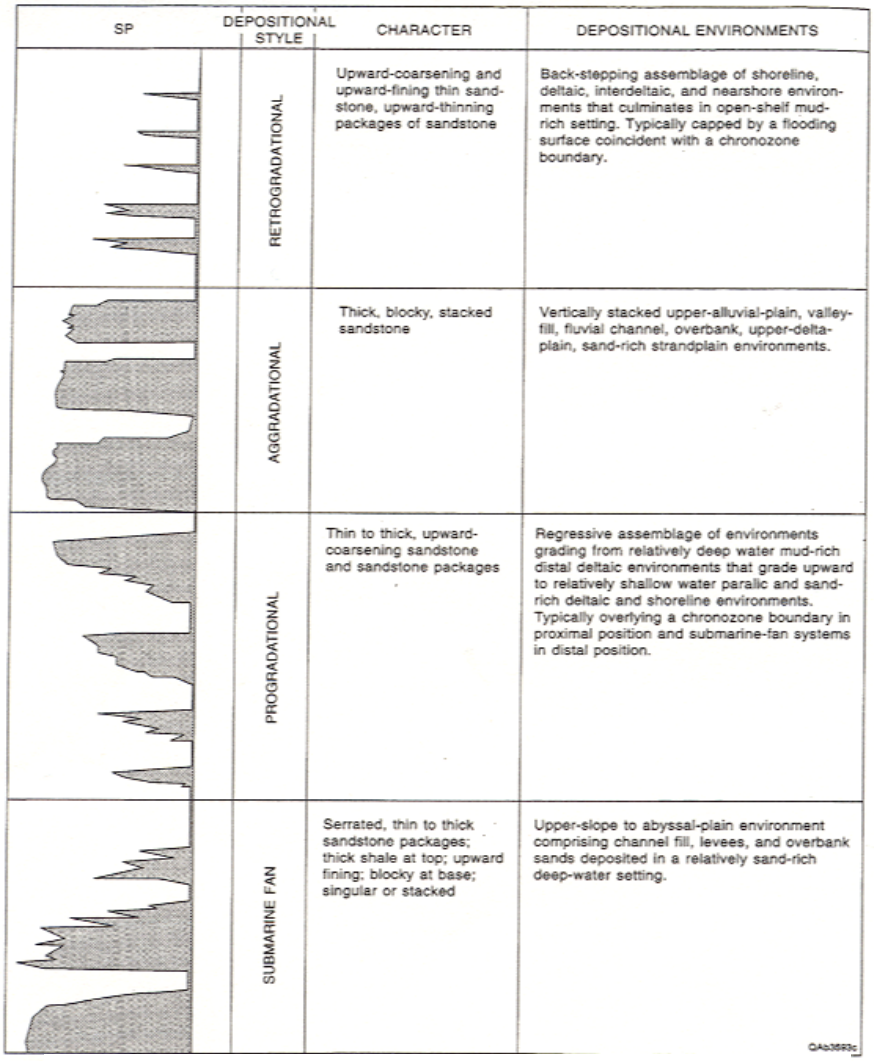

Figure 3.5. Representative electric-log patterns of the progradational, aggradational, retrogradational, and submarine-fan depositional styles and interpreted depositional environments (Seni et al., 1997).

3.3.3. Petrophysical Log Analysis

Petrophysical logs provide valuable detailed descriptions of shale cuttings, in terms of lithology, sediment chemistry, and depositional style. Unfortunately for this study, however, there was only one petrophysical log available, for well OCS 6032 #1. Despite the limited coverage of the formation evaluation profile in the study area, this single well log provided valuable data by providing information on lithologic character. Figure 3.6 is an example from the petrophysical formation evaluation log for well 6032 #1.

3.3.4. Rate of penetration log analysis

Rate of penetration (ROP) logs provide useful information on the speed at which a given layer of sediment in the subsurface was drilled through. The relative speed that a particular layer was drilled through is determined by factors such as the relative amount of cementation. Thus, if a layer of sediment is highly cemented, the ROP log should show that the layer was drilled relatively slowly. For this study values of penetration rate were recorded from the ROP log for well OCS 6032 #1 in units of feet per hour. The inverse of penetration rate, drillbit transit time, is actually a more sensitive indicator of zones of slow penetration rate than ROP. Drillbit transit time in hr/m was calculated from rate of penetration data. Results were tabulated and are shown in Chapter 4 of this thesis.

3.4. Fluid Pressure

Determining fluid pressure variations with depth is an integral part of identifying the location of overpressured zones. Several techniques were used by this author to obtain fluid pressure data for the wells of the Matagorda Island 519 field. The types of data from which fluid pressures are calculated include mudweights, shale resistivities, pressure logs, and Repeat Formation Test (RFT) logs. Table 3.3 is a conversion table for pressure in units of mudweight, pounds per square inch (psi), bars, pascals (Pa), and megapascals (Mpa).

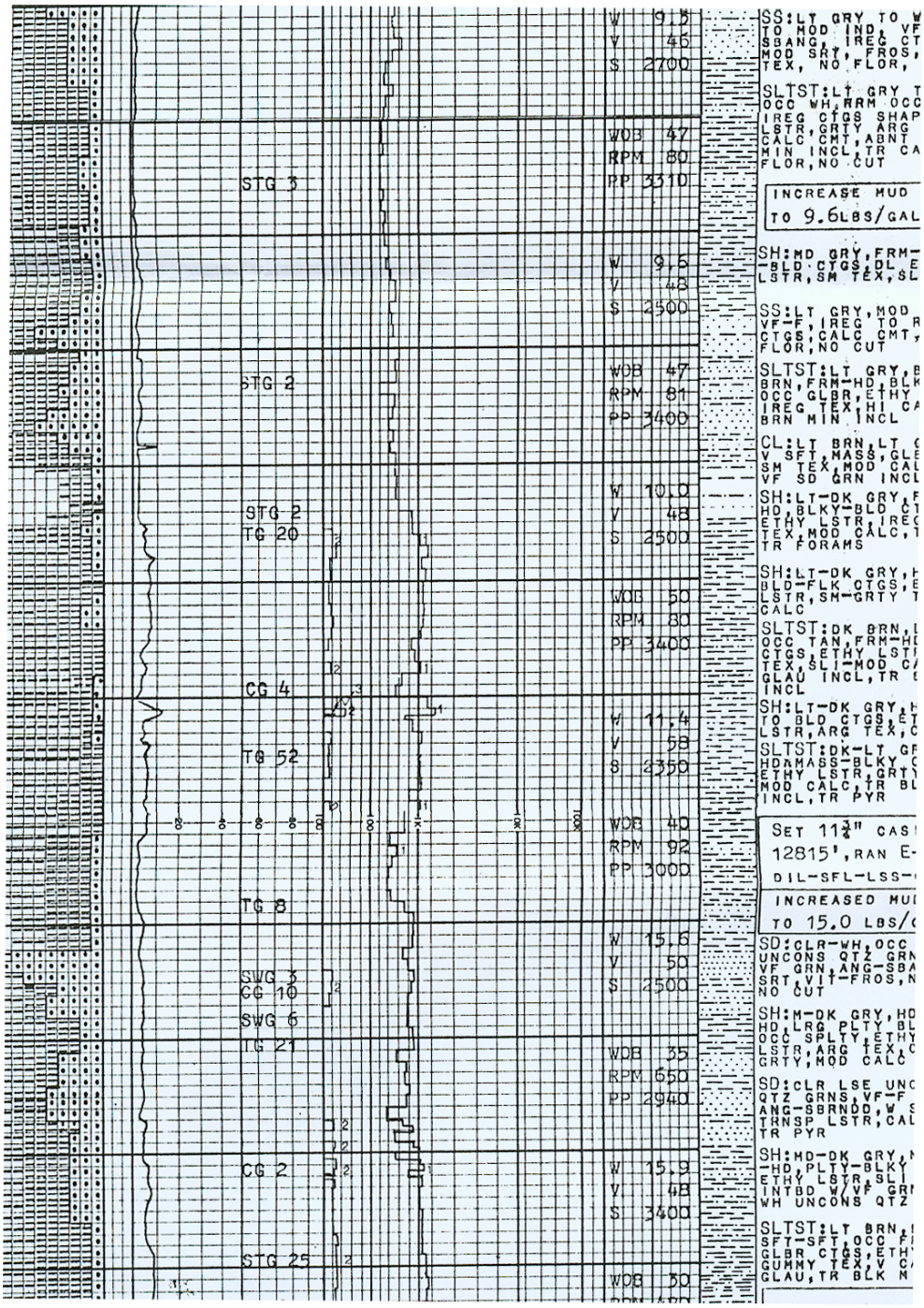

Figure 3.6. Example from the petrophysical formation evaluation log for well 6032-1.

Table 3.3. Conversion table for pressure terms and units used in this study.

Term or Abbreviation	Units	Equivalence and Conversion
Mudweight	Pounds per gallon	Mass per unit volume of drilling fluid
psi	Pounds per square inch	Normal atmospheric pressure = 14.7 psi psi = mudweight*0.052*depth psi = 2.036 in Hg
atm	Atmospheres	Normal atmospheric pressure = 1 atm 1 atm = 14.7 psi
bar	Bars	1 bar =0.9868 atm =100000 Pa =14.5 psi
Pa	Pascals	1 Pa = 1 Newton per square meter 1 atm = 101325 Pa Pa = psi*6894.757
Mpa	Megapascals	1,000,000 pascals

3.4.1. Mudweight-Derived Fluid Pressure

Fluid pressure was calculated from drilling mudweights, which are reported on the log header for each logging run as the density of the drilling fluid. The density of the drilling fluid is adjusted in order to maintain bottom-hole pressures that are higher than pore pressures but not high enough to exceed the fracture gradient of the formation (Hearst and Nelson, 1985). Geostatic ratio, Gs, is defined as the ratio of fluid pressure at a given depth to the total height of the fluid column (Nikiel, 1998), and is calculated from mudweight based on the following relation (Wesselman and Heath, 1977):

$$\text{Geostatic ratio (psi/ft)} = \text{mudweight (lb/gal)} \times 0.052 \text{ (gal/in}^2 \text{ ft)} \quad (3.1)$$

Once the geostatic ratio is calculated, fluid pressure is then calculated by multiplying geostatic ratio by depth.

The primary disadvantage to using mudweights for obtaining fluid pressure data is that the method yields only a first-order approximation of geostatic ratios, due to use of overweighted drilling muds. Drilling muds that are often overweighted in order to prevent well blowouts will yield erroneously high geostatic ratios. Thus, it is necessary to multiply the geostatic ratio by depth in order to determine the absolute fluid pressure at a given depth. For this study, mudweight versus depth at specific depth points was available for all of the wells (Brewster, personal communication) and a log of mudweight versus depth over a continuous depth interval was available for well OCS 6032 #2.

3.4.2. Shale Resistivity-Derived Fluid Pressure

An alternative technique for calculating fluid pressure involves the use of shale resistivities. This technique has been widely used for calculating fluid pressure (George, 1965; Fertl, 1982; Bray and Hanor, 1990; Funayama, 1990; Hagiwara and Jackson, 1995; Foster and Whalen, 1999; Hottman and Johnson, 1999; Nikiel and Hanor, 1999). The George

(1965) method for calculating fluid pressure from shale resistivity provides a good approximation of geostatic ratios for variable depths (Figure 3.7).

Funayama (1990) developed an algorithm for calculating geostatic ratios based on the George method, in which geostatic ratios are calculated from shale resistivities from one of the following relations:

$$Gs = (5000*(Rsh - 0.1)) / D \qquad (3.2)$$

$$Gs = (-20000*(Rsh - 0.1)) / 3.18*D + 1.05 \qquad (3.3)$$

where Gs is the geostatic ratio, Rsh is measured shale resistivity in ohm-meters, and D is depth in feet. Funayama (1990) warned that if calculated geostatic ratios are too high to plot on the George graph, then the George method can not be used. Nikiel (1998) noted that the George method produced inaccurate results in the eastern Louisiana continental shelf for depths shallower than 7500 feet (2290 meters) because of decreased salinity. Brewster et al. (1998) published figures showing fluid pressure versus depth for each of the wells used in this study. The fluid pressures have been calculated using a proprietary technique that utilizes shale resistivity.

3.4.3. Pressure Log

Direct pressure measurements involving measuring the shut-in pressure of a well are extremely valuable, but also rare because of their cost. A single pressure log was available for use in this study, for well OCS 6032 #2. The direct pressure measurements in well 6032 #2 were useful because they were used to check the accuracy of the other methods of calculating fluid pressure, such as mudweight-derived and shale resistivity-derived fluid pressure in the OCS 6032 #2 well. This calibration was then applied to the other wells in the study area.

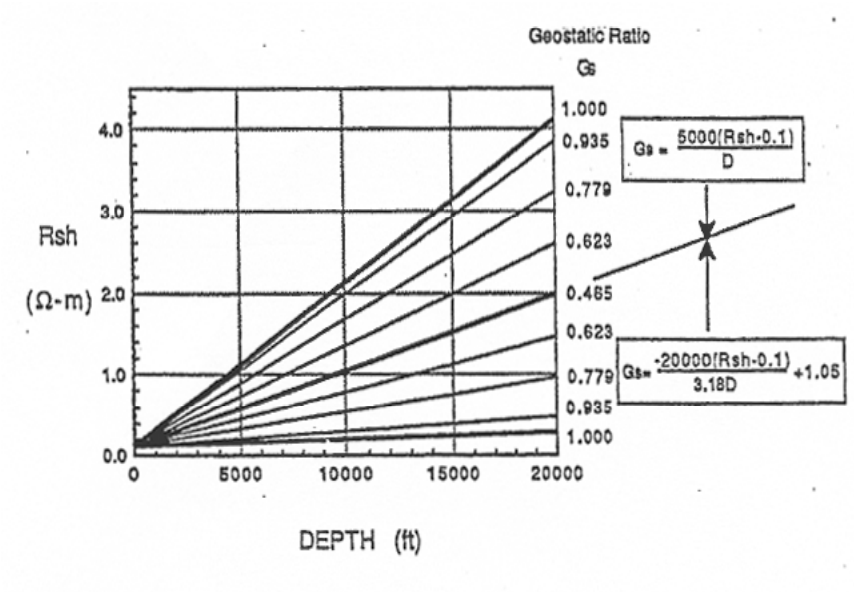

Figure 3.7. George method for calculating geostatic ratio from shale resistivity (from Funayama, 1990).

3.4.4. RFT Log

Repeat Formation Test (RFT) logs are also a valuable source of information on fluid pressure regimes within a well. RFT log data was available for only one well, State Lease (SL) 79414. This limited RFT information is still important, however, because it also can be compared against other methods of calculated fluid pressures.

3.5. Temperature

3.5.1. Corrected BHT Temperatures

Formation temperatures were calculated from the bottom hole temperatures (BHT) recorded for each logging run on the well log header for each well. Linear interpolation was used to determine temperatures at depths other than at the bottom of each logging run by assuming a linear temperature gradient between each BHT reading and an assumed seabottom temperature of 68^{o}F (20^{o}C), based on the determination by Li et al. (1997) of average annual bottom water temperature on the Texas-Louisiana continental shelf. Uncorrected formation temperatures were corrected using the Kehle et al. (1971) correction curve, which accounts for cooling effects during drilling (Figure 3.8).

3.5.2. Temperature Log Analysis

In addition to the bottom hole temperature information obtained from individual well log headers, a temperature log was available for one of the wells, OCS 6032 #2. Temperature logs are rare because of the cost associated with continuously monitoring and recording temperature within a well. Thus, continuous temperature data over the entire depth range of even one well provided a first order method of calibrating the temperatures calculated using the BHT temperatures. Temperature gradient calculations were performed using data from the temperature log for well 6032 #2 in order to provide the most accurate

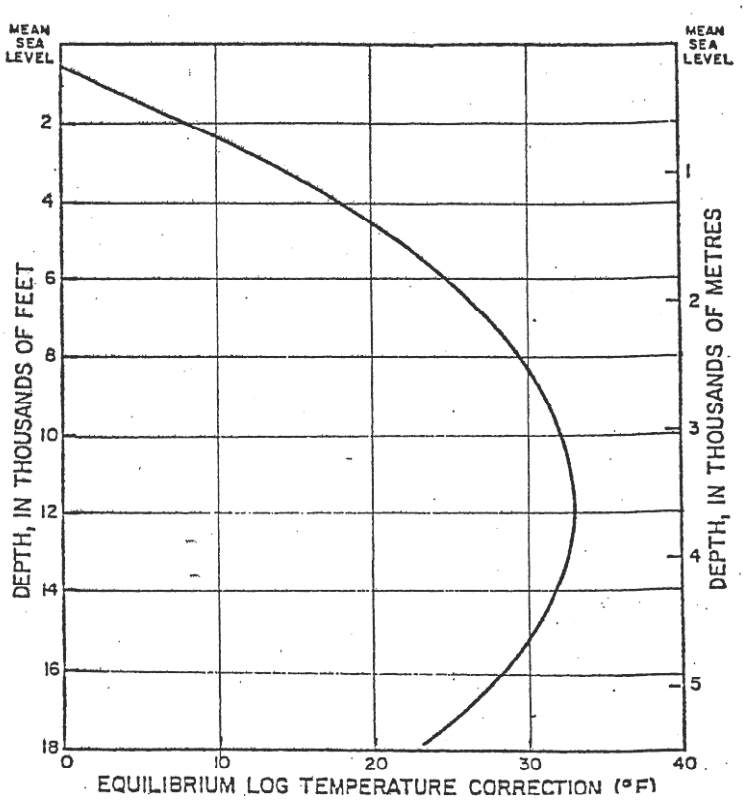

Figure 3.8. Kehle correction curve to correct BHT for cooling effects (from Bray, 1989).

estimate of the actual temperature gradient at Matagorda Island 519. Results are shown in Chapter 4.

3.5.3. Temperatures from Isotopic Analysis

Klein et al. (1998) calculated temperatures within the study area based on Sr, O, and C isotopic analysis of rock samples. Figure 3.9 shows how Klein et al. (1998) interpreted a linear covariation trend between $\delta^{18}O$ and $\delta^{13}C$ values to represent a mixing between end member detrital calcite and authigenic calcite phases. Based on the inferred $\delta^{18}O$ of the authigenic calcite and using typical $\delta^{18}O$ values for the subsurface Gulf of Mexico (4.9 to 5.6 per mill, PDB), Klein et al. (1998) estimated that calcite cementation temperatures at Matagorda Island 519 were between 205° F and 256°F (96°C and 124°C) (Figure 3.10).

3.6. Salinity

3.6.1. Connate Salinity

Connate salinity, the salinity of pore waters trapped at the time of deposition, can be approximated if the primary depositional environments active during each interval are known. Thus, connate salinity was approximated at Matagorda Island 519 from knowledge of depositional environments determined in the investigation of lithostratigraphy.

3.6.2. Salinity Calculated from SP Logs

Formation salinity can be estimated using various types of well log data. In this study apparent salinity was calculated primarily from spontaneous potential (SP) logs, from apparent formation water resistivity (Rwa) logs, and from fluid analyses. The SP technique used in this research is based on the method of Bateman and Konen (1977) and Bateman (1985), and follows revisions made to the method by Funayama (1990) and Hanor (1999, personal communication).

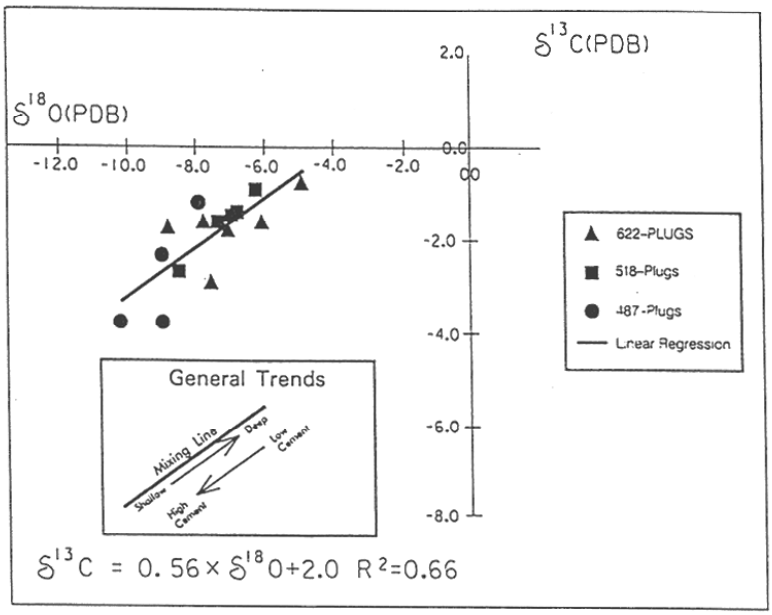

Figure 3.9. Illustration of the mixing trend between detrital calcite and authigenic calcite at Matagorda Island 519, based on detailed oxygen and carbon isotope data (from Klein et al., 1998).

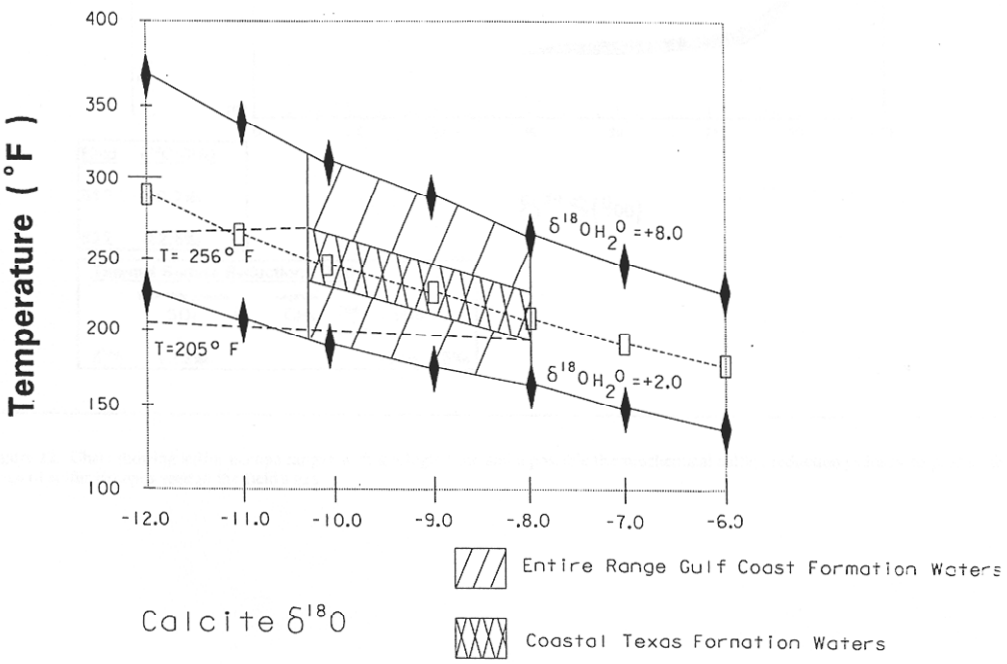

Figure 3.10. Oxygen isotope data used by Klein et al. (1998) to infer calcite cementation temperatures at Matagorda Island 519 (from Klein et al., 1998).

Following the procedure of the Bateman and Konen algorithm, the input data that was used to calculate apparent salinity from SP response is listed. First, depth, sand thickness, mudweight, uncorrected formation temperature, mud resistivity (Rm), temperature at which Rm was measured (Tm), resistivity of the mud filtrate (Rmf), and temperature at which Rmf was measured (Tmf) were recorded from the log header for each logging run. Next, static spontaneous potential (SSP) was measured as the maximum negative deflection from the shale baseline for clean sands having a minimum thickness of 40 feet (12 meters). Measured static spontaneous potential (SSP) response in millimeters was then recorded, and the conversion factor (millivolts per millimeter) was determined from data for each logging run in order to calculate and record SSP in millivolts.

When all of the required input data for each well were recorded in Microsoft Excel spreadsheets a sequential series of calculations were performed. Appendix B contains data tables of salinity versus depth for all wells in the Matagorda Island 519 field.

Although sand picks were carefully chosen on each of the SP logs, some of the sands picked did not meet the minimum thickness and/or the clean sand requirements of the Bateman and Konen algorithm. Thin sands, clayey sands, and sandy or fractured shales all typically result in a suppressed SSP response (Rider, 1996), and thus an erroneously low calculated salinity. In order to reduce the effect of thin beds at Matagorda Island 519 a simple data "quality-control" filter was applied to the salinity results. This data filter was a simple 'If-Else' function within the Excel spreadsheet for each well, in which salinity reported for beds less than or equal to 30-ft (9-m) thick was filtered out. Thus, only salinity for beds at or near the required thickness was reported.

These kinds of unaccounted errors explain why this technique can only estimate true formation salinity, and future work needs to be done in order to correct for such problems as

thin beds and dirty sands. In addition to these errors, other input parameters can be affected by inaccurate well logging procedures, such as malfunctioning logging tools, improper sampling, or inaccurate recording of data on the well log header (Bray, 1989; Nikiel, 1998; Spears, 2000).

3.6.3. Salinity from Rwa Logs

Rwa (apparent formation water resistivity) logs are another useful means by which to calculate apparent formation salinity. Limited salinity data was also available in the form of unpublished Amoco reports of fluid analyses (Brewster, personal communication) that proved to be useful as a way to check the accuracy of the calculated salinity results.

3.7. Fluid Viscosity and Density

Fluid viscosity was determined according to the McCain et al. (1991) equation:

$$\mu_w = AT^{-B} \qquad (3.4)$$

where $A = 109.574 - 8.40564S + 0.313314S^2 + 8.72213x10^{-3}S^3$, $B = 1.12166 - 2.63951x10^{-2}S + 6.79461x10^{-3}S^2 + 5.47119x10^{-5}S^3 - 1.55586x10^{-6}S^4$, T is in degrees Fahrenheit, S is salinity in weight percent, and μ_w is in centipoises. Fluid density was determined according to the Batzle and Wang (1992) equations for freshwater density (3.5I) and brine density (3.5II):

$$\rho_W = 1 + 1x10^{-6}(-80T - 3.3T^2 + 0.00175T^3 + 489P - 2TP + 0.016T^2P - 1.3x10^{-5}T^3P - 0.333P^2 - 0.002TP^2) \qquad (3.5I)$$

$$\rho_B = \rho_W + S(0.668 + 0.44S + 1x10^{-6}(300P - 2400PS + T(80 + 3T - 3300S - 13P + 47PS))) \qquad (3.5II)$$

where ρ_W and ρ_B are in g/cm^3, S is NaCl mass fraction in $ppm/10^6$, P is pressure in megapascals, and T is temperature in degrees Celsius.

3.8. Porosity

Porosity was derived using three different methods, all of which are based on well log data. Porosity logs, which allow direct calculation of porosity from both neutron and density logs, are not common because of the difficulty and cost associated with them. Thus, porosity is generally indirectly determined from other sources of log information. Neutron logs, density logs, combined neutron-density logs, and sonic logs all contain data from which porosity can be determined, and each was used to determine porosity for the wells in the Matagorda Island 519 field. Calculated neutron-density porosities were used in this study for depths from approximately 14,000-16,000 ft (4267-4876 m). Shale porosity was calculated from sonic transit time, following the method of Hart et al. (1995):

$$\phi = 1 - (\Delta t_{ma} / \Delta t)^{1/x} \qquad (3.6)$$

where Δt_{ma} and Δt are log-derived matrix and sonic traveltime, and x is a constant. Following Hart et al. (1995) and Issler (1992), values of Δt_{ma} = 220 μs/m and x = 2.19 were used.

3.9. Sediment Bulk Chemistry

3.9.1. Previous Research on Sediment Bulk Chemistry at MI 519

Amoco previously determined sediment bulk chemistry for wells in the Matagorda Island 519 field from shale cuttings and core samples. Oxide weight percent data was determined from shale cuttings that were hand screened with a magnet to remove drill bit fragments. Also, debris from drilling fluids was removed under a binocular scope. Thus, only uncontaminated shales were analyzed. Analysis of these shale cuttings was performed by XRAL, at Dons Mills Ontario, with X-ray Fluorescence (XRF) techniques (Brewster, personal communication).

According to Klein (1998), shale cuttings were selected based on the rationale that mudrocks should not be as prone as sandstones to display chemical composition variations due to changes in provenance. Thus changes in mudrock chemistry may reflect the diagenetic effects of geopressure cell formation and water-rock interactions imposed by basin-scale fluid flow (Klein, 1998).

3.9.2. MI 519 Sediment Bulk Chemistry Data: Analysis and Manipulation

Research on diagenesis conducted for this study relied on bulk chemistry, mineralogy, and petrology of cuttings and core samples from four wells in the Matagorda Island 519 field, 6032-1, 79413, 88562, and 5169. Sediment bulk chemistry at Matagorda Island 519 was investigated in terms of the behavior of major oxides with depth and in the behavior of some key elements and oxides in relation to one another. In order to describe the behavior of major cations with increasing depth, analysis of the relative mobility of oxides containing these cations was performed.

Figure 3.11is a chart showing the relative mobility of various elements, based on variations in both ionic radius and charge. Ions for which data was available in this study are highlighted on this figure in order to show the potential relative mobility of each ion analyzed in this study.

Sediment bulk and isotopic chemistry in this thesis is based on the previous analyses performed by Amoco, while considering the previously mentioned limitations. Data on oxide weight percent is especially valuable in this thesis research. Oxide weight percent data is versatile because this data can be used for examining elemental enrichment or depletion versus depth in the subsurface and used as input data for a modeling program created for this thesis that calculates normative mineralogy for sediments. The data on sediment bulk

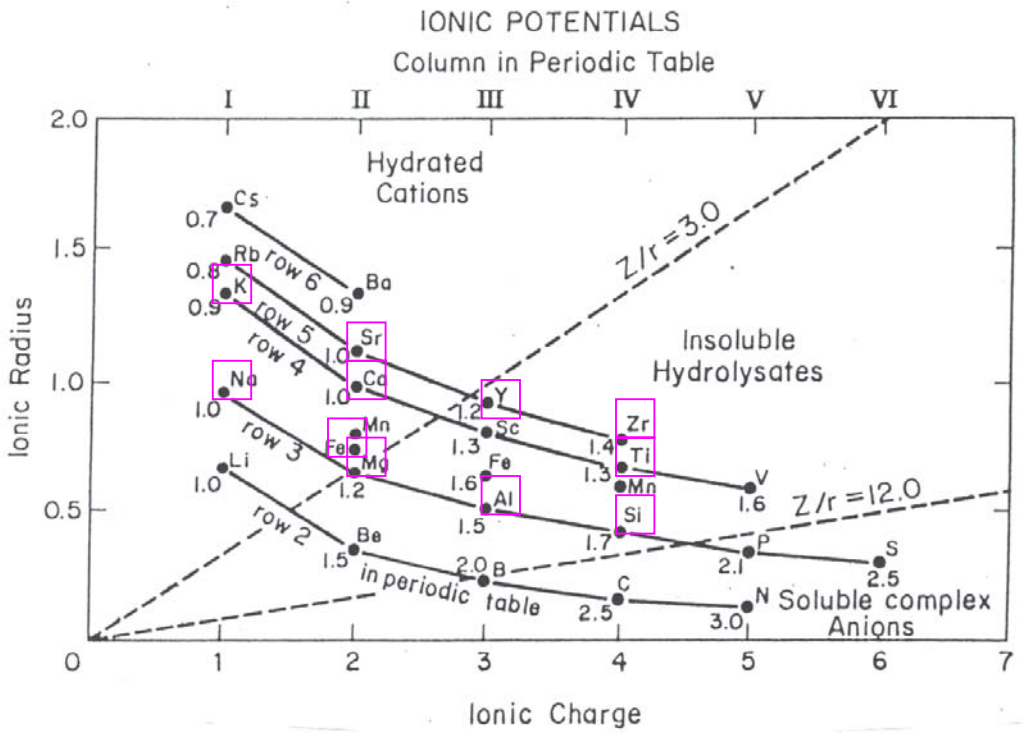

Figure 3.11. Chart of ionic radius and ionic charge to illustrate relatively mobile and relatively immobile elements. Boxes highlight those elements that were considered key in this investigation in order to show the relative ionic radius and ionic charge of each.

chemistry available for this study was used to analyze ratios of selected oxides in order to understand enrichment and depletion trends with depth at Matagorda Island 519. Also, molal relations between elements and oxides determined to be present in certain mineral phases were established from analysis of plots of various elemental and oxide phases. Results of plots for selected oxides are shown in Chapter 4.

3.10. Sediment Mineralogy and Petrology

3.10.1. Previous Research on Sediment Mineralogy and Petrology at MI 519

Sediment mineralogy was previously determined for Amoco for the Matagorda Island 519 field from X-ray diffraction analysis of both whole-rock and clay-fraction samples by Mineralogy Inc., in Tulsa, Oklahoma. Figure 3.12 shows the depth range and well number for all samples analyzed by x-ray diffraction at Amoco. As evidenced by the data presented in this figure, limitations associated with the mineralogy reported by Amoco obtained for this thesis are that the depth range in some wells is either very small or sporadic, and that analyses were not available for all wells in this thesis research.

Because of the limited range of available mineralogical data from Amoco for wells in the Matagorda Island 519 field study area, an additional method was used to determine mineralogy. Normative analyses involving sediments and sedimentary rocks have been performed and published for various sedimentary basins around the world, utilizing computer programs such as SEDNORM (Cohen and Ward, 1991), LPNORM (DeCaritat et al., 1993,1994), and MODAN (Paktunc, 2000).

3.10.2. MUDNORM

The MUDNORM program developed by Hanor (personal communication) for normative analysis of mudstones uses a Visual Basic program code embedded into a

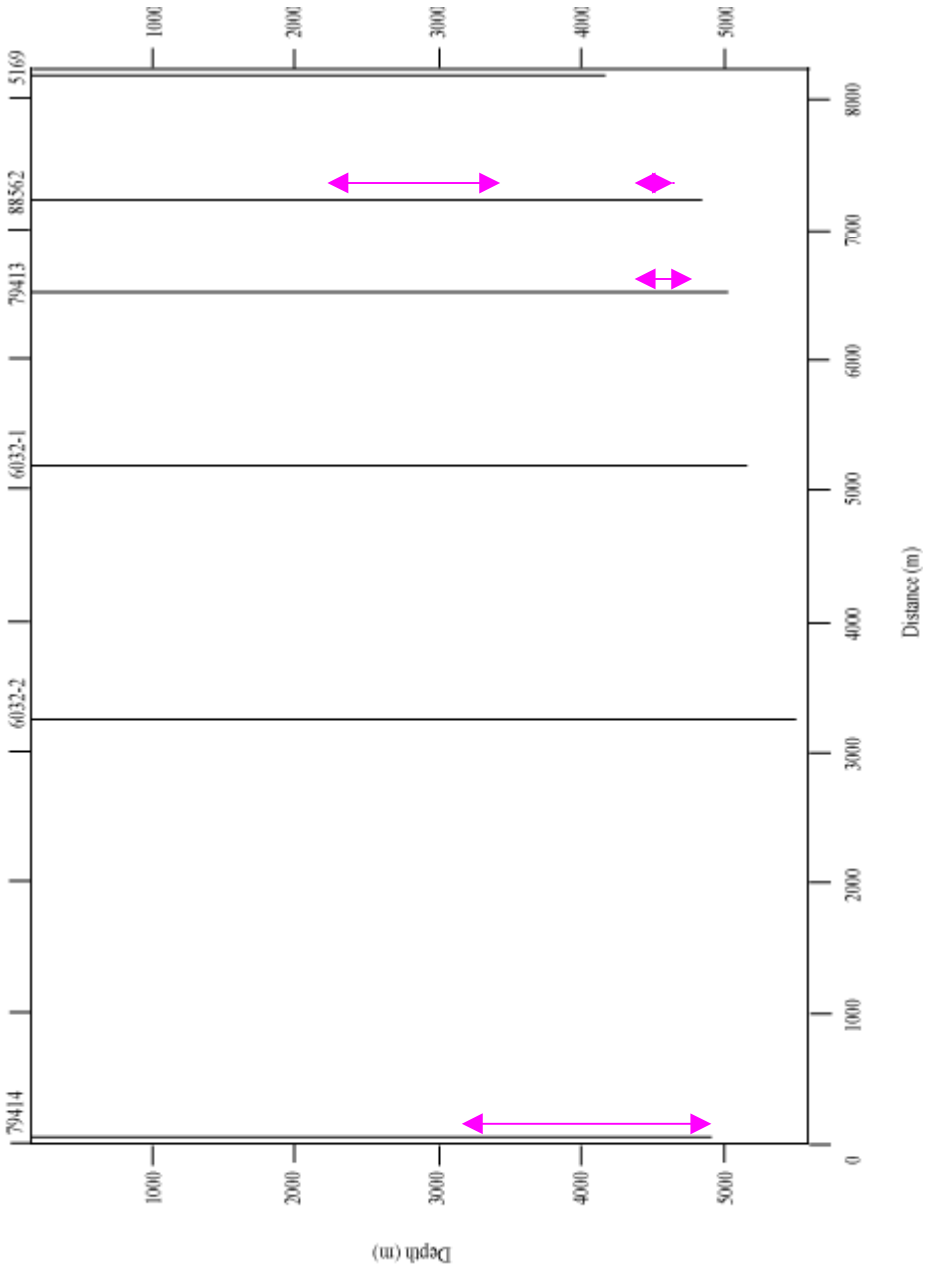

Figure 3.12. Illustration of the locations of Amoco X-ray diffraction data from three wells in the Matagorda Island 519 field. Arrows indicate depth range of XRD samples analyzed for each well.

Microsoft Excel workbook to manipulate the input data via matrix inversion algebra in order to produce results that provide estimates of mineralogic abundance. Initial mineral stoichiometries must beestimated and input into the program. Table 3.4 illustrates the mineral compositions used in the MUDNORM program from mass balance calculations in Lynch (1997).

Eight major mineral phases were known to be present in these sediments, based on the XRD analyses performed by Amoco. These mineral phases include quartz, plagioclase, K-feldspar, calcite, kaolinite, chlorite, illite, and smectite. Compositions for each of these mineral phases were not precisely known based solely on available XRD analysis data, and thus it was necessary to assume reasonable stoichiometries for the mineral phases present at Matagorda Island 519.

The MUDNORM study began using the initial mineral stoichiometries as those of Lynch (1997, Table 6). These mineral compositions were then adjusted in order to yield a better approximation to the mineral abundances reported from Amoco's XRD analyses. Appendix C contains results of normative mineralogy determined from simulation one of MUDNORM versus depth. MUDNORM was developed in order to meet objectives set in this thesis research. Conversion to mineral composition and abundance from bulk oxide data allows for the estimation of the percentage of each mineral phase present. Normative analysis translates oxide weight percent data, such as CaO and K_2O, into more intuitive data on sediment mineralogy, such as calcite and K-feldspar. MUDNORM thus enhances the mineralogic data available for this research.

3.10.3. Sandstone Petrography and Fluorescent Microscopy

Sandstone petrography in this thesis is based on previous research conducted by Amoco. Thin sections from cored sections of sandstone in wells SL 88562 and OCS 5169

Table 3.4. Mineral chemistry used in simulation one of MUDNORM. Data are from mass balance calculations in Lynch (1997).

Quartz	SiO_2
K-feldspar	$KAlSi_3O_8$
Plagioclase feldspar	$Na_{0.7}Ca_{0.3}Al_{1.3}Si_{2.7}O_8$
Albite	$NaAlSi_3O_8$
I-S ~20%I (at 7000 ft)	$K_{0.12}Na_{0.25}(Al_{1.41}Fe_{0.22}Mg_{0.41})(Si_{3.88}Al_{0.12})O_{10}(OH)_2$
I-S ~85%I (at 15000 ft)	$K_{0.65}Na_{0.08}(Al_{1.68}Fe_{0.14}Mg_{0.20})(Si_{3.41}Al_{0.59})O_{10}(OH)_2$
Illite	$K_{0.75}(Al_{1.75}Fe_{0.1}Mg_{0.2})(Si_{3.4}Al_{0.6})O_{10}(OH)_2$
Kaolinite	$Al_2Si_2O_5(OH)_4$
Chlorite	$(Al_{1.77}Fe_{3.27}Mg_{0.96})(Si_{2.89}Al_{1.11})O_{10}(OH)_8$

were available for this study from previous Amoco studies. Petrographic observations are made from these data, and other data, such as photomicrographs, used in this study are from previous research (Brewster, unpublished). Fluorescent microscopy analysis was performed in this study on all of the available thin sections in order to determine the nature of fluid inclusions at Matagorda Island 519. Results from sandstone petrographic analysis and fluorescent microscopy analysis are shown in Chapter 4.

3.11. Hydraulic Gradient and Hydraulic Force Field

The hydraulic gradient and hydraulic force field are important because they can provide information on the flow regime in an area by showing the magnitude and direction of hydraulic force or head within the area. Vertical and lateral hydraulic gradients were calculated at the Matagorda Island 519 field using data on fluid pressure, depth, and spatial distance between wells. The vertical and lateral components of hydraulic force were calculated according to the following equations:

$$Hz = - (dP/dz) + \rho g \qquad (3.6)$$

$$Hx = - (dP/dx) \qquad (3.7)$$

where Hz is the vertical hydraulic gradient in Pa/m, Hx is the lateral hydraulic gradient in Pa/m, P is pressure in Pa, z is vertical distance in m, x is horizontal distance in m, and ρg is specific weight. Hy was not calculated in this thesis because of the lack of data control in the third dimension.

The hydraulic force field was estimated at Matagorda Island 519 from hydraulic force gradient magnitude and direction, using fluid pressure and density data from two wells within the field. The magnitude and direction of the hydraulic force field at Matagorda Island 519 and resultant hydraulic force vectors were calculated from simple geometric relationships:

$$H = Hx + Hz \qquad (3.8)$$

$$|H| = \sqrt{(a^2 + b^2)} \qquad (3.9)$$

$$\theta = \cos^{-1}(a/c) \qquad (3.9)$$

where H is total hydraulic force, Hx is lateral hydraulic gradient, Hz is vertical hydraulic gradient, $|H|$ represents the magnitude of the hydraulic force field, a represents the vertical hydraulic gradient, b represents the lateral hydraulic gradient, and θ represents the orientation of the hydraulic force. A visual representation of how hydraulic force vectors were produced is shown in Figure 3.13. These vectors can determine the direction of fluid flow for variable depths throughout the study area.

3.12. Fluid Velocities and Permeability

The relation between fluid velocity, hydraulic force, and permeability is given by Darcy's Law:

$$v = (k\,\phi\eta) / (-\nabla P + \rho g) \qquad (3.10)$$

where k is permeability in m^2, v is fluid velocity in m/s, ϕ is fractional porosity, η is fluid viscosity in Pa-s, $-\nabla P$ is the pressure gradient, and ρg is specific weight. In terms of hydraulic force this can be rewritten as:

$$v = (k\,\phi\eta) / H \qquad (3.11)$$

where H is hydraulic force (Hanor, 1987).

Pressure, temperature, and salinity in SI units are needed in order to determine density, viscosity, pressure gradient, and specific weight necessary to calculate permeability. Reasonable estimates for fluid velocity and porosity were made, based on regional average values and well log data. Vertical pressure gradient at a given depth was calculated from

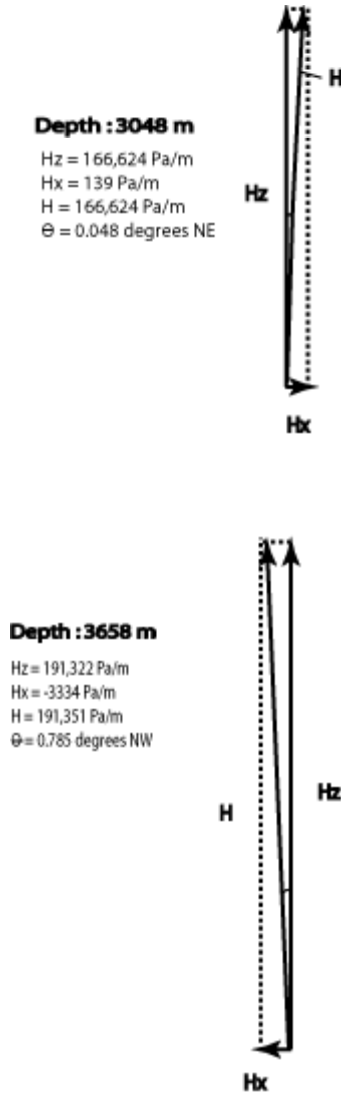

Figure 3.13. Hydraulic force vectors were produced from simple geometric relations between the vertical and lateral components of hydraulic force. Example shown is from well 6032 #2.

fluid pressure divided by depth. Specific weight was determined by multiplying density by gravitational force, using an average value of 9.81 for gravitational force. A spreadsheet algorithm was created for this study to estimate permeability at any given depth from the input data mentioned here by manipulating Darcy's Law.

CHAPTER 4. RESULTS FROM ANALYSIS OF SEDIMENT AND PORE FLUID PROPERTIES

4.1. Structural Geology

Matagorda Island 519 can be characterized structurally on the basis of limited data from Amoco and previously published regional and field scale research (Morton et al., 1985; Seni et al., 1997; Brewster et al., 1998; Klein et al., 1998). A base map showing the relative locations of each borehole is shown in Figure 4.1. The structural features interpreted from seismic were superimposed on the accordion-fold cross sectional view of well penetrations to show the proximity of each well to major structural features. The locations of major and minor faults are shown on the structural cross section seen in Figure 4.2, as well as the locations of other important structural features, such as a rollover anticline and a shale ridge. A major regional growth fault lies at the base of all wells. Because the cross section is a somewhat oblique-to-strike view, the locations of faults in the study area, especially the regional growth fault, appear distorted. Because the regional growth fault is listric, the fault plane moves upsection in the updip direction, which is to the northeast.

Most of the wells in this study penetrate the large growth fault and reach their total depth just below this feature. The most updip well, OCS 5169, penetrates a shale ridge and reaches total depth at the crest of this ridge. There is also a prominent tear fault located between wells OCS 6032 #1 and OCS 6032 #2.

The growth fault is one of many large growth faults that are common to the Gulf of Mexico continental shelf. The location of this growth fault between wells OCS 6032-2 and SL 79414 corresponds to and is likely the cause of the reversal in dip direction of the top of overpressure between these two wells. The location of smaller normal faults found between

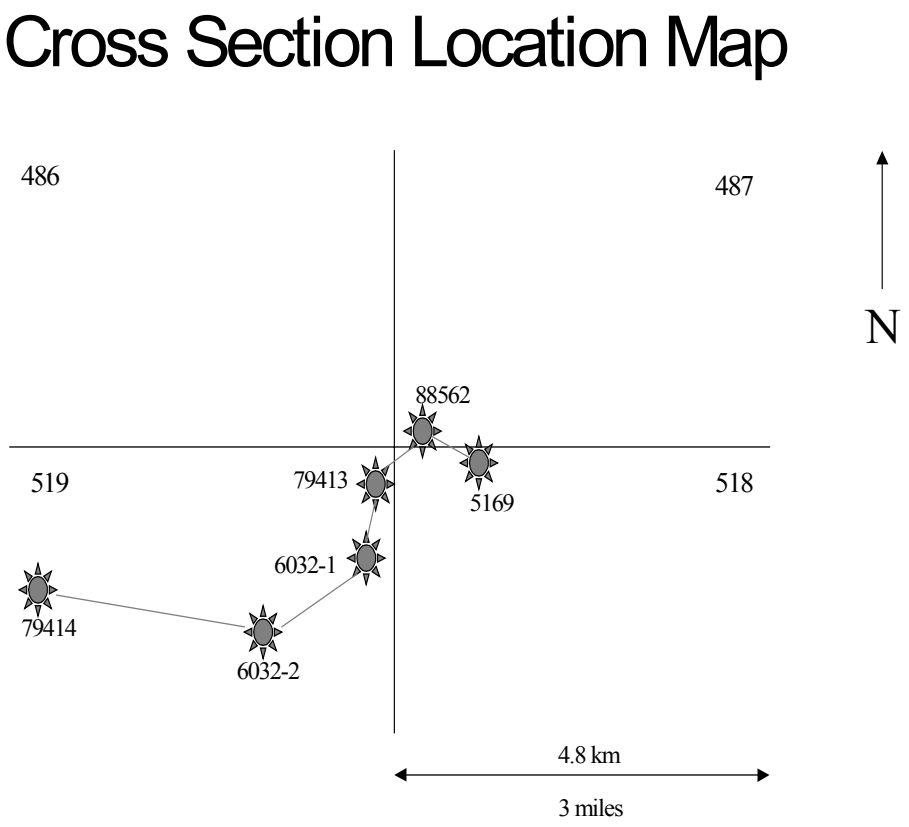

Figure 4.1. Base map shows locations of wells, accordion-fold cross section, and seismic line for the Matagorda Island 519 field, which extends from Matagorda Island Block 519 into Matagorda Island Block 487 and Matagorda Island Block 518.

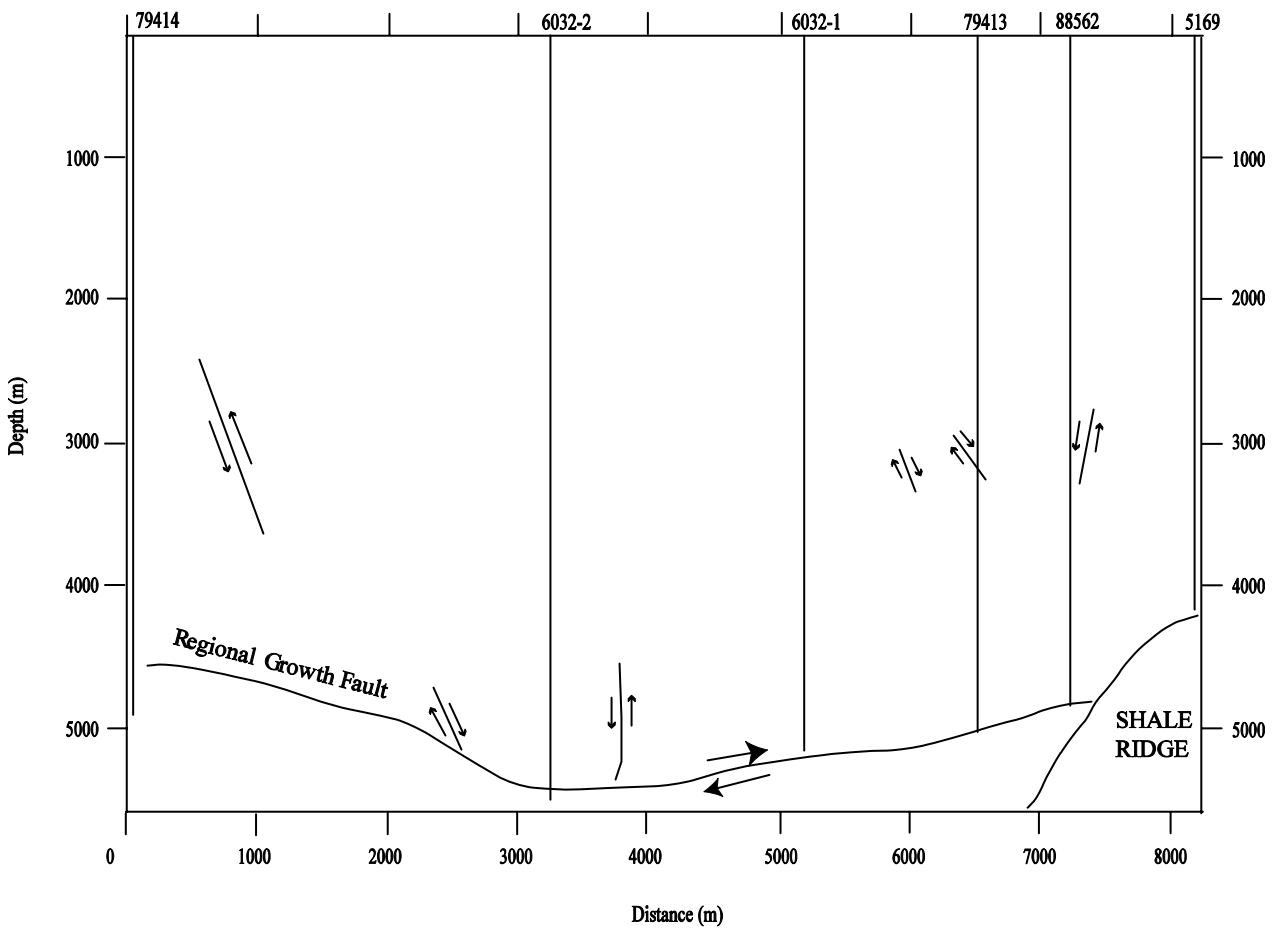

Figure 4.2. Structural cross section based on interpretation of seismic profile.

several of the wells in the field may represent fluid flow conduits. The shale ridge was penetrated by well 5169, which proved to be uneconomic because of cementation, with no commercial recovery of oil or gas.

4.2. Chronostratigraphy

4.2.1. MMS Paleontologic Reports

In well OCS 6032#1 the Middle Miocene *Camerina* 1 is identified at 4940 ft (1506 m) depth (Table 4.1), with no identification of the depth of either the top or base of the Middle Miocene. The first identification of the Lower Miocene in this well is made at 7520 ft (2292 m) depth, and the last identification of the Lower Miocene is made at 14,660 ft (4468 m) depth, with no report of the depth of the base of the Lower Miocene. In well OCS 5169 the Lower Miocene is identified at depths of 12,940 ft (3944 m) and 14110 ft (4301 m), with no identification of either the top or base of the Lower Miocene (Table 4.2).

4.2.2. Core Paleontologic Data

Table 4.3 summarizes core paleontological data from Amoco paleontology reports for well OCS 5169 through a depth interval from 13,572-13,592 ft (4137-4143 m). This interval, which is dominated by shale, contains species of foraminifera that include *Bigenerina humblei, Eponides antillarum, and Textularia sp,* and species of nannofossils that include *Dictyococcites productus, Discoaster deflandrei, Braarudosphaera bigelowii, and Discoaster divaricatus*. These species of foraminifera and nannofossils represent Lower and Middle Miocene ages. It should be noted that there was also observed reworking of Cretaceous nannofossils as well.

4.2.3. Regional Thickness of Chronostratigraphic Units

The regional thickness of Miocene and younger chronostratigraphic units along the Texas Gulf Coast and within the Matagorda Island and surrounding offshore areas is estimated here

Table 4.1. Paleontologic descriptions from MMS public data for Well OCS 6032#1 (Modified from MMS Paleo for Public Release report).

Well Number: OCS 6032#1

Measured Depth (feet)	Paleo Description
4490	Sand
4491	Pyrite
4520	Oxidized Shale
4760	Local marker faunal increase
4940	Middle Miocene Camerina 1=Operc.Sp.=Cris.54-Epon.14
5240	Local marker faunal increase
5420	Local marker faunal increase
5421	Pyrite
6860	Local marker faunal increase
7520	Lower Miocene Disc. Bol.=Rob. Cham.=Cris A"=Disc."B"
7640	Gray Shale
8060	Local marker faunal increase
8120	Sand
8300	Lower Miocene Marginulina "A"=Marg. Ascensionensis
8480	Gray Shale
8630	Sand
9980	Gray Shale
10520	Sand
10521	Local marker faunal increase
10820	Oxidized Shale
11360	Gray Shale
11390	Local marker faunal increase
11480	Local marker (general)
11720	Sand
11960	Local marker faunal increase
12410	Gray Shale
12825	Cement
12920	Sand
13190	Lower Miocene Lenticulina Hanseni
14270	Sand
14660	Lower Miocene Cris. "R"=Lent. Jeff.=Liebusella Fauna
14990	Gray Shale
15320	Sand
16790	Sand

Table 4.2. Paleontologic descriptions from MMS public data for Well OCS 5169 (Modified from MMS Paleo for Public Release report).

Well Number: OCS 5169

Measured Depth (feet)	Paleo Description
12940	Lower Miocene Disc.Bol.=Rob.Cham.=Cris.”A”=Disc.”B”
14110	Lower Miocene Siphonina Davisi

Table 4.3. Paleontological data from well OCS 5169 (Brewster, unpublished).

Measured Depth (feet)	13,572.50	13,575.50	13,592.30
Lithology	90% shale 10% sand	80% shale 20% sand	90% shale 10% sand
Environment (Ecologic Zone)	2	2 - Weak	2
Foraminifera observed	Bigenerina cf. Humblei (V) Eponides antillarum (V)	Textularia sp. (V)	Bigenerina humblei (V) Textularia sp. (V)
Nannofossils observed	Dictyococcites productus (V) Discoaster deflandrei (V)	None	Braarudosphaera bigelowii (V) Dictyococcites productus (V) Discoaster deflandrei (V) Discoaster divaricatus (V)
Reworked Cretaceous	Frequent	Rare	Rare
Oldest Age Diagnostic Species Foraminifera	None	None	Bigenerina humblei
Oldest Age Diagnostic Species Nannofossil	Discoaster deflandrei	None	Discoaster deflandrei

based on studies by Morton et al. (1985) and Seni et al. (1997) (Table 4.4). There are at least 1700 m (5300 ft) of Lower Miocene strata, overlain by 1500 m (4500 ft) of Middle Miocene strata and 350 m (1150 ft) of Upper Miocene strata. Overlying the Miocene, Pliocene-Pleistocene-Holocene thickness is roughly 600 m (1800 ft).

4.2.4. Thickness of Chronostratigraphic Units at MI 519

Age control at the Matagorda Island 519 field and assumed thicknesses for individual chronostratigraphic units at Matagorda Island 519 are based on paleontologic data obtained for two of the wells, OCS 6032-1 and OCS 5169 (Table 4.5). The Lower Miocene is at least 2176 m (7140 ft) thick, and is overlain by at least 786 m (2580 ft) of Middle Miocene strata. The Upper Miocene, Pliocene, Pleistocene, and Holocene together are no more than 1506 m (4940 ft) thick.

4.2.5. MI 519 Chronostratigraphy and Regional Chronostratigraphic Thickness

Lower Miocene sediments occur from depths of approximately 2300-4500 m (7,500-14,750 ft) at Matagorda Island 519, indicating that there was a large volume of sediment deposited in the study area during the Lower Miocene (Table 4.5). These results are consistent with the regional thickness of the Lower Miocene along the Texas Gulf Coast shown in Table 4.4, which is approximately 1700 m (5,300 ft). The Middle Miocene chronostratigraphic unit, with a thickness of approximately 1500 m (4,500 ft), overlies the Lower Miocene in the study area, indicating that a substantial amount of sediment supply was still available to the Matagorda Island 519 field during this time (Table 4.5).

Thickness estimates for the Lower Miocene and Middle Miocene are consistent with thickness estimates for these units determined from data presented by both Morton et al. (1985) and Seni et al. (1997). Thicknesses for the Upper Miocene could not be determined because of

Table 4.4. Estimated regional thickness of Lower Miocene and younger chronostratigraphic units from the Texas Gulf Coast.

Chronostratigraphic Unit(s)	Thickness		Cumulative Depth at Base		Time Interval
	(feet)	(meters)	(feet)	(meters)	(my)
Pliocene-Pleistocene-Holocene	1800	600	1800	600	0 - 5
Upper Miocene	1150	350	2950	950	5 - 11
Middle Miocene	4500	1500	7450	2450	11 - 16
Lower Miocene	5300	1700	12750	4150	16 – 24

Table 4.5. Estimated thickness of Lower Miocene and younger chronostratigraphic units from the Matagorda Island 519 field.

Chronostratigraphic Unit(s)	Thickness		Cumulative Depth at Base		Time Interval
	(feet)	(meters)	(feet)	(meters)	(my)
Upper Miocene-Pliocene-Pleistocene-Holocene	4940	1506	4940	1506	0 - 11
Middle Miocene	2580	786	7520	2292	11 - 16
Lower Miocene	7140	2176	14660	4468	16 – 24

the lack of paleontologic data for this chronostratigraphic unit. Thus, the estimated thickness of the Upper Miocene, Pliocene, Pleistocene, and Holocene combined is only approximately 1000-1500 m (3,000-4,000 ft) at Matagorda Island 519 (Table 4.5). This is consistent with the combined regional thicknesses of the Upper Miocene and Pliocene-Pleistocene-Holocene from Morton et al. (1985) shown in Table 4.4, 950 m (2,950 ft). The slightly thicker estimates in this study are likely due to poor data control at the Upper Miocene-Pliocene boundary. Chronostratigraphic results indicate that there was a significant decrease in sediment supply to the Matagorda Island 519 area after the Middle Miocene (Table 4.5).

4.3.Lithostratigraphy

4.3.1. Interpreted Depositional Setting from SP Log

Figure 4.3 shows portions of SP log responses from wells in the Matagorda Island 519 field that match typical SP log responses known to be characteristic of specific depositional environments (Figure 3.5). According to the criteria defined by Seni et al. (1997) for interpreting depositional setting from SP log character, sediments at the Matagorda Island 519 field represent progradational, aggradational, and retrogradational depositional environments.

Progradational depositional environments are represented by thin to thick, upward coarsening sandstone and sandstone packagaes, aggradational depositional envrionments are represented by thick, blocky, stacked sandstones, and retrogradational depositional environments are represented by upward-fining and upward-thinning packages of sandstone.

Sedimentary facies ranging from relatively deepwater mud-rich distal deltaic environments to relatively shallow water paralic and sand-rich deltaic and shoreline environments are suggested by progradational character. Facies including vertically stacked upper alluvial plain, valley- filled, fluvial channel, overbank, upper delta plain, and sand-rich

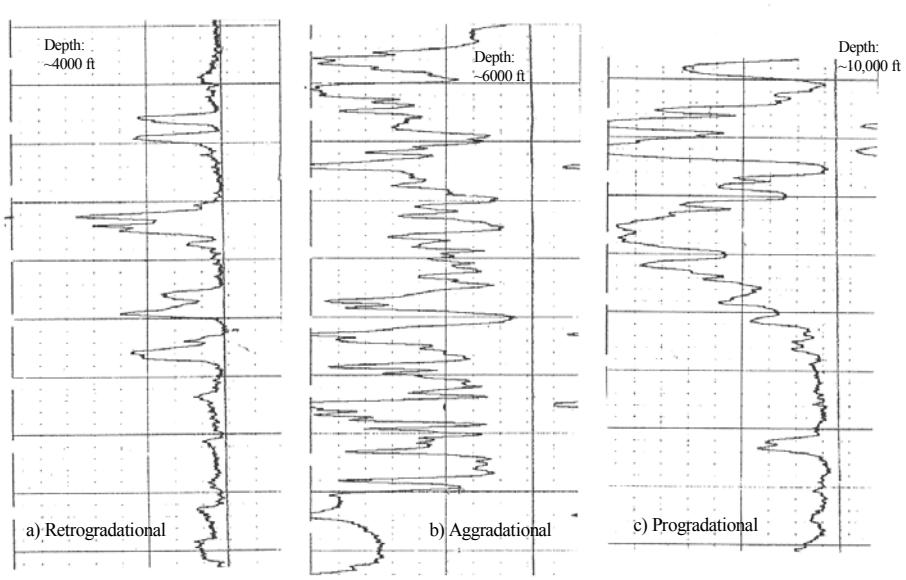

Figure 4.3. Portions of SP log response that represent a) retrogradational, b) aggradational, and c) progradational depositional environments at Matagorda Island 519. Retrogradational depositional environments are typical in the Plio-Pleistocene, while aggradational depositional environments are typical in the Middle-Upper Miocene, and progradational depositional environments are typical in the Lower Miocene.

strandplain systems are suggested by aggradational character. Facies typical of retrogradational environments include back-stepping assemblages of shoreline, deltaic, interdeltaic, and nearshore environments.

Holocene-Pleistocene-Pliocene sediments at Matagorda Island 519 represent retrogradational depositional environments, reflecting decreased sediment input to the area. Upper Miocene and Middle Miocene sediments at Matagorda Island 519 are characterized by aggradational depositional environments. Progradational depositional environments generally represent the Lower Miocene in the study area.

4.3.2. Well SL 79414

Figure 4.4 shows the distribution of sandy and shaly packages within successive 100-ft (30-m) vertical intervals for well SL 79414, in which the depth range is from 975-16,000 ft (300-4900 m) depth. Because this well covers the largest vertical depth range, it is the most representative of Matagorda Island 519 lithostratigraphy.

The distribution of lithology by age for well SL can be summarized as follows. The Holocene-Pleistocene-Pliocene section, from 0-600 m (0-1800 ft), is predominantly mud-rich with a few sandy intervals. The Upper Miocene section, from 600-950 m (1,800-2,950 ft) is also predominantly mud-rich, with some sandy intervals. The Middle Miocene section, from 950-2400 m (2,950-7,450 ft) contains one prominent sand package in the lower portion of the section and is generally sandy in the upper portion of the section.

The upper part of the Lower Miocene section in well SL 79414, from 2400-3500 m (7,450-11,000 ft) is sand-rich, consisting of a large sand package in the upper portion of the section and another sand package in the lower portion of the section that are separated by a shaly interval. The lower part of the Lower Miocene section, from 3500- 4550 m (11,000-14,500 ft)

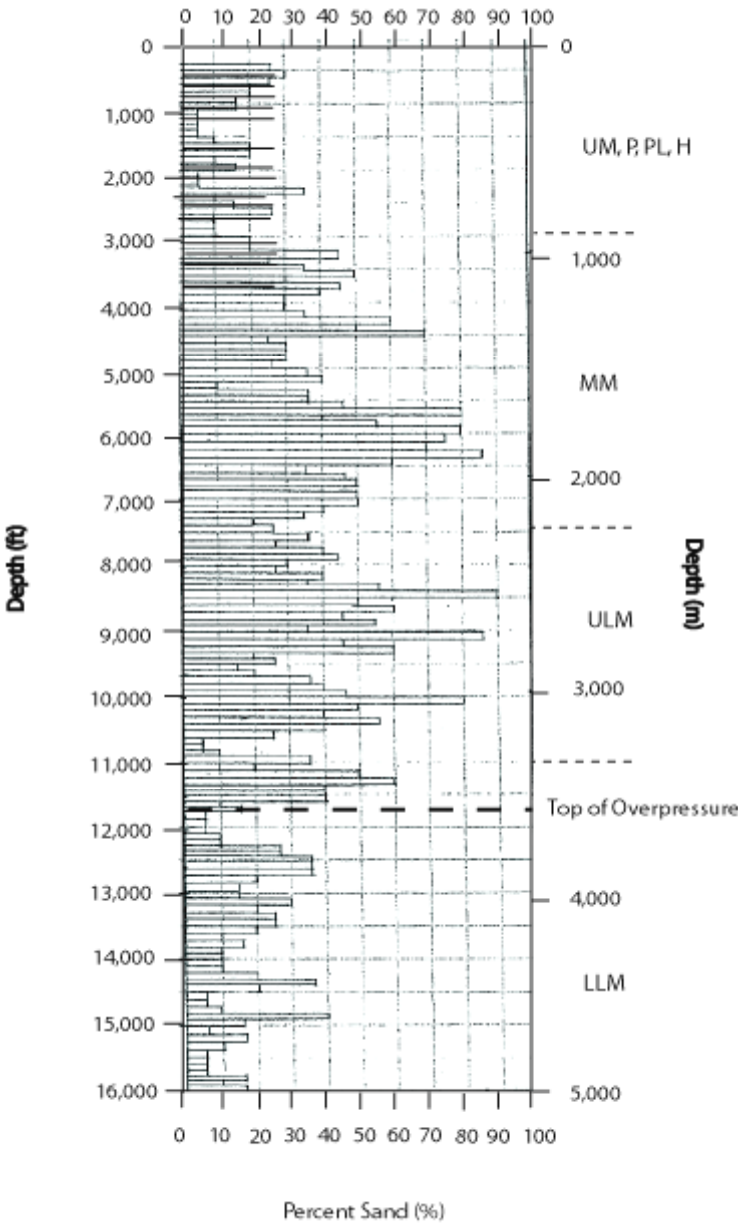

Figure 4.4. Distribution of sandy and shaly vertical intervals in well SL 79414. See chapter 6 for a discussion of the top of overpressure.

is characterized by interbedded sandy and shaley packages. A single sandy package is observed in the upper portion of this section, followed by a large shaley interval from 3500-3800 m (11,600-12,300 ft). Shales and fine sands are interbedded from 3800-4550 m (12,300-14,500 ft).

4.3.2. Well OCS 6032 #1

The lithostratigraphy at well OCS 6032#1 is illustrated by the bar graph of vertical distribution of sands and shales seen in Figure 4.5. The total depth interval represented on this bar graph is from 4,900-16,700 ft (1500-5100 m). In general, observed patterns in the vertical distribution of sands and shales, as well as the distribution of lithology by age, for well OCS 6032 #1 are similar to those observed and described previously for well SL 79414.

The distribution of lithology by age for well OCS 6032 #1 is presented for only those chronostratigraphic units that are represented in the lithostratigraphic bar graph for this well, the Middle Miocene and the Lower Miocene. The Middle Miocene section, from 1460-2300 m (4,800-7,500 ft), is predominantly sand-rich, with little to no shaly intervals. The upper part of the Lower Miocene section, from 2300-3500 m (7,500-11,000 ft), contains a prominent sand package in the upper portion of the section and a less prominent sand package in the lower portion of the section. There are some shaly intervals interspersed, located just above and below the prominent sand package. The lower part of the Lower Miocene section, from 3500-4550 m (11,000-14,500 ft), is similar to that of well SL 79414, with a large shaly interval observed from 3450-3600 m (11,400- 11,800 ft). From 3800-4550 m (12,300-14,500 ft) fine sands appear to be dominant.

4.3.3. Well SL 88562

The lithostratigraphy for well SL 88562 is generally similar to that of wells SL 79414 and OCS 6032 #1, with similar observed patterns in lithology by both depth and age (Figure 4.6).

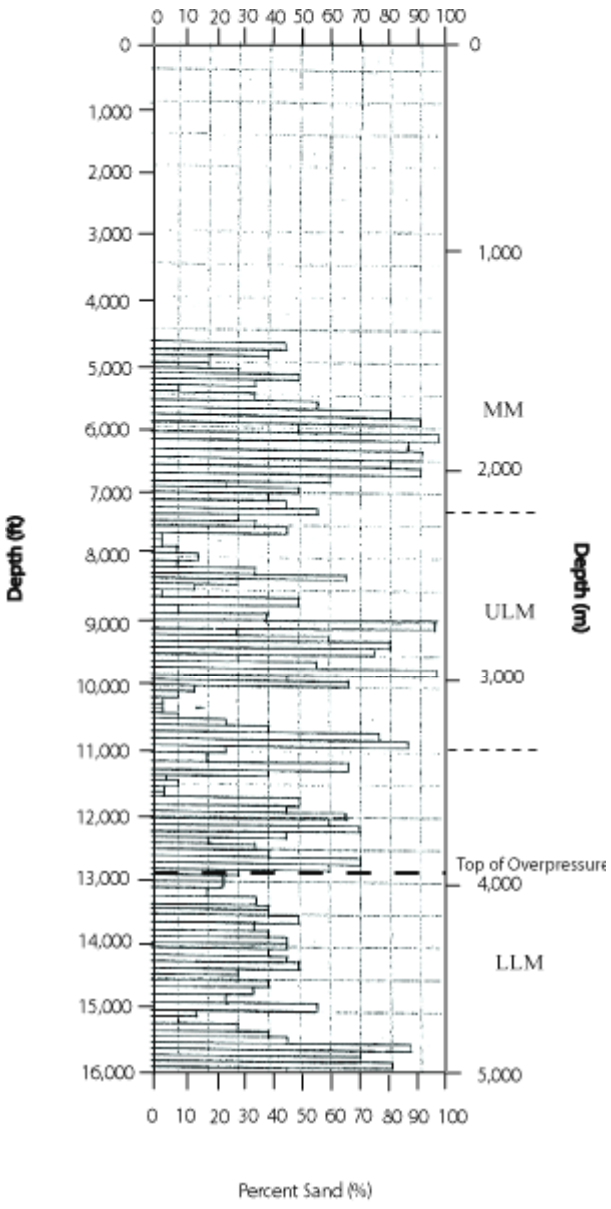

Figure 4.5. Bar graph showing distribution of sandy and shaly packages within successive 100-foot vertical intervals for well OCS 6032#1.

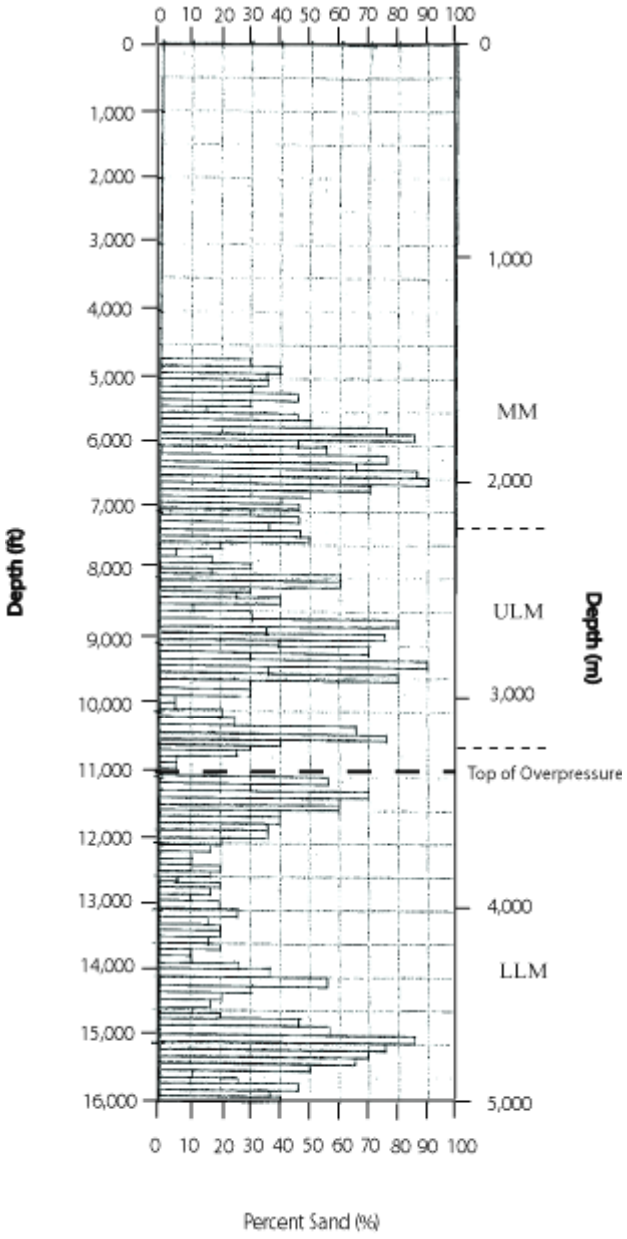

Figure 4.6. Distribution of sandy and shaly packages within successive 100-foot vertical intervals for well SL 88562.

The vertical distribution of sands and shales at well SL 88562 is almost identical to that of well OCS 6032 #1 from 4900 ft (1500 m) to 12,000 ft (3650 m), represented by the same prominent sand packages and shaly intervals. From 12,000 ft (3650 m) to 14,500 ft (4400 m) the vertical distribution of sands and shales at well SL 88562 is almost identical to that of well SL 79414, represented by interbedded shales and fine sands.

The depth range of well SL 88562 is similar to that of well OCS 6032 #1 and the vertical distribution of sands and shales is similar for the upper portion of both wells. Thus, the distribution of lithology by age at well SL 88562 is inferred to be similar to that of well OCS 6032 #1 for the Middle Miocene section from 1460-2300 m (4,800-7,500 ft) and the upper part of the Lower Miocene section from 2300-3500 m (7,500-11,000 ft). For the same reasons, the distribution of lithology by age at well SL 88562 is inferred to be similar to that of well SL 79414 for the lower part of the Lower Miocene section.

4.3.4. Wells 6032 #2, 79413, and 5169

Figure 4.7 shows bar graphs for the depth interval from 11,000-13,000 ft (3350-3950 m) in wells 6032-2, 79413, and 5169. This depth interval is generally characterized by coarsening upward successions in all wells, with the sandiest intervals in the upper portion of this depth interval. In the upper portion of this depth interval, a sandy interval is represented by percent sand values ranging from 50 percent in wells 6032-2 and 79413 to 70 percent in well 5169. An overall decrease in sand content with depth is observed for wells 79413 and 5169, with percent sand values dropping to 5-10 percent throughout the lower portion of the depth interval. Well 6032-2 displays a decrease in sand content below the initial sandy interval, then a second sandy interval near 12,150 ft (3700 m), followed by a decrease in sand content with depth below 12,150 ft (3700 m).

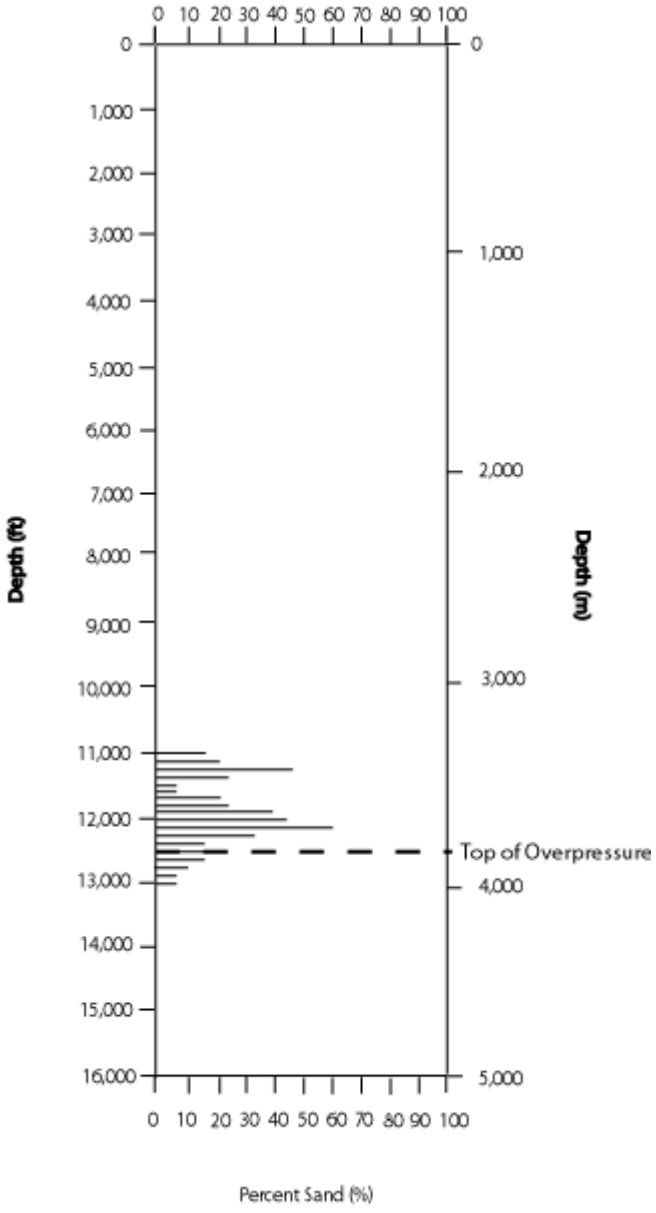

Figure 4.7(a). Bar graph of sandy and shaly vertical intervals within successive 100-foot vertical intervals that correspond to the depth of overpressure in well 6032-2.

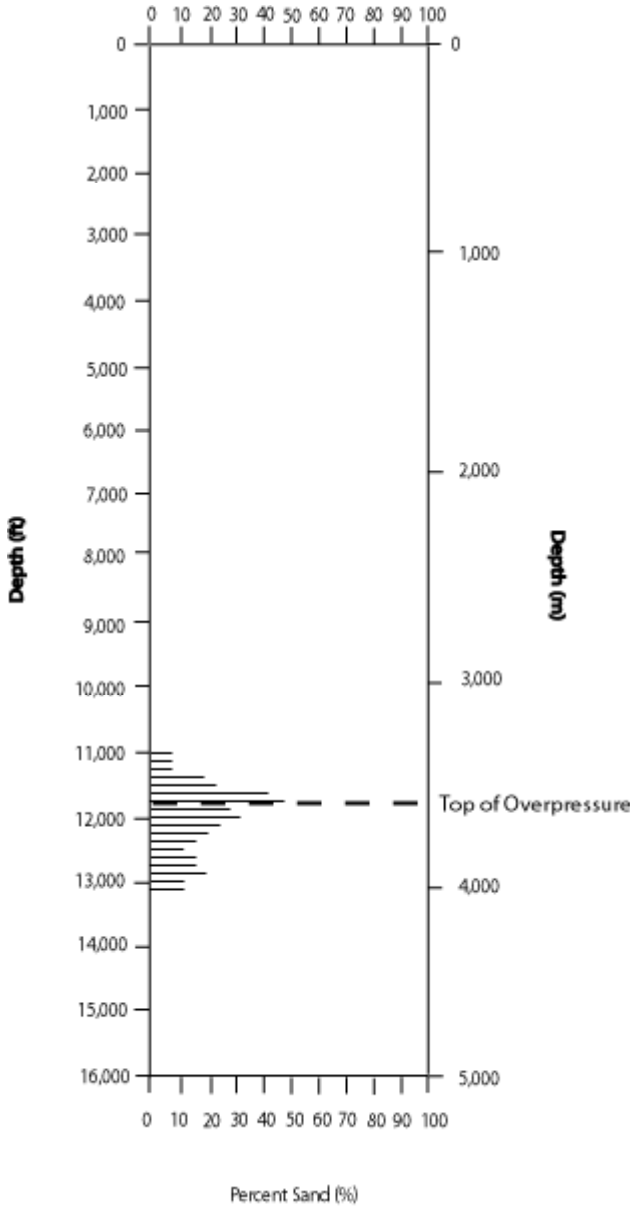

Figure 4.7(b). Bar graph of sandy and shaly vertical intervals within successive 100-foot vertical intervals that correspond to the depth of overpressure in well 79413.

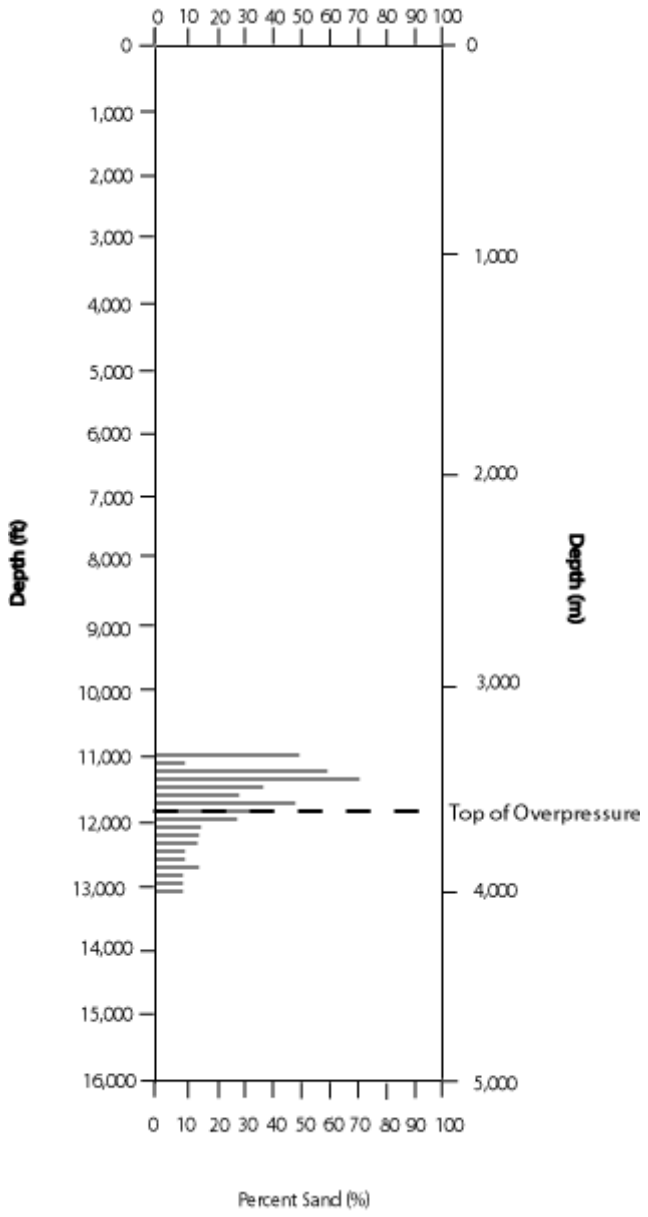

Figure 4.7(c). Bar graph of sandy and shaly vertical intervals within successive 100-foot vertical intervals that correspond to the depth of overpressure in well 5169.

The depth interval shown on these bar graphs, from 3350-3950 m (11,000-13,000 ft), represents a portion of the Lower Miocene chronostratigraphic unit. The Lower Miocene is represented by a progradational stacking pattern, with coarsening upward successions. The Lower Miocene contains 1 to 2 prominent sand packages in the intervals studied here, separated by large shaly packages.

4.3.5. Summary

Figures 4.8(a) and 4.8(b) show the cross-sectional distribution of sands and shales within the Matagorda Island 519 field with sandy packages represented by values of 50% percent sand and greater, and shaly packages represented by values of 5% sand and lower. A prominent sandy package is correlated across the field at approximately 2,000 m (6,500 ft). There is evidence to suggest that a shaly package across the field can be correlated at 3500-4000 m (11,500-13,000 ft), although this is not compelling from the figures.

According to the paleogeographic reconstructions from Galloway et al. (2000), the Lower Miocene depositional environment at Matagorda Island 519 was characterized by deposition of the prominent *Marginulina A* marine shale tongue, and also by deltaic deposition associated with the Corsair deltaic system. Lithostratigraphy from this study shows that an interfingering between sands and shales exists in the Lower Miocene at Matagorda Island 519, with several packages of sand-rich sediments and several intervals consisting of fine-grained sediments (Figure 4.8). The locations of these fine-grained packages are consistent with descriptions by Galloway et al. (2000) of pulses of marine shales deposited during the Lower Miocene, and the locations of sand-rich packages correspond to delta progradation during the Lower Miocene documented by Galloway et al. (2000).

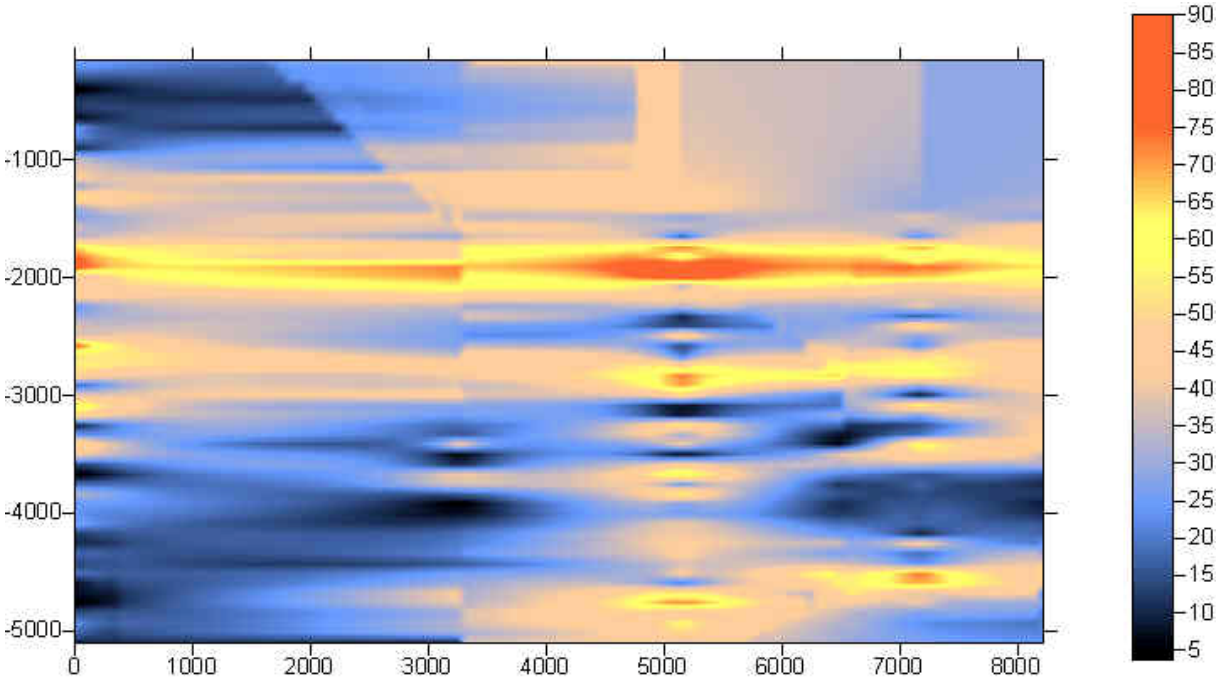

Figure 4.8 (a). Spatial distribution of sandy and shaly packages within successive 100-ft (ca. 30-m) vertical intervals in study area. Sandy packages are represented by percent sand values of 50% and greater (red) and shaly packages are represented by percent sand values of 5% and lower (blue). Distance in meters is measured from well 79414 (0 meters) to well 5169 (8000 meters) and is shown on the x-axis. Elevation in meters is on the y-axis. Color bar represents values for percent sand beds. Note that the top of overpressure occurs fieldwide between 3500 and 3800 m depth.

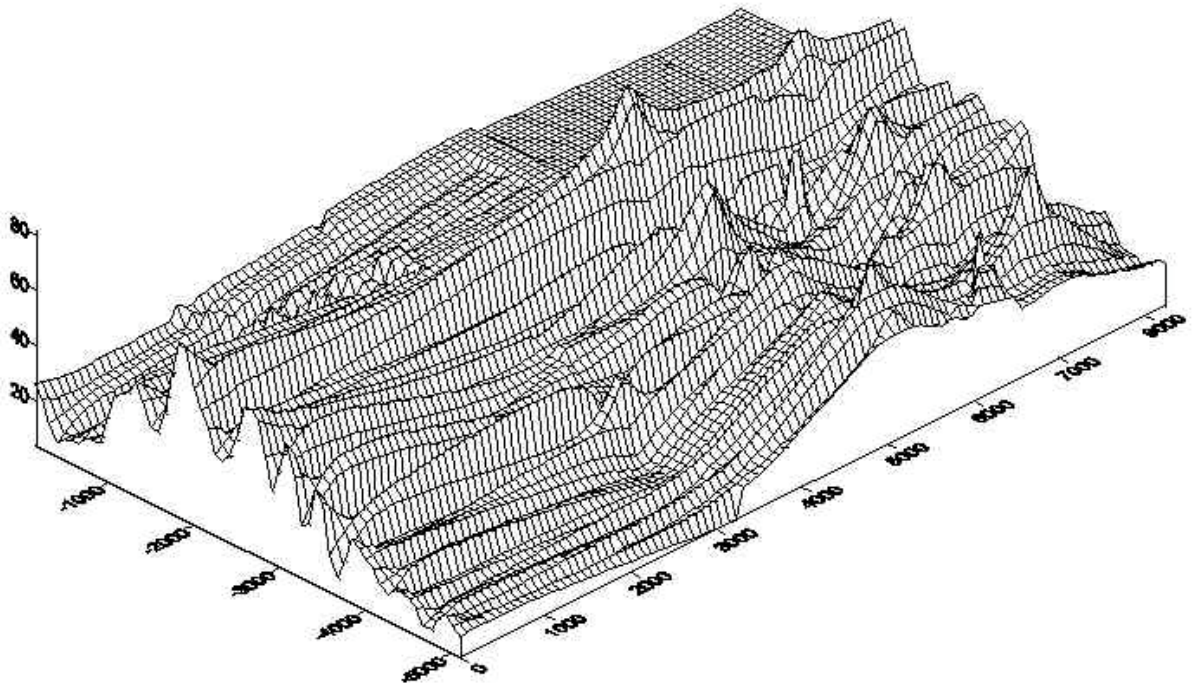

Figure 4.8 (b). Three-dimensional view of the spatial distribution of sandy and shaly packages within 100-foot vertical intervals in study area. Percent sand is represented on the z-axis, elevation in meters is on the y-axis, and distance in meters is on the x-axis.

The location of a large shaly package at a depth of approximately 3560-3750 m (11,700-12,300 ft) in the study area (Figure 4.8) is of significance because this shaly package appears to correspond to the top of overpressure at Matagorda Island 519, as will be described in chapter 6. Also of interest is the location of a sandy package immediately overlying this shaly package at a depth of approximately 3300-3500 m (11,000-11,500 ft).

4.3.6. Petrophysical Log Analysis

Table 4.6 lists results for lithology and relative percent calcite cement recorded on the petrophysical well log for well 6032 #1. These results are shown to determine the amount of calcite cement present within all lithologies in the study area. Figure 4.9 shows that there are several peaks in calcite cement throughout the depth interval shown, and there is a large increase in calcite cementation at the overpressure transistion zone. Values reported here represent relative abundance of calcite cement as reported on the cuttings log description, with 0 representing no calcite cement, 25 representing slight calcite cement, 50 representing moderate calcite cement, and 75 representing abundant calcite cement.

4.3.7. Rate of Penetration Log Analysis

Figure 4.10 shows drillbit transit time, which was calculated from the rate of penetration well log for well 6032 #1, versus depth. From depths of 500-1500 m, drillbit transit time is low, with values less than 0.1 hr/m, which means that this section was drilled relatively rapidly. There is a peak of increased drillbit transit time that occurs at 1900 m, with a value of 0.17 hr/m that represents an interval that was drilled relatively. Below 1900 m drillbit transit time increases in a uniform fashion with depth until 3300 m. At 3300 m drillbit transit time increases to 0.39 hr/m, which represents a section that was drilled unusually slow compared to those above it. This peak is followed by a larger peak at 3850 m, with drillbit transit time increasing to 0.57

Table 4.6. Data from petrophysical analysis log for well 6032 #1, showing both lithology and relative abundance of calcite cement present in shale cuttings, 0 = absent, 25 = slight, 50 = moderate, 75 = abundant.

Depth (ft)	Lithology	Abundance of Calcite Cement
10090	Siltstone	50
10180	Shale	50
10260	Siltstone	75
10340	Shale	50
10420	Siltstone	50
10480	Shale	50
10550	Siltstone	50
10620	Sandstone	50
10700	Silty Sand	25
10810	Sand	25
10900	Siltstone	75
10980	Sandstone	75
11060	Sandstone	50
11140	Siltstone	50
11190	Sandstone	75
11290	Siltstone	50
11500	Shale	25
11570	Siltstone	50
11640	Shale	25
11720	Sandstone	50
11800	Sandstone	50
11900	Sandstone	50
11970	Siltstone	50
12110	Sandstone	0
12170	Siltstone	50
14690	Sandstone	50
14800	Sandstone	50
14910	Shale	50
12320	Shale	25
12370	Sandstone	50
12420	Siltstone	75
12480	Clay	50
12530	Shale	50
12600	Shale	50
12650	Siltstone	50
12710	Shale	50
12750	Siltstone	50
12920	Sand	0
12970	Shale	50
13040	Sand	50
13100	Shale	25
13170	Siltstone	75
13300	Sand	25
13360	Sand	25
13420	Siltstone	75
13490	Shale	50
13570	Siltstone	50
13640	Sand	25
13700	Siltstone	75
13800	Siltstone	0
13870	Siltstone	75
13930	Siltstone	50
14010	Sand	25
14080	Siltstone	25
14150	Siltstone	25
14160	Siltstone	50
14230	Sandstone	50
14310	Siltstone	50
14370	Siltstone	50
14430	Sand	25
14540	Siltstone	75
14610	Siltstone	50

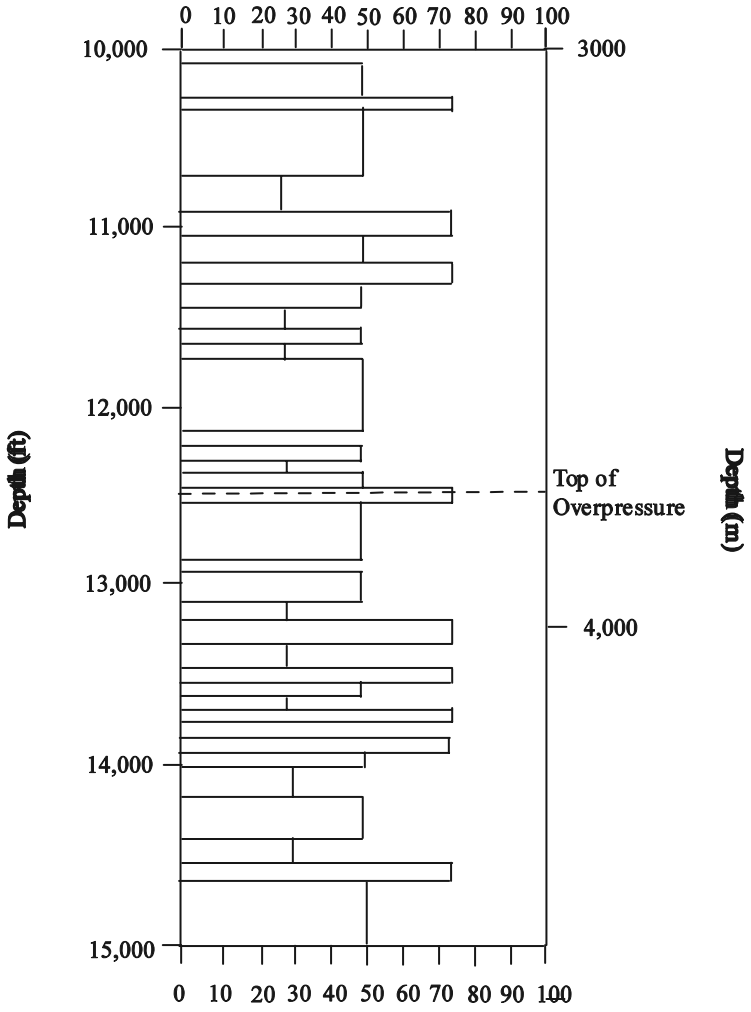

Figure 4.9. Bar graph showing relative abundance of calcite cementation with depth. Data from petrophysical formation evaluation log for well 6032 #1.

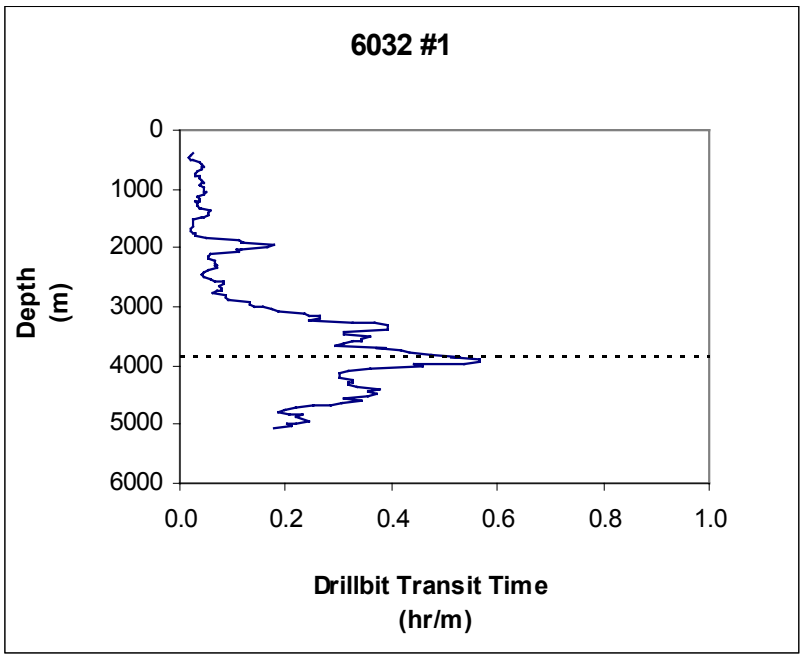

Figure 4.10. Drillbit transit time, obtained from rate of penetration (ROP) well log analysis, versus depth for well 6032 #1. Spikes in this curve represent sections that were drilled relatively slowly. Dashed line represents the top of overpressure.

hr/m, indicating that this interval was drilled more slowly than any of the intervals overlying it. There is a third peak in drillbit transit time of 0.38 hr/m at 4350 m, representing an interval that was drilled slower than those immediately above or below it. This depth interval also corresponds to the interval of high calcite cement observed in well 6032 #1 on the petrophysical formation evaluation log.

4.3.8. Additional Well Log Analyses

In addition to petrophysical log analysis, analysis of responses from SP, gamma ray, resistivity, and neutron-density porosity well logs across the top of overpressure provides information on lithology and pore fluid chemistry. SP and gamma ray logs have been shown to exhibit a specific response to massively cemented zones, observed as positive deflections, and massively cemented zones can cause resistivity spikes that are similar in appearance to high-resistivity hydocarbon kicks (McManus, 1991). These high-resistivity kicks can be confirmed as cemented zones with analysis of neutron-density porosity logs that show low porosity within the cemented zone and analysis of cuttings to show cemented sands (McManus, 1991).

4.4. Fluid Pressure

Figure 4.11 shows the variation in calculated fluid pressure versus depth for well 6032 #1. Two plots are shown, one for fluid pressures calculated from mudweights, the other for fluid pressures calculated from shale resistivity. Fluid pressure versus depth plots for all wells in this study show that fluid pressure increases at or near the top of overpressure fieldwide. Mudweight-derived fluid pressures increase slightly deeper than resistivity-derived fluid pressures throughout the field (Figure 4.11). Resistivity-derived fluid pressures more accurately reflect in-situ subsurface conditions than mudweight-derived fluid pressures, due to corrections that are made to drilling fluids in order to prevent well blowouts.

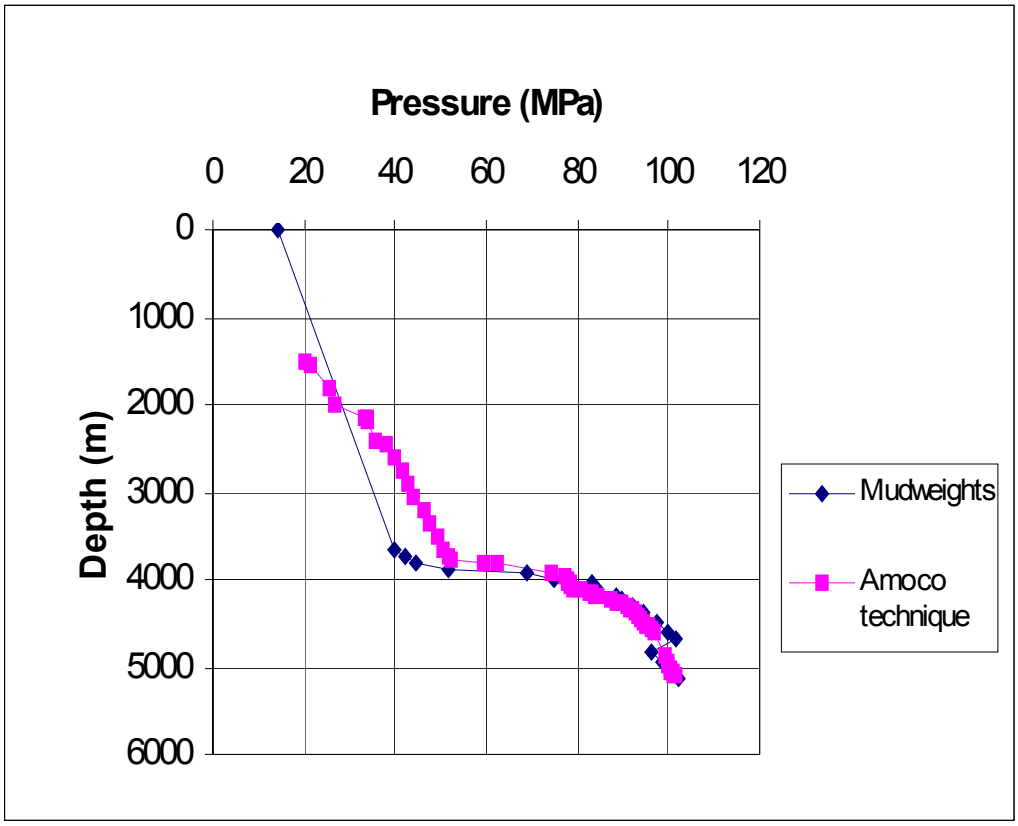

Figure 4.11. Comparison of fluid pressure versus depth for well OCS 6032 #1, using fluid pressures calculated from mudweights and from Amoco calculations.

4.4.1. Mudweight-Derived Fluid Pressures

Figure 4.12 shows fluid pressure versus depth for all wells in the Matagorda Island 519 field using the mudweight technique. Fluid pressure determined from mudweight data shows a range from approximately 5 MPa near the surface to approximately 100 MPa at a depth of 5000 m (16,400 ft) in the study area. The fluid pressure versus depth profile generated from mudweight data does exhibit some kinks and reversals near the top and bottom of logged portions of wells. This can be attributed to drilling activity, such as adjusting the specific weight of the drilling fluids in certain intervals.

Calculated fluid pressures track along a hydrostatic gradient at shallow depths and then show an abrupt transition to overpressured conditions at depths of approximately 3600-4200 m (11,800-13,800 ft). The transition occurs over depth intervals of approximately 100-200 m (325-650 ft). At these depths fluid pressure increases by 20-40 MPa within the study area.

4.4.2. Resistivity-Derived Fluid Pressures

Although there is some data scatter, fluid pressure generally tracks along a hydrostatic gradient until depths of approximately 3500-3900 m (11,500-12,800 ft), where there is a sharp increase in fluid pressure over a very small depth interval, similar to that observed with mudweight-derived fluid pressures (Figure 4.13). There is an increase in fluid pressure of 20 to 30 MPa over depth intervals of approximately 100-200 m (325-650 ft) in all wells. The two most downdip wells, however, show fluid pressure increases that appear to be more gradual relative to the increases observed in the other four wells, with the pressure increase occurring over a larger depth interval in these two wells than in the other four wells.

4.4.3. Comparison of Calculated Pressures

There is overall agreement between fluid pressure curves derived from mudweights and those calculated by Amoco based on shale resistivity. Mudweight-derived fluid pressures are

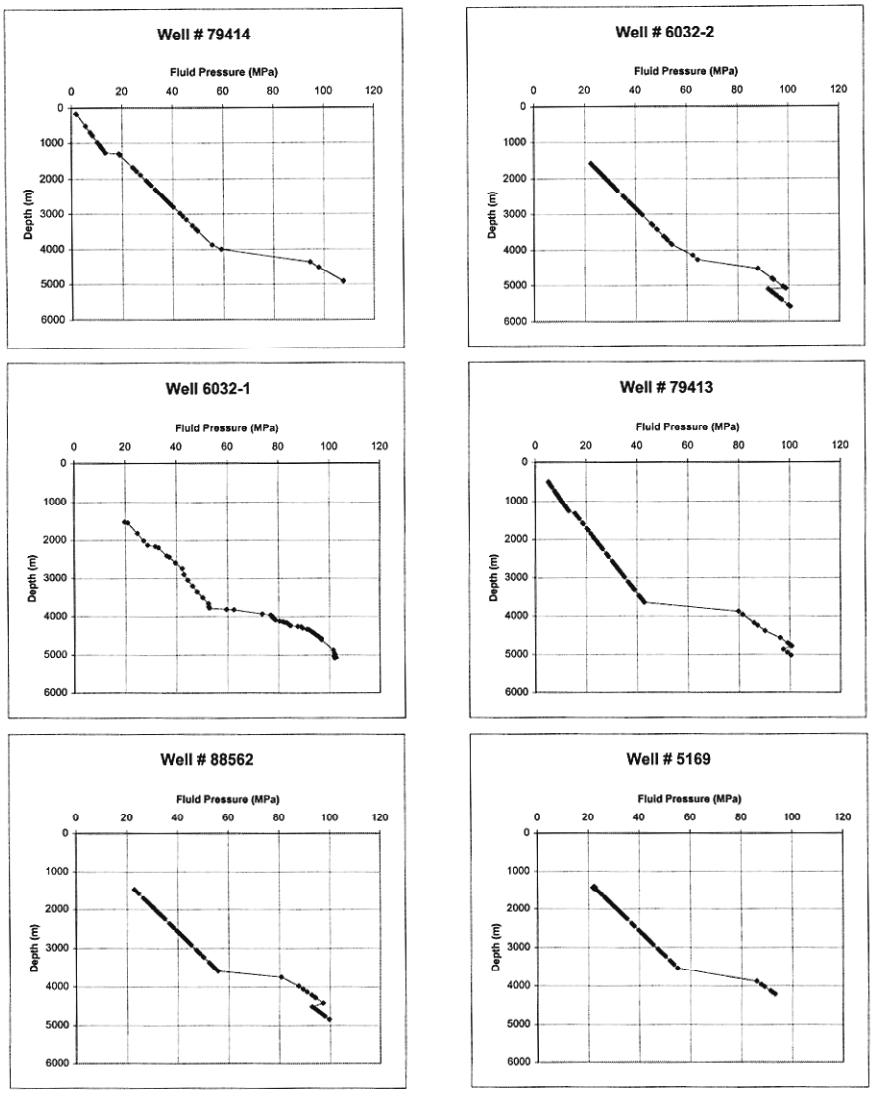

Figure 4.12. Fluid pressure versus depth profiles for all wells in Matagorda Island 519 field used in this research. Fluid pressures were determined from mudweight data.

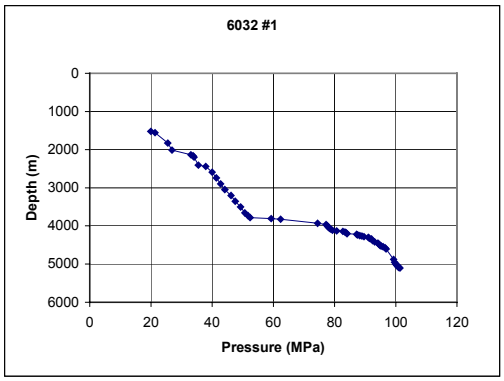

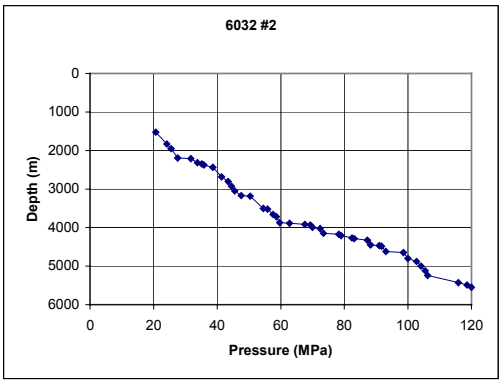

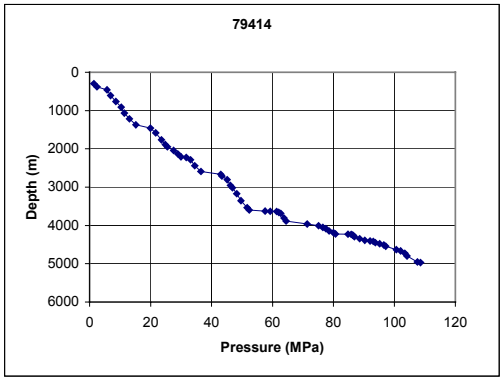

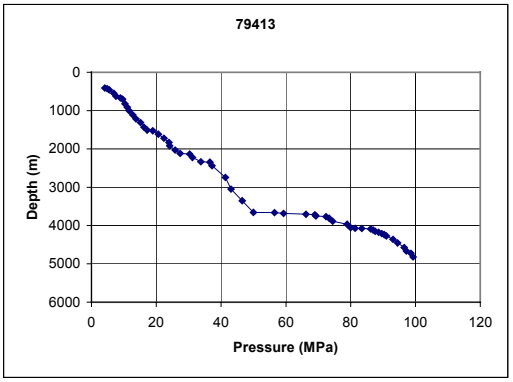

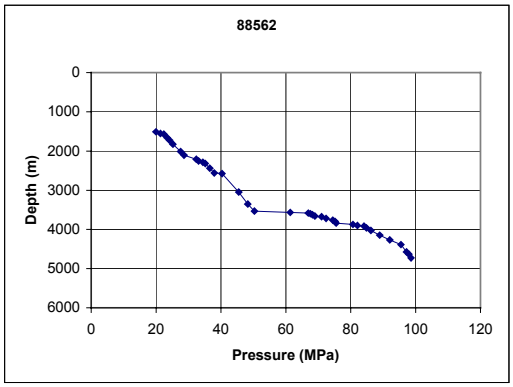

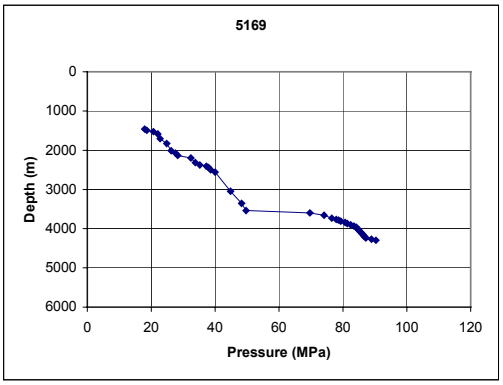

Figure 4.13. Fluid Pressure versus depth profiles for all wells in the Matagorda Island 519 field used in this study. Fluid pressures were determined by Amoco from shale resistivity.

slightly lower than resistivity-derived fluid pressures at shallow depths, and slightly higher than resistivity-derived fluid pressures in the deeper part of the section. These discrepancies are likely due to drilling muds being underweighted upsection and overweighted downsection in order to minimize blowout risk in the well.

Curves of fluid pressure versus depth for resistivity-derived fluid pressures are not as smooth as the curves of mudweight-derived fluid pressure versus depth. This is likely due to the fact that more data points for fluid pressure are generated from the shale resistivity method than from the mudweight method. In contrast to mudweight-derived fluid pressures, the abrupt increase for resistivity-derived fluid pressures appears to occur just above 4000 m (16,400 ft) for all wells. The resistivity-derived fluid pressures are probably more accurate estimates of true fluid pressures in the subsurface at the Matagorda Island 519 field because of the effects due to over- and underweighting drilling fluids on mudweight.

Figure 4.14 is a comparison plot of Amoco-derived fluid pressures versus depth for all wells in the Matagorda Island 519 field. The largest lateral difference in fluid pressures is between wells 5169 and 6032-2. Figure 4.15 illustrates resistivity-derived fluid pressures versus depth for these wells to highlight the lateral pressure differences between the two wells. Fluid pressures are generally similar in both wells to depths of approximately 3000 m (10,000 ft). From 3000-3600 m (10,000-11,800 ft), fluid pressures are approximately 1-5 MPa higher in well 6032 #2 than in well 5169. The trend is reversed from 3600-4200 m (11,800-13,800 ft), with fluid pressures in well 5169 approximately 8-16 MPa higher than in well 6032 #2. Fluid pressure data from each of these wells was used to determine the lateral hydraulic gradient at Matagorda Island 519, results of which are presented in section 4.10.

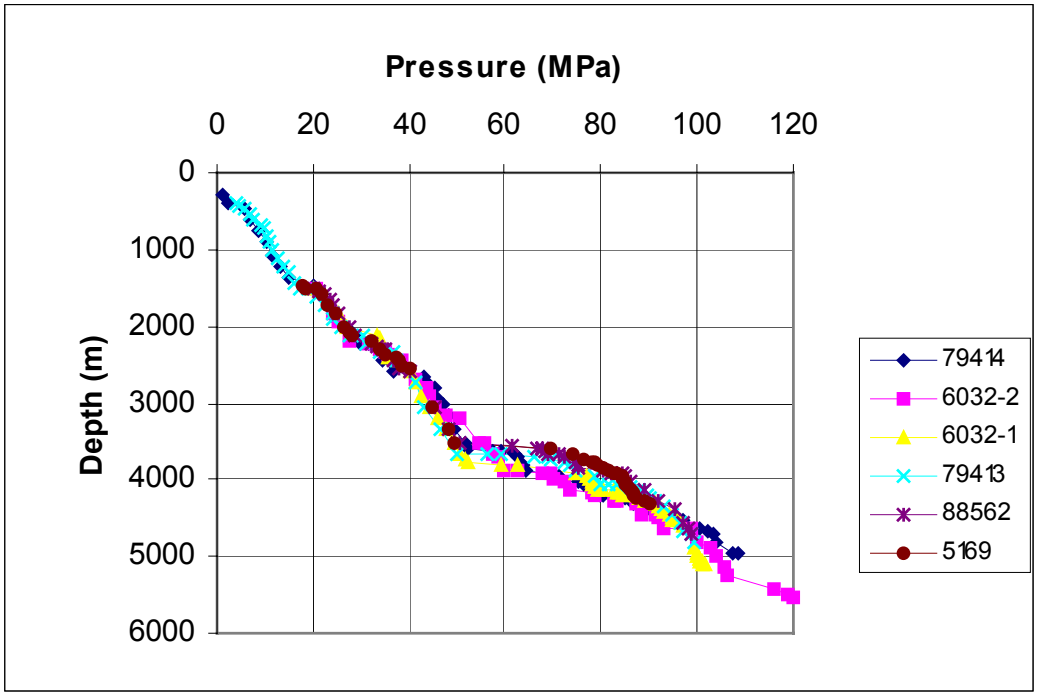

Figure 4.14. Comparison of resistivity-derived fluid pressure versus depth in all wells.

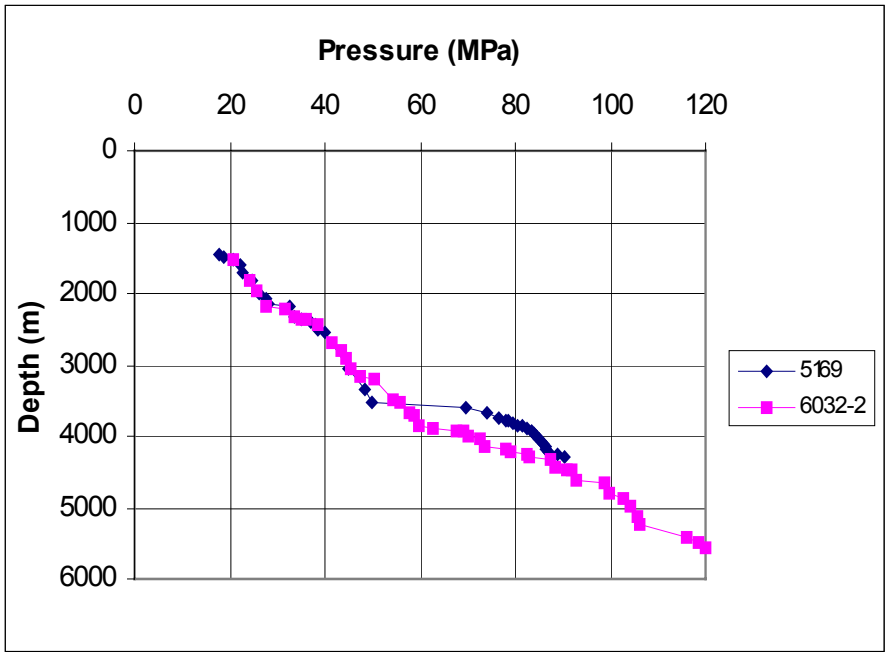

Figure 4.15. Resistivity-derived fluid pressure versus depth in wells 5169 and 6032-2.

4.4.4. Excess Pressure

Figure 4.16 illustrates the spatial variation in excess pressure, the magnitude of the difference between fluid pressure and hydrostatic pressure in MPa, which is a proxy for determining the magnitude of overpressure in the study area. Excess pressure throughout Matagorda Island 519 increases abruptly within a depth interval of approximately 3500-4200 m (11,500-13,800 ft). Within this depth interval excess pressure increases from approximately 15-20 MPa to approximately 45-48 MPa. These results are consistent with the placement of the overpressure transition zone within a depth interval of 3500-3900 m (11,500-12,800 ft) in the study area.

4.4.5 Vertical Pressure Gradient

The pressure gradient at Matagorda Island 519 is defined as the first derivative of pressure versus elevation in MPa per meter, and is shown in Figure 4.17. From the surface to a depth of approximately 2400 m (8,000 ft) there is a constant increase in the pressure gradient from 0.0005-0.0016 Mpa/m. The pressure gradient decreases to 0.0014-0.0015 Mpa/m for all wells in the study area from 2400-3350 m (8000-11,000 ft), and increases again to 0.0016 Mpa/m after 3350 m (11,000 ft).

An abrupt increase in the pressure gradient occurs at approximately 3650 m (12,000 ft), especially in the more updip wells, where the pressure gradient increases from 0.0016 Mpa/m to 0.0020 Mpa/m over a depth range of approximately 100-200 m (325-650 ft). The pressure gradient then returns to a more gradual trend of increase with depth from 3950-4900 m (12,950-16,100 ft) for all wells in the study area, with pressure gradient increasing from 0.0020 Mpa/m to 0.0022 Mpa/m for this depth interval. The top of overpressure is defined for each well at the depth in which an abrupt increase in the first derivative of fluid pressure occurs.

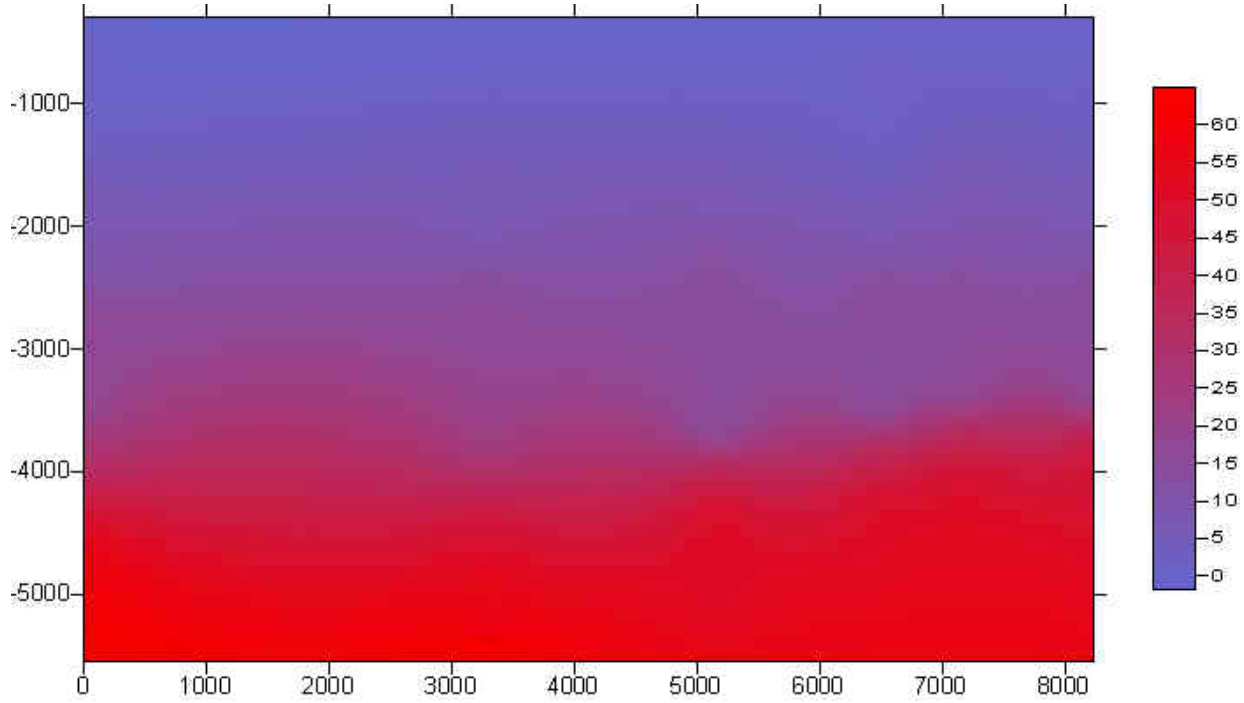

Figure 4.16. Spatial variation in excess pressure in the study area. Color bar shows that red represents highest values of excess pressure and blue represents lowest values of excess pressure.

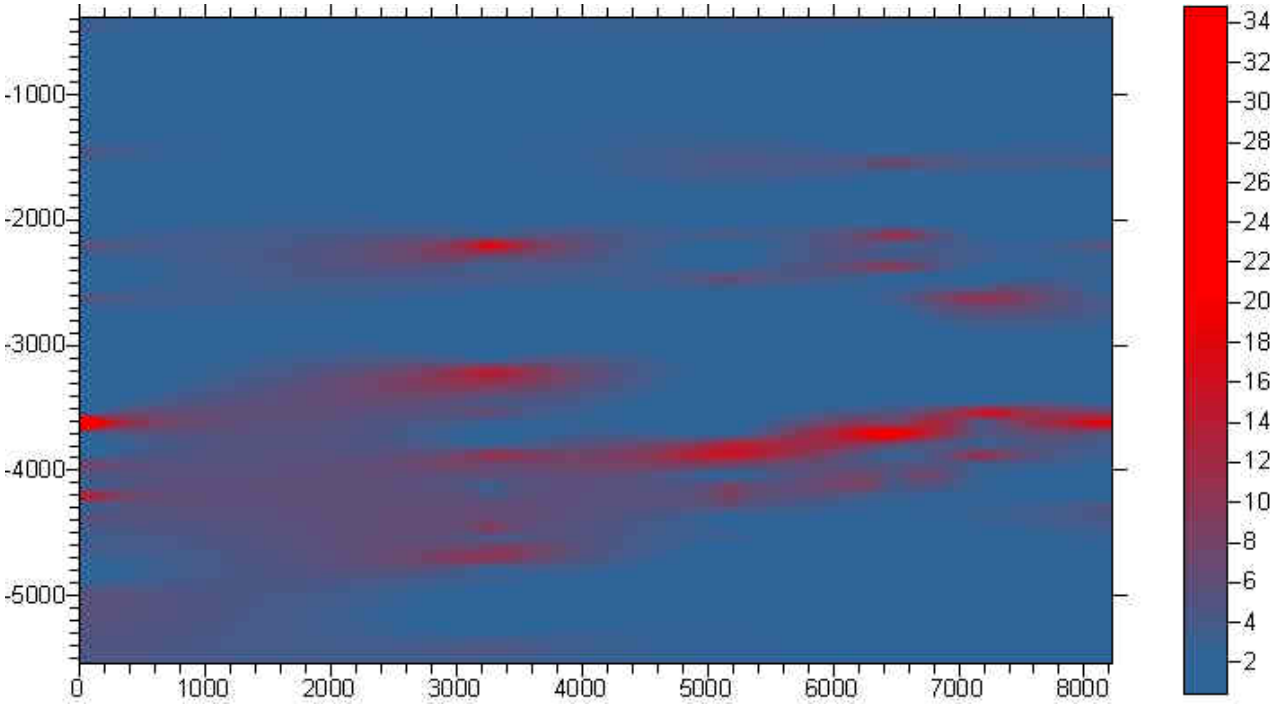

Figure 4.17. Spatial variation in the pressure gradient at Matagorda Island 519. Color bar shows that highest values of pressure gradient are in red and lowest values of pressure gradient are in blue.

4.4.6. Summary

Resistivity-derived fluid pressures show an increase in every well that corresponds to the location of the top of overpressure (11,500-12,800 ft) (Figure 4.13 and Figures 4.41 a-e). The fluid pressure gradient fieldwide also shows an increase that corresponds to the top of overpressure. Results of spatial variation in the fluid pressure gradient at Matagorda Island 519 (Figure 4.17) show that an increase from 0.0016 Mpa/m to 0.0019 Mpa/m occurs within a depth interval of 200-300 ft (60-100 m) at a depth of approximately 12,000 ft (3650 m). This interval of increased fluid pressure gradient corresponds to the top of overpressure in all wells. Spatial variation in excess pressure throughout the study area (Figure 4.16) suggests that excess pressure also increases from 15 Mpa to 25 Mpa at a depth of approximately 12,000 ft (3650 m) in all wells.

4.5. Temperature

4.5.1. Temperature Versus Depth from Corrected BHT and Temperature Log

Figure 4.18 illustrates temperature versus depth profiles for all wells in the Matagorda Island 519 field, using temperatures calculated from corrected bottom hole temperatures (BHT). Table 4.7 lists temperature versus depth from a continuous temperature log of well 6032 #2, and the temperature versus depth curve from this data is illustrated in Figure 4.19. Temperatures are listed in degrees Fahrenheit, and are shown for a depth range from 3500-4500 m (11,500-14,950 ft). Values of temperature recorded on the temperature log range from 182-254 °F (83-123 °C), which are slightly higher, but generally consistent with values for temperature obtained from corrected BHT temperatures, 50-160 °F (122-301 °C), for all wells in the Matagorda Island 519 field.

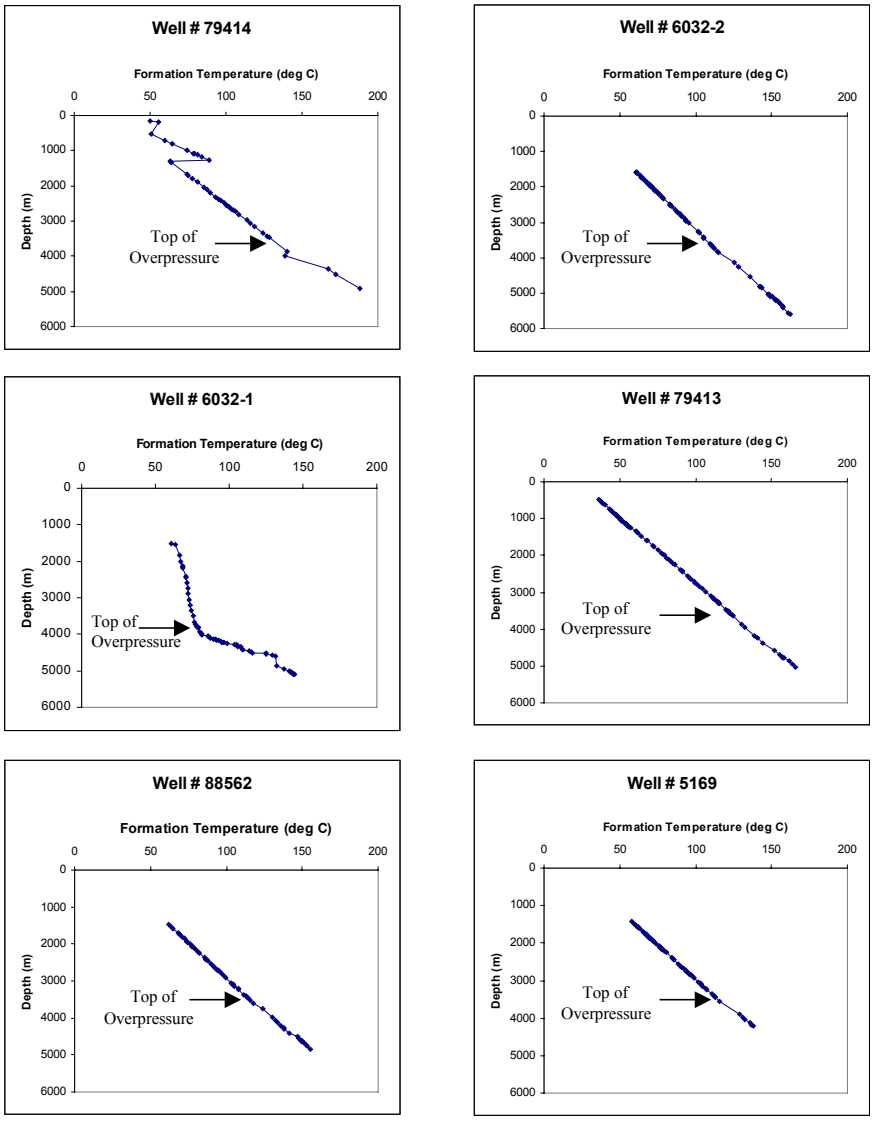

Figure 4.18. Temperature versus depth profiles for all wells, using corrected BHT. Note the location of the top of overpressure in each well.

Table 4.7. Temperature data from temperature log of well 6032#2.

Depth (ft)	Temperature (°F)
11500	182
11550	186
11600	188
11650	188
11700	189
11750	187
11800	190
11850	190
11900	191
11950	192
12000	190
12500	192
12550	193
12600	192
12650	199
12700	200
12750	199
12800	195
12850	196
12900	196
12950	209
13050	217
13100	208
13400	207
13450	208
13550	210
13600	201
13650	204
13700	207
13750	209
13800	205
13850	204
13900	208
13950	209
14000	208
14050	207
14100	209
14150	211
14200	215
14250	218
14300	217
14600	242
14650	245
14700	242
14750	242
14800	250
14850	251
14900	257
14950	254

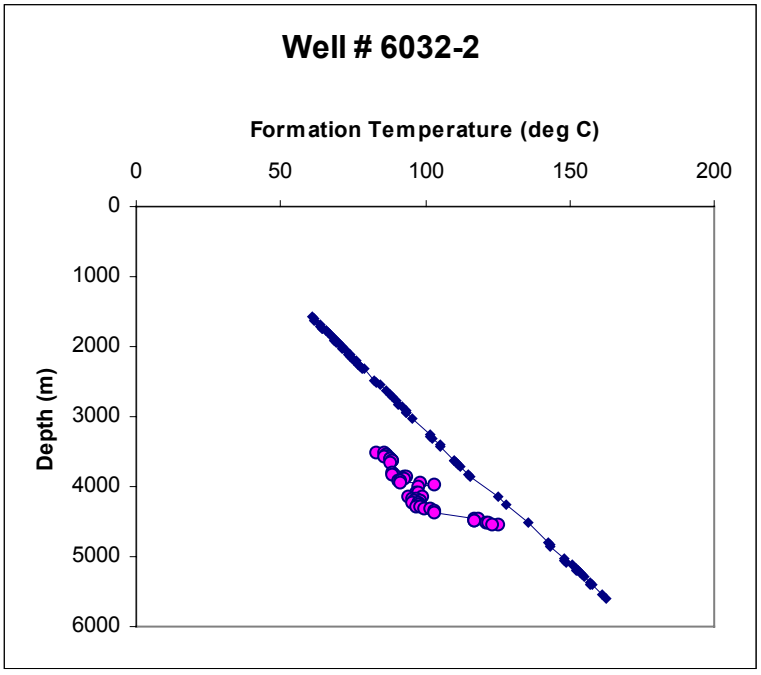

Figure 4.19. Temperature versus depth from temperature log (shaded circles) and from BHT data (solid diamonds) at well 6032-2.

4.5.2. Temperature Gradient from Temperature Log

The temperature gradient at the Matagorda Island 519 field is approximately linear in all wells. Specific values for temperature gradient are reported here for well 6032 #2. For well 6032 #2 the temperature gradient at 3500 m (11,500 ft) is 6.78 °C/km (1.58 °F/100 ft). At 3900 m (12,800 ft) the temperature gradient in well 6032 #2 is 5.95 °C/km (1.52 °F/100 ft), representing a slight decrease with depth. The temperature gradient again increases to 6.31°C/km (1.61 °F/100 ft) at 3950 m (12,950 ft), followed by another decrease to 5.83 °C/km (1.54 °F/100 ft) at 4080 m (13,400 ft). The next large increase in the temperature gradient is observed at 4450 m (14,600 ft), in which the temperature gradient increases from 5.41 °C/km (1.52 °F/100 ft) to 5.89 °C/km (1.66 °F/100 ft). At 4540 m (14,900 ft) the temperature gradient increases to 6.06 °C/km (1.72 °F/100 ft), and at 4550 m (14,950 ft) decreases to 5.94 °C/km (1.70 °F/100 ft).

The temperature gradient according to the temperature log for well 6032 #2 is approximately 6.78 °C/km (1.58 °F/100 ft) at 3500 m (11,500 ft), and approximately 5.95 °C/km (1.52 °F/100 ft) at 3900 m (12,800 ft). Because the temperature log directly recorded formation temperatures, it is considered the most accurate representation of the temperature gradient at Matagorda Island 519.

4.5.3. BHT and Temperature Log Data

Corrected bottom hole temperatures data and temperature log data suggest that the temperature gradient increases at or near the top of overpressure in most wells. Temperature versus depth profiles (Figure 4.18) show that an increase in the temperature gradient occurs just above 4000 m (13,000 ft) in the study area. According to corrected BHT data, this increase in temperature gradient occurs slightly above the top of overpressure at the Matagorda Island 519

field. The temperature gradient for well 6032 #2 increases from 5.95-6.31 °C/km (1.52-1.61 °F/100 ft) at a depth of 3917-3947 m (12,800-12,950 ft), which corresponds to the top of overpressure in well 6032 #2.

4.5.4. Temperatures Reported from Previous Research at MI 519

Table 4.8 lists calculated calcite cementation temperatures and temperature ranges for thermosulfate reduction (TSR) of sulfate from the underlying Eagle Mills evaporate obtained from isotopic analyses of core samples from wells in the Matagorda Island 519 field performed by Klein et al. (1998). The depth(s) from which their isotopic analysis samples were taken are not given. According to Klein et al., calcite cementation temperatures range from 205-256 °F (96-124 °C) at Matagorda Island 519. Klein et al. (1998) suggest that this range of cementation temperatures is inconsistent with shallow calcite precipitation, because the local geothermal gradient reported a temperature of 180 °F (82 °C) at 8000 ft (2400 m). According to Klein et al. (1998), these high temperatures of calcite cementation suggested by oxygen isotope analysis could be reconciled with shallow calcite cementation depths if hydrothermal fluids migrating upward through expansion fault systems were the cementing fluids.

4.6. Salinity

Profiles of calculated salinity versus depth for all wells in the Matagorda Island 519 field are shown in Figure 4.20. All of the profiles display two distinct zones of salinity variation within each well. The upper zone, from depths of 1200 m to 3350-3650 m (4000 ft to 11,000-12,000 ft), is represented by a general increase in salinity with depth, and a high degree and frequency of variability in salinity values throughout the zone. Salinity ranges within this upper zone between 50,000 and 100,000 ppm. There is a salinity reversal at the base of the upper zone at depths of approximately 3350-3650 m (11,000-12,000 ft). Below this reversal is a zone of

Table 4.8. Temperature data for Matagorda Island 519 field from Klein (1998).

Description	Temperature (°F)
Local geothermal gradient (at 8000 ft depth)	180
Calcite cementation	205 – 256
TSR of sulfate from Eagle Mills evaporate	330 – 360

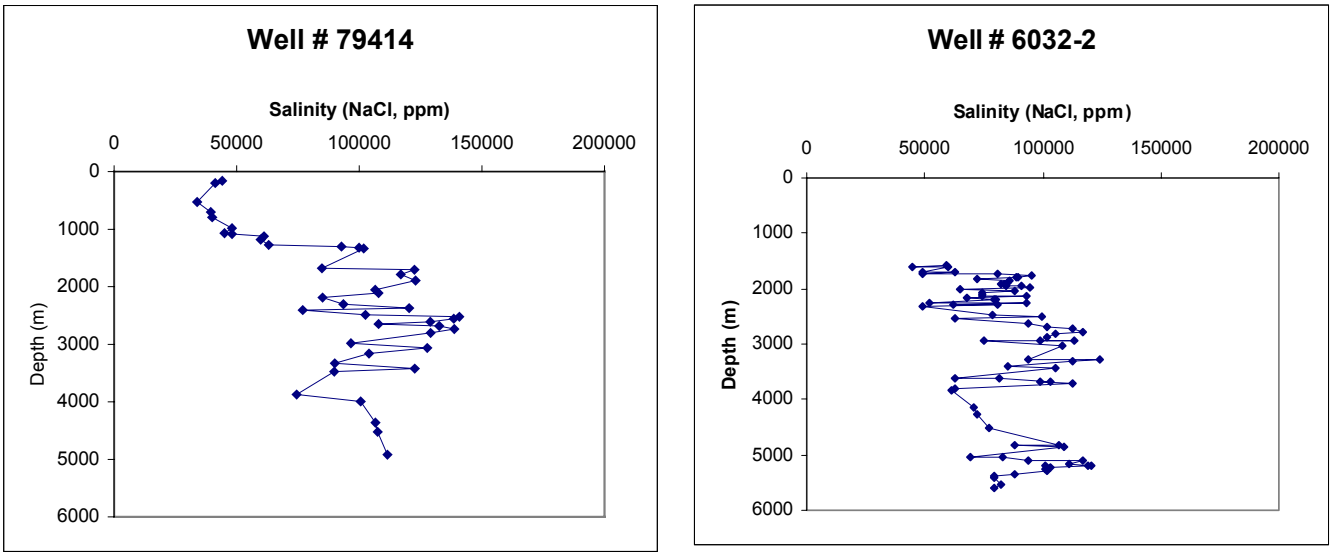

Figure 4.20 (a). Salinity versus depth for wells 79414 and 6032-2.

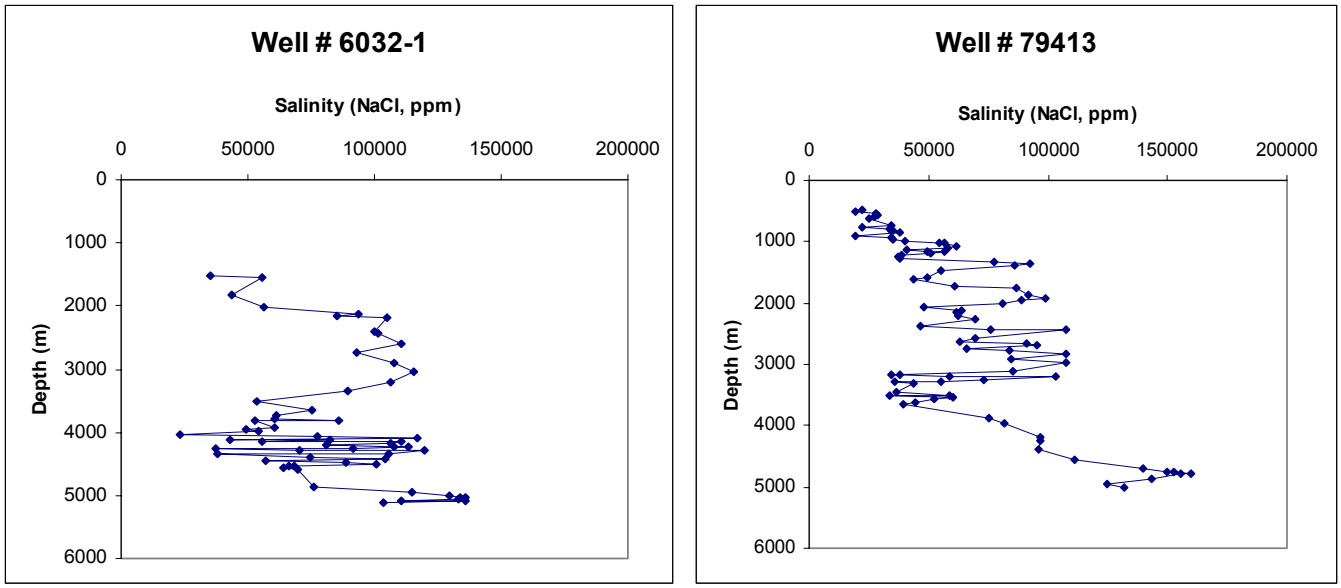

Figure 4.20 (b). Salinity versus depth profiles for wells 6032-1 and 79413.

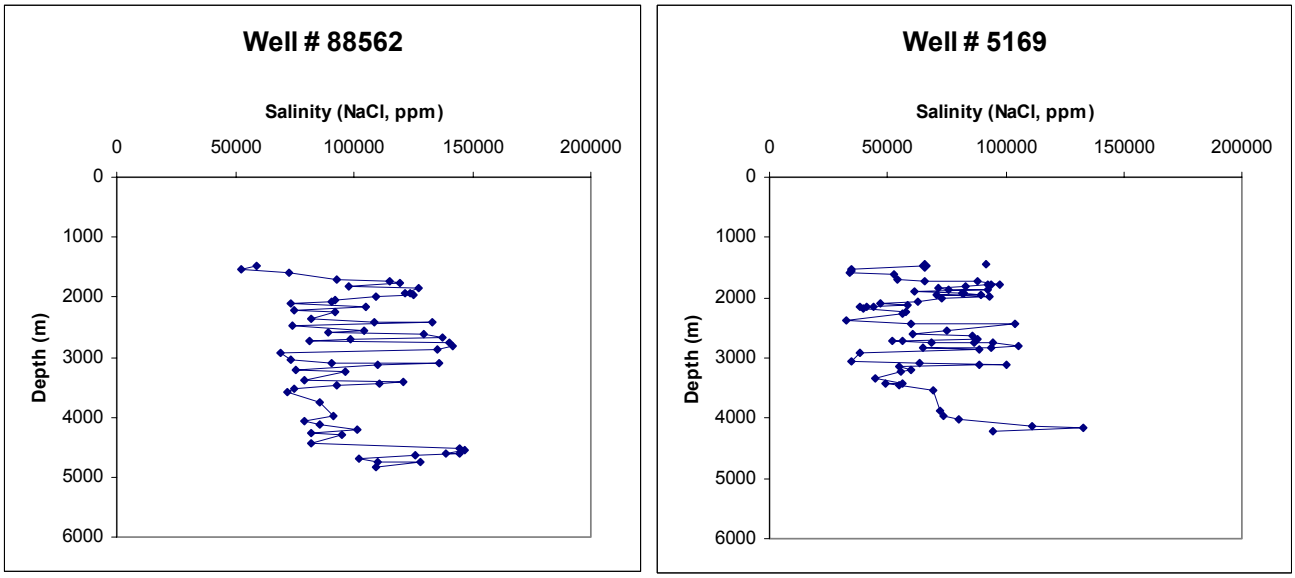

Figure 4.20 (c). Salinity versus depth profiles for wells 88562 and 5169.

high salinity. The deeper zone, from depths of 3350-3650 m to 4900-5200 m (11,000-12,000 ft to 16,000-17,000 ft) exhibits a generally linear increase in salinity with depth, and a lower degree and frequency of variability in salinity values throughout the zone.

Figure 4.21 illustrates the spatial variation in salinity across the study area. In general, there is a high degree of spatial variation in salinity at the Matagorda Island 519 field. However, most wells show a zone of relative low salinity that ranges from depths of 3000-4000 m (10,000-13,000 ft). This zone of lower salinity appears to be more prominent in the updip wells, and may not actually correlate across the fault between wells 6032#1 and 6032#2.

Highest salinity values in all wells are found at or near the base of each salinity zone, with the exception of well 79414. There is a fieldwide pattern of transition between the upper and lower zones that occurs at depths between 3000-4000 m (9,800-13,100 ft) . Lowest salinity values are in the uppermost portion of the upper zone of salinity for all wells, with well 79413 showing a salinity low that is below seawater salinity within this zone.

4.7. Porosity

Porosity information is available from density and neutron porosity logs for wells 6032 #2, 6032 #1, and 5169, and from sonic logs for well 6032 #1 and 6032 #2. Neutron-density logs for these wells report calculated porosity in porosity units (PU) from 0.0 to 0.6. The porosity unit values obtained from porosity logs were multiplied by 100 in order to obtain porosity in percent from 0-60 %. One or more corrections, such as neutron-density cross-plots, are necessary in order to obtain the most accurate estimate of porosity at a given depth. However, a close approximation to true porosity can be made directly from well log data. Table 4.9 lists porosity versus depth within the study area for porosities obtained from neutron-density logs. Note that porosity values were only recorded over a depth range of 3889-5108 m (12760-16760 ft).

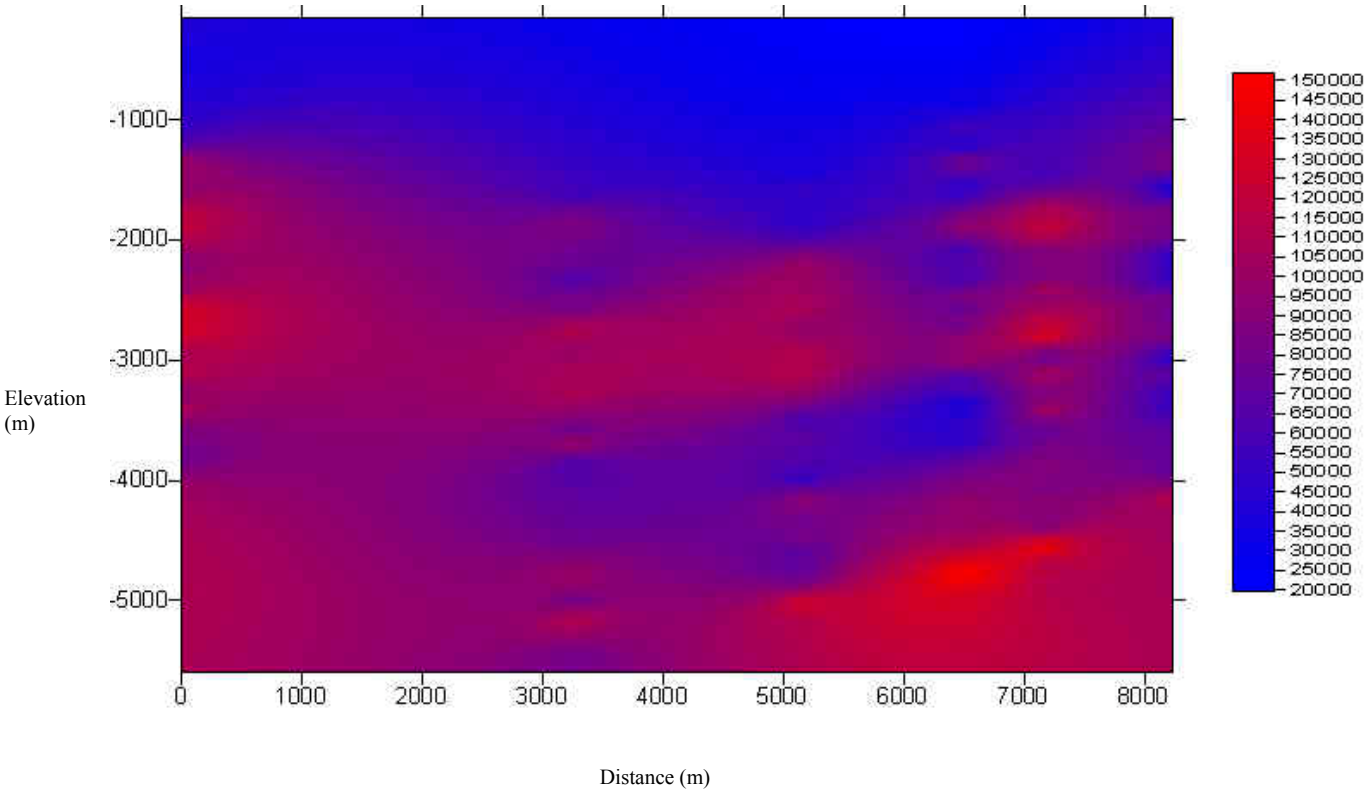

Figure 4.21. Spatial variability in salinity at the Matagorda Island 519 field. Color bar shows that red represents highest values of salinity and blue represents lowest values of salinity.

Table 4.9. Porosity versus depth values from neutron-density logs at Matagorda Island 519.

Well No.	Depth (ft)	Porosity (%)
5169	12760	34
	13030	35
	13205	28
	13560	25
	13675	30
	13825	21
6032-1	13870	22
	14100	26
6032-2	14850	44
	15790	18
	15860	22
	15900	21
	16520	14
	16570	13
	16700	13
	16760	9

Porosity ranges for the depth intervals available on porosity well logs are generally between 10 and 30 percent fieldwide, with a few exceptions.

Figure 4.22 shows the variation in porosity with depth at the Matagorda Island 519 field for porosities obtained from neutron-density logs. Results from calculations to determine shale porosity are shown in Figure 4.23. In this figure shale porosity versus depth is plotted in order to determine whether the overall trend in shale porosity follows a normal compaction trend. Results from shale porosity versus depth plots show that shale porosity at Matagorda Island 519 decreases with depth, from 0.25-0.30 at depths of 2000 m (6,500 ft) to 0.10-0.15 at depths of 4000 m (13,100 ft).

4.8. Hydraulic Gradient and Hydraulic Force Field

Results from calculations of the hydraulic gradient at two wells in the study area, OCS 6032#2 and OCS 5169, are discussed in this section. Table 4.10 lists values for the vertical fluid pressure gradient at each of these wells. Table 4.11 shows the lateral hydraulic gradient between these two wells and the vertical hydraulic gradient in each well. The magnitude and direction (azimuth) of the total hydraulic force for selected depths is shown in Table 4.12. It is important to note that the direction of H is reversed from the depth of 3048 m (10,000 ft) to the depth of 3658 m (12,000 ft) at Matagorda Island 519.

Figure 4.24 illustrates the flow field, with vectors representing magnitude and direction of flow within the study area, and the depth of the top of overpressure throughout the field. Above the top of overpressure flow is oriented at 0.485 ° NE in well 6032 #2 and 0.1° NE in well 5169. Within the overpressured zone, however, the direction of flow is reversed, and fluids flow toward the northwest, with orientations ranging from 0.6 ° to 0.9 ° NW. These directions of flow are generally perpendicular to the orientation or dip of the top of overpressure within the Matagorda Island 519 field.

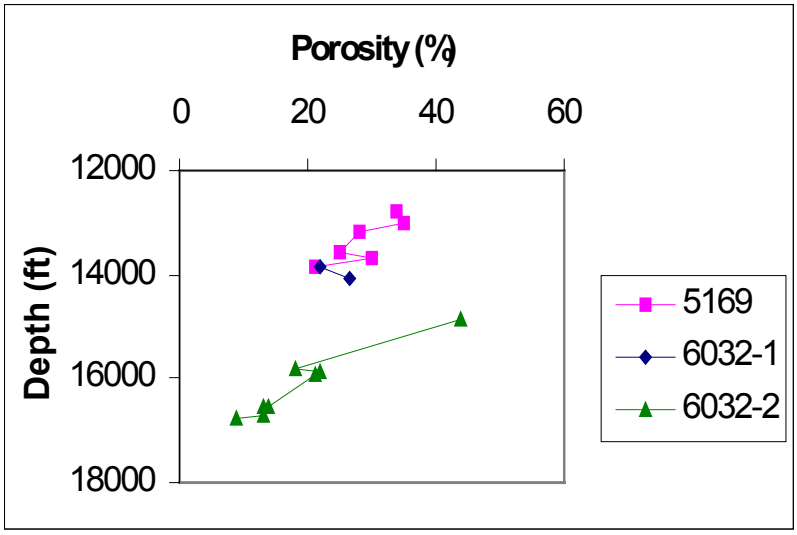

Figure 4.22. Porosity versus depth at the Matagorda Island 519 field for porosity obtained from neutron-density logs.

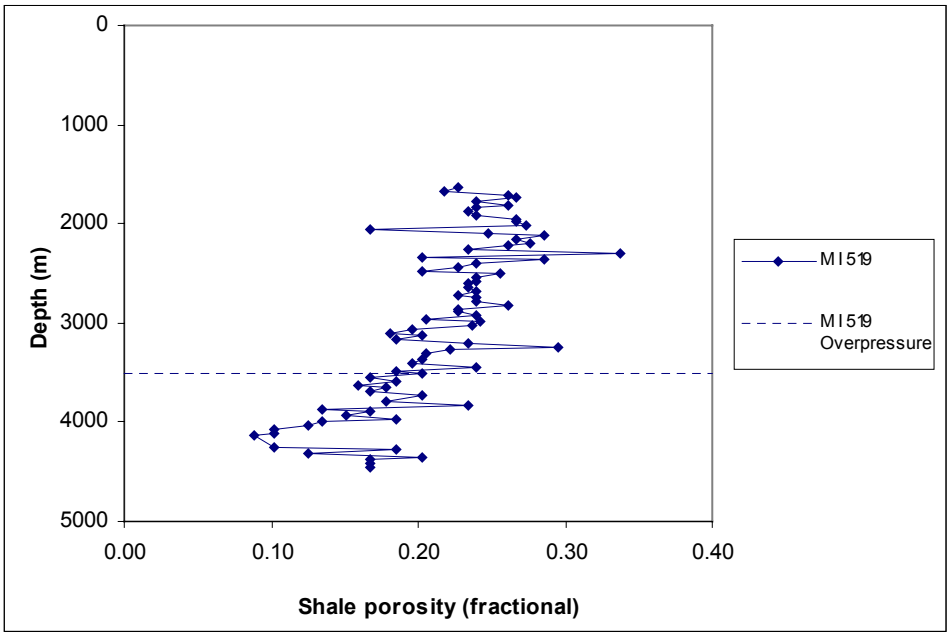

Figure 4.23. Shale porosity versus depth at Matagorda Island 519 well 6032 #1. Shale porosity was calculated from shale transit time determined from the sonic log.

Table 4.10. Vertical fluid pressure gradient at wells OCS 6032#2 and OCS 5169.

Depth (m)	dP/dZ (Pa/m) Well 6032 #2	dP/dZ (Pa/m) Well 5169	ρg (Pa/m)
3048	177,139	147,034	10,515
3658	201,514	202,643	10,515
3871	203,817	210,176	10,515
3932	212,114	212,178	10,515
3993	208,253	211,528	10,515
4023	210,654	210,783	10,515

Table 4.11. List of pressure, distance, vertical pressure gradient, vertical hydraulic gradient, lateral hydraulic gradient, and hydraulic force magnitude and direction for wells OCS 6032#2 and OCS 5169.

Depth (m)	**dP (Pa)**	**dD (m)**	**Hz-6032#2 (-dP/dz-ρg) (Pa/m)**	**Hz-5169 (-dP/dz-ρg) (Pa/m)**	**Hx (-dP/dx) (Pa/m)**
3048	-689,475	4964	166,624	136,519	139
3658	16,547,417	4964	191,322	192,451	-3334
3871	21, 718,485	4964	193,604	199,963	-4375
3932	14,134,252	4964	201,935	201,999	-2848
3993	14,478,989	4964	198,085	201,360	-2917
4023	12,410,562	4964	200,571	200,700	-2500

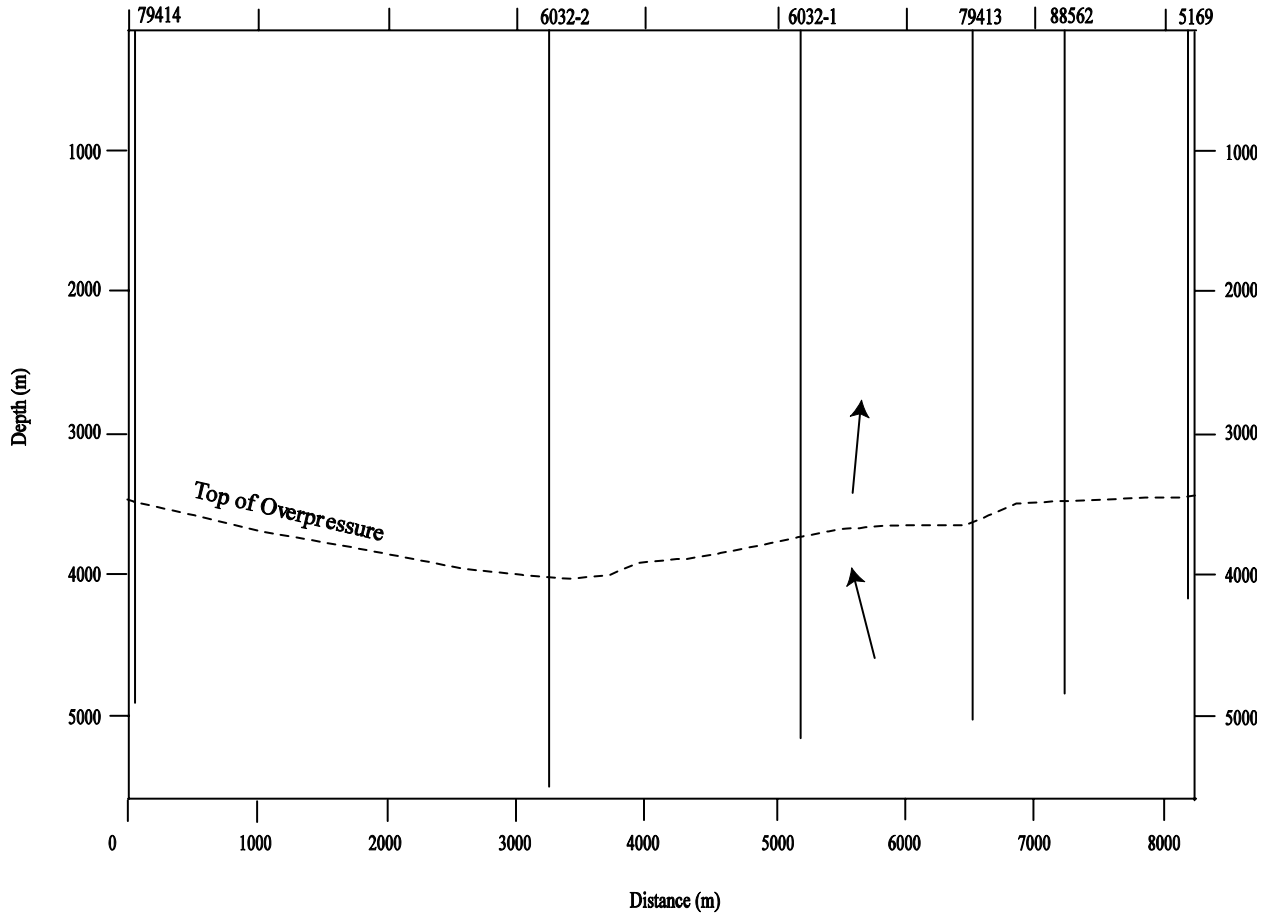

Figure 4.24. Variation in direction of the flow field at Matagorda Island 519. Magnitude and direction of flow are shown. Orientation of the top of overpressure is indicated.

4.9. Permeability

Figure 4.25 shows calculated relations between intrinsic permeability, fluid velocity, and porosity. For fluid velocities of 10^{-5} m/s to 10^{-11} m/s (315 m/yr to 0.000315 m/yr) and porosities of 0.001 to 0.2 pu, permeabilities would fall within the range of 10^{-17} m^2 to 10^{-20} m^2. This range of permeabilities would be within the range of permeabilities required for a pressure seal to form, according to results in Deming (1994, 2001, in press) and in He and Corrigan (1995). Results from permeability calculations performed using the permeability algorithm developed in this study are shown in Figure 4.26. Calculated permeabilities in the study area show a range of permeability from 10^{-16} m^2 to 10^{-19} m^2 at Matagorda Island 519, which is generally consistent with the calculated permeability ranges produced in this study. At the top of overpressure in well 6032 #1 permeability is on the order of 10^{-18} m^2 to 10^{-19} m^2, which is within the calculated permeability range for this study and is sufficiently low enough permeability for a pressure seal to form.

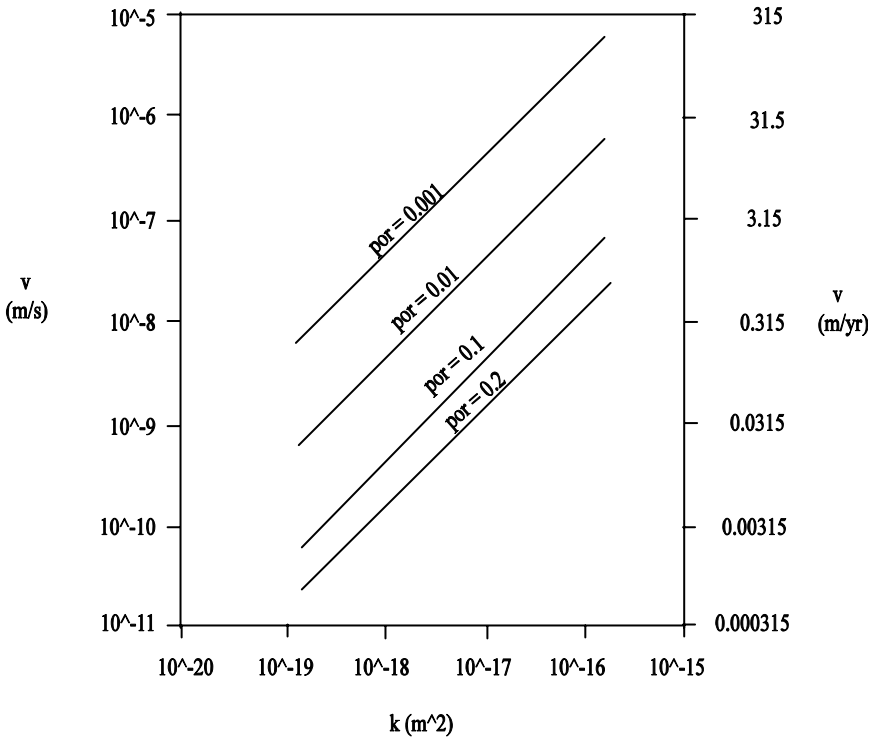

Figure 4.25. Calculated relations between intrinsic permeability, fluid velocity and porosity.

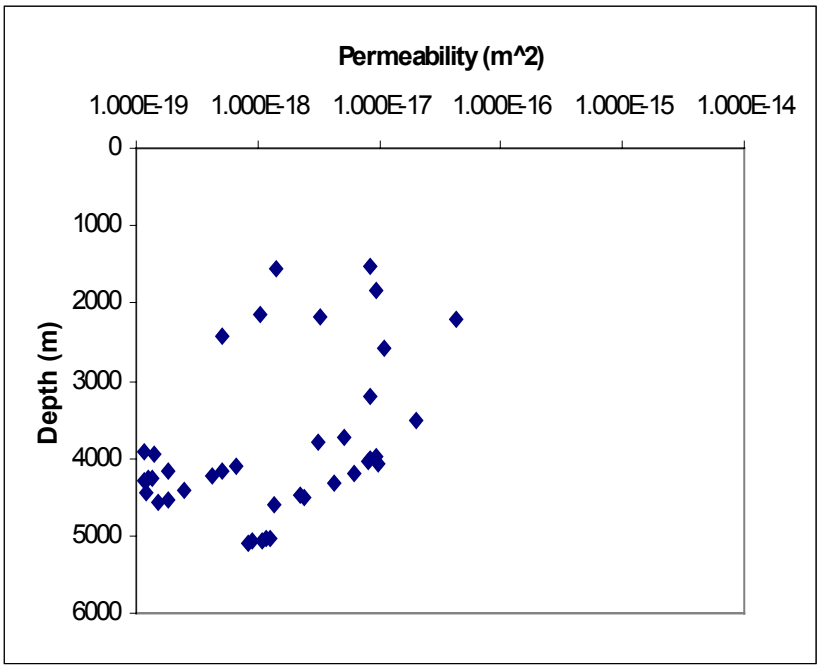

Figure 4.26. Calculated permeability ranges for shales at well 6032-1.

CHAPTER 5. RESULTS FROM ANALYSIS OF SEDIMENT CHEMICAL PROPERTIES

5.1. Mudstone Bulk Chemistry

Table 5.1 lists representative analyses of major oxides and some key elements from well 88562 to illustrate the types of analyses that were available for this study. Detailed spreadsheet data on bulk chemistry versus depth at all wells was available for four wells in the Matagorda Island 519 field in this study, OCS 6032 #1, SL 79413, SL 88562, and OCS 5169.

5.1.1. Elemental Covarience

Figure 5.1 shows Ca versus CO_2 fieldwide and Mg versus CO_2 for mudstones fieldwide. These plots were made to determine whether or not the Ca in the study area is present primarily as calcite ($CaCO_3$) and if any of the Mg is present as dolomite ($CaMg(CO_3)_2$). Ca shows a linear increase in abundance with increasing CO_2, while Mg appears to be relatively constant relative to increasing CO_2. There is a 1:1 slope of increase in Ca with increase in CO_2, while Mg displays a nearly horizontal, flat trend with increased CO_2. Thus, most of the Ca and CO_2 appears to be present as calcite. There is a slight excess in Ca which probably represents Ca present in apatite and in silicate phases. However, the Mg does not appear to be present as dolomite, and thus is present in silicates in the Matagorda Island 519 field. Sr versus Ca is plotted in Figure 5.2. There is a slight correlation in Sr with Ca, although there is a high degree of scatter.

Graphs of selected key elements are presented here in order to understand the nature of elemental mobility at the Matagorda Island 519 field. Figure 5.3 plots the elements Titanium (Ti), Yitrium (Y), and Zirconium (Zr) versus the element Aluminum (Al) fieldwide to determine whether these elements are present in constant proportions with increasing depth throughout the study area, thus testing the potential immobility of all these elements. Patterns versus depth in

Table 5.1. Representative analyses of major oxides and key elements versus depth in the study area with data from well 88562.

Depth (ft)	**SiO_2** (wt%)	**CaO** (wt%)	**MgO** (wt%)	**Na_2O** (wt%)	**K_2O** (wt%)	**Fe_2O_3** (wt%)	**Al_2O_3** (wt%)	**Sr** (ppm)	**Y** (ppm)	**Zr** (ppm)
8290	59.0	3.33	1.86	1.48	2.41	5.8	15.4	260	50	240
8440	60.6	3.10	1.84	1.18	2.55	4.81	15.4	200	30	270
8710	59.1	1.57	1.88	1.47	2.59	5.96	16.6	260	50	230
9100	57.3	6.15	1.93	1.48	2.67	4.72	14.2	350	50	230
10540	53.8	5.36	2.08	1.42	2.96	5.17	16.6	310	50	440
11560	53.1	6.65	1.99	1.38	3.10	5.18	15.7	330	40	190
12220	52.2	8.32	1.98	0.98	2.70	4.48	15.7	310	30	150
12490	50.4	10.9	1.88	0.87	2.51	4.29	14.2	300	20	160
13480	47.9	12.5	1.69	0.93	2.58	4.00	14.1	330	30	150
13660	49.3	10.7	1.73	0.92	2.72	4.44	15.0	330	30	830
13990	53.8	6.34	2.04	1.27	3.02	5.07	15.7	290	20	150
15440	51.8	6.48	1.95	0.66	4.61	4.06	17.8	240	40	180

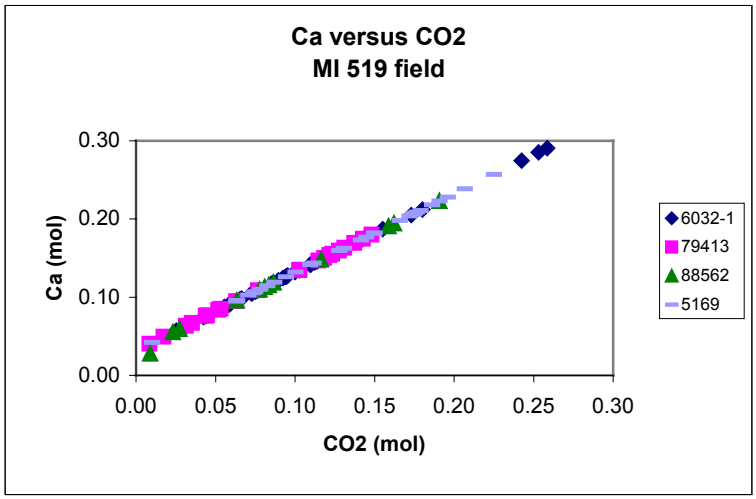

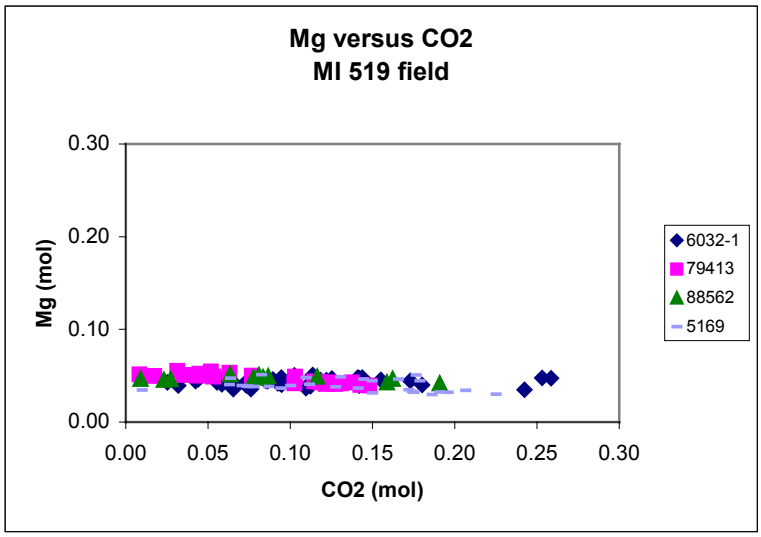

Figure 5.1. Ca versus CO_2 and Mg versus CO_2 at Matagorda Island 519.

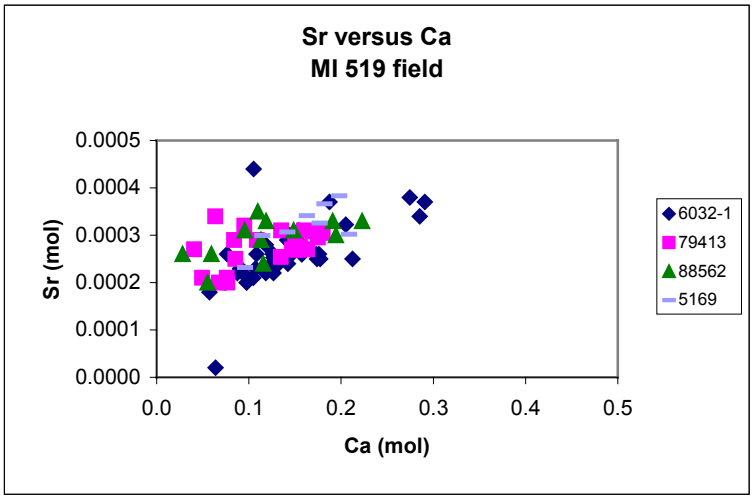

Figure 5.2. Sr versus Ca at Matagorda Island 519.

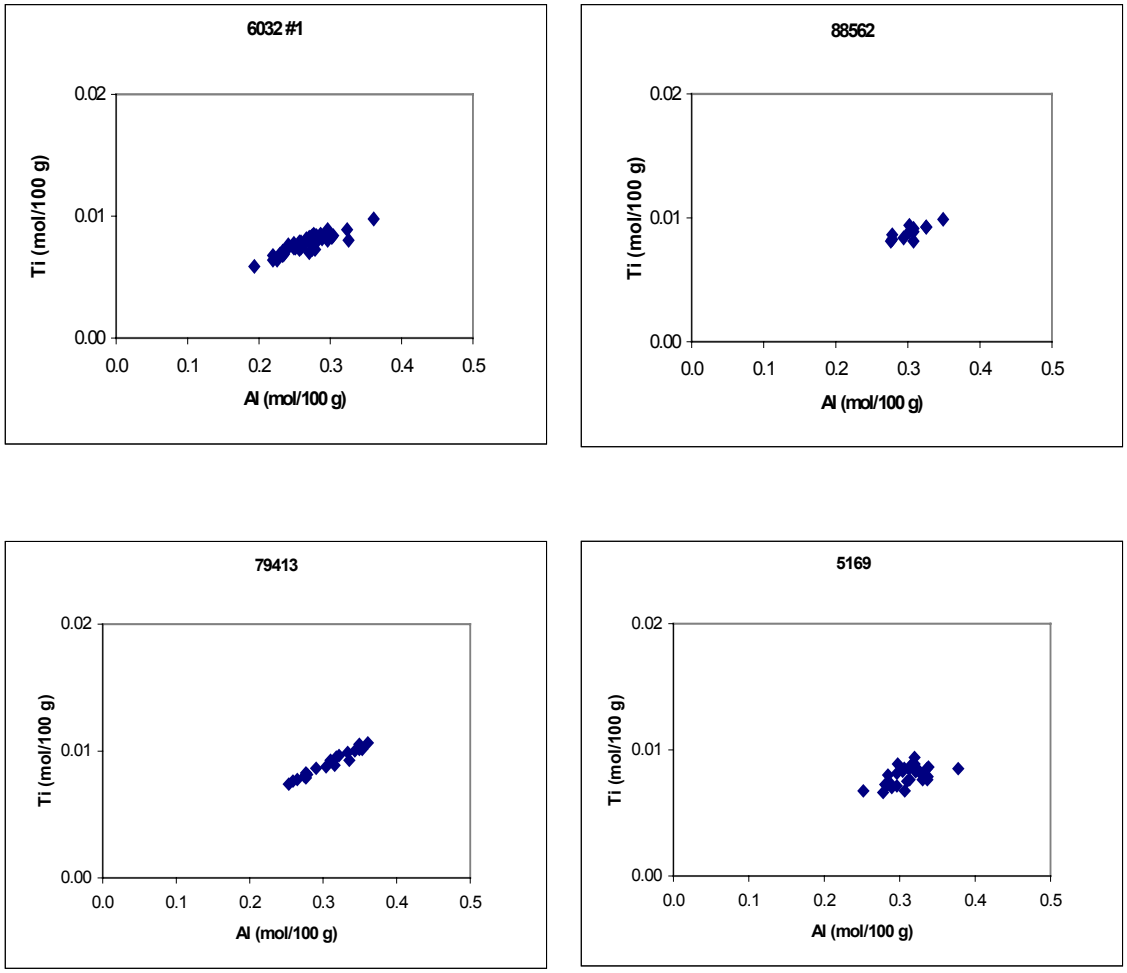

Figure 5.3 (a). Elemental analysis showing Ti versus Al in the study area.

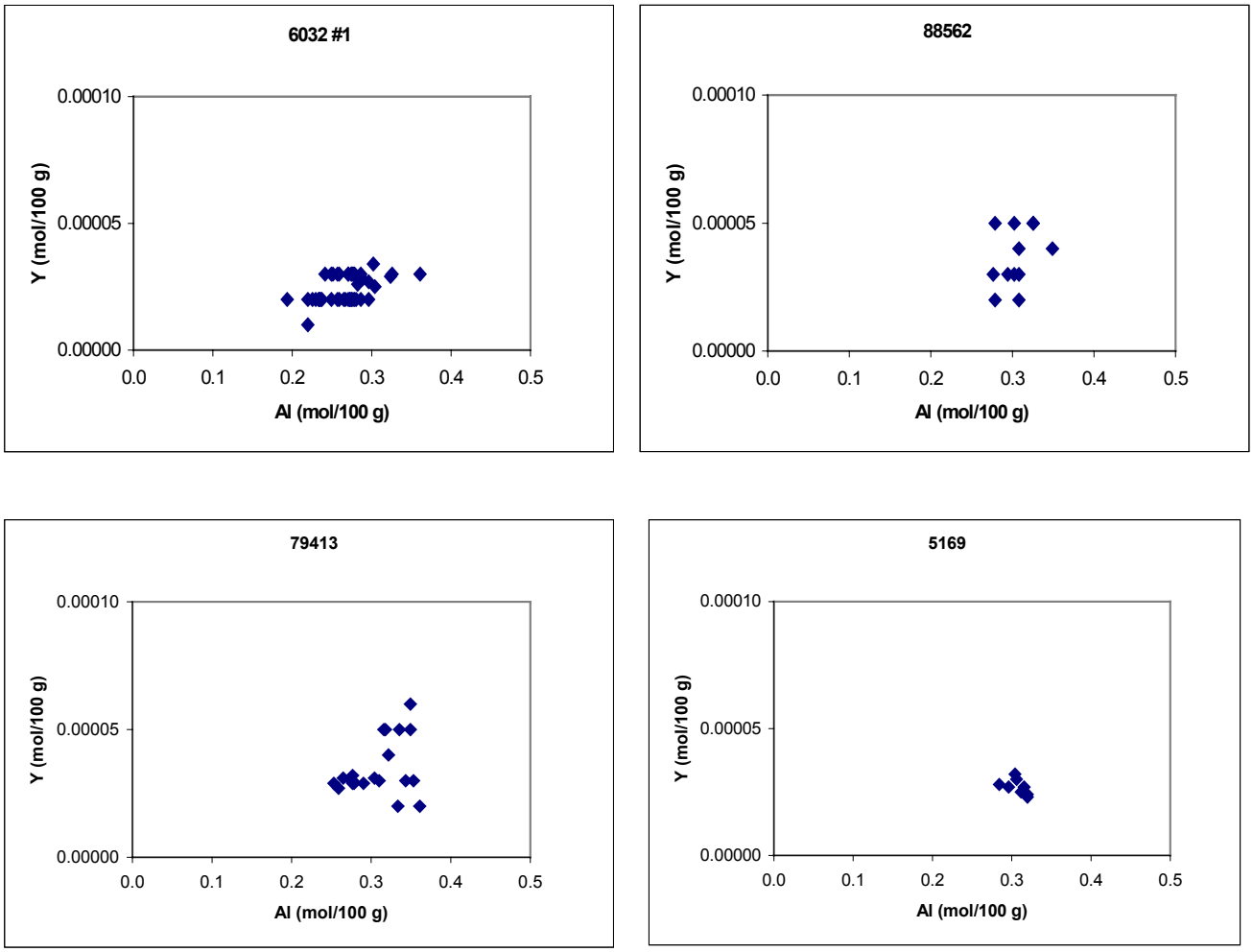

Figure 5.3 (b). Elemental analysis showing Y versus Al in the study area.

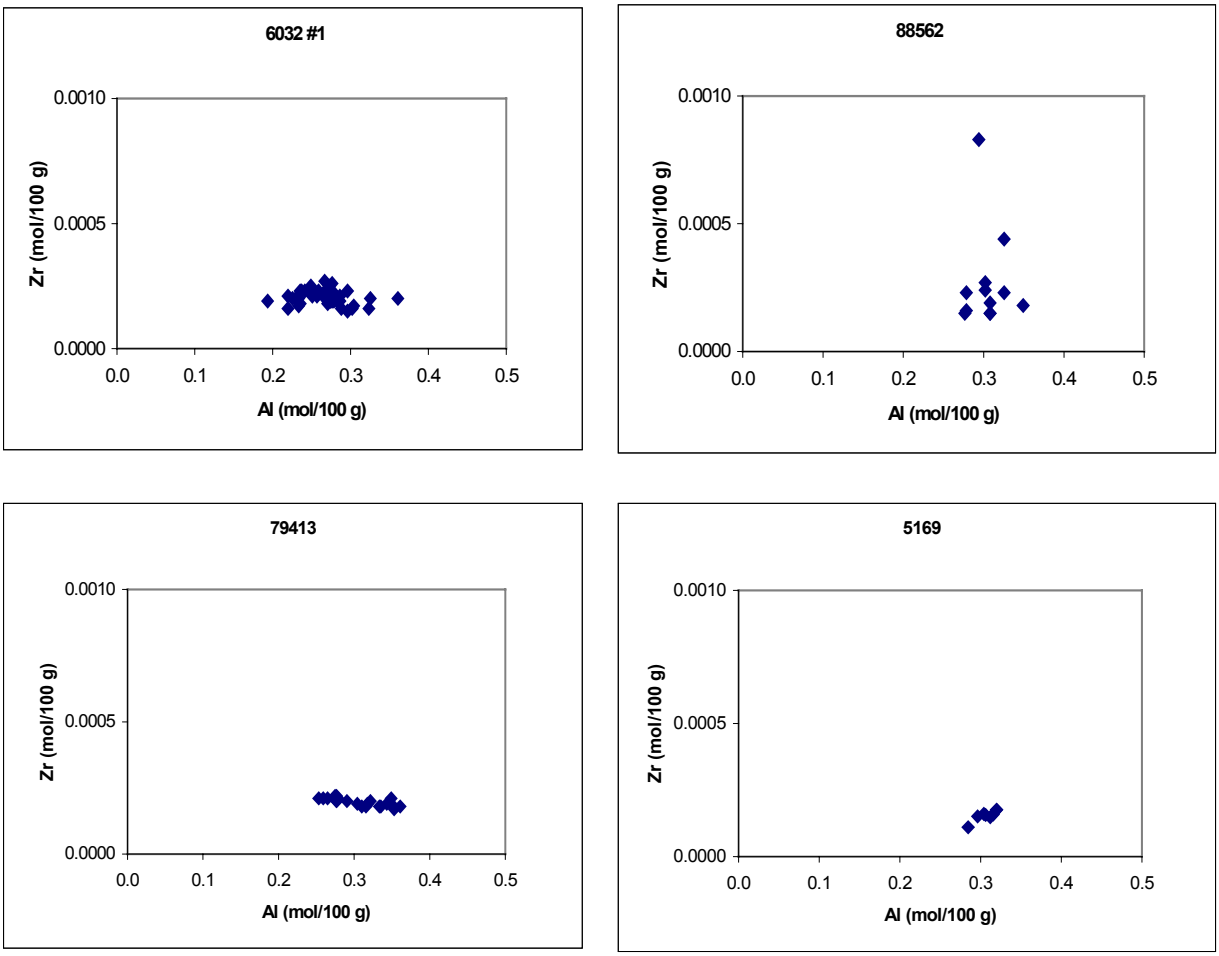

Figure 5.3 (c). Elemental analysis showing Zr versus Al in the study area.

the Matagorda Island 519 field show that Ti covaries with Al, whileY is slightly less constant with increased Al than Ti, and shows slight scatter in wells 88562 and 79413. Zr generally behaves conservatively relative to Al fieldwide, yet is less conservative than Ti or Y, as evidenced by the observed scatter in Zr with increased Al in well 88562.

5.1.2. Depth Variation in Absolute Abundance

Figure 5.4 shows plots of Fe_2O_3/Al_2O_3 versus depth for wells 6032 #1, 79413, 88562, and 5169. Fe is important for Miocene sediments at Matagorda Island 519 because of the reported Fe abundance in Tertiary sediments of the Texas Gulf Coast, due to an influx of volcanics from West Texas during this time (Lynch, 1997; Galloway, 2000). The weight ratio of Fe to Al decreases with depth in all wells. The relation of the top of overpressure to trends in Fe abundance with depth is shown with the dashed line in each figure representing the top of overpressure in that well. There is at least a slight relative decrease in abundance of Fe that corresponds to the top of overpressure in all wells, and then Fe enrichment within the overpressured interval just below the top of overpressure.

Sodium (Na) is an important element to consider at the Matagorda Island 519 field, because of the elevated levels of NaCl-rich brines within the field. The behavior of Na with increasing depth may allow for a determination of how sediments in the study area react to the introduction of NaCl-rich brines. The overall trend in abundance of Na with depth is an increase for wells 79413 and 5169 and a decrease in wells 6032 #1 and 88562 (Figure 5.5). All wells appear to have a similar trend in Na enrichment with depth to that of the upper zone of salinity profile from depths of approximately 1800-3650 m (6,000-12,000 ft). There is a relative decrease in Na abundance in all wells that corresponds to the top of overpressure, which is consistent with the salinity reversal observed at the top of overpressure in all wells.

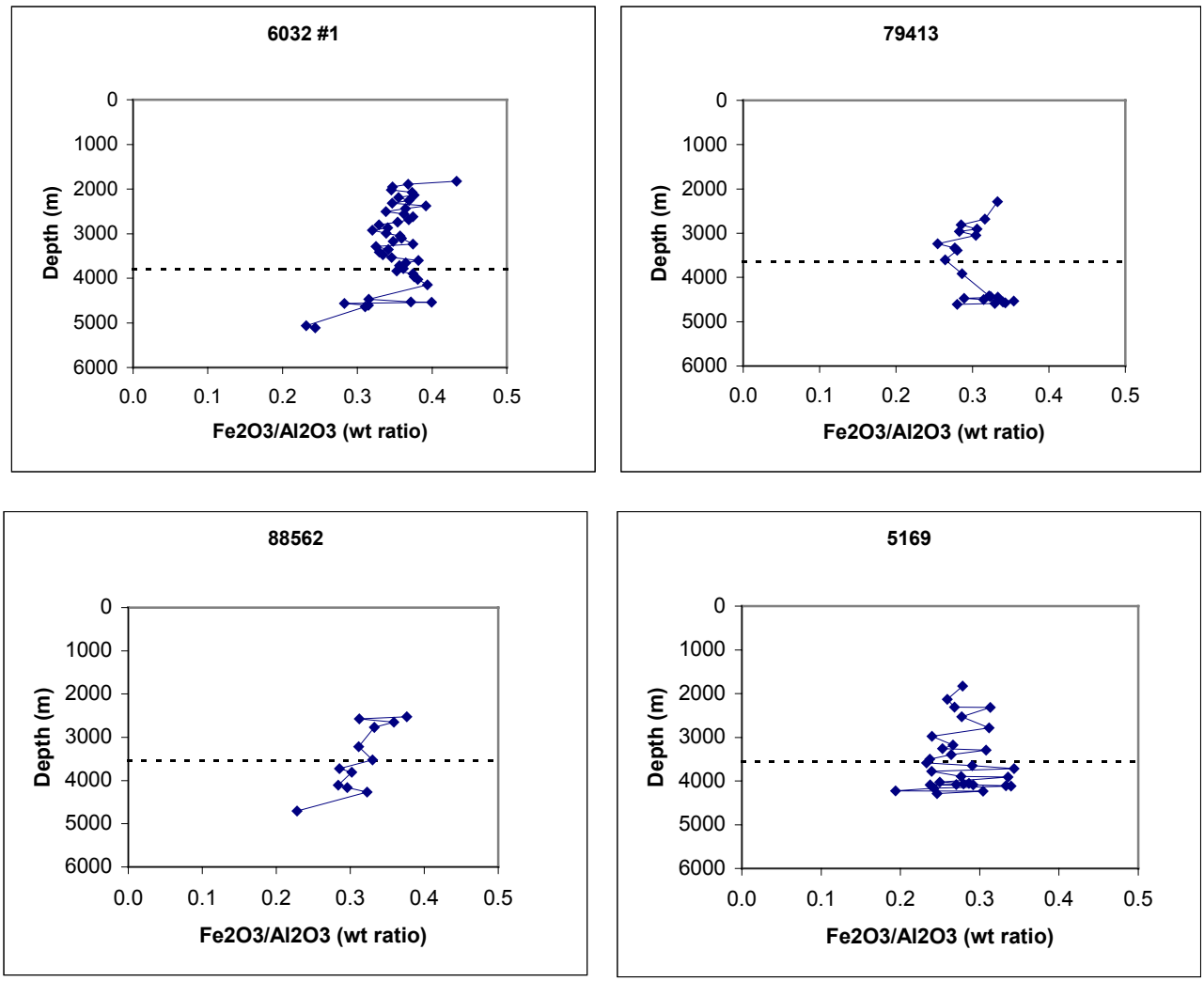

Figure 5.4. Depth variation in the ratio of Fe to Al versus depth in study area.

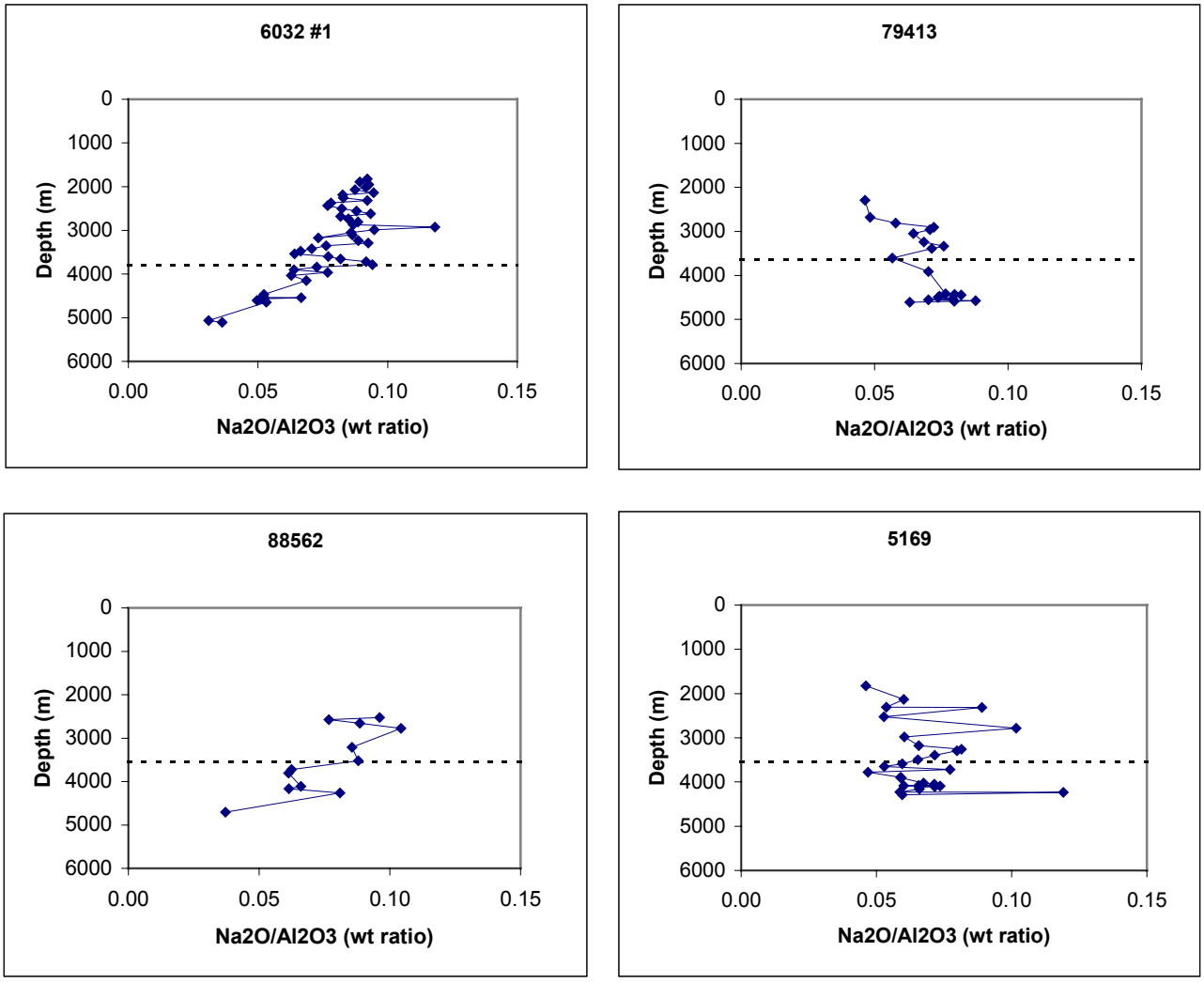

Figure 5.5. Depth variation in the ratio of Na to Al versus depth within study area.

5.1.3. Elemental Ratios

SiO_2 shows an overall depletion with depth in wells 6032 #1 and 88562, a general enrichment with depth in well 79413, and a relatively constant profile with increasing depth in well 5169 (Figure 5.6a). The top of overpressure, indicated with a dashed line for all wells, occurs just below a zone of relatively enriched SiO_2.

CaO (Figure 5.6b) shows two distinct zones of enrichment in all wells, an upper zone between 2000-3000 m (6,600-9,800 ft) and a second zone between 3200-4200 m (10,500-13,800 ft). The top of overpressure, marked with a dashed line for all wells, corresponds to the middle of the second zone of enriched CaO in all wells.

K_2O is much less abundant in relation to both SiO_2 and CaO, (Figure 5.6c). There is overall K_2O enrichment with depth for most wells, with no apparent irregularities representing unusually high or low values for K_2O. The top of overpressure, indicated with the dashed line in all wells, corresponds to the base of an interval of relatively depleted K_2O in all wells, and K_2O is relatively enriched in the overpressured zone below the top of overpressure in all wells.

Trace element profiles used by Klein et al. (1998) include Fe_2O_3, SiO_2, MgO, CaO, and K_2O ratios to the sum of the oxide and TiO_2, e.g. $Fe_2O_3 / (Fe_2O_3 + TiO_2)$, versus depth. The same oxides versus depth for well 6032 #1 were plotted by this author in order to determine whether or not evidence for the type of fluid flow suggested by Amoco exists in the Matagorda Island 519 field. Ratios of each oxide to TiO_2, Al_2O_3, and the sum of the oxide plus TiO_2 versus depth were plotted for comparison. Figure 5.7 shows the comparison between the three different types of analyses in order to determine whether or not results from each method are consistent with one another.

In Figure 5.7a Fe_2O_3 versus depth trends appear to be relatively consistent for all methods, showing a relatively stable trend of abundance with depth until approximately 4000-

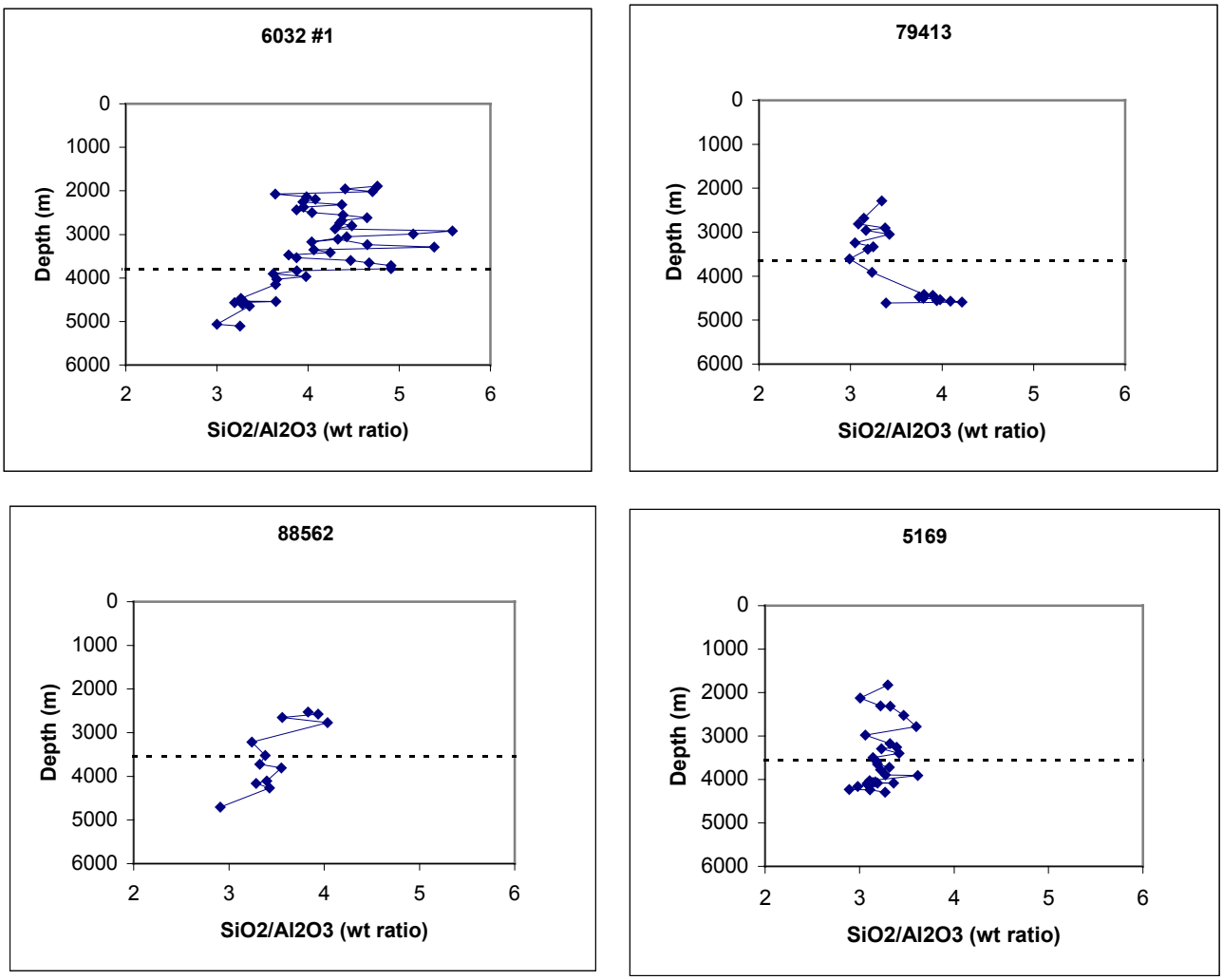

Figure 5.6 (a). SiO_2/Al_2O_3 versus depth fieldwide.

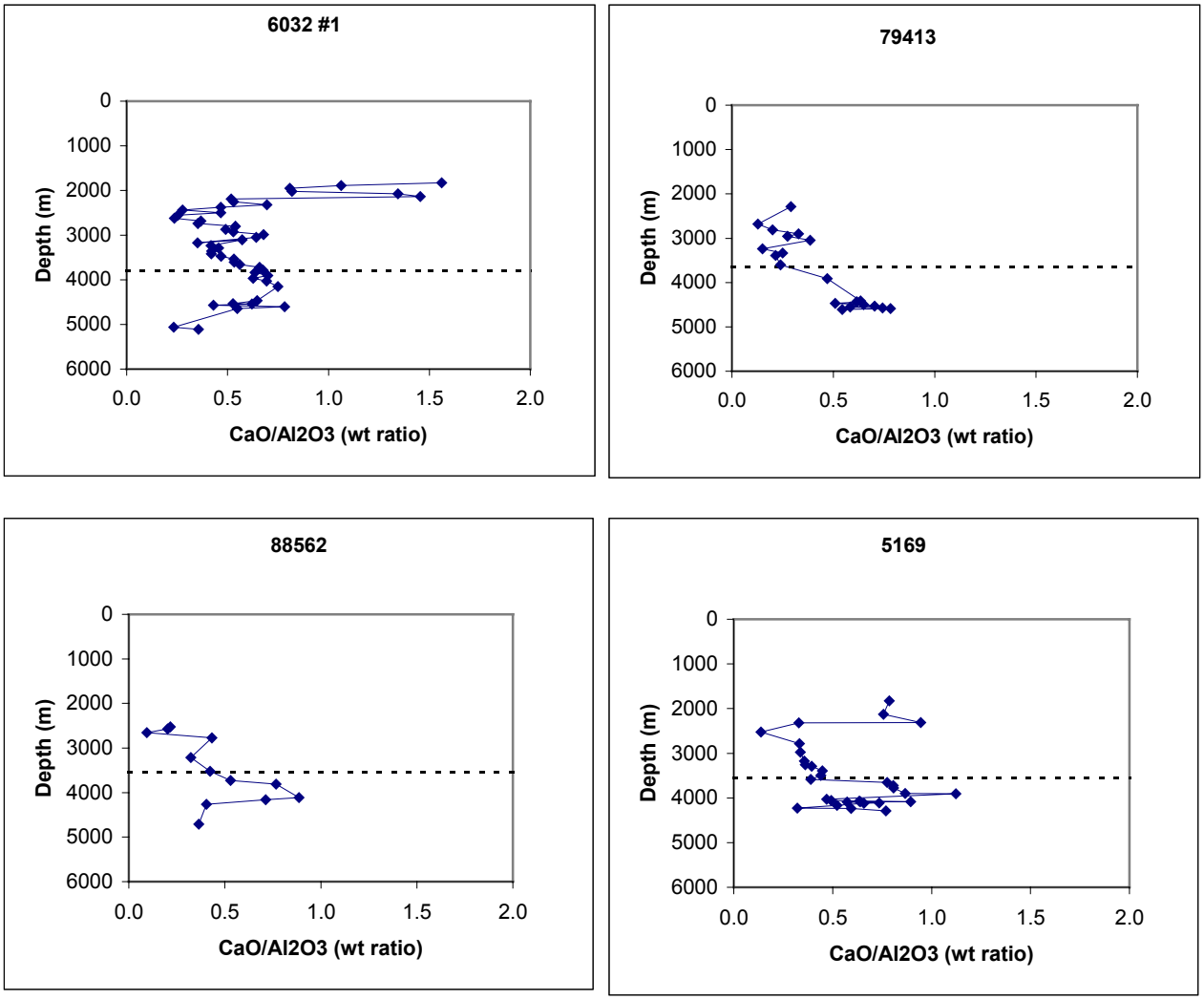

Figure 5.6 (b). CaO/Al_2O_3 versus depth fieldwide.

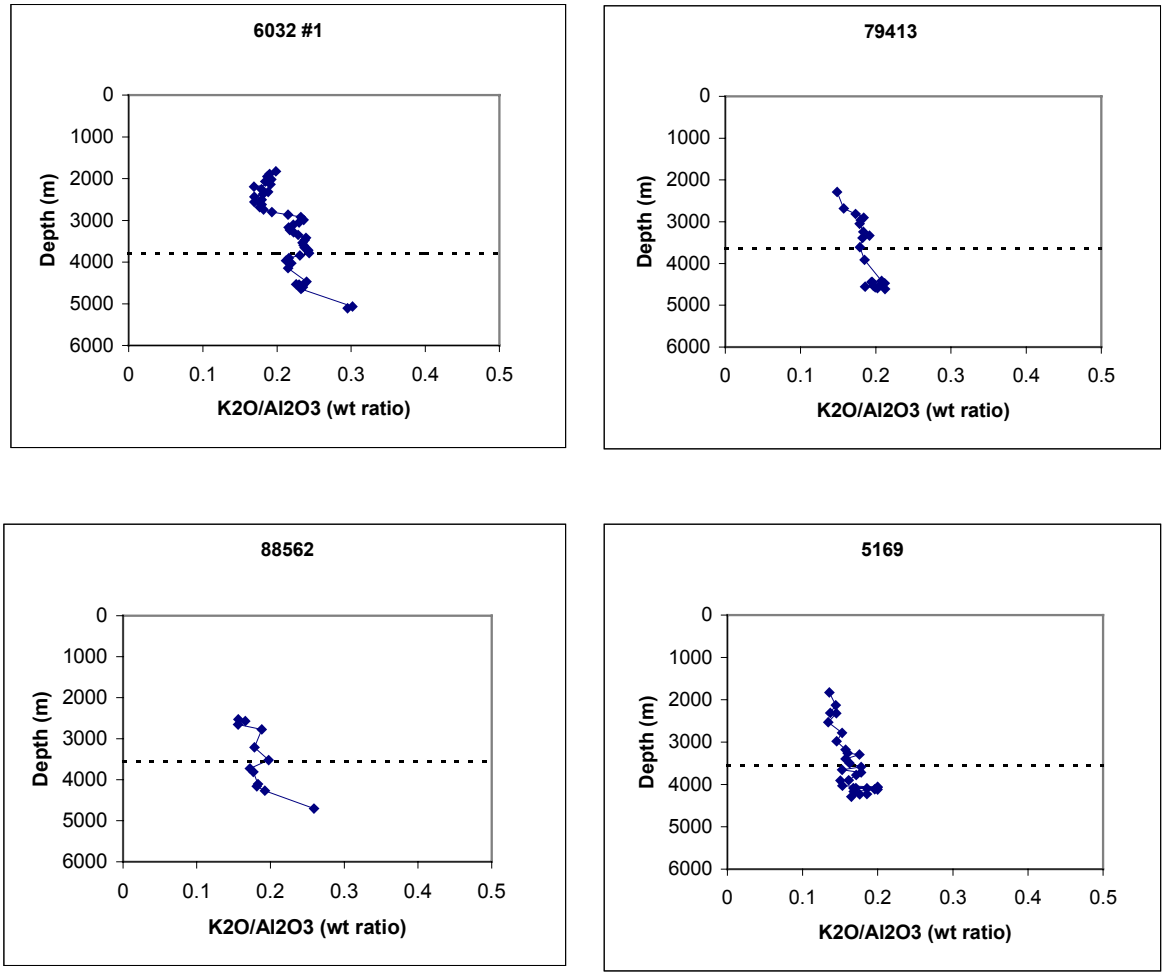

Figure 5.6 (c). K_2O/Al_2O_3 versus depth fieldwide.

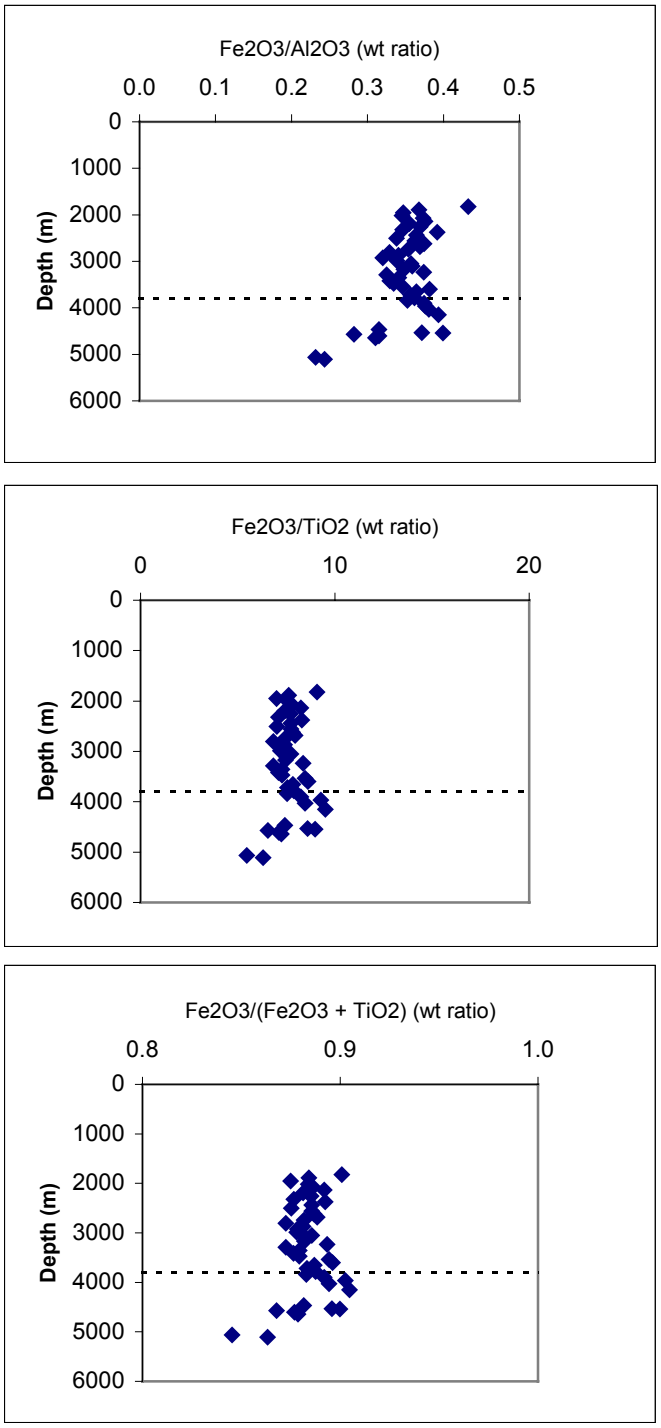

Figure 5.7 (a). Comparison of three different methods to evaluate Fe_2O_3 enrichment and depletion versus depth at well 6032 #1.

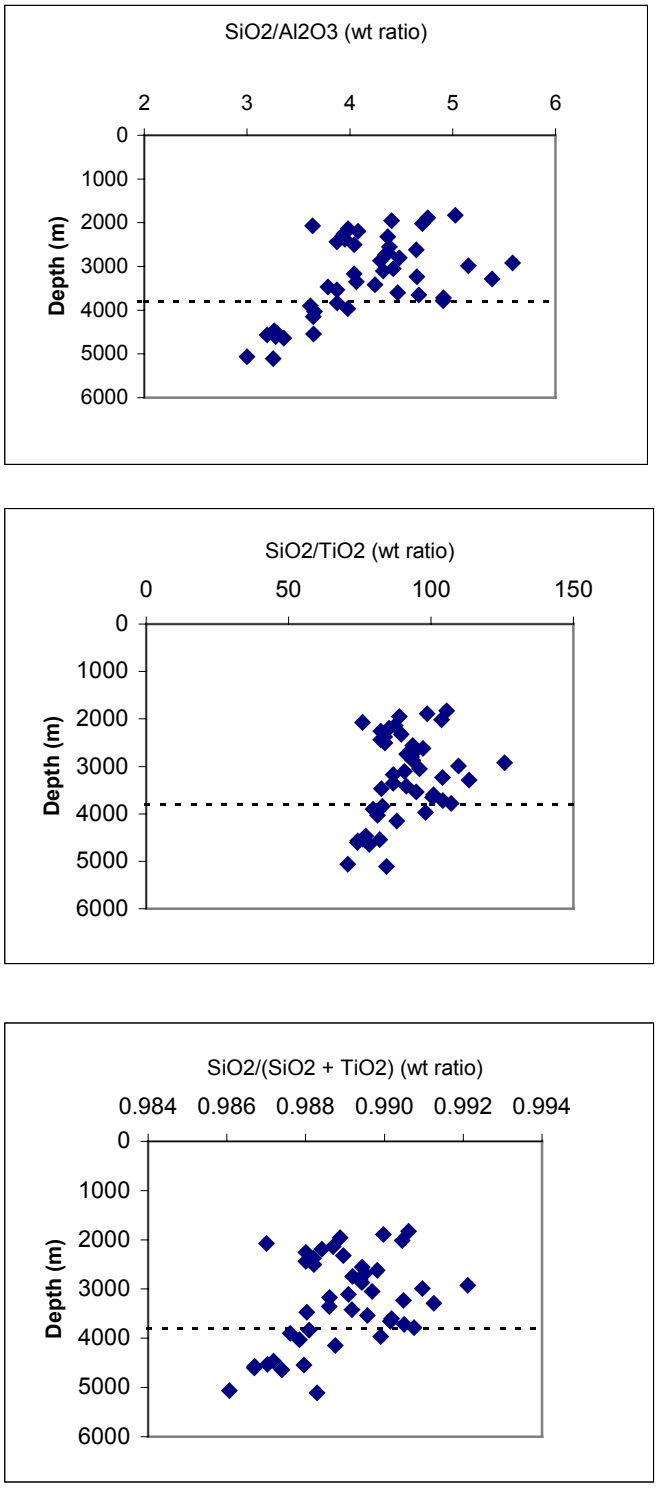

Figure 5.7 (b). Comparison of three different methods to evaluate SiO_2 enrichment and depletion versus depth at well 6032 #1.

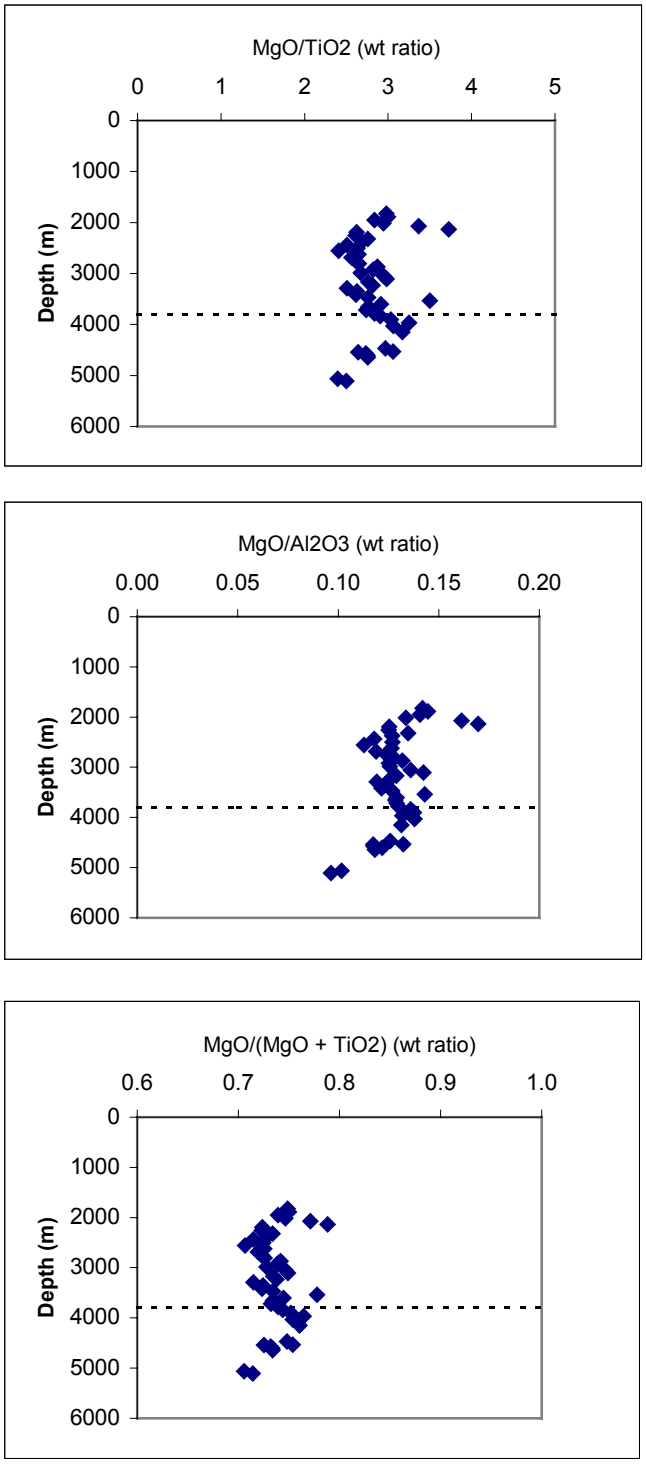

Figure 5.7 (c). Comparison of three different methods to evaluate MgO enrichment and depletion versus depth at well 6032 #1.

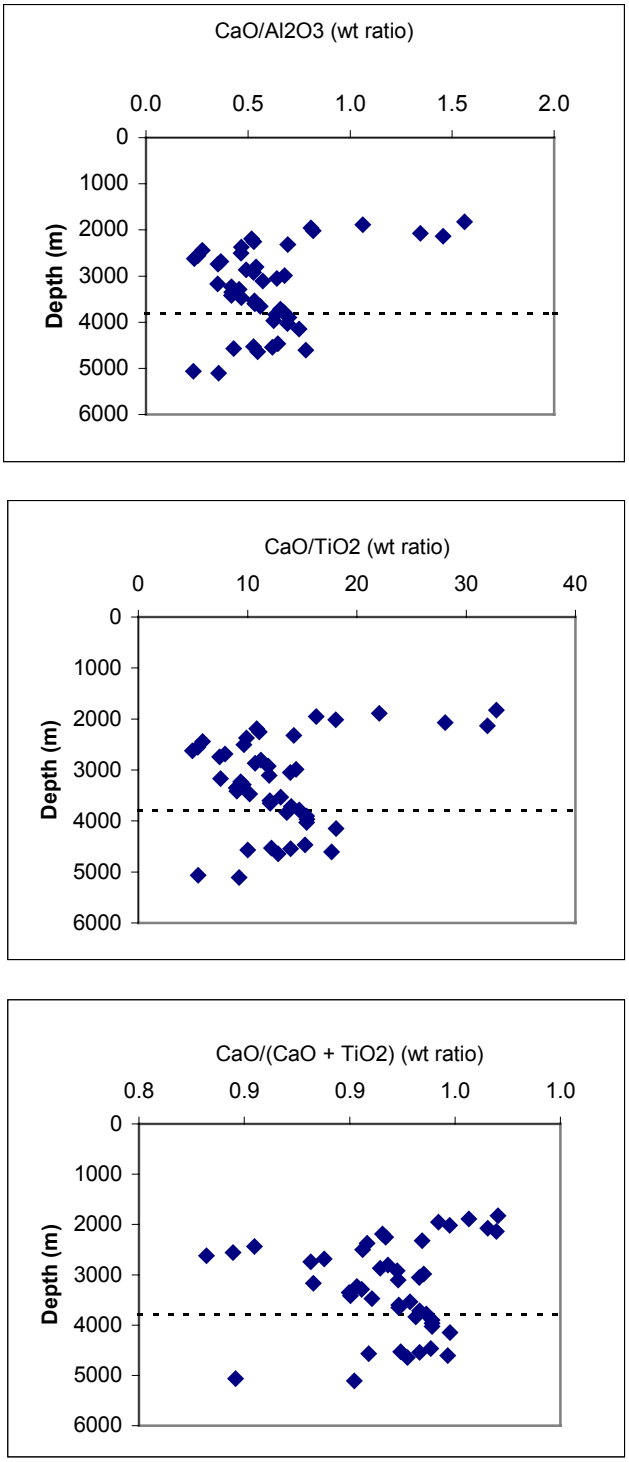

Figure 5.7 (d). Comparison of three different methods to evaluate CaO enrichment and depletion versus depth at well 6032 #1.

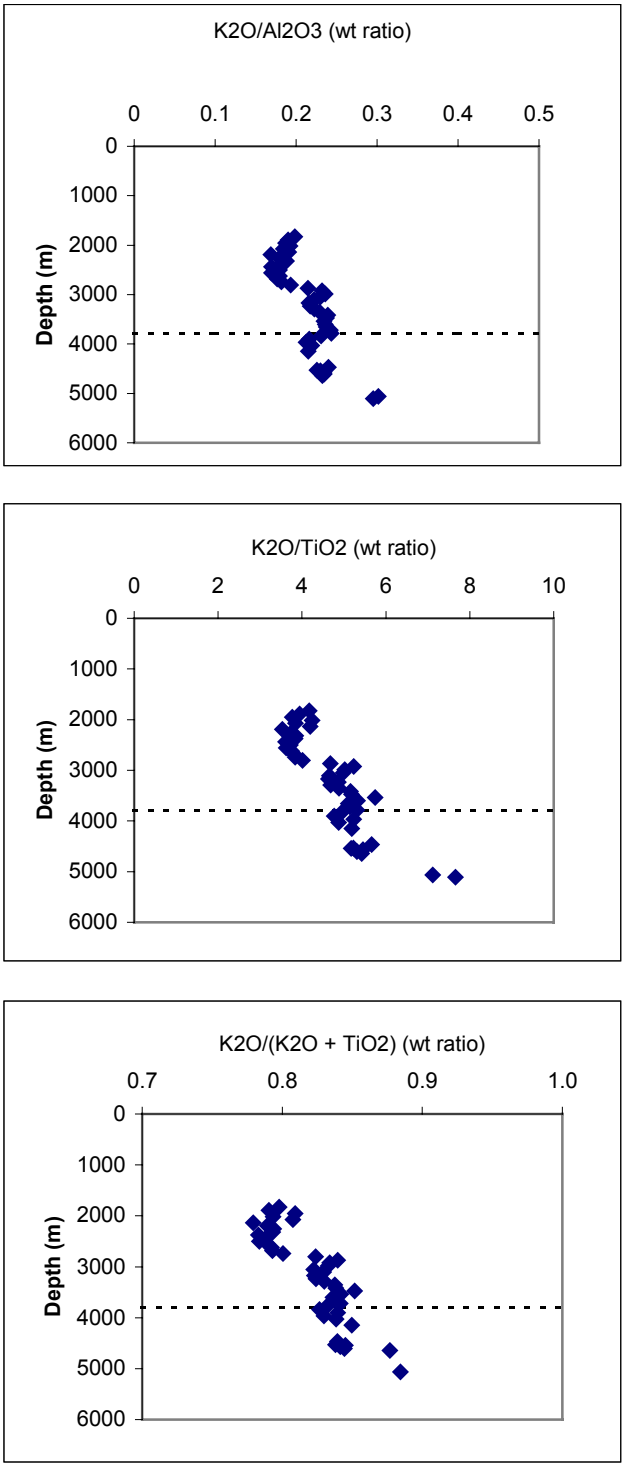

Figure 5.7 (e). Comparison of three different methods to evaluate K_2O enrichment and depletion versus depth at well 6032 #1.

4500 m (13,100-14,750 ft), where an abrupt depletion is observed for all wells. Figure 4.31b results for SiO_2 versus depth show a consistent trend for all three methods, with an overall trend depletion with depth. In figure 5.7c the overall shapes of the curves for MgO abudance with depth are very similar. An initial enrichment peak for MgO occurs at 2000 m (6,600 ft) for all wells and a second enrichment peak occurs from 3000-4000 m (9,900-13,100 ft), followed by a depletion with depth below 4000 m (13,100 ft) for all wells.

CaO versus depth trends are generally similar for all wells (Figure 5.7d), with two prominent enrichment peaks at 2000 m (6,600 ft) and 4000 m (13,100 ft), followed by a depletion with depth below 4000 m (13,100 ft). The overall trend of enrichment with depth for K_2O is consistent for all methods (Figure 5.7e). Thus, the results from comparative analyses of the three methods for studying relative oxide enrichment/depletion with depth appear to be relatively consistent with one another, implying that any of these methods are valid at Matagorda Island 519. Thus, results of analyses of sediment bulk chemistry performed in this thesis are consistent with results from previous Amoco research on sediment bulk chemistry.

5.2. Sediment Mineralogy and Petrology

5.2.1. Sandstone Mineralogy

Brewster et al. (1998) and Klein et al. (1998) report results from sandstone petrology, and petrophysical log analysis of cuttings reports relative abundances of various cements directly observed in sandstone intervals in well 6032 #1. Sandstone mineralogy within the depth range from 13,500-16,000 ft (4115-4877 m) is characterized by evidence of precipitation of chlorite, cementation and dissolution of calcite, and cementation of ankerite, pyrite, and polycrystalline quartz (Brewster et al., 1998; Klein et al., 1998). Sandstone mineralogy determined from petrophysical log analysis of cuttings from well 6032 #1 for the depth interval from 11,000-14,000 ft (3353-4267 m) is characterized by multiple intervals of calcite cementation, along with

quartz cementation, as well as cementation of ankerite, pyrite, and other mineral phases, such as glauconite.

5.2.2 Mudstone XRD Mineralogy

Figure 5.8 shows variations in relative mineral abundances in mudstones, as determined by XRD versus depth. XRD analyses were performed on samples from wells 79414, 79413, and 88562. Quartz is consistently the most abundant mineral phase in mudstones at Matagorda Island 519, followed by plagioclase, K-feldspar, and calcite, which all show similar ranges in abundance. Kaolinite, chlorite, illite, smectite, and mixed I-S are all less abundant.

5.2.3. Mudstone Normative Mineralogy

Results are reported for two runs of the MUDNORM program the first using mineral stoichiometries based on Lynch's 1997 work and the second using mineral stoichiometries from Awwiller (1993). Figures 5.9 a and b show assumed stoichiometries from simulation one and simulation two. A comparison between the results from simulation one and simulation two is presented in Figures 5.10 a, b, and c. Results from well 6032 #1 were used for comparison in this figure. Comparisons are shown for the mineral phases quartz, calcite, feldspar, illite, smectite, chlorite, and kaolinite to highlight similarities and differences between the results from each simulation of the MUDNORM program.

Most of the mineral phases analyzed show the same overall trends with depth for simulation one and for simulation two. However, the absolute weight percents for individual mineral phases differ significantly between simulations. Calculated abundance of quartz is significantly greater in simulation one than in simulation two. Calcite shows similar trends and magnitudes of weight percent for both simulations. Feldspar shows the same general trend for both simulations, although magnitudes are generally higher in simulation one.

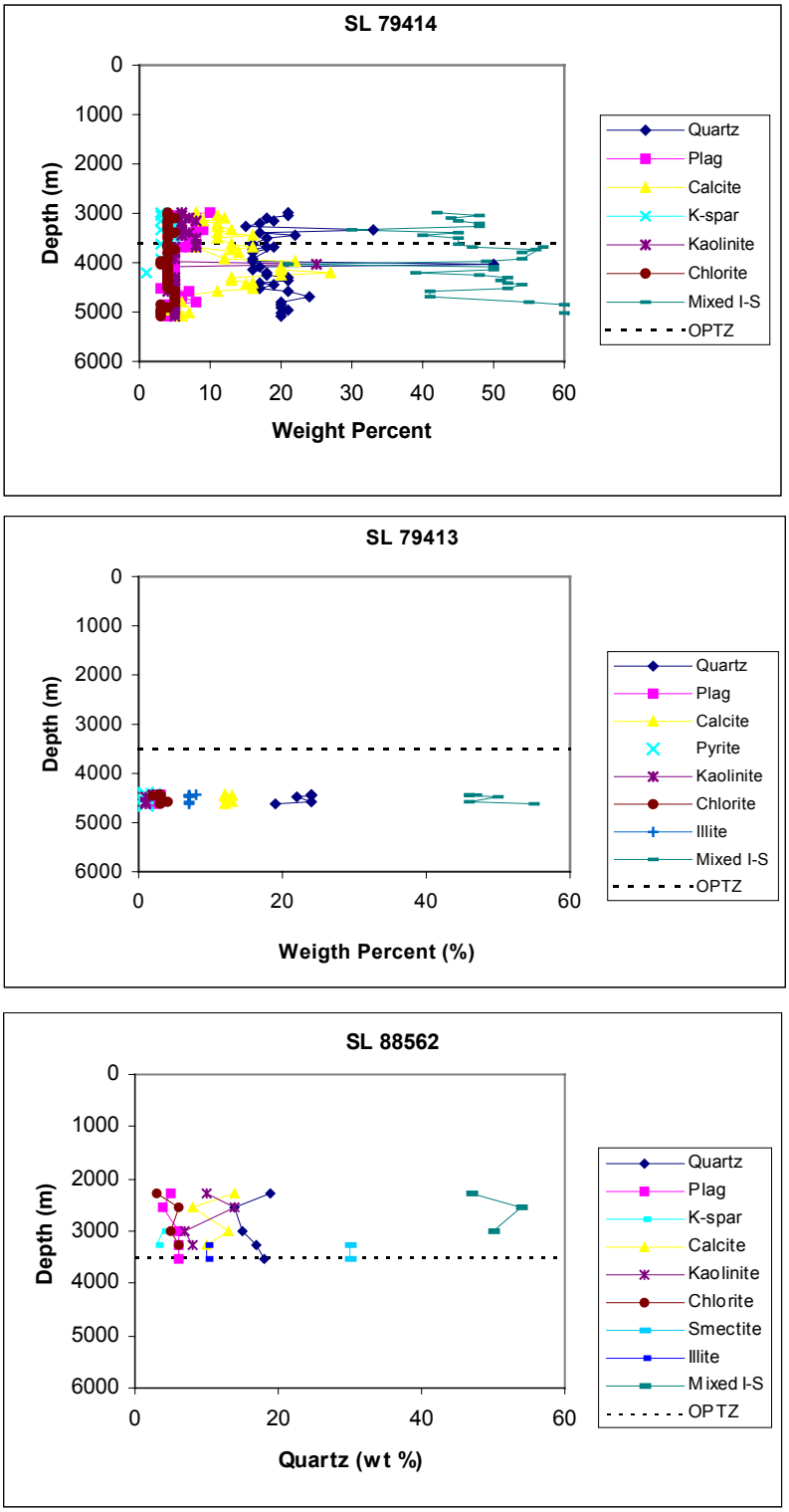

Figure 5.8. Variations in the mineral composition of mudstones at Matagorda Island 519, as determined by XRD analysis results for wells 79414, 79413, and 88562.

Simulation:	mat 519 sim 1 112901 kgs
==========	
pyrite	FeS2
ilmenite	FeTiO2
chromite	(Mg0)0.5(Fe0)0.5(Cr2O3)
apatite	Ca5(PO4)3(OH)
calcite	CaCO3
siderite	FeCO3
quartz	SiO2
kaolinite	Al2Si2O5(0H)4
++++++++++++++++++++++++++++++++	
Na-beidellite	moles/10 Oxy
Si	3.670
Al	2.330
Na	0.080
K	0.050
Mg	0.000
Fe(ll)	0.100
&&&&&&&&&&&&&&&&&&&&&&&&&&&&	
Illite	moles/10 Oxy
Si	3.360
Al	2.453
Na	0.000
K	1.000
Mg	0.050
Fe(ll)	0.050
************************************	
Chlorite	moles/10 oxy
Mg	2.045
Fe(ll)	2.955
<><><><><><><><><><><><><><><><><><><><>	
Feldspar	moles/8 Oxy
Albite	0.500
K-feldspar	0.500
:-) :-) :-) :-) :-) :-) ':-) :-) :-) :-) :-) :-) ':-) :-) :-)	

Figure 5.9 (a). Assumed mineral chemistry from simulation one of the MUDNORM program, based on Lynch (1997).

Simulation:	mat 519 sim 2 041602 kgs	
==========		
pyrite	FeS2	
ilmenite	FeTiO2	
chromite	(Mg0)0.5(Fe0)0.5(Cr2O3)	
apatite	Ca5(PO4)3(OH)	
calcite	CaCO3	
siderite	FeCO3	
quartz	SiO2	
kaolinite	Al2Si2O5(0H)4	
++++++++++++++++++++++++++++++++		
Na-beidellite	moles/10 Oxy	
Si	3.800	
Al	1.470	
Na	0.250	
K	0.180	
Mg	0.430	
Fe(ll)	0.550	
&&&&&&&&&&&&&&&&&&&&&&&&&&&&&&		
Illite	moles/10 Oxy	
Si	3.510	
Al	2.160	
Na	0.000	
K	0.520	
Mg	0.190	
Fe(ll)	0.290	
************************************		
Chlorite	moles/10 oxy	
Mg	1.100	
Fe(ll)	3.250	
<><><><><><><><><><><><><><><><><><><><><><>		
Feldspar	moles/8 Oxy	
Albite	0.600	
K-feldspar	0.400	
:-) :-) :-) :-) :-) :-) ':-) :-) :-) :-) :-) :-) ':-) :-) :-)		

Figure 5.9 (b). Assumed mineral chemistry of the second run of the MUDNORM program, based on Awwiller (1993).

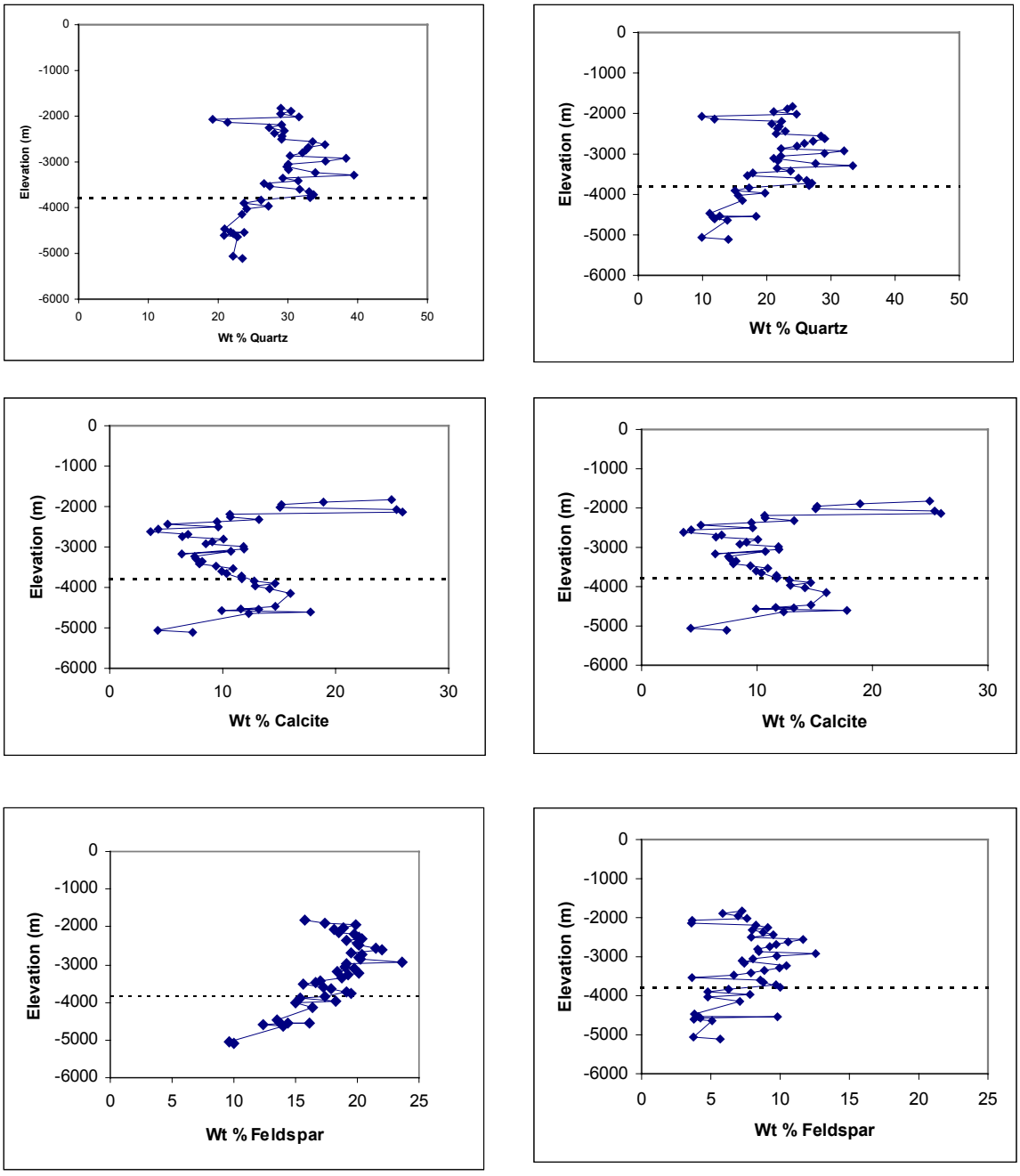

Figure 5.10 (a). Comparison of results from simulation one (left) and simulation two (right) of the MUDNORM program. Results are shown for quartz, calcite, and feldspar from well 6032 #1.

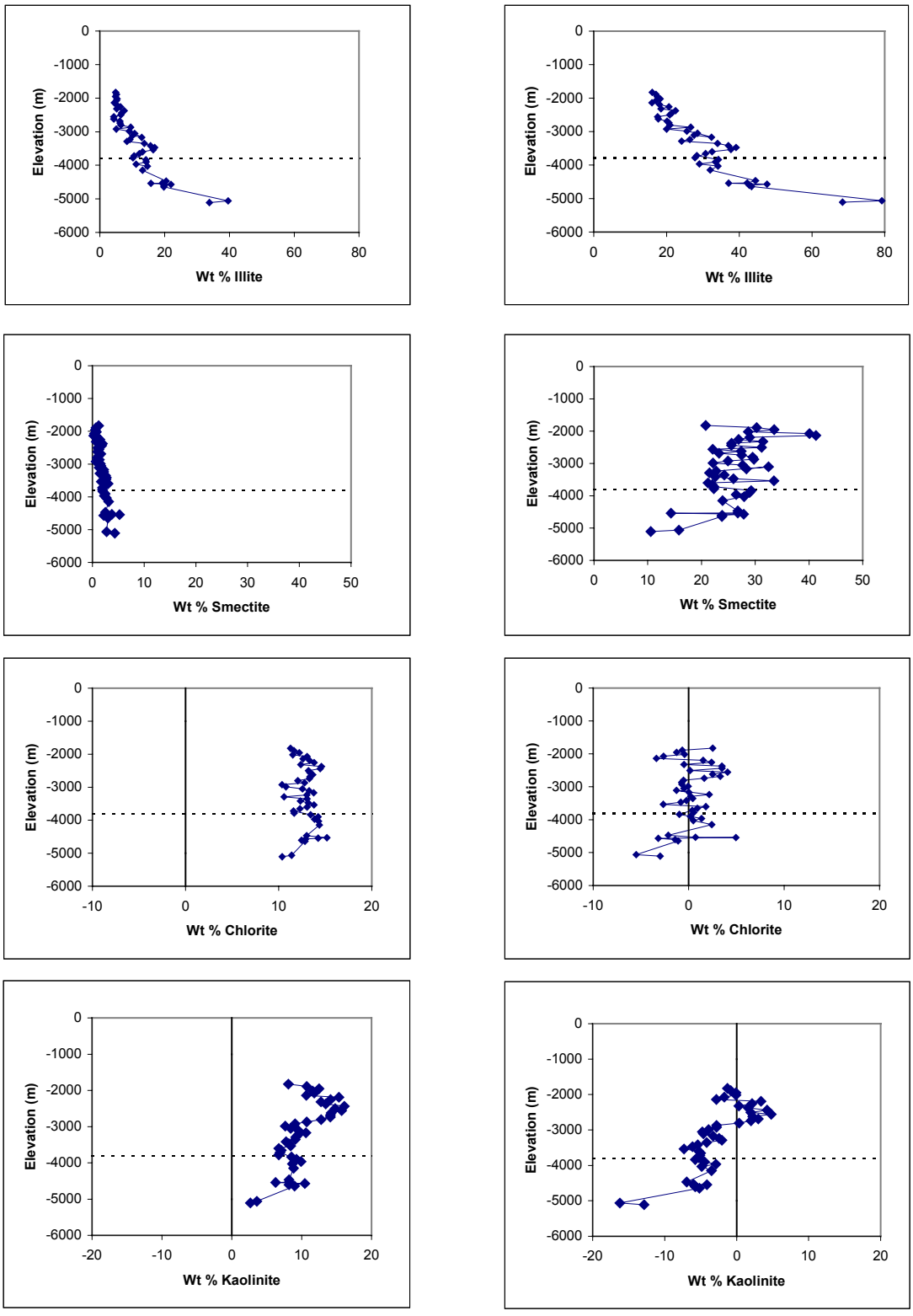

Figure 5.10 (b). Comparison of results from simulation one (left) and simulation two (right) of the MUDNORM program. Results are shown for illite, smectite, chlorite, and kaolinite from well 6032 #1.

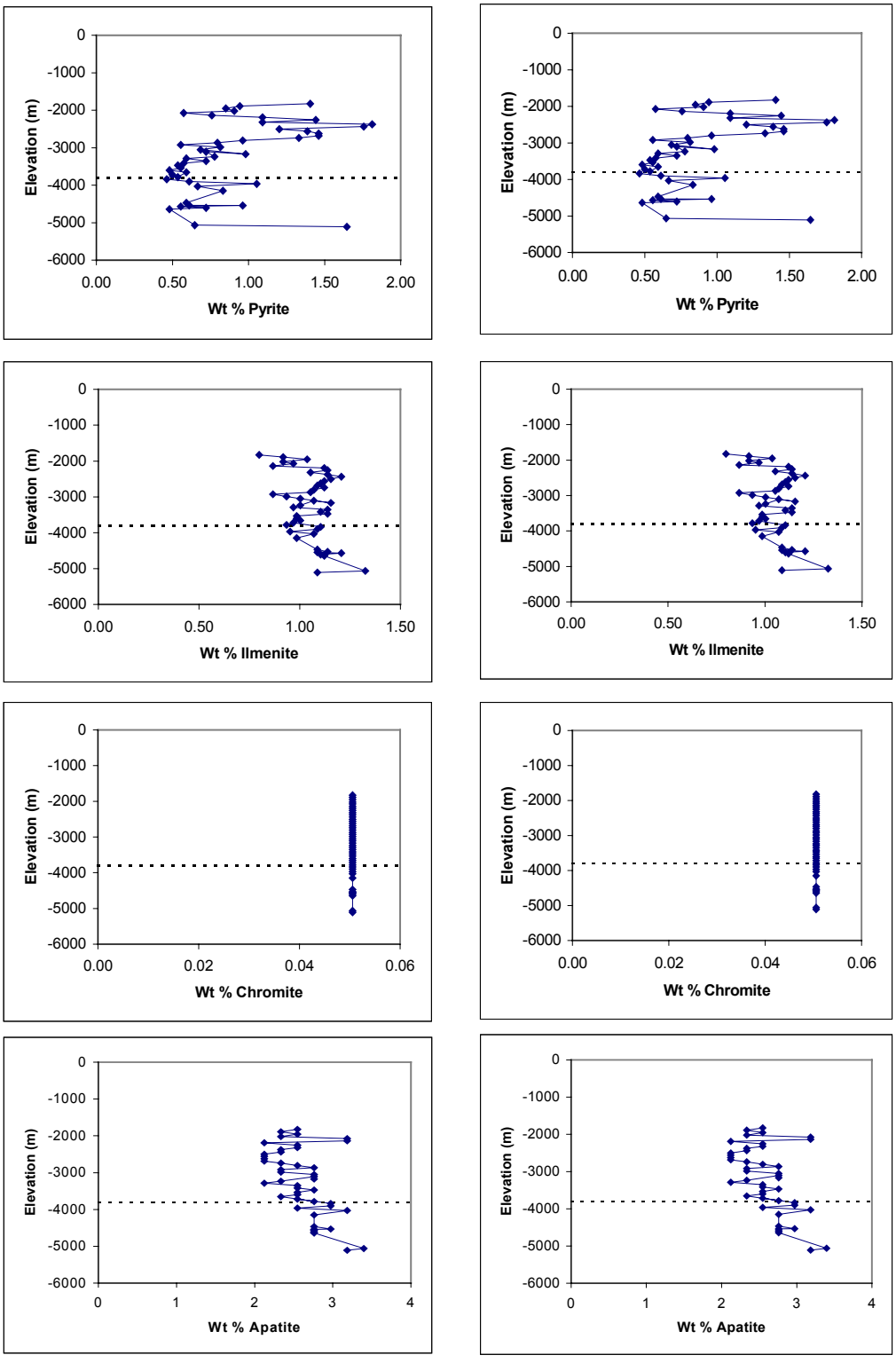

Figure 5.10 (c). Comparison of results from simulation one (left) and simulation two (right) of the MUDNORM program. Results are shown for pyrite, ilmenite, chromite, and apatite from well 6032 #1.

Illite shows the same trend for both simulation one and simulation two, yet there is a large difference in observed magnitudes between the two simulations. Smectite shows a great amount of variation in both the overall trend and the magnitude of values between simulation one and simulation two. The overall trend for chlorite is similar for both simulation one and simulation two although values from simulation one are higher than those for simulation. Kaolinite displays a very similar trend for both simulations, yet the magnitude of values is greater for simulation one than for simulation two. Negative values are generated in simulation two for both chlorite and kaolinite, and these are the result of inaccurate assumptions regarding mineral stoichiometries.

Overall trends and magnitudes of values for the minor mineral phases pyrite, ilmenite, chromite, and apatite are similar for both simulation one and simulation two. There is little to no observed difference between the results of simulation one and those of simulation two for these phases.

In general, both simulations produce similar results. However, simulation two fails in this study because it yields significantly negative values for both chlorite and kaolinite (Figure 5.10). Results from simulation one are valid for this study, with the exception that simulation one seems to underestimate smectite. Thus, because the results from simulation one are valid for this study, future reference to MUDNORM results will be understood to reflect results from simulation one, unless otherwise noted.

Normative mineralogy versus depth for well 6032 #1 (Figure 5.10) shows the highest abundance for quartz at depths between 2400-3650 m (8,000–12,000 ft), followed by a general decrease with depth. Calcite shows two peaks in abundance, at approximately 1800 m (6,000 ft) and from 3350-4300 m (11,000–14,000 ft). Illite displays an overall increase with depth.

Smectite appears to increase with depth. Feldspar and kaolinite both generally decrease with depth. Figure 5.11 shows normative mineralogy versus depth for wells 79413, 88562, and 5169.

Figure 5.11a shows normative mineralogy versus depth at well 79413. Quartz initially decreases with depth until 3650 m (12,000 ft), then increases with depth below 3650 m (12,000 ft). Calcite initially peaks at 3000 m (10,000 ft), then decreases until 3650 m (12,000 ft), and increases with depth below 3650 m (12,000 ft). Illite and smectite both appear to be relatively constant with depth, although some variability is observed in each curve. Feldspar shows an increase in abundance with depth and kaolinite shows overall decrease in abundance, with increasing depth.

Figure 5.11 b illustrates normative mineralogy versus depth for well 88562. There is an overall decrease of quartz with depth. Calcite shows a small peak near 3000 m (10,000 ft), then a large peak from 3650-4300 m (12,000–14,000 ft). Illite appears to increase with depth, especially at the base of the well. Smectite is relatively constant with increasing depth. Albite is characterized by an overall decrease with depth, and a region of unusually lowered abundance from 3650-4300 m (12,000–14,000 ft) represents a kink in the general trend at well 88562. Kaolinite displays an overall decrease to a depth of 4300 m (14,000 ft).

Normative mineralogy versus depth in well 5169 is illustrated in Figure 5.11 c. Quartz shows an overall increase in abundance with depth until approximately 2400 m (8,000 ft), then a decrease with depth below 2400 m (8,000 ft). Abundance of calcite is elevated from 1800-2400 m (6,000–8,000 ft), then decreases at 2400 m (8,000 ft). Calcite increases with depth from 2400-3650 m (8,000–12,000 ft), then is elevated from 3650-4300 m (12,000–14,000 ft). There is a decrease in abundance of illite with depth initially, then an increase with depth below 2400 m (8,000 ft). Smectite appears to be relatively constant with depth. Albite exhibits a relatively

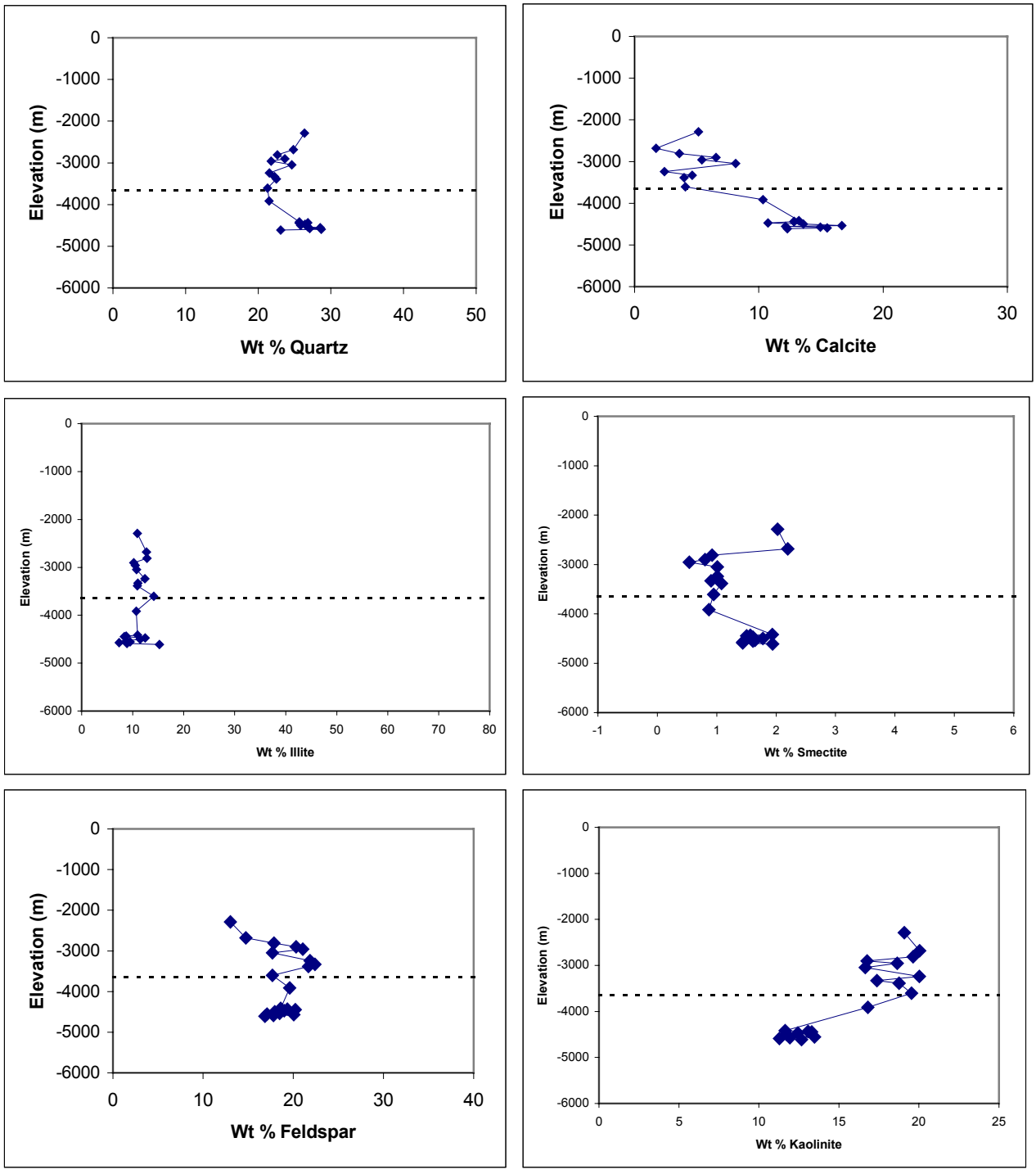

Figure 5.11 (a). Normative mineralogy versus depth for well 79413 using results determined from simulation one of MUDNORM.

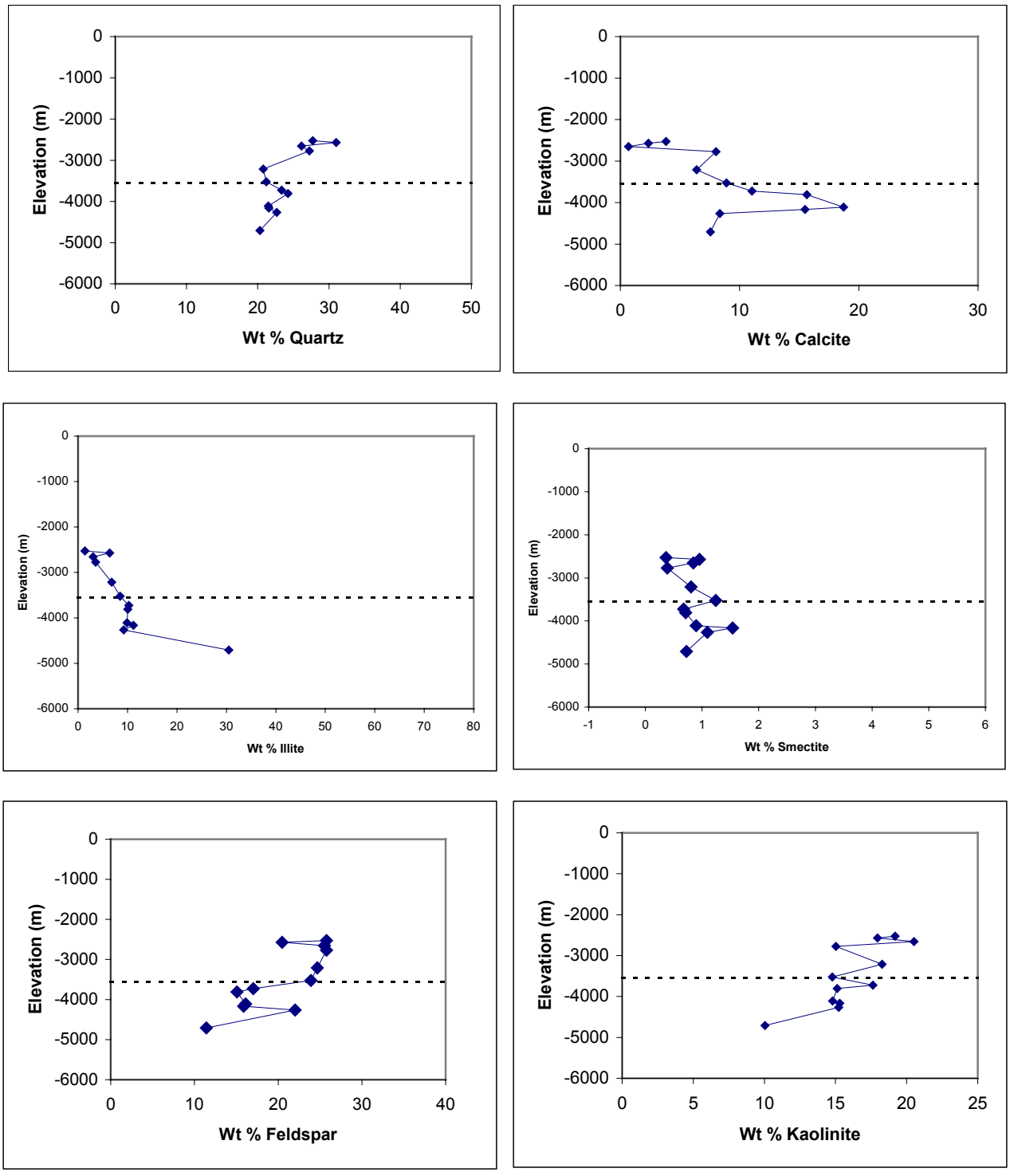

Figure 5.11 (b). Normative mineralogy versus depth for well 88562 using results determined from simulation one of MUDNORM.

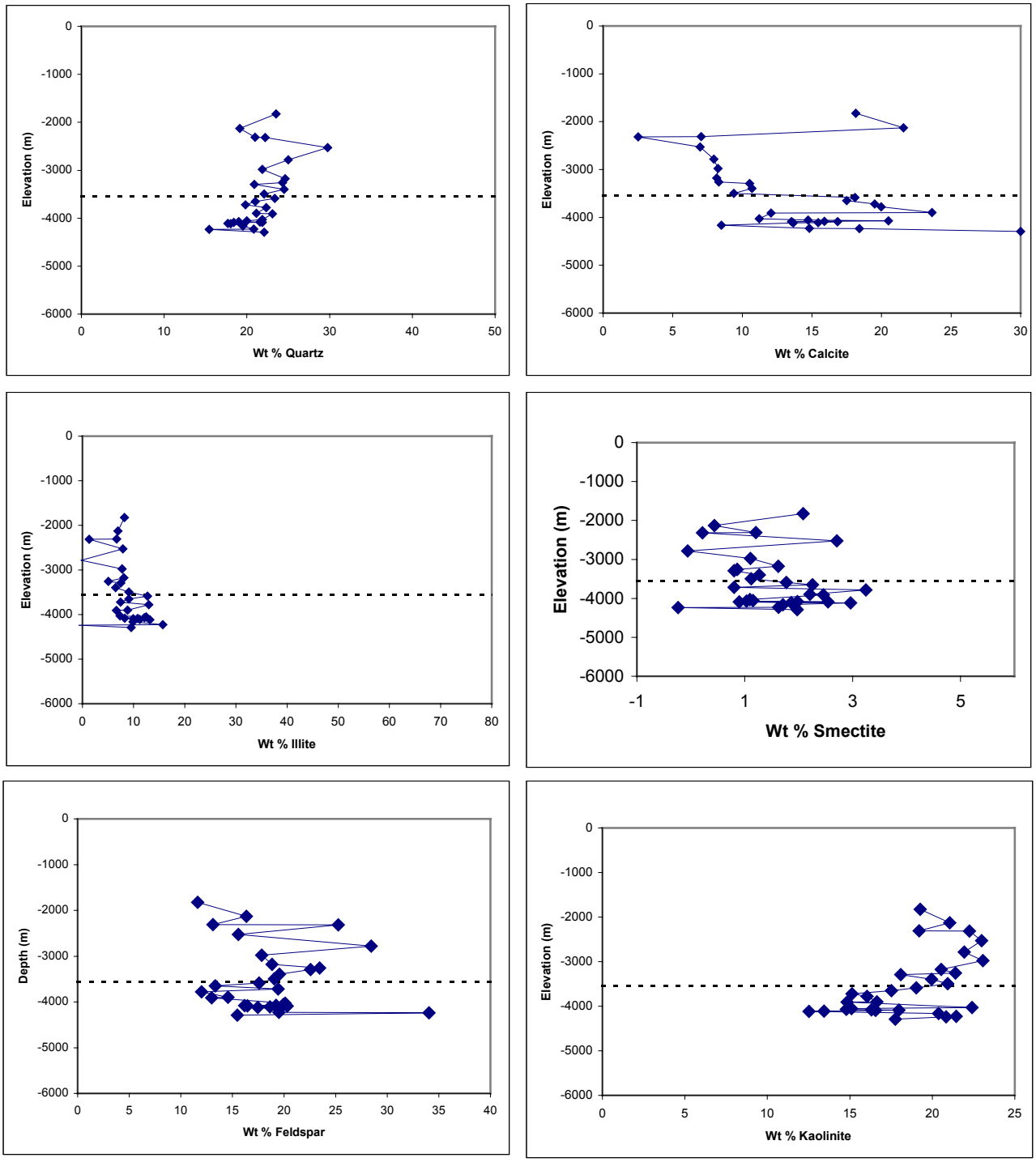

Figure 5.11 (c). Normative mineralogy versus depth for well 5169 using results determined from simulation one of MUDNORM.

high degree of variability with depth, showing an overall increase with depth, and a zone similar to that observed in well 88562 of lowered values of albite is observed from 3650-4300 m (12,000–14,000 ft). Kaolinite displays an overall decrease with depth.

5.2.3.1. Calcite

Calcite versus depth plots for all wells show an overall trend of calcite enrichment with depth (Figure 5.11). Two peaks of calcite abundance are observed on all plots. A first peak of slightly enriched calcite occurs near 2400 m (8,000 ft) in most wells. A second peak is observed between 3500-5000 m (10,500-15,000 ft) in all wells. This second calcite enrichment interval roughly corresponds to the top of overpressure fieldwide, although the highest values of calcite enrichment occur below the top of overpressure in some wells. Results of normative calcite enrichment versus depth are consistent with results for CaO enrichment versus depth at Matagorda Island 519, reflecting that most of the available Ca is incorporated into calcite in this field (Figures 5.6b and 5.11).

5.2.3.2. Quartz

Normative mineralogy versus depth plots for all four wells (Figure 5.11) consistently show that quartz is the most abundant mineral with depth, although some wells show that illite becomes more abundant than quartz at depths below 4875 m (16,000 ft). The overall trend in abundance of quartz with depth shows a decrease for all wells, while the overall trend in abundance of illite with depth shows a slight increase with depth to approximately 4260 m (14,000 ft) and then a large increase with depth to 5500 m (18,000 ft).

5.2.3.3. Smectite

Smectite abundance with depth is relatively stable (Figure 5.11), with a slight trend of enrichment to depths of 4260 m (14,000 ft) and loss of smectite below 4260 m (14,000 ft). Smectite abundance is consistently 5% or less in all wells (Figure 4.35).

5.2.3.4. Chlorite

Normative chlorite versus depth shows similar trends in all wells, with enrichment to a depth of 2400 m (8,000 ft), followed by loss to a depth of 3050 m (10,000 ft). Then, slight enrichment occurs briefly, followed by loss until 3650 m (12,000 ft). Below 3650 m (12,000 ft) chlorite is enriched in wells 6032 #1 and 5169 and is lost slightly in wells 79413 and 88562.

5.2.3.5. Feldspar

Normative feldspar versus depth results show that feldspar is initially enriched with depth and then is depleted with depth in all wells, with the exception of well 5169 (Figure 5.11). The depth range for the transition from enriched feldspar to depletion of feldspar is between 2400-3350 m (8,000-11,000 ft). In well 5169 feldspar is enriched at several depth intervals, the largest enrichment occurring at a depth of 4260 m (14,000 ft).

5.2.3.6. Kaolinite

Kaolinite versus depth results show that kaolinite is relatively enriched until a depth of 2400 m (8,000 ft) in all wells (Figure 5.11), then is less stable with depth below 2400 m (8,000 ft). There is an overall trend of slight decrease in abundance of kaolinite with depth below 2400 m (8,000 ft). In most wells kaolinite is rapidly lost in the same depth interval in which illite is rapidly gained (Figure 5.11). Thus, kaolinite is being destroyed as illite is gained at Matagorda Island 519.

5.2.4. Comparison of MUDNORM Results to Previous Mineralogy Research at MI 519

According to Brewster et al. (1998) and Klein et al. (1998) the most abundant mineral phase as determined by XRD at Matagorda Island 519 was a mixed layer illite-smectite, represented by a weight percent range from 20-60%. This is fairly consistent with results from this study, which report values for illite and smectite individually at Matagorda Island 519 that together would total a weight percent range from 25-40%. The next most abundant mineral

phase reported by Amoco was quartz, with a weight percent range from 15-25%. Results for weight percent of quartz are more consistent with those reported in this study, which are generally between 20% and 30%. The next most abundant mineral phase was calcite, with a weight percent range from 10-20% at Matagorda Island 519. This range for calcite is generally consistent with the range of calcite weight percent values calculated in this study, from 5-30%.

Remaining results reported by Amoco include mineral abundances for feldspars, kaolinite, and chlorite, which are all reported to have weight percent values of less than 10%. In this study, feldspar abundance was represented by albite with a range from 15-25%, which is slightly higher than the sum of plagioclase and K-feldspar weight percents reported by Amoco at near 10%. Kaolinite abundance reported by Amoco was significantly lower than that calculated in this study, with Amoco reporting a weight percent range of less than 10% and this study reporting a weight percent range from 10-20%. Chlorite weight percent ranges reported by Amoco are also lower than those reported in this study, with Amoco reported weight percent ranges for chlorite of less than 10% and weight percent ranges for chlorite reported in this study from 10-15%.

5.3. Fluid Chemistry

5.3.1. Introduction

Only three partial analyses of produced waters from Matagorda Island 519 were in the Amoco data set used in this study. However, a fairly large data base has been published for the Picaroon and Doubloon fields in the Corsair Trend, approximatlely 30 km southeast of Matagorda Island 519 (Taylor and Land, 1996). Because of the similarity in geologic setting between the three fields, a brief discussion of Taylor and Land's results will be presented here to provide information on the possible chemistry of Matagorda Island 519 waters.

5.3.2. Fluid Chemistry at Picaroon and Doubloon

Two lines of information are available on the properties of formation waters in the Corsair trend, fluid inclusion studies and analyses of produced waters (Taylor and Land, 1996). Inclusions in ankerite from reservoir sands at depths of ~ 4940 to 5180 m (16,200 to 17,000 ft) yield homogenization temperatures of 120 to 188°C. Inclusion melting temperatures yield salinities of 15 to 25 weight % equivalent NaCl. Fluid inclusions in barite have homogenization temperatures of 109 to 178°C.

Taylor and Land (1996) report partial and detailed analyses of formation waters from the Picaroon and Doubloon fields. Salinities range from 151 g/L to 244 g/L at Picaroon and from 63 to 74 g/L at Doubloon. The measured Picaroon salinities are thus similar to the range in salinities in ankerite fluid inclusions.

The Sr isotopic composition of formation waters at Picaroon and Doubloon ranges from 0.70992 to 0.7111 and are thus more radiogenic than either the early calcite cements (0.7083 to 0.7086) and late stage ankerites (0.70963 to 0.70970). Taylor and Land invoke acquisition of radiogenic Sr from smectite (0.715) and K-feldspar (0.711 to 8.0). Oxygen isotopic values of produced waters range from $\delta^{18}O$ of 8.05 to 9.3 per mil SMOW at Picaroon and $\delta^{18}O$ 7.8 per mil SMOW at Doubloon and are consistent with predicted values resulting from shale diagenesis. Picaroon brines have high B concentrations and are depleted in $^{11}\delta B$.

Additional important conclusions beyond those published by Taylor and Land can be made about the chemistry of the formation waters at Picaroon and Doubloon. There is a positive linear correlation between dissolved chloride and salinity for all of the Picaroon and Doubloon waters (Figure 5.12), which is not surprising because chloride here, as with saline formation waters world-wide, is by far the dominant contributor to anionic charge (Hanor, 2001). There

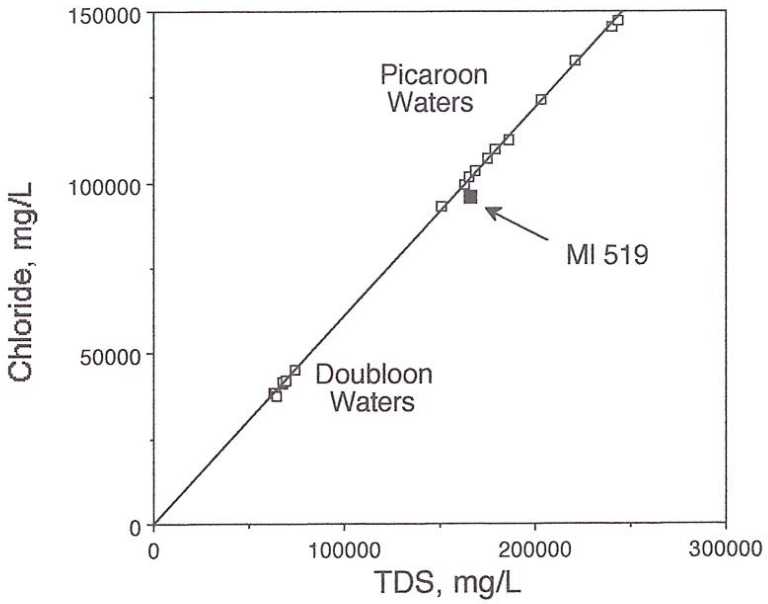

Figure 5.12. Positive linear correlation between dissolved chloride and TDS at Picaroon and Doubloon.

are also statistically good ($r^2 > 0.925$) linear positive correlations between chloride and Na and Ca (Figure 5.13), Sr (not shown), and Br (Figure 5.14). There is a nearly perfect negative correlation between $^{87/86}Sr$ and chloride (Figure 5.15) and a negative linear correlation with $^{11}\delta B$ (Figure 5.16). Boron and the cations K and Mg also show positive correlations with chlorinity, but with a great deal more scatter than the other cations. In contrast to the cations and Br, total alkalinity shows a general negative correlation with chloride concentration, a relation also noted in formation waters world-wide (Hanor, 1994a).

Much of the elemental and isotopic chemistry of the waters at both the Picaroon and Doubloon fields can thus be explained by simple conservative mixing of two end-member waters, a lower salinity formation water having low Ca concentrations but elevated alkalinities and a high salinity water having high Ca concentrations but low alkalinity. Taylor and Land do not report pH values for any of their analyses, so it is not possible to calculate well-head or subsurface saturation sates of the waters with respect to calcite. However, mixing of a high-Ca, low-alkalinity water with a low-Ca, high alkalinity water has the potential of precipitating calcite (Morse et al., 1997).

5.3.2. Chemistry of Waters at MI 519

Three partial analyses of formation waters are present in the Amoco data set. Of these, two are of waters having salinities less than 1500 mg/L and appear to represent waters produced by condensation of water vapor from cooling of natural gas rather than actual formation waters. The third analysis, however, appears to be of a co-produced formation water from 6032#2 at a depth of 17,000 ft. The salinity of this water, 166 g/L, is consistent with salinities calculated from SP response for this portion of the field. The MI 519 water has a sallinity and chemical

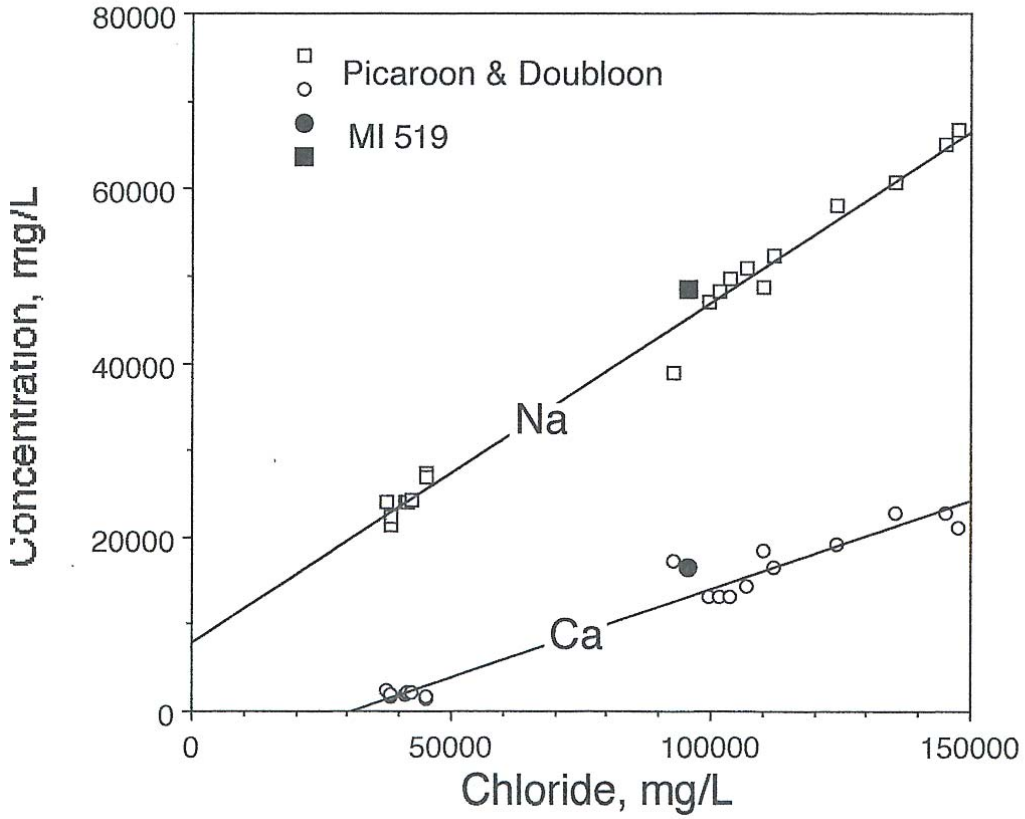

Figure 5.13. Na and Ca versus dissolved chloride at Picaroon and Doubloon, showing positive linear correlation.

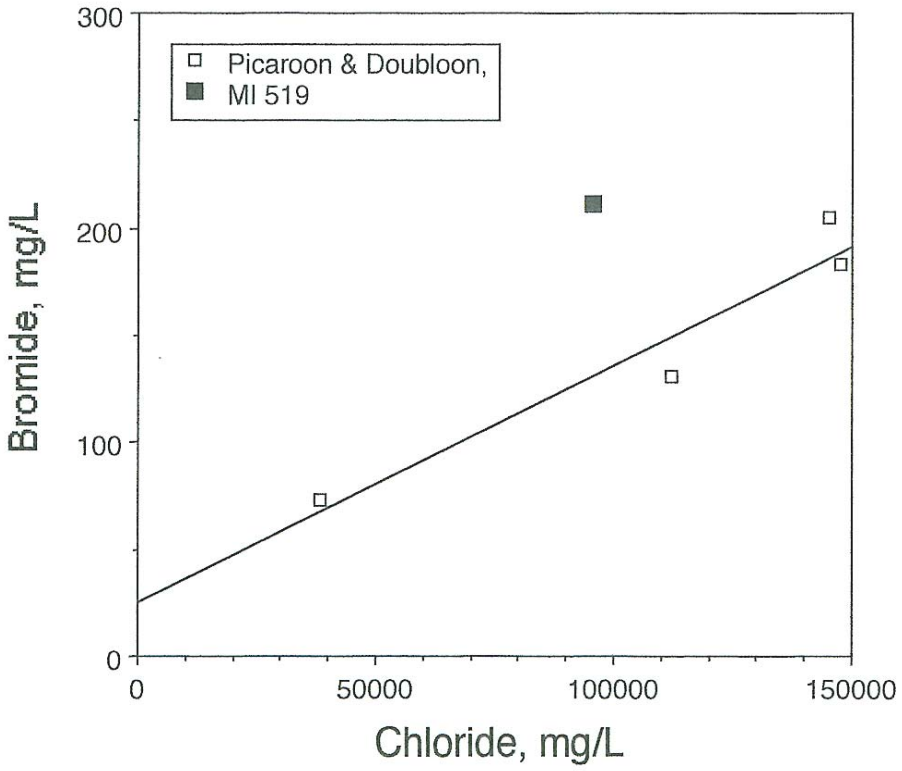

Figure 5.14. Br versus dissolved chloride at Picaroon and Doubloon, showing positive linear correlation.

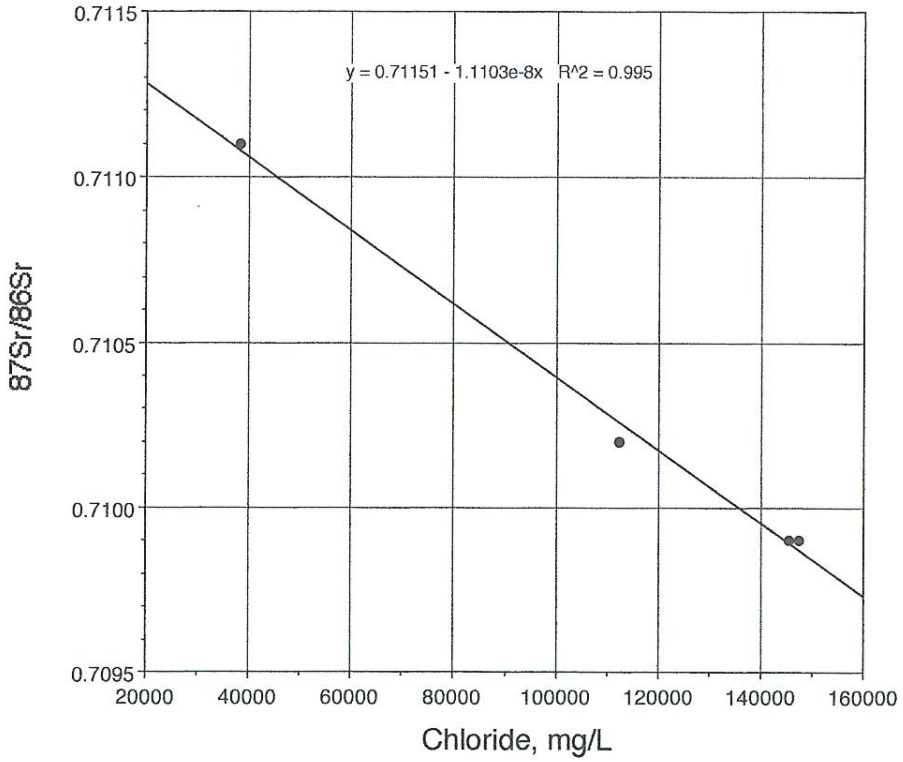

Figure 5.15. $^{87/86}$Sr versus dissolved chloride at Picaroon and Doubloon, showing negative linear correlation.

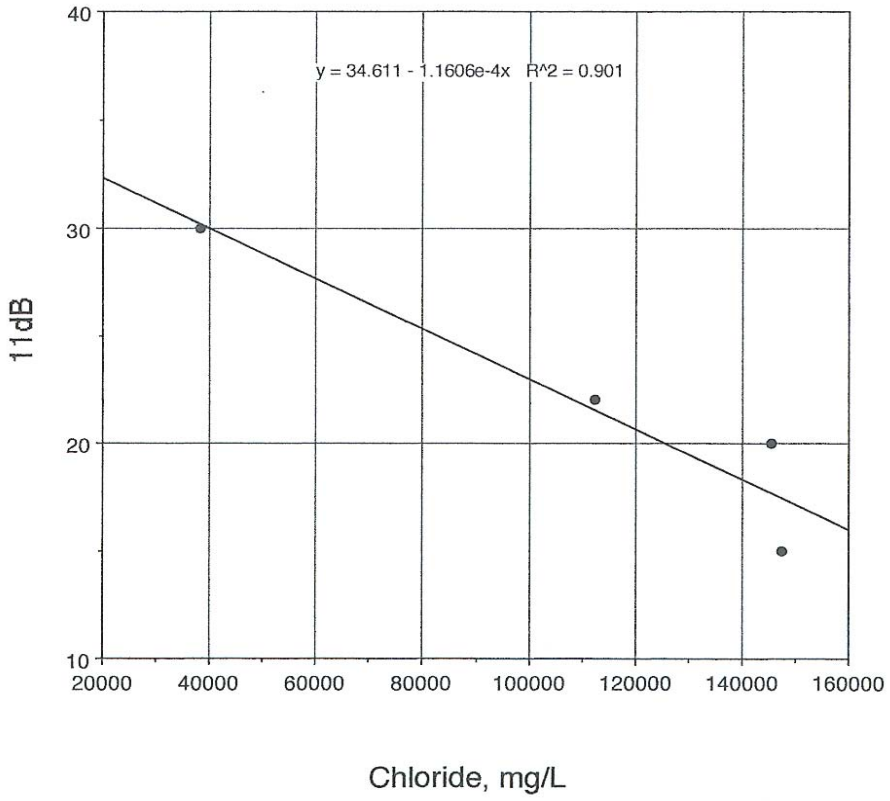

Figure 5.16. $^{11}\delta B$ versus dissolved chloride at Picaroon and Doubloon, showing negative linear correlation.

composition very similar to the lower salinity waters at Picaroon (Figures 5.12 – 5.16) and may also have been derived from a similar endmember source.

5.3.3. Gas Compositions

Both the Picaroon and Doubloon natural gases contain significant concentrations of CO_2. Taylor and Land cite figures of 4.5 to 4.7 % at Picaroon and 2.7% at Doubloon. The $\delta^{13}C$ isotopic composition of methane at Picaroon ranges from -31.8 to -31.5 per mil PDB and is -37.6 per mil for a single sample from Doubloon (Taylor and Land, 1996). The methane at MI 519 is lighter with values of ca -40 to -43 per mil PDB (Klein et al., 1998). MI 519 H_2S has a $\delta^{34}S$ of +1.9 to 3.9 ppt CDT. According to Klein et al., the CH_4 and H_2S isotopic compositions are consistent with thermogenic sulfate reduction (TSR). For reasons not stated, Klein et al. prefer an Eagle Mills Trassic evaporite source for the sulfate (12 ppt), rather than a Jurassic Louann source (16 ppt).

CHAPTER 6. RESULTS: PROPERTIES OF THE OVERPRESSURED ZONE AT MATAGORDA ISLAND 519

6.1. Introduction

A summary of the nature of the seal at Matagorda Island 519 is provided here in terms of fluid pressure, fluid pressure gradient, lithology, salinity, and mineralogy. Figures showing all of these properties versus depth for the depth range in which the pressure seal occurs are presented for each of the six wells in order to examine the nature of the seal (Figures 6.1-6.6). All wells have data for fluid pressure, fluid pressure gradient, lithostratigraphy, and salinity, however, wells 79414 and 6032 #2 do not include mineralogy because these data were not available.

6.2. Fluid Pressure and Pressure Gradient

The top of the overpressure transition can be correlated across the study area between depths of 3600 m and 3800 m. Above the top of overpressure, all wells show a generally linear, hydrostatic increase in fluid pressure with depth. Below the overpressure transition zone there are several intervals in which fluid gradients return to nearly hydrostatic values. These intervals are separated vertically by zones in which fluid pressure shows an abrupt increase. These deeper intervals in which fluid pressure gradients alternate between low and high values are consistent with the existence of isolated vertical pressure compartments or intervals. Future research could determine whether there is additional evidence that three-dimensional pressure compartments exist at Matagorda Island 519, as defined in chapter 1. Well 6032 #2 shows two abrupt increases in the fluid pressure gradient that are more shallow than that used to define the top of overpressure (Figure 6.2). This discrepancy is an artifact of the steep slope

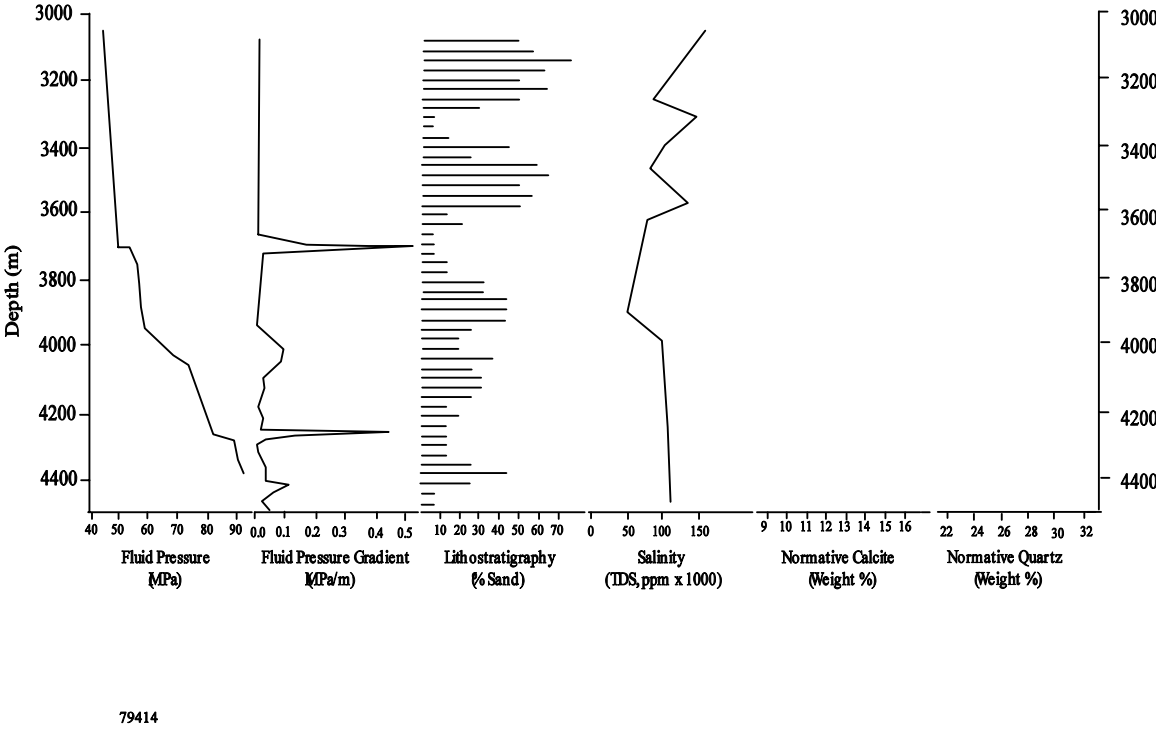

Figure 6.1. Characterization of the nature of the pressure seal in well 79414, using fluid pressure, fluid pressure gradient, lithostratigraphy, and salinity data versus depth. The top of overpressure occurs at approximately 3700 m.

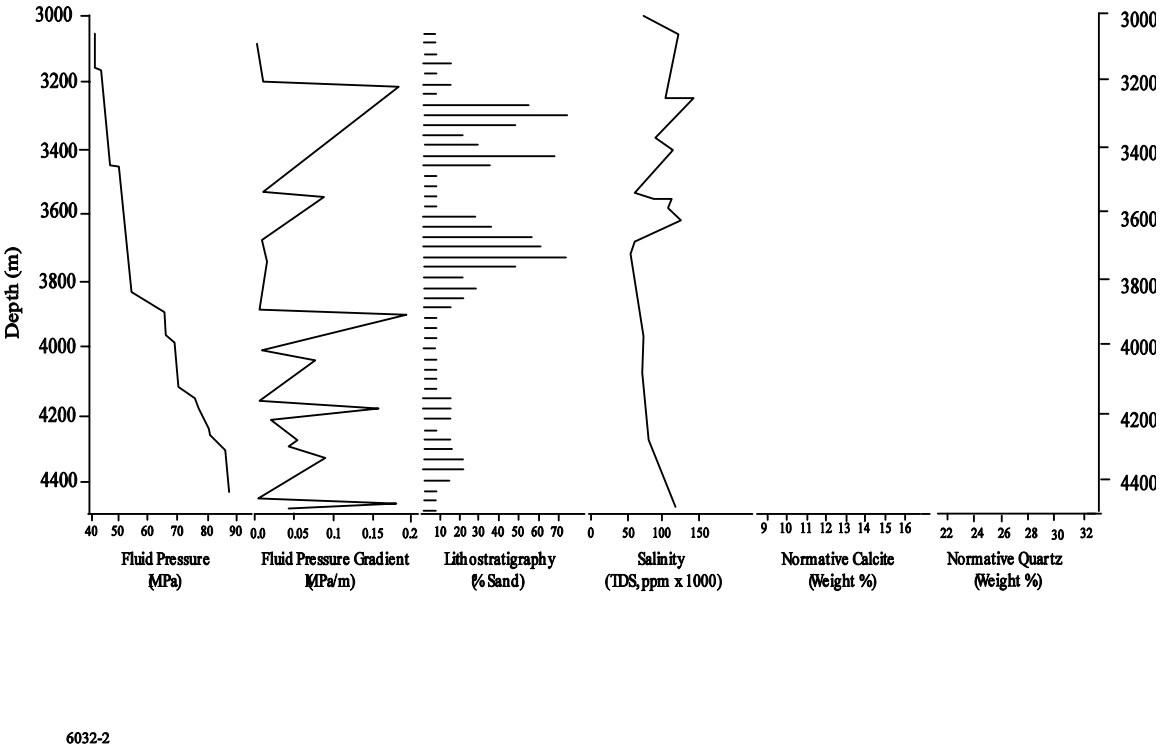

Figure 6.2. Characterization of the nature of the pressure seal in well 6032 #2, using fluid pressure, fluid pressure gradient, lithostratigraphy, and salinity data versus depth. The top of overpressure occurs at approximately 3800 m.

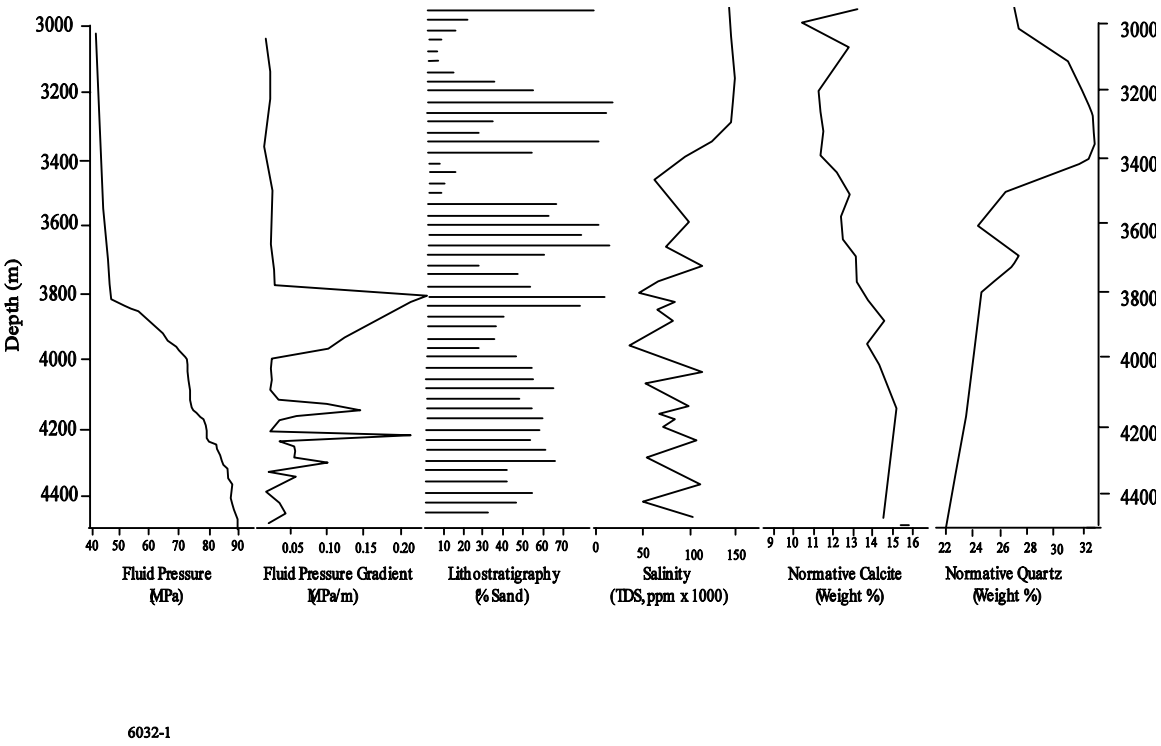

Figure 6.3. Characterization of the nature of the pressure seal in well 6032 #1, using fluid pressure, fluid pressure gradient, lithostratigraphy, salinity, and normative mineralogy data versus depth. The top of overpressure occurs at approximately 3800 m.

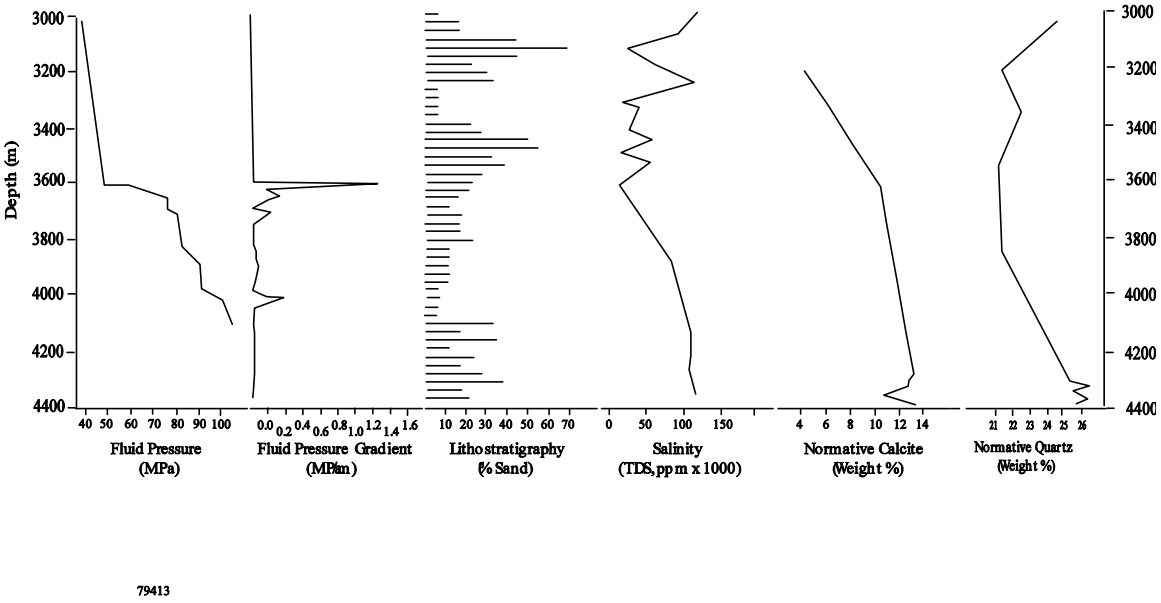

Figure 6.4. Characterization of the nature of the pressure seal in well 79413, using fluid pressure, fluid pressure gradient, lithostratigraphy, and salinity data versus depth. The top of overpressure occurs at approximately 3600 m.

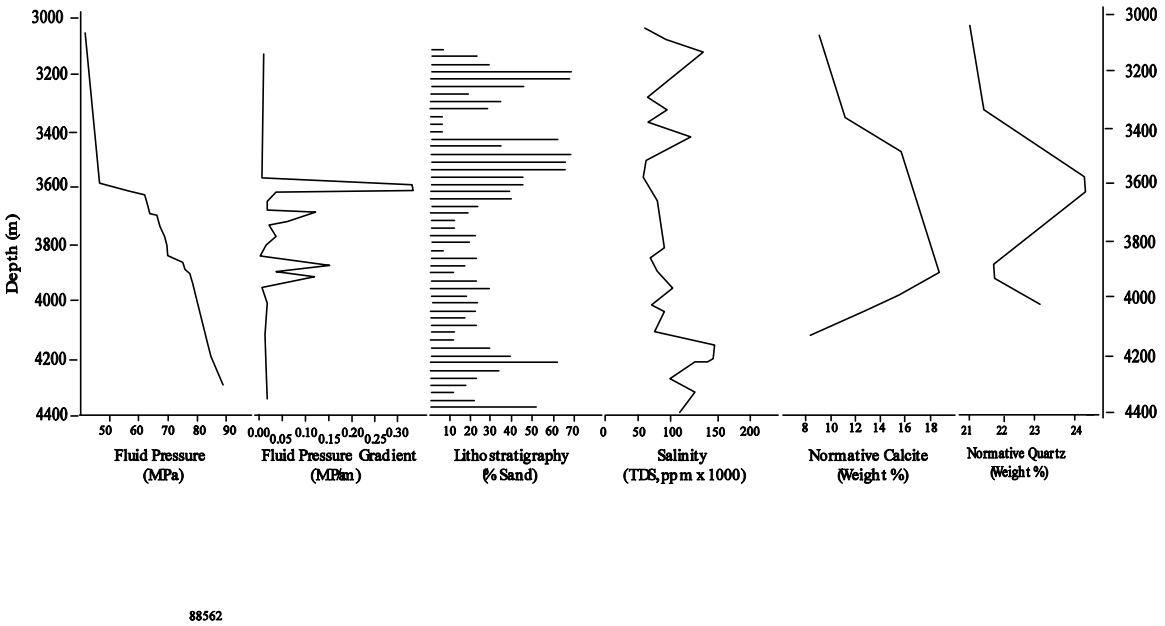

Figure 6.5. Characterization of the nature of the pressure seal in well 88562, using fluid pressure, fluid pressure gradient, lithostratigraphy, and salinity data versus depth. The top of overpressure occurs at approximately 3600 m.

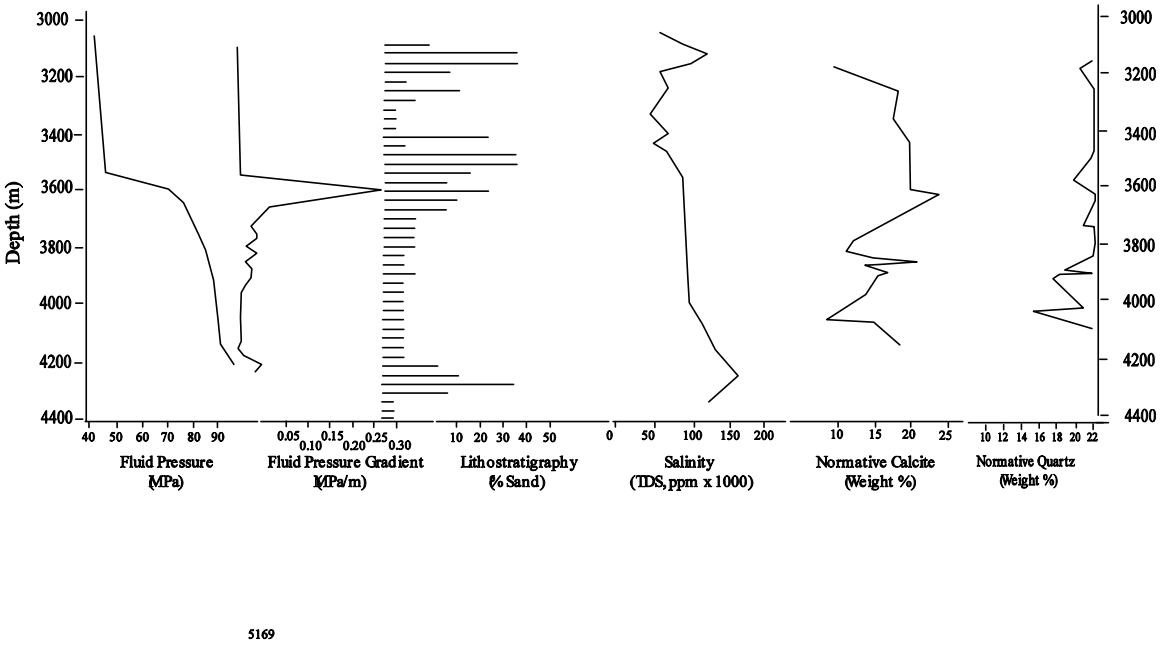

Figure 6.6. Characterization of the nature of the pressure seal in well 5169, using fluid pressure, fluid pressure gradient, lithostratigraphy, and salinity data versus depth. The top of overpressure occurs at approximately 3550 m.

between adjacent data points for fluid pressure in well 6032 #2, because the absolute increase in fluid pressure with depth is minimal at these depths.

6.3. Lithostratigraphy

In general, the overpressure transition zone occurs within a fining downward sequence. In some wells, such as 79414 and 6032 #2, the top of overpressure occurs within a shaly interval at the base of this fining downward sequence, yet in other wells, such as 6032 #1 and 88562, the top of overpressure occurs within a silty to sandy interval at the top of the fining downward sequence (Figures 6.1-6.6). This lack of a correlation across the field between the top of overpressure and lithology indicates that the seal is likely cutting across lithostratigraphy at Matagorda Island 519. Thus, the seal is not controlled strictly by lithology and is controlled by some other feature, such as diagenesis. Also of relevance, fining downward successions are observed in connection with the deeper overpressured intervals previously defined.

6.4. Salinity

An overall decrease in salinity with depth into overpressure occurs for all wells except 5169, reflecting a salinity reversal at the top of overpressure. The magnitude of decrease varies somewhat between each well, yet there is a consistent pattern of salinity reversal that is associated with the top of overpressure in most wells. However, one well shows a lowered salinity above the top of overpressure. Because salinity was calculated from SP log response, this apparent inconsistency at the scale of interest may be due to inaccuracies associated with the SP method. Below the top of overpressure salinity increases with depth in all wells.

6.5. Normative Calcite

Calcite generally increases with depth into overpressure in wells at Matagorda Island 519. The depth interval of calcite enrichment begins slightly above the top of overpressure in all wells, and continues until just below the top of overpressure. Thus, there is sufficient evidence to indicate that calcite enrichment may be indicative of pressure seal development in this study area.

6.7. Normative Quartz

Quartz enrichment occurs above the top of overpressure throughout the study area, and quartz depletion with depth occurs below the top of overpressure. Thus, quartz dissolution and reprecipitation may be playing a key role in the development and maintaining of a pressure seal at Matagorda Island 519, potentially supplementing the underlying calcite enrichment to preserve the seal.

6.8. Characterization of the Pressure Seal: All Properties

All wells show a consistent abrupt increase in both fluid pressure and the first derivative of fluid pressure, the fluid pressure gradient, within the same general depth interval, representing the overpressure transition and the uppermost pressure seal. In addition, most wells also show evidence for at least one additional, deeper interval of overpressure that is vertically bounded by a deeper seal.

The pressure seal is marked by a consistent fining with depth in all wells, although the lithology of the pressure seal is not consistent in all wells. This indicates that the seal may cut across lithology at Matagorda Island 519, supporting the hypothesis that the pressure seal is maintained by diagenesis. Salinity reversals occur at or just below the pressure seal in most wells, which is consistent with deep clay mineral dewatering causing overpressure to develop in this area.

Observed patterns in normative mineralogy with depth suggest that calcite enrichment occurs just above and within the pressure seal. Evidence of calcite enrichment at the pressure seal reflects the diagenetic nature of the seal. In addition, quartz enrichment is observed above the pressure seal as well, just above the zone of calcite enrichment. This evidence suggests that there may be a relation between zones of calcite and quartz enrichment, and that these zones of enrichment are complimenting one another in producing the pressure seal at Matagorda Island 519.

6.9. Well Log Response to Overpressure

Well log signatures across the overpressure transition zone are of particular interest because well log responses are influenced by many of the physical and chemical properties of sediments that were analyzed in this study. For example, lithology and salinity influence SP log response, while resistivity log response is influenced by lithology and pressure, and conductivity log response is also influenced by pressure. In addition, diagenetic cementation influences both the SP and resistivity logs.

Table 6.1 lists abbreviations used for each type of well log, along with a translation of each abbreviation. Figures 6.7 (a-f) illustrate typical well log responses across the overpressure transition zone, showing gamma ray, SP, resistivity, and conductivity responses to overpressure. The wells in these figures are arranged in order from southwest to northeast in the Matagorda Island 519 field.

Gamma ray response to overpressuring in the study area is generally a sharp positive deflection that is observed as a shift in the gamma ray log curve to the right, representing an increase in gamma ray emmission. Overpressuring typically causes the SP log curve to also deflect to the right, reflecting a positive SP response. Resistivity log

Table 6.1. Abbreviations used for each type of well log used in this study, along with translation for each abbreviation.

Abbreviation	Translation	Unit
GR	Gamma Ray	GAPI
SP	Spontaneous Potential	millivolts
ILD	Deep Induction Resistivity	ohm-meters
SFLA	Spherically Focused Resistivity	ohm-meters
IDPH	Deep Phasor Induction Resistivity	ohm-meters
CILD	Conductivity Deep Induction	millimho
TENS	Cable Tension	pounds
AMP GUARD	Amplitude Focused Resistivity	ohm-meters
GUARD	Guard Electrode Focused Resistivity	ohm-meters
DEEP	Deep Resisitivity	ohm-meters

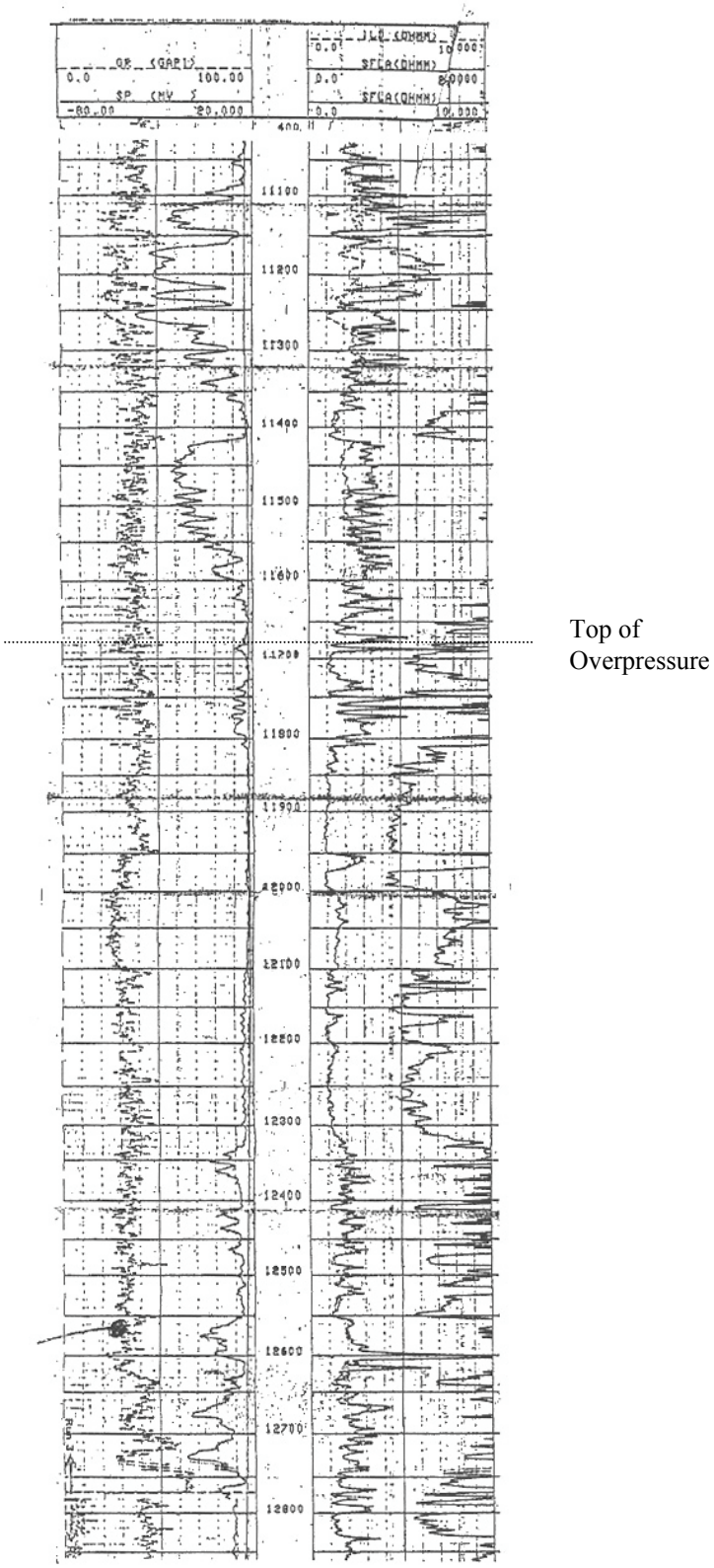

Figure 6.7 (a). Well log response to the overpressured zone in well 79414.

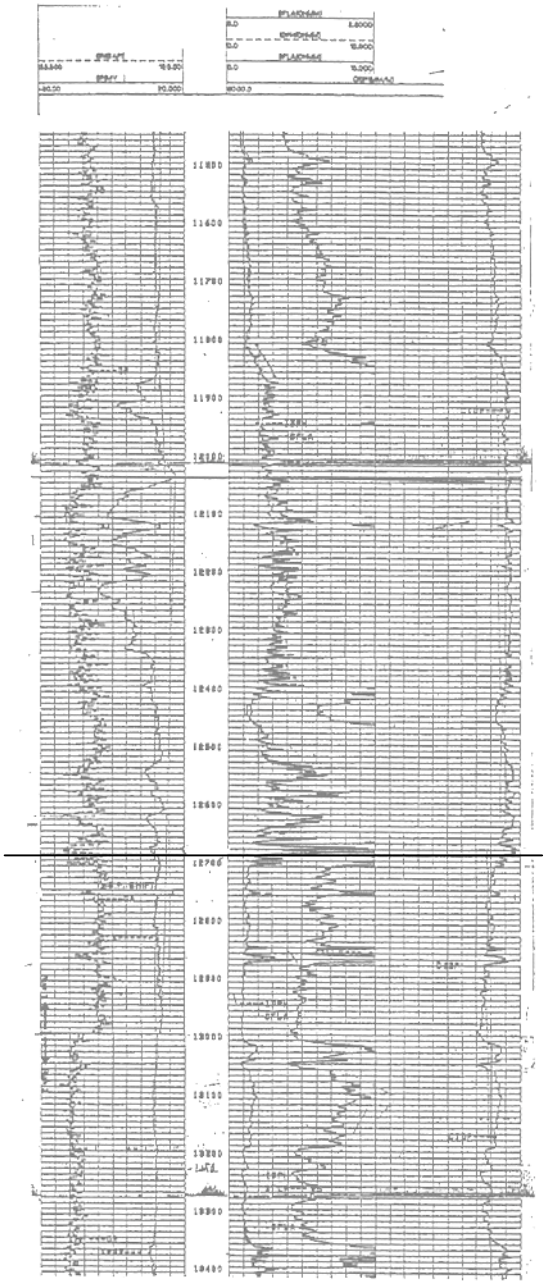

Figure 6.7 (b). Well log response to the overpressured zone in well 6032 #2.

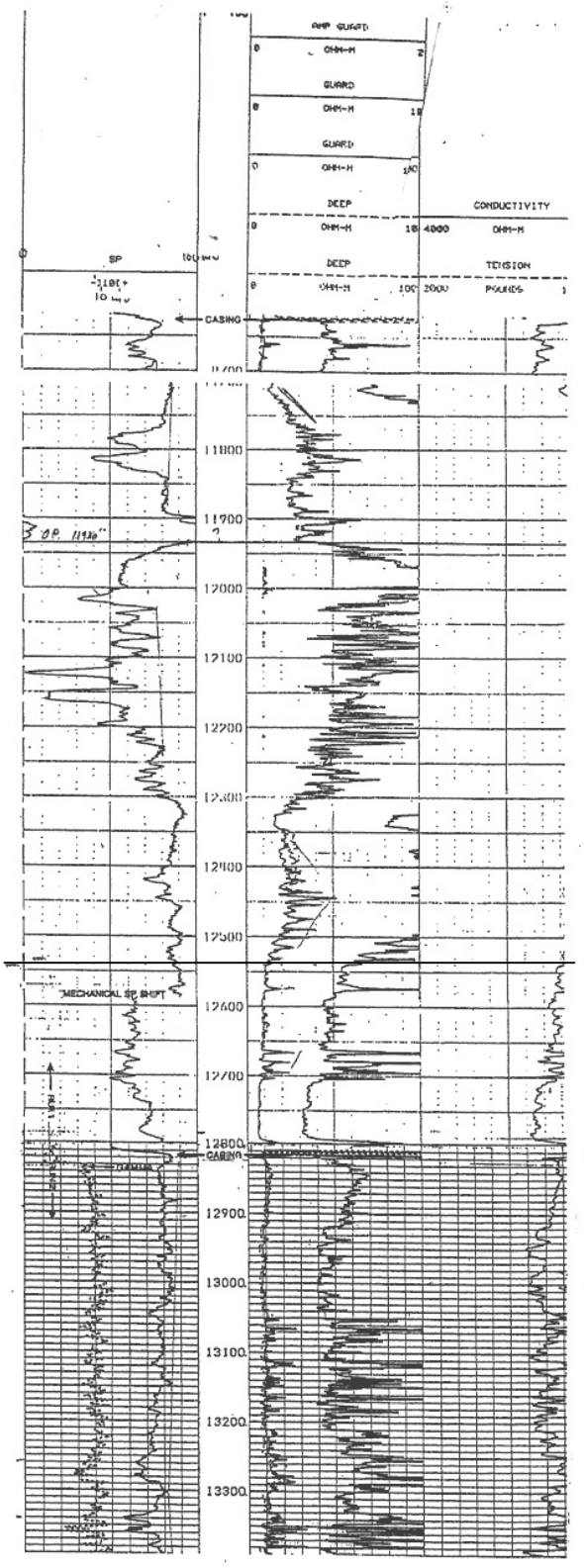

Figure 6.7 (c). Well log response to the overpressured zone in well 6032 #1.

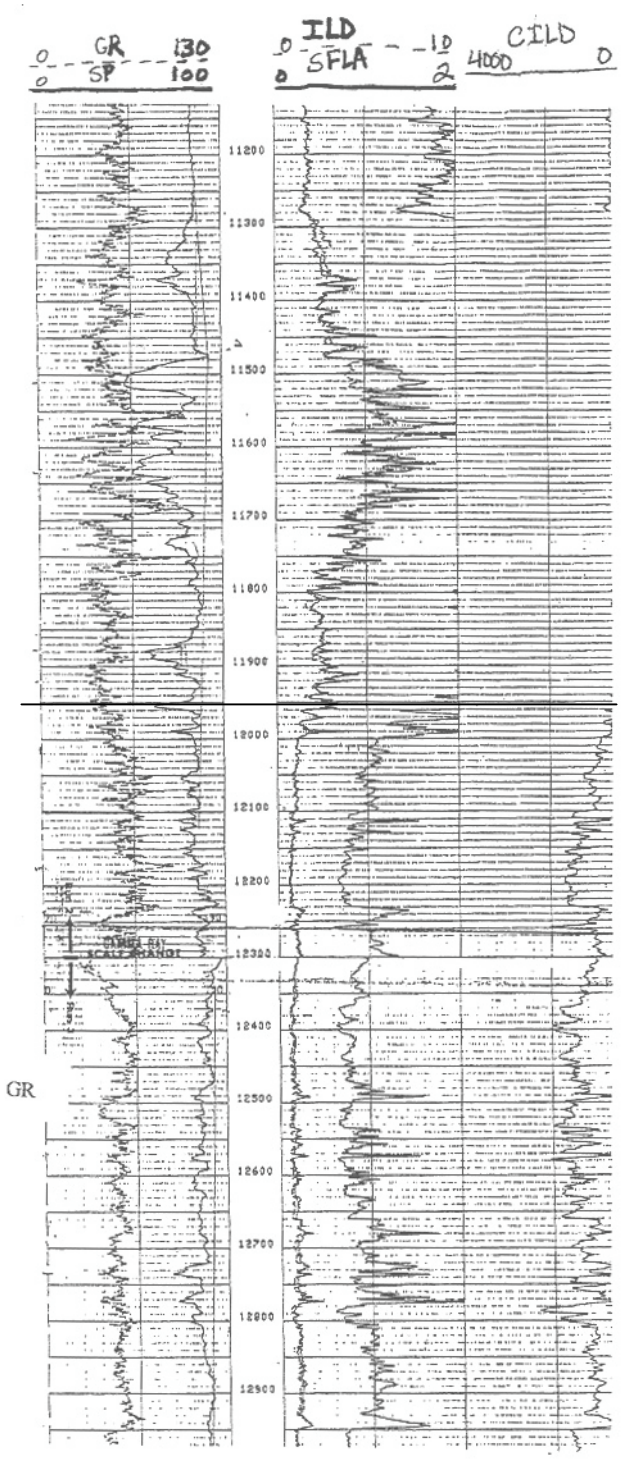

Figure 6.7 (d). Well log response to the overpressured zone in well 79413.

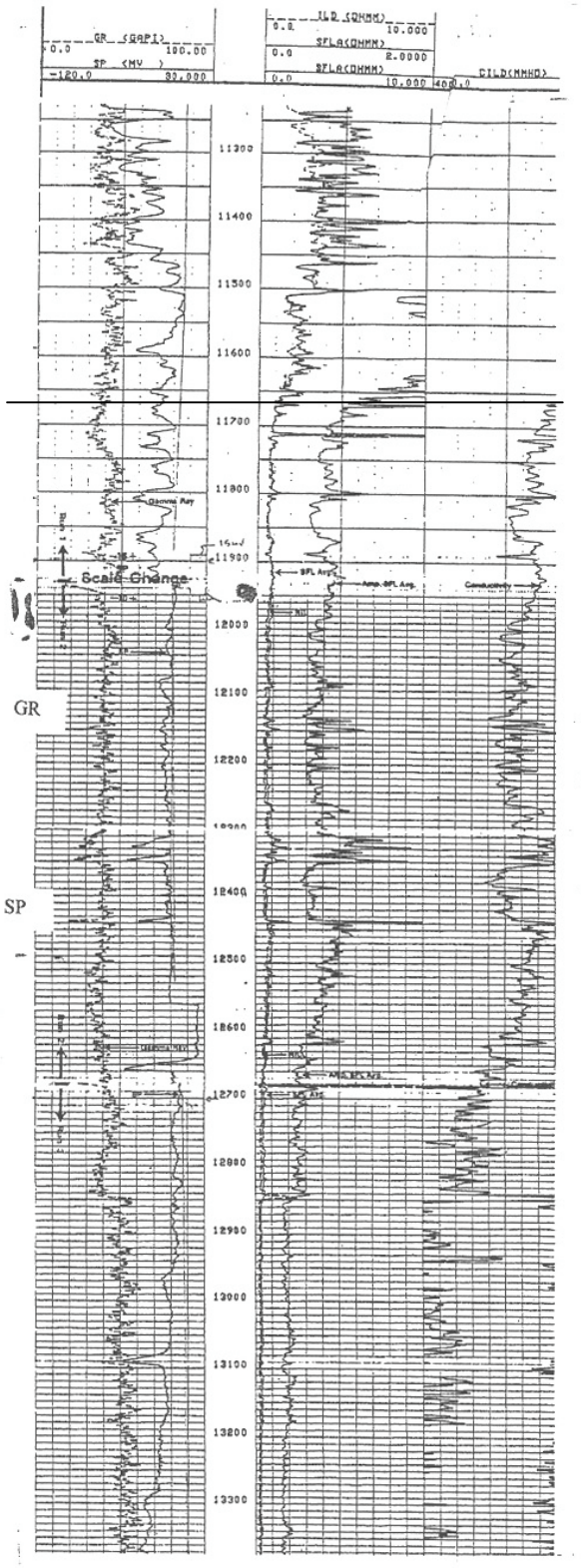

Figure 6.7 (e). Well log response to the overpressured zone in well 88562.

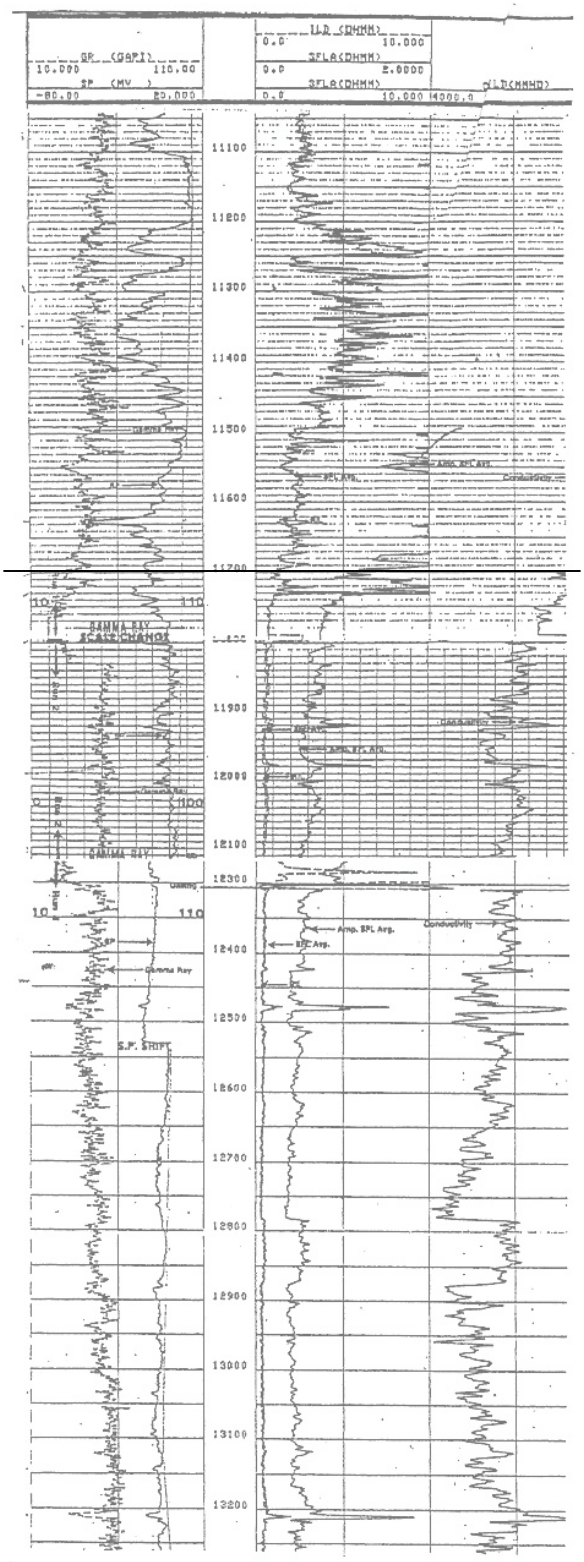

Figure 6.7 (f). Well log response to the overpressured zone in well 5169.

curves shift to the left as overpressure is encountered in a well, representing a decrease in resistivity. Conductivity response to overpressuring is typically a shift in the log curve to the left as well, but, because of the convention used to represent the conductivity scale, this deflection represents an increase in conductivity.

CHAPTER 7: DISCUSSION

7.1. Nature of the Pressure Seal at the Top of Overpressure

Pressure seals are thought to be produced by: 1) thick successions of low permeability sediments, 2) capillary forces, and/or 3) diagenesis. Of these three processes, diagenesis appears to be the primary cause of the development of the pressure seal at Matagorda Island 519 with a thick region of normative calcite enrichment observed within the pressure seal, and a prominent increase in normative quartz just above the top of overpressure. Normative mineralogy results show that calcite enrichment begins above the top of overpressure, and this enrichment trend continues with depth into overpressure, and quartz enrichment occurs just above the top of overpressure, and quartz is depleted with depth below the top of overpressure (Figure 5.11).

Results from analysis of the petrophysical log show that the pressure seal corresponds to a thick zone of increased calcite cementation (Figure 4.9). In addition, drillbit transit time, calculated from rate of penetration data, shows an abrupt increase that corresponds to the depth of the pressure seal (Figure 4.10) and probably represents a tightly-cemented sequence.

The overpressure transition zone in the study area does occur within a relatively fine-grained zone approximately 200 m (650 ft) thick, but it is overlain by a thick sequence of Miocene interbedded sands and mudstones. This is unlike the overpressured section in south Louisiana, which is within a thick mudstone sequence (Hart et al., 1995; Nikiel and Hanor, 1999; Spears, 2000; Stump and Flemings, 2000).

Capillary forces could be contributing to the development of the pressure at Matagorda Island 519, although there is no direct evidence of this. Capillary forces are forces that prevent the interface between an aqueous fluid and a hydrocarbon fluid from

passing through a pore throat that is small in diameter (Figure 7.1). This interface would typically have the smallest possible surface area if undisturbed, and work must be done to deform the hydrocarbon-aqueous fluid interface in order to pass it through a small pore throat. The capillary pressure or force acts against the direction of fluid flow (Davis, 1994; Benzing and Shook, 1996; Shosa and Cathles, 1996; Ingram and Urai, 1999). Constriction of pore throat diameters due to cementation, and the enhanced wetting ability of saline fluids would enhance the capillary effect.

7.2. Vertical Pressure Compartments

Assuming that the fluid pressure data used in this study are accurate, there are potentially at least three overpressured compartments that are vertically bounded by pressure seals at Matagorda Island 519 (Figure 7.2). Plots of fluid pressure versus depth and fluid pressure gradient versus depth show that there is one major pressure transition interval at the top of overpressure and at least two more underlying minor overpressure transition intervals that occur in all wells in the study area. Zones of large increases in fluid pressure with depth are separated by depth intervals in which fluid pressure returns to more near the hydrostatic pressure gradient (Figure 7.2).

7.3. Lateral Pressure Seals

Maintaining overpressure requires three-dimensional sealing, with both vertical and lateral seals necessary. Analysis of structural cross-sections in the vicinity of the Matagorda Island 519 field (Morton et al., 1985) shows that numerous near-vertical faults are located in the Miocene section in this area. These faults have the potential for creating laterally isolated compartments (Figure 2.9). Precipitation of diagenetic cements within faults could potentially caused lateral sealing.

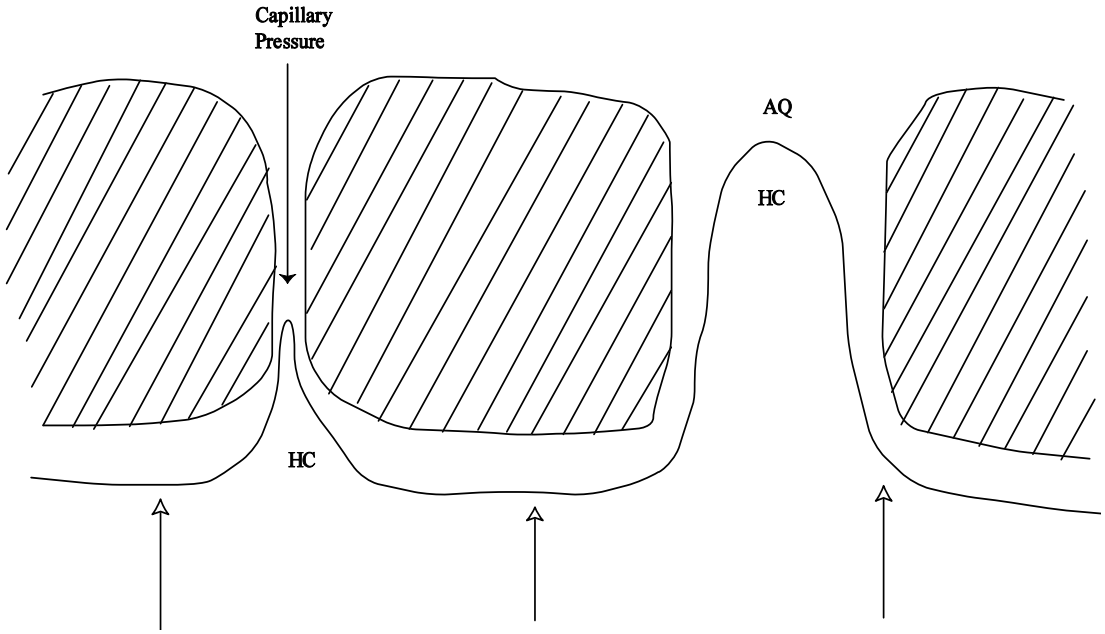

Figure 7.1. Capillary pressure prevents the interface between a hydrocarbon (HC) and an aqueous fluid (AQ) from moving through a small pore throat (left). Large pore throats are not subject to such intense capillary pressure and the HC-AQ interface moves more freely through large pore throats. Unshaded arrows indicate direction of fluid flow involving the HC-AQ interface.

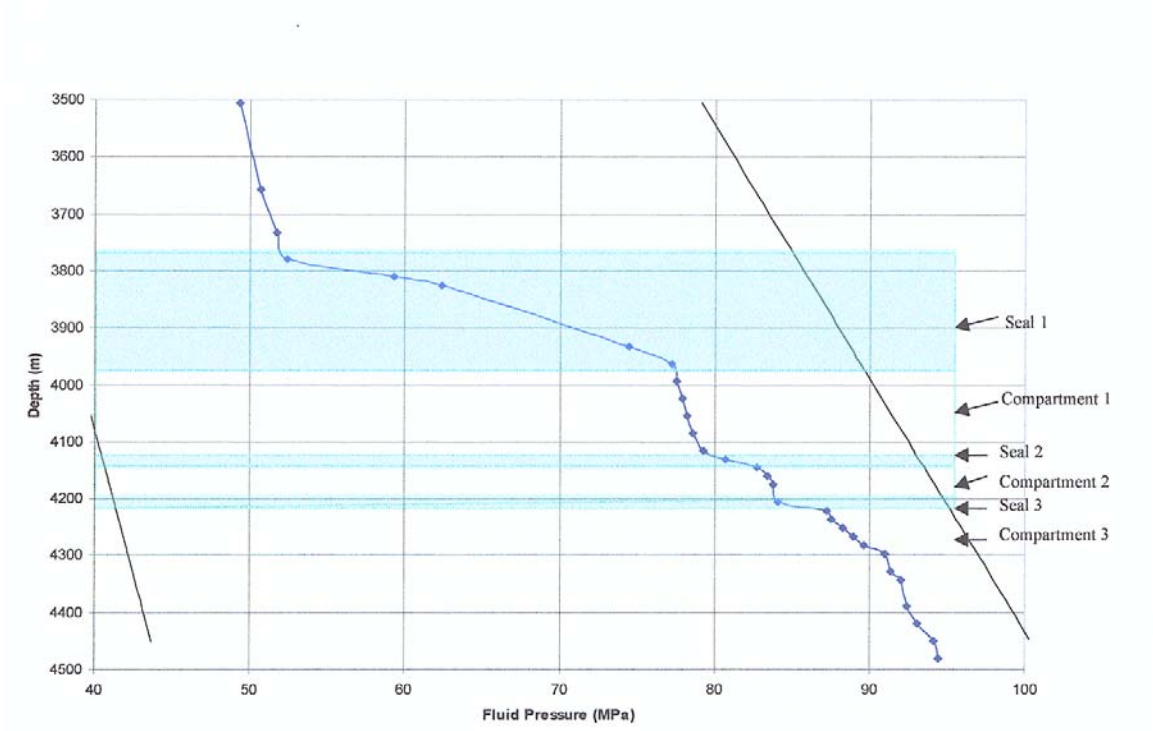

Figure 7.2. Illustration of the three pressure compartments and associated pressure seals at Matagorda Island 519. Fluid pressure data is from well 6032 #1.

7.4. Comparison with Amoco research on Overpressuring at MI 519

The locations of three potential vertical pressure compartments proposed in this study on the basis of changes in fluid pressure gradient roughly correlate to the locations of compartments or intervals B, C, and D proposed by Amoco. However, the locations of each individual compartment and seal as determined based on fluid pressure gradients differ from the Amoco compartments. Compartment A identified by Amoco (Brewster et al., 1998; Klein et al., 1998) was not identified as an overpressured compartment in this study because this region did not contain a sharp increase in the fluid pressure gradient. Compartment B roughly corresponds to the pressure seal identified in this study. Compartment C roughly corresponds to compartment 1. Compartment D roughly corresponds to compartments 2 and 3, although the base of compartment 3 is unknown and pressure seal 2 from this study is not identified within compartment D of Amoco.

As shown in Figure 2.24, the percentage of expandable layers of smectite-illite decreases in a uniform fashion with depth into overpressure. This evidence supports the hypothesis that conversion of smectite to illite, known as clay mineral dewatering, may be responsible in part for generating overpressure at Matagorda Island 519. The ratio of smectite to smectite + illite was plotted against depth in this study in order to determine whether results from MUDNORM provided similar trends in smectite enrichment and depletion with depth to that shown from Amoco research. Because enrichment smectite determined from simulations one and two of MUDNORM appeared inconsistent with regional averages, a third simulation of MUDNORM was performed. Figure 7.3 shows that trends for both smectite and illite enrichment and depletion from the third simulation of MUDNORM are similar to that of Amoco.

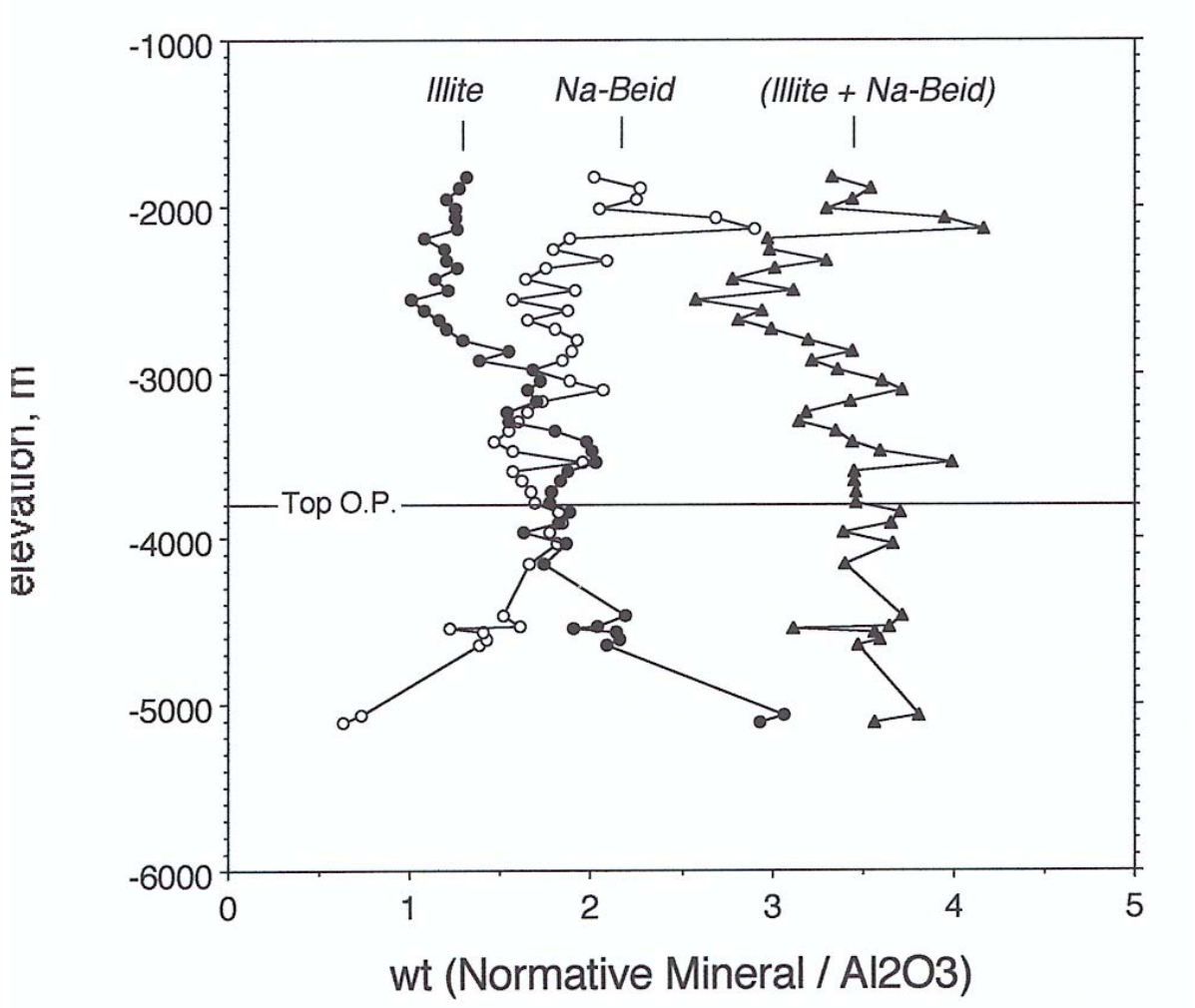

Figure 7.3. Ratio of normative weight percent smectite to smectite plus illite times 100 versus depth at Matagorda Island 519. The top of overpressure is indicated with a solid line.

7.5. Comparison with Other Previous Research on Overpressuring

The occurrence of overpressured compartments identified from fluid pressure versus depth profiles at Matagorda Island 519 is similar to compartmentalized overpressuring in the Cook Inlet fields of Alaska (Hunt, 1990). Here, pressures follow the hydrostatic pressure gradient from the surface to a depth of approximately 10,000 ft (3000 m) (Figure 1.3). The pressure seal in this area occurs in a depth interval of high fluid pressure (gradient) from 10,000-14,000 ft (3000-4300 m). An overpressured compartment is inferred to exist in the region below the pressure seal, in which fluid pressure returns to the hydrostatic gradient. Precipitation of diagenetic cements, such as calcite, at the pressure seal in all wells at Matagorda Island 519 is consistent with previous research documenting diagenetic bands of calcite in association with pressure seals (Al-Shaieb et al., 1994).

7.6. Causes of Overpressure

7.6.1. No Evidence for Significant Compaction Disequilibrium at MI 519

Overpressuring due to compaction disequilibrium is common in the central Gulf of Mexico basin, as a result of the rapid sedimentation associated with the Mississippi River depositional system (Dickinson, 1953 *in* Deming, 2002; Bredehoft and Hanshaw, 1968; Bethke, 1986; Bredehoft et al., 1988; Mello et al., 1994; Morse et al., 1997; Deming, 2002). Shales are undercompacted because they did not have sufficient time for pressure equilibration, due to rapid burial. Overpressure is indicated by a reversal in the normal compaction curve (Figure 3.2), and can be observed on plots of shale conductivity and shale porosity versus depth (Figure 3.3) for Gulf Coast shales. Shale porosity typically shows an increase below the top of overpressure due to undercompaction (Hart et al., 1995; Stump and Flemings, 2000). An example of compaction disequilibrium at Eugene Island 330 (Hart et al., 1995) is shown in Figure 7.4.

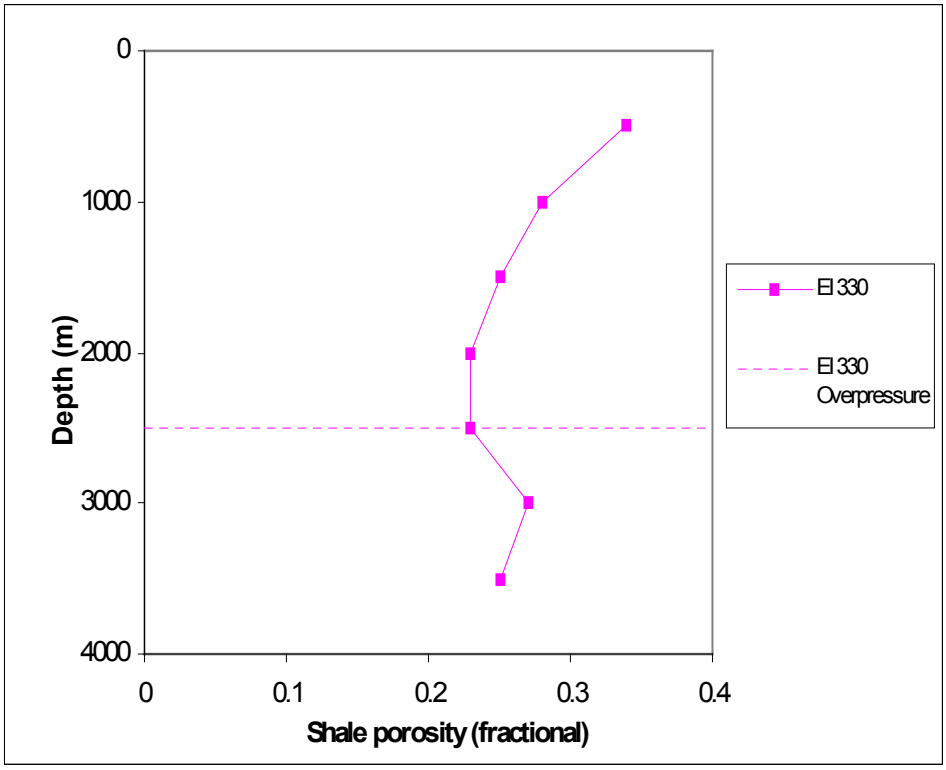

Figure 7.4. Compaction disequilibrium is illustrated with the shale porosity versus depth curve for Eugene Island 330 (from Hart et al., 1995). The top of overpressure at EI 330 is indicated with a dashed line. An abrupt increase in shale porosity corresponds to the top of overpressure.

Calculated shale porosity versus depth for Matagorda Island 519 (Figure 4.23) does not show evidence of significant undercompaction that corresponds to the overpressured zone, as is typically seen in the central Gulf of Mexico. Figure 7.5 compares shale porosities at Matagorda Island 519 to those of Eugene Island 330 in the central Gulf of Mexico to highlight the differences in shale porosity patterns at overpressure in these two areas.

On the basis of these results, compaction disequilibrium does not play a major role in the development of overpressures in this study area. The lack of influence from compaction disequilibrium at Matagorda Island 519 is consistent with low post-Miocene depositional rates in this field (Figures 4.4 -4.6). These low post-Miocene depositional rates at Matagorda Island 519 are consistent with reports in Galloway et al. (2000) of a shift in major sediment dispersal axes away from the Texas Gulf Coast and toward the central Gulf of Mexico as the Mississippi River system began to develop in the Middle to Late Miocene. Further research is necessary to determine how Matagorda Island 519 compares with other areas of the northwest Gulf of Mexico in terms of the lack of influence from compaction disequilibrium on overpressuring.

7.6.2. Possible Causes of Increased Fluid Pressure at MI 519

If compaction disequilibrium, resulting from undercompacted shales, is not the major force contributing to increased fluid pressures in this study, then some other force or combination of forces must be responsible for increasing fluid pressures at Matagorda Island 519. Possible forces that are responsible for causing increased fluid pressures at the Matagorda Island 519 field include aquathermal pressuring, osmotic diffusion, clay mineral dewatering, and petroleum generation. It is possible from the available information to eliminate some of these forces as being primarily responsible for creating overpressuring at Matagorda Island 519.

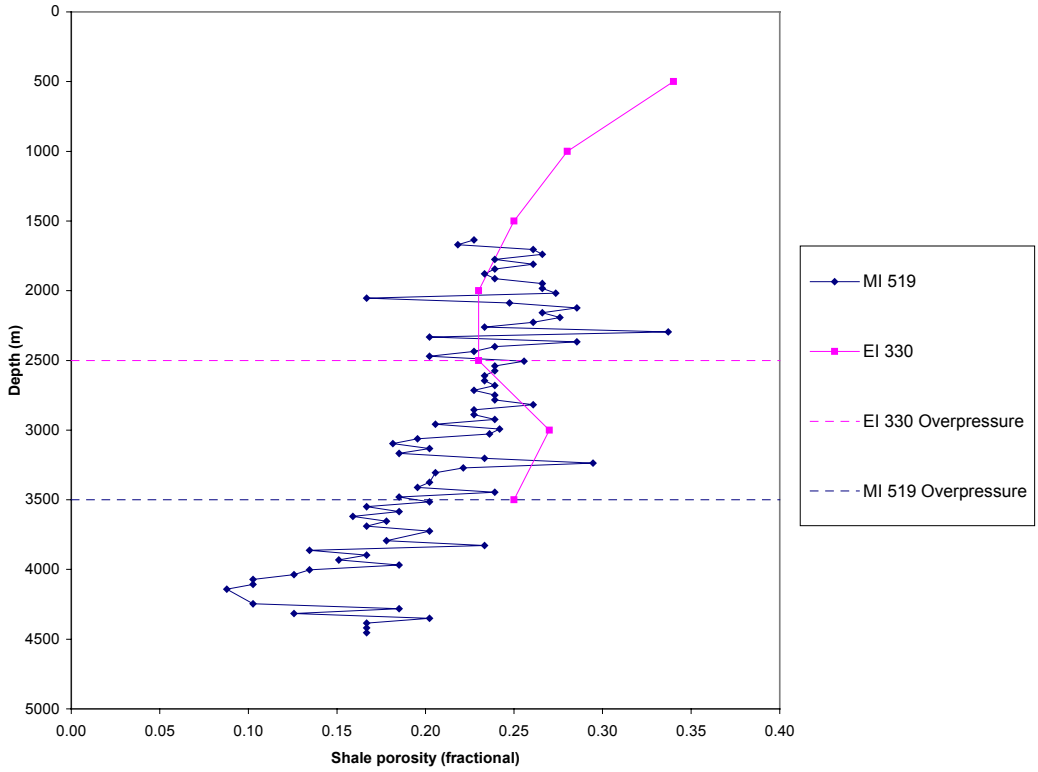

Figure 7.5. Comparison showing calculated shale porosity from Matagorda Island 519 and shale porosity from Eugene Island 330 in the central Gulf of Mexico from Hart et al. (1995). The approximate location of the top of overpressure is shown for each field. Compaction disequilibrium plays a key role in the development of overpressure at EI 330, whereas MI 519 does not show evidence of a reversal in shale porosity that corresponds to the top of overpressure.

Aquathermal pressuring has been reported as a mechanism that causes increased fluid pressure along the Texas Gulf Coast (Barker, 1972; Dutta, 1983). According to Prensky (1992) zones of overpressuring can be detected with analysis of the temperature gradient because sharp breaks in the thermal gradient occur at the top of overpressured reservoirs. The increased water content in overpressured shales, due to undercompaction and/or clay diagenesis, results in an increase in geothermal gradient (Prensky, 1992). The resulting "dog-leg" in the geothermal gradient may serve as a predictor of overpressuring (Lewis and Rose, 1970; George, 1970; Jones, 1975, and Pilkington, 1988, *in* Prensky, 1992).

According to Dutta (1983), the geothermal gradient plays an important role in shale overpressuring because the magnitude of overpressure increases as temperature rises, which causes a large drop in effective stress. At Matagorda Island 519, however, there has essentially been no subsidence and no significant increase in temperature since the end of the Pliocene, which is when overpressure is believed to have developed here. Thus, aquathermal pressuring can be ruled out as a primary cause of overpressuring at Matagorda Island 519.

The role of osmotic diffusion of fluids through semipermeable strata into sediments containing more saline fluids in the generation of overpressuring within the Gulf of Mexico is described in Hanor (1987). Osmotic diffusion is unlikely the cause of overpressuring at Matagorda Island 519 because fresh waters underlie the pressure seal at this field. Water should thus diffuse upward through the pressure seal into the more saline waters, which would effectively lower pressure.

Clay mineral dewatering, especially in the conversion of smectite to illite, during burial diagenesis in low permeability sediments is considered by many authors to be a major factor influencing overpressure development in sedimentary basins (Hanshaw and Bredehoft, 1968; Al-Shaieb et al., 1994; Awwiller, 1993; Land et al., 1997; Lynch, 1997). Clay mineral

dewatering may be playing a major role in the development of increased fluid pressure at Matagorda Island 519. According to XRD and normative mineralogy results from this study, illite is gained and smectite is lost within the overpressured zone in the study area (Figures 5.8 and 5.11), which is evidence of clay mineral dewatering. Results from this study are consistent with results from previous research that clay mineral dewatering, namely the transition from smectite to illite, is a possible cause of increased fluid pressures along the Texas Gulf Coast (Lynch, 1997).

Petroleum generation has been shown to contribute to the development of increased fluid pressure, as hydrocarbons are converted into liquids and gases (Barker, 1990; Neuzil, 1995). Petroleum generation presumably occurs in the much deeper sections underlying the overpressured zone at Matagorda Island 519. In order to determine whether or not petroleum generation contributes to overpressuring, evidence of hydrocarbon gas within the pressure seal is needed. This evidence could be found indirectly from well log analysis, or directly from additional data, such as core and/or fluid samples from within the overpressured zone at Matagorda Island 519.

Future research is necessary to determine which of these forces plays a major role in the development of overpressuring in this study area. Evidence presented in this study shows that osmotic diffusion is unlikely the cause of overpressuring at Matagorda Island 519, while clay mineral dewatering is most likely the major contributor to overpressuring at this field. However, further study is needed to investigate the role of aquathermal pressuring and petroleum generation in the development of overpressuring at Matagorda Island 519.

7.7. Diagenesis

7.7.1. Mudstone Diagenesis as an Open System Process

There has been extensive debate in the literature on whether shales behave as open or closed geochemical systems. Results from this study support researchers such as Lynch (1997) and Land and Milliken (2000), who proposed that mudstone diagenesis is largely an open system process in which mass is exchanged between mudstones and adjacent sandstones. If mudstone chemistry and mineralogy were initially vertically uniform, as assumed by previous workers in the northwest Gulf of Mexico (Awwiller, 1983; Taylor and Land, 1996; Lynch, 1996, 1997; Land et al., 1997; Lynch et al., 1997; Land and Milliken, 2000), then there must be some process responsible for the presently observed vertical heterogeneity in mudstone chemistry and mineralogy at Matagorda Island 519. Mineralogic evidence suggests that mudstones act as open geochemical systems at Matagorda Island 519, and exchange of diagenetic components has occurred.

Normative mineralogy results suggest that enrichment and depletion trends in minerals such as calcite, quartz, and illite correlate with changes in lithology that occur in connection with the pressure seal. Sands occur at and above the seal and mudstones occur within and below the seal (Figures 4.4 - 4.7). Calcite and illite in mudstones show relative enrichment with depth into the overpressured zone, while quartz shows relative enrichment above the pressure seal, and relative depletion at the pressure seal and within the overpressured zone (Figure 5.11). Smectite appears to be lost with depth into overpressure. Elemental mobility trends at Matagorda Island 519 have been determined from analysis of sediment bulk chemistry. The most mobile elements at this field include Ca, Fe, and Na, while the most immobile element is Al, followed by Ti, Y, and Zr (Figures 5.3 and 5.6).

7.7.2. The Role of Diagenesis in Overpressuring

Mineralogic evidence suggests that diagenetic reactions, such as precipitation of calcite and conversion of smectite to illite, are contributing to the formation of a pressure seal and overpressuring at Matagorda Island 519, as described previously in section 5.1. These results are consistent with previous research proposing that diagenetic reactions, such as conversion of smectite to illite and precipitation of calcite cements are responsible for creating overpressuring and pressure seals in sedimentary sequences along the Texas Gulf Coast (Awwiller, 1993; Land et al., 1997; Lynch, 1997; Brewster et al., 1998; Klein et al., 1998).

7.8. Aqueous Fluids/Formation Waters and Fluid Flow

Aqueous fluid or formation water characteristics, such as salinity, provide evidence of large-scale fluid flow within the Matagorda Island 519 study area, as well as evidence for fluid mixing. Mixing of fluids of variable salinity may be responsible for precipitating diagenetic cements, such as calcite, that contribute to overpressuring at Matagorda Island 519. In addition to salinity data, fluid analyses from two fields near Matagorda Island 519, Doubloon and Picarron in the Corsair Trend (Figure 2.26), are discussed as they may represent the most reasonable estimates of pore fluid compositions at Matagorda Island 519.

Connate salinity estimates ranged from seawater salinity to brackish to near freshwater during the Miocene and younger intervals of Matagorda Island 519 at the time of deposition. Estimated pore fluid salinities at Matagorda Island 519 show that present-day salinities are much greater than seawater salinities, in the range of hypersaline conditions throughout the study area. However, there are no significant salt structures in the vicinity of the Matagorda Island 519 field. Thus, dissolution of salt from a large salt body can be considered negligible within this study area.

At Matagorda Island 519 salinity versus depth plots show that brines and fresher waters have been present and have mixed. Molecular diffusion most likely occurred in the overpressured zone at Matagorda Island 519, due to low fluid velocities and low permeabilities. Because of the presence of a shallow lens of freshwater that overlies a dense brine regime, topographically-driven flow associated with thermohaline circulation most likely occurred in the shallowest section.

Transporting of fluids containing dissolved salts from onshore to offshore is a possible means by which highly saline fluids have developed in the Lower Miocene section at Matagorda Island 519. Salinity evidence suggests that the potential exists for fluid flow from onshore salt domes in Matagorda County into offshore Lower Miocene sediments at Matagorda Island 519.

7.8.1. Hydraulic Force Field Vectors as Indicators of Flow Field

Hydraulic force field calculations show that above the overpressured zone fluids flow between well 6032 #2 and well 5169 in slight northeastern orientation, approximately 0.1 degrees NE. The top of overpressure and corresponding pressure seal at Matagorda Island 519 dips towards the southwest from well 5169 to well 6032 #2 at an angle of approximately three degrees. Within the overpressured zone fluids flow from well 5169 to well 6032 #2 in a slight northwestern direction, approximately 0.8 degrees NW. These results prove that: 1) the direction of fluid flow is reversed once overpressure is encountered, and 2) within the overpressured zone fluids flow in a direction that is approximately perpendicular to the position of the top of overpressure.

7.8.2. Salinity Indicative of Large-Scale Lateral Fluid Flow

Estimated salinities are highly variable (<35,000 ppm to >150,000 ppm), with alternating zones of fluids with salinities of less than or equal to seawater and fluids of

salinities significantly higher than seawater (Figure 4.20). However, evidence shows that there are no significant salt structures near the Matagorda Island 519 field that could have provided a local source of NaCl to the field. According to the structural map for onshore Matagorda County, Texas (Figure 2.6), the nearest salt structures to Matagorda Island 519 are approximately 50-65 km (30-40 mi) away. Pore fluid salinity results combined with information on the relative locations of salt structures suggests that another mechanism has been responsible for creating the observed salinities at Matagorda Island 519. In order to create such elevated pore fluid salinites with no immediate source of salt, large-scale lateral fluid flow must have occurred in the Matagorda Island 519 area to transport dissolved salts into the field.

The presence of hypersaline pore fluids within this study area suggests that fluid flow involving long-distance transport of dissolved salts into the Matagorda Island 519 field has occurred. At least two different flow regimes are proposed to occur simultaneously at this field. An upper flow regime in the shallowest section appears to be dominated by topographically-driven flow in which fresh waters are driven from shallow onshore environments to deeper offshore areas and are overlying a thick sequence of more dense, saline brines. A lower flow regime of density-driven flow and molecular diffusion appears to be occurring at transition between dense, saline brines and less saline waters found at the overpressure transition zone in Matagorda Island 519. Both of these flow regimes, in which both freshwater and dissolved salts are transported over large lateral distances from salt domes presently in the onshore environment to the offshore environment are consistent with processes of advective-dispersive mixing that have been observed within the Gulf of Mexico basin.

The potential for large-scale lateral fluid flow at Matagorda Island 519 is supported the study by Funayama and Hanor (1995), in which salinity evidence proved that large-scale lateral fluid flow has occurred in the Eocene Wilcox Formation of central Louisiana, where no significant salt structures are found presently. The scale of fluid flow proposed in this study, on the order of 50-65 km (30-40 mi), is well within the range of fluid flow proposed by Funayama and Hanor, which is on the order of hundreds of kilometers. In the Funayama and Hanor study, density-driven fluid flow was proposed as the mechanism transporting dissolved salts from updip salt domes in northern Louisiana to their study area in central Louisiana.

Evidence of shallow lateral meteoric fluid flow from the onshore environment to the offshore environment supports Dutton (1994), in which topographically-driven lateral fluid flow is proven to occur in the groundwater system of Matagorda County. Dutton (1994) suggests that there is evidence of interaction between fluids of varying salinity, by showing that a freshwater lens has been transported from onshore to offshore into the marine environment, where fluids of seawater salinity are typically found.

7.8.3. Pore Fluid Salinity and Membrane Filtration

The observed salinity reversal with depth at the onset of overpressure in Matagorda Island 519 indicates that membrane filtration has not occurred at this field, because the salinity versus depth profiles in these wells are the opposite of salinity versus depth profiles expected from membrane filtration, according to Hanor (1994). Hanor (1994) showed that pore fluid salinity decreased with the onset of overpressure in the Gulf of Mexico, which proved that membrane filtration is not responsible for generating overpressure in such sedimentary sequences.

7.8.4. Origin of Picaroon and Doubloon Waters

As Taylor and Land (1996) have noted, the low Br/Cl ratios of the brines at Picaroon must reflect the dissolution of halite, rather than high Br/Cl bittern brines or the dissolution of high-Br, late-stage Mg and K evaporite minerals, as the source of chloride in the Picaroon formation waters. They invoke the long-distance vertical migration of Picaroon waters along faults from the Mesozoic section at depths of 3.0 to 4.5 km below the Corsair fault at Picaroon, or a total depth of 9 km. Taylor and Land note that salt is rare in the Texas offshore, but propose that the Middle Miocene sediments of the Corsair trend were deposited over a salt substrate that was mobilized by rapid sedimentation and subsequently evacuated, presumably during the Miocene and cite a study by Bradshaw et al. (1993). Based on burial history and the timing of ankerite crystallization, emplacement of brines began no earlier than 6 Ma ago.

Taylor and Land do not specifically address the origin of the waters at Doubloon. However, these waters are similar in salinity and chemical composition to waters which have originated by the dissolution of salt diapirs in the Gulf of Mexico basin (Hanor, 1994b). The nearest salt diapirs at Doubloon, Picaroon, and MI 519 are approximately 30 to 50 km updip, but there is ample evidence for the potential for regional, down-dip, density-driven fluid fluid flow of brine in the Gulf Coast.

The difference in the salinity of the formation waters at Picaroon and Doubloon can be explained as follows. Although both water types most likely originated as ca. 350 - 400 g/L halite-saturated brines produced by the subsurface dissolution of salt, there is a significant difference in the hydrogeology of how these saline formation waters were delivered to the Corsair trend in the Texas offshore. It is proposed here that the salinity of the Doubloon end member represents a significant mixing of diapir brines by kinematic

dispersion with ambient formation waters having the salinity of seawater, 35 g/L, or less, over fluid flow path lengths in the order of 10s of km. The mixing has produced waters of moderate salinity, 50-100 g/L.

End-member Picaroon brines probably had salinities of 250 g/L or more. Salinities this high are uncommmon around salt domes, even near the salt-sediment interface (e.g., Bennett and Hanor, 1987) because of dispersive mixing. These values, however, are characteristic of salinities of formation water above deeply-buried bedded salt, where there is density stratification of highly-saline formation water (Hanor, 1998). Focused flow of highly-saline fluid along faults would reduce the chance for mixing with ambient, lower-salinity waters and thus retain the original salinity of the precursor fluids.

7.9. Fluid Flow and Diagenesis

7.9.1. Picaroon and Doubloon Fields

Evidence presented by Taylor and Land supports the hypothesis that brines in the Miocene section at Picaroon Field represent formation waters that originated from deeper, Mesozoic sources. According to Taylor and Land, these Mesozoic-sourced fluids migrated upward through isolated conduits within the Corsair fault system during episodic fluid flow produced by release of overpressure. Brine chemistry data for Picaroon field is shown in Table 7.1.

The Taylor and Land (1996) model for calcite dissolution at Picaroon involves localized hydrodynamic and chemical processes. Acidity was produced by reverse weathering of kaolinite into Mg and Na silicates. Hot, acidic fluids from underlying Mesozoic sections were episodically injected along faults. They reacted with calcite and feldspar in lower temperature reservoir sands, resulting in dissolution of calcite and, to a lesser degree, feldspars. Removal of 6 to 15% calcite in more porous sands requires removal

of only 1.5 to 2% of the total bulk volume of calcite. Other possible dissolution processes may have involved organic acids, silicate hydrolysis, reverse weathering, and changes in P_{CO_2}. Taylor concluded that development of secondary porosity occurred at depths of between 2.6 and 3.0 km (8500 and 9850 ft) and that ankerite formed at depths of 3.0 to 5.1 km, (9850 to 16,800 ft). However, there is no reason from the information given that secondary porosity could not have developed later and at greater depth.

The reservoir sands at Doubloon and Plank do not show evidence for development of secondary porosity. The Doubloon waters are also very different in chemical composition, as noted above, and probably had a much different origin.

Silicate dissolution, as discussed by Taylor and Land, could explain the more radiogenic nature of the ankerite cements at Picaroon. However, the present day formation waters are even more radiogenic than the ankerites, and this may reflect continued diagenetic reactions involving silicates. For example, much of the conversion of smectite to illite and release of radiogenic Sr may have occured after precipitation of the ankerite.

Fluid flow involving transport of diagenetic cements, such as calcite, at Picaroon is believed to be driven by periodic release of overpressure during which fluid flow pulses occur along isolated fault conduits within the Corsair fault system. This hypothesis is consistent with the hypothesis proposed in this study that fluid flow is episodic and occurs along fault conduits and/or small fractures within the overpressured zone. Thus, brines at Matagorda Island 519 may also be sourced from deeper, Mesozoic sections. Large-scale upward fluid flow at Matagorda Island 519 has also been proposed by Amoco researchers (Brewster et al., 1998; Klein et al., 1998).

Table 7.1. Examples of brine compositions at Picaroon field, Corsair Trend, Offshore Texas (from Taylor and Land, 1996). Brine compositions at Matagorda Island 519 may be similar to those of Picaroon field.

Well:	A19 B-1	A19 D-2
Cl	147420	145360
Br	183	205
Total Alk.	210	230
Na	66900	65200
K	1980	1320
Ca	21200	22800
Mg	720	1040
Fe	438	312
TDS	243903	240400

7.9.2. Matagorda Island 519 Field

There is evidence for establishing potential relations between diagenesis and fluid flow at Matagorda Island 519. Calcite has been shown to increase in abundance at the pressure seal in this study area (Figures 6.10, 6.17, 6.24, and 6.31). Fluid mixing is invoked as the mechanism responsible for precipitating enough calcite to account for present accumulations. Large-scale transport is invoked to be responsible for the observed calcite cements at the pressure seal in Matagorda Island 519, which is consistent with previous researchers (Land, 1984, 1991; McManus and Hanor, 1993; Land et al., 1997; Lynch, 1997; Land and Milliken, 2000).

7.9.4.3. Fluid Mixing and Diagenesis

According to Morse et al. (1997), mixing of fluids of highly variable concentrations of total dissolved solids may potentially create waters of intermediate composition that are both supersaturated and undersaturated with respect to various mineral phases, thus inducing mineral diagenesis. Their focus was on a "…thermodynamic examination of the influences that the movement and mixing of basinal waters have on calcite dissolution and precipitation, (thus analyzing) the role of physical processes in driving chemical reactions involving carbonate minerals" (Morse et al., 1997).

Field studies in the south Louisiana Gulf Coast have provided evidence that several types of advective flow occur simultaneously within this portion of the Gulf of Mexico basin. Topographically-driven flow is occurring in the shallowest portion of this area to drive meteoric waters from elevations of 100 m (300 ft) or less to depths of up to a kilometer (3280 ft) in the subsurface over lateral distances of 10-100 km (6.2-62 mi) (Morse et al., 1997). This thermohaline circulation is thought to be driven by variations in fluid density caused by spatial variations in temperature and salinity. Underlying this zone of thermohaline

circulation is a zone of overpressure containing fluids of seawater salinity or less, in which the principal flow direction is up and laterally out of the overpressured section into overlying hydropressured sediments, with faults potentially acting as preferential conduits for upward flow (Morse et al., 1997).

Hydrodynamic dispersion, mixing resulting from differential velocity of the various components within a fluid, is an important physical process in sedimentary basins such as the Gulf of Mexico because it can produce fluids of varying composition, even in the absence of chemical reactions (Morse et al., 1997). Molecular diffusion occurs when a solute moves at different net velocities than adjacent water molecules due to chemical potential gradients, and kinematic dispersion occurs when small parcels of fluid of spatially varying composition are advected at different velocities through a porous medium, due to factors such as variable path lengths and/or slowing around grain surfaces (Morse et al., 1997). Molecular diffusion dominates at zero and low fluid velocities, and the rate of kinematic dispersion increases as fluid velocity and dispersivity increase (Morse et al., 1997).

Large-scale transport and large volumes of fluid are required to account for the volumes of diagenetic features, such as authigenic quartz and calcite cements in sedimentary basins such as the Gulf of Mexico. Mass-balance arguments for such transport and fluid volumes required for diagenetic features have been made by various workers (Land, 1984, 1991; McManus and Hanor, 1993; Land et al., 1997; Lynch, 1997; Morse et al., 1997; Land and Milliken, 2000).

The end member fluids chosen by Morse et al. (1997) to analyze the effect of mixing of end member basinal fluids of widely contrasting salinity on carbonate diagenesis are 1) a dilute solution whose composition is equivalent to dissolving calcite in pure water at a fixed and specified P_{CO2} and 2) highly saline waters having TDS values of up to 300,000 mg/L.

Major ion activity coefficients for 25°C and 1 bar were calculated by Morse et al. (Figure 7.6). Examples proved that mixing of meteoric waters and brines in the subsurface has the potential to produce carbonate cements and cause dissolution of carbonate minerals (Morse et al., 1997). Results showed that the P_{CO2} of meteoric water, when in equilibrium with calcite, has a strong influence on the volume of calcite cement that can precipitate, while the P_{CO2} of brine only has a minor influence of the volume of calcite cement that can precipitate, due to the high dissolved calcium concentrations demanding that the carbonate ion activity must remain small for brines (Morse et al., 1997).

The influence of temperature and pressure on the chemistry of subsurface waters with increasing depth, particularly the influence of overpressure, presented by Morse et al. (1997) is of interest to this study. Fractures occurring within overpressured zones that allow fluid flow to take place can result in a rapid pressure drop that can change the saturation state of a fluid with respect to carbonate minerals (Morse et al., 1997).

An example is presented in Morse et al. in which a 200,000 mg/L TDS brine at 100°C and 600 bars initially in equilibrium with calcite undergoes a drop in pressure to 300 bars and the resulting solution then becomes supersaturated with respect to calcite. The extent of supersaturation for different initial P_{CO2} values is shown in Figure 7.7, where a gradual increase in supersaturation from ~12 times to 19 times occurs with increasing P_{CO2} up to about 0.1 bars, followed by a rapid decrease in supersaturation to about 3 times at a P_{CO2} of 1 bar (Morse et al., 1997). This model suggests that supersaturation with respect to calcite should occur within the overpressured regime at Matagorda Island 519 if fluid flow occurs within fractures.

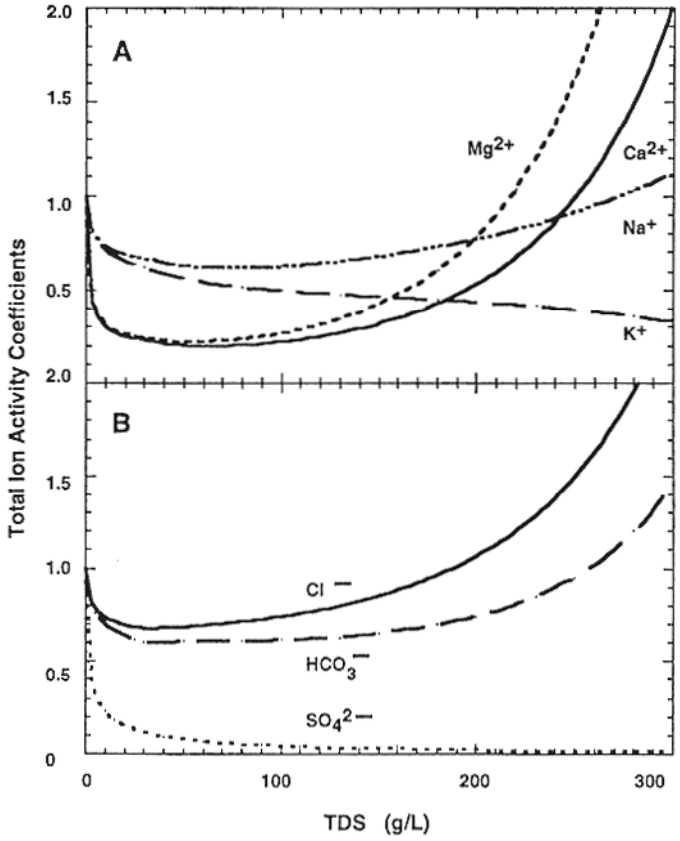

Figure 7.6. Major ion activity coefficients under STP conditions (25 °C and 1 bar) versus TDS (from Morse et al., 1997).

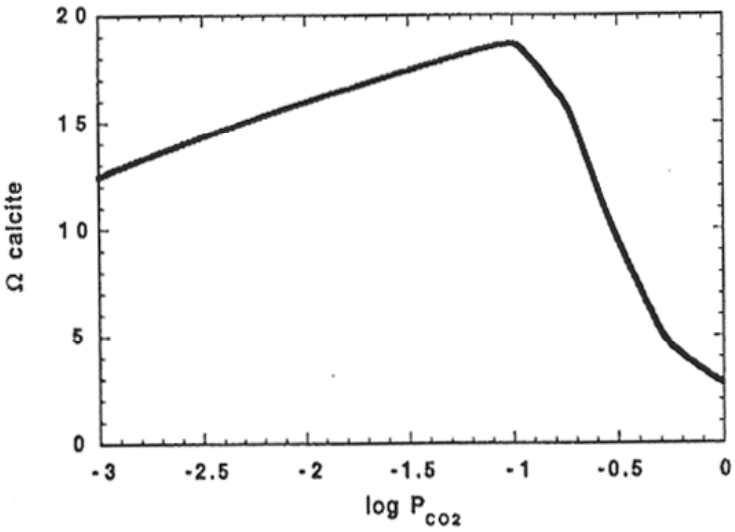

Figure 7.7. The influence of overpressure is shown on this plot of the supersaturation with respect to calcite of a 200,000 mg/L brine, initially in equilibrium with calcite at 100°C, 600 bars, and different initial P_{CO2} values resulting when pressure is reduced to 300 bars as a result of fluid flow in fractures within the overpressured zone (from Morse et al., 1997).

A detailed analysis of the role of reactive transport involving rock-buffered fluids of varying salinity is provided by Hanor (2001). According to Hanor (2001), sufficient volumes of diagenetic minerals such as calcite can theoretically be precipitated from initially conservative mixing of rock-buffered fluids of varying salinity with cation concentrations that are initially a function of physical mixing without reaction to account for the presently observed enrichment of mineral phases at Matagorda Island 519. Hanor (2001) concluded that large volumes of individual mineral phases could theoretically be dissolved or precipitated as a result this type of mixing without the need for the flow-through of large volumes of fluid, as fluid-mineral reactions attempt to rebuffer fluid compositions. Evidence from this study suggests that diagenetic cements at Matagorda Island 519 may have been transported into the area from distances far outside of the field, which is inconsistent with Hanor (2001).

7.9.4. Comparison with Sharp et al. (2001)

Based on the theoretical model of Sharp et al. (2001), calculated pore fluid salinities and permeabilities from this study suggest that diffusion is the most likely mechanism of solute transport at Matagorda Island 519. Sharp et al. (2001) predicted that diffusion will occur for the ranges of salinity, permeability, and thickness of the pressure seal calculated at Matagorda Island 519 (Figure 7.8). The focus of Sharp et al. (2001) was to prove that salinity reversals observed at overpressure transitions in the south Texas Gulf Coast are indicative of convective overturn. Evidence from pore fluid salinity versus depth profiles at Matagorda Island 519 showing a salinity reversal at the pressure seal is consistent with Sharp et al. (2001). However, there is no evidence that convection occurs at Matagorda Island 519.

7.10. Well Log Response to Overpressuring

There is a distinct signal associated with the pressure seal and overpressured compartments at Matagorda Island 519. In all wells the location of the pressure seal is marked by unique and consistent responses from the SP, gamma ray, resistivity, and conductivity logs (Figure 6.32). The observed pressure seal and corresponding overpressured compartments at Matagorda Island 519 are seen as increases in SP that appear to be consistent with the SP response for a shale, although slightly more negative than the shale base line.

Pressure seals are typically identified on SP logs as increased SP response. Overpressured zones are identified on gamma ray log curves as increases in the gamma ray log curve. The SP and gamma ray log responses typically increase due to increased shale content associated with overpressuring. Resistivity is known to decrease in response to overpressure (Rider, 1996). Conductivity log response to overpressure is widely known to manifest as an abrupt increase in conductivity as overpressure is encountered. This increase in conductivity is typically due to increased shale porosity in overpressured intervals (Rider, 1996), however, this is inconsistent with evidence presented for Matagorda Island 519 showing that shale porosity decreases with overpressure.

The pressure seal at Matagorda Island 519 is identified by an increased gamma ray log response (Figure 7.9). Resistivity logs show that the top of the pressure seal corresponds to a high-resistivity kick and that resistivity then generally decreases with depth into overpressure below the pressure seal for all wells (Figure 7.9). There are, however, several additional high-resistivity kicks that are observed in all wells within the overall decrease in resistivity. Conductivity response to the pressure seal at Matagorda Island 519

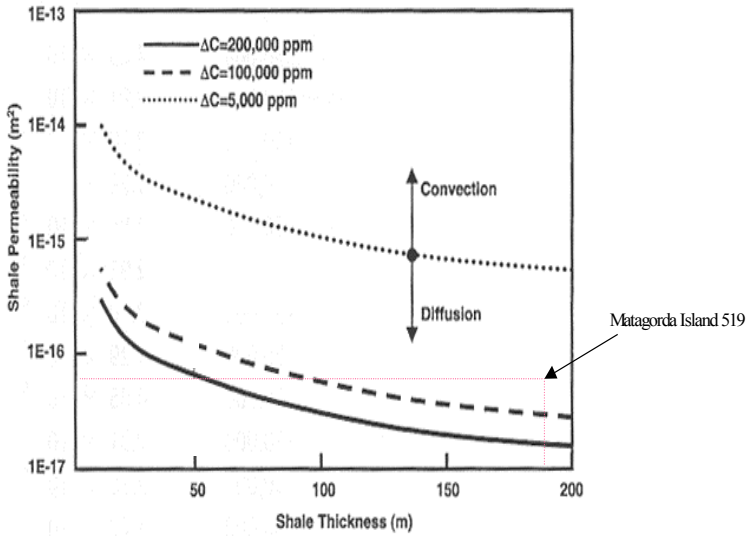

Figure 7.8. Based on the theoretical model presented by Sharp et al. (2001), diffusion is the most likely mechanism of solute transport at the overpressure transition zone in Matagorda Island 519 (modified from Sharp et al., 2001).

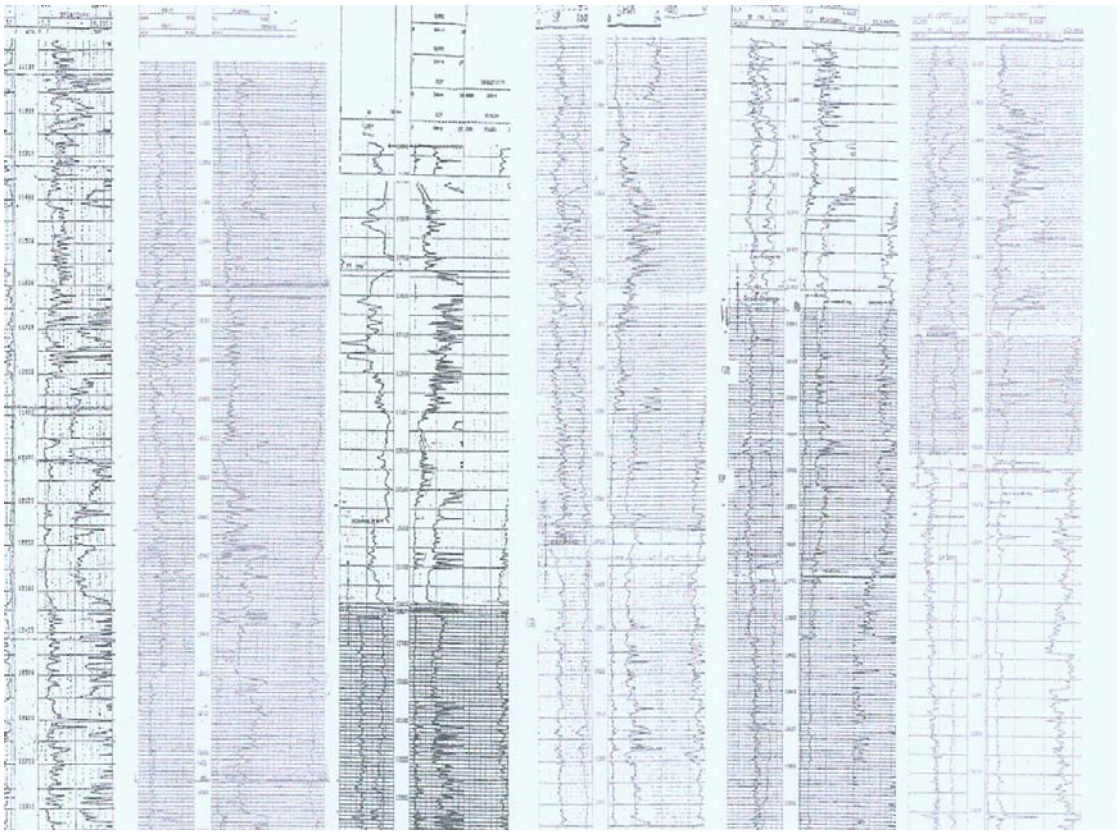

Figure 7.9. Well log response of all wells available for this study in Matagorda Island 519 to the pressure seal and overpressured zone. The top of overpressure and corresponding pressure seal are shown in each well, represented by the solid black line.

is represented by an increase with increasing depth into overpressure that correlates with the decreasing resistivity log response (Figure 7.9).

Neutron-density porosity logs were not available at the top of overpressure, thus, the observed response of porosity logs to the pressure seal is not described for the Matagorda Island 519 field. However, porosity was calculated from sonic log response. Shale porosity thus calculated is approximately 15-20% at the pressure seal, with an overall decrease in sonic transit time and porosity observed at the pressure seal (Figure 4.23).

If the pressure seal at Matagorda Island 519 is influenced by massively cemented calcite zones, then responses of the SP, gamma ray, resistivity, sonic, and neutron-density porosity logs should provide evidence for massively cemented calcite that corresponds to the top of overpressure. Figure 7.10 shows an example of the response of each of these types of logs to a massively calcite cemented zone from the West Hackberry field in Louisiana (McManus, 1991). Analysis of responses from SP, gamma ray, resistivity, conductivity, sonic logs within overpressure at Matagorda Island 519 are consistent with the response for massively cemented calcite.

At Matagorda Island 519 the resistivity log response at the pressure seal is consistent with the presence of a massively cemented zone. According to analysis of well log responses to a massively cemented zone at the West Hackberry field in Louisiana, massively cemented zones can cause resistivity spikes that are similar in appearance to high-resistivity hydrocarbon kicks (McManus, 1991). These high-resistivity kicks can be confirmed as cemented zones with analysis of neutron-density porosity logs that show low porosity within the cemented zone and analysis of cuttings to show cemented sands (McManus, 1991). Also, analysis of both the deep and medium range resistivity curves simultaneously can determine

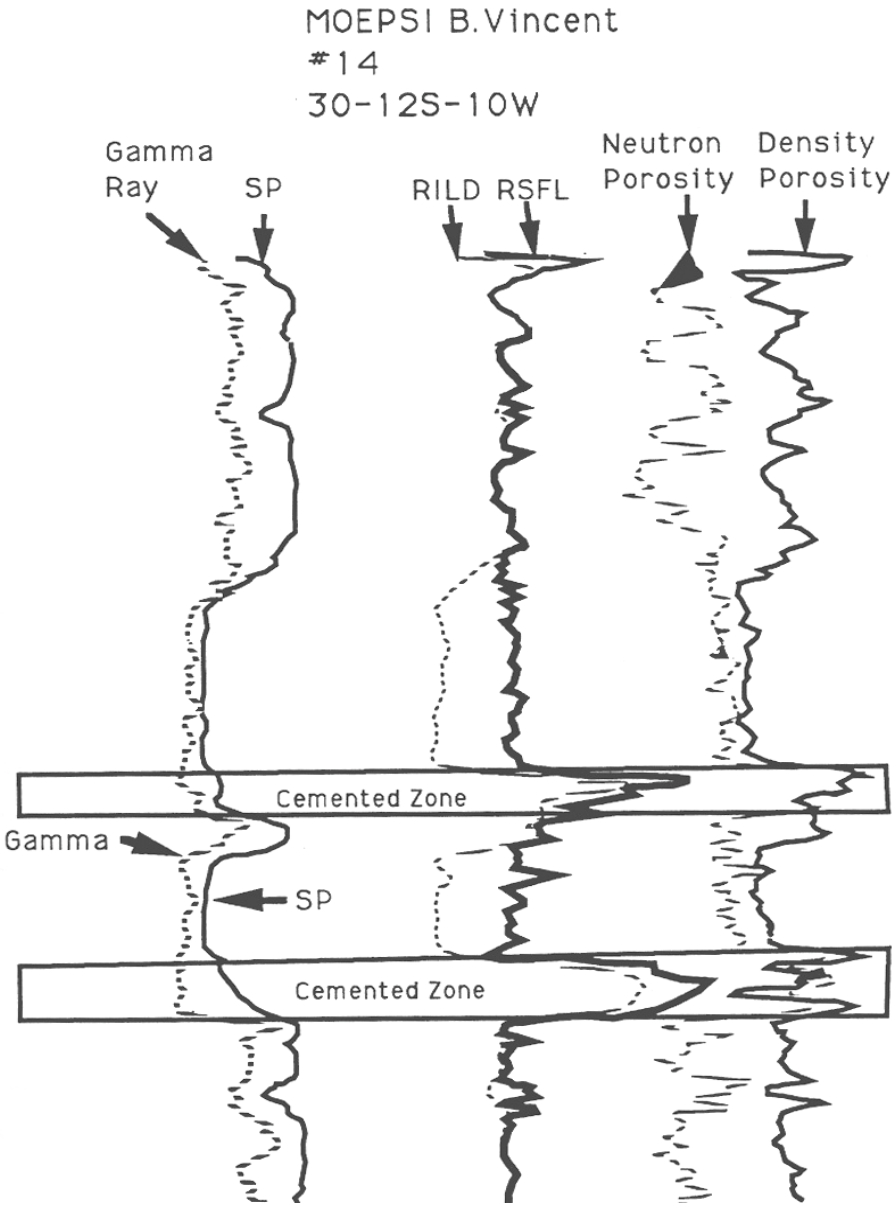

Figure 7.10. Typical response of gamma ray, SP, resistivity, neutron porosity, and density porosity logs to overpressure caused by a massively cemented zone (from McManus, 1991). Well log data is from the West Hackberry field in Louisiana.

whether the interval of interest is very salty, salty, fresh, tight, or is filled with hydrocarbons (Figure 7.11).

Brewster et al. (1998) and Klein et al. (1998) identified four overpressured compartments based on conductivity log response. These reports state that spikes of increased conductivity represent individual overpressured compartments at Matagorda Island 519. In this study the top of overpressure and associated pressure seal corresponds to an interval of increased conductivity relative to overlying sections (Figure 5.8), which is consistent with the findings of Amoco researchers. Spikes of increased conductivity within the overpressured zone below the pressure seal are observed in some of the wells in the Matagorda Island 519 field, however, a more detailed analysis is needed in order to provide conclusive determination regarding conductivity spikes and pressure compartments.

7.11. Conceptual Model for MI 519 Development

7.11.1. Stage 1

Stage 1 of the conceptual model for development of the Matagorda Island 519 field involves processes that have occurred from < 17 Ma (Figure 7.12). In Stage 1, haline-driven siliciclastic diagenesis, represented by reactions such as: $CH_2O + SO_4^{2-} + Ca^{2+} \rightarrow CaCO_3 + FeS_2$, drives early calcite cementation within two specific zones. Active deposition and subsidence occur from approximately 17-10 Ma. Diffuse, 50-km lateral flow transports fluids from updip salt domes, resulting in the introduction of 50-100 g/L brines.

7.11.2. Stage 2

By the end of the Pliocene (Stage 2) deep overpressure development occurs (Figure 7.13). Continued lateral flow from updip salt domes occurs during this stage. Stage 2 represents the onset of focused flow, which is responsible for transporting Mesozoic brines of high Pco_2 and TDS of ~200 g/L into the Miocene sections. Carbonate dissolution,

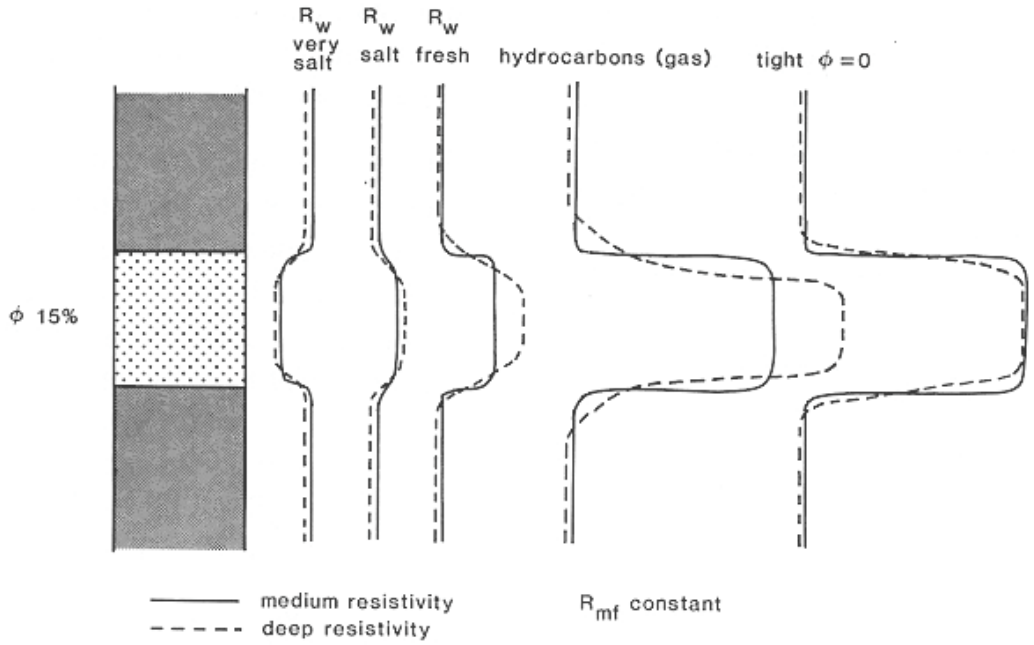

Figure 7.11. Analysis of the deep and medium range resistivity curves simultaneously can determine whether a given interval is very salty, salty, fresh, tight, or is filled with hydrocarbons (from Rider, 1996).

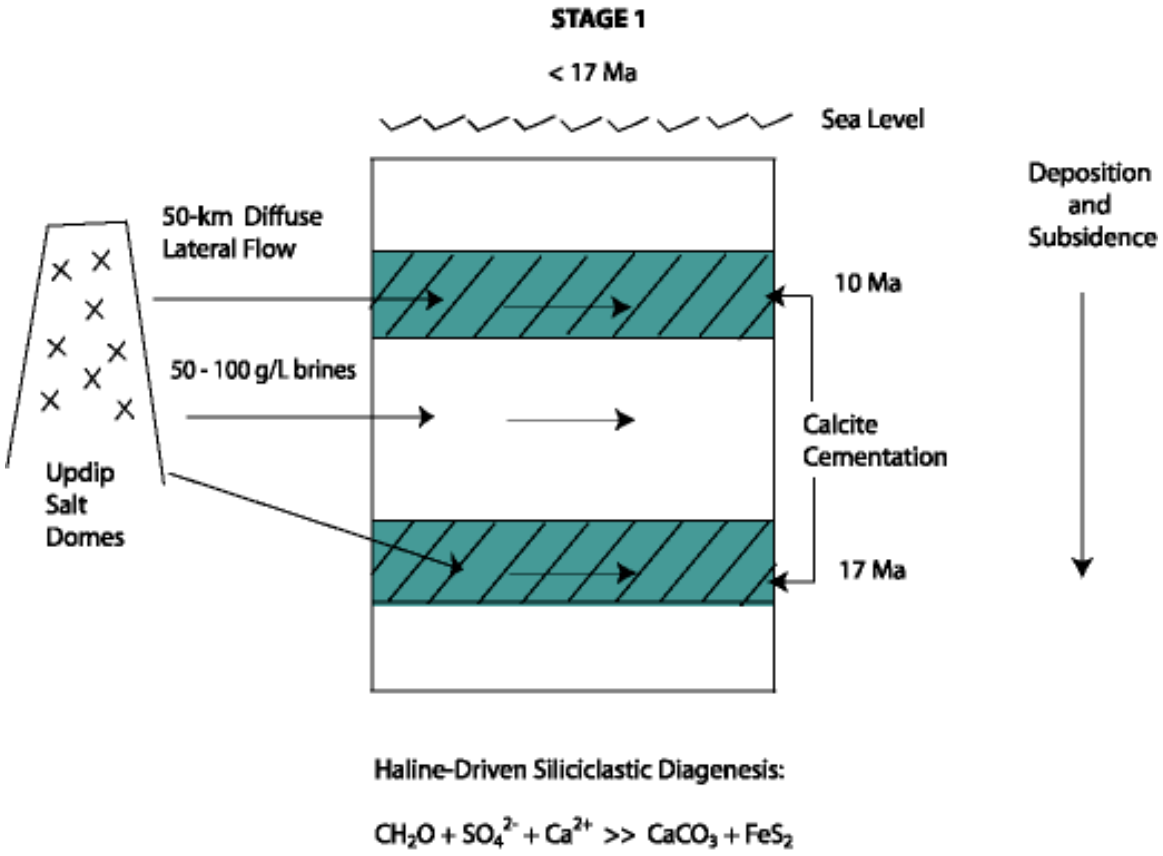

Figure 7.12. Stage 1. Haline-driven siliciclastic diagenesis drives early calcite cementation (<17Ma) within two specific zones (highlighted in figure), active deposition and subsidence occur from approximately 17-10 Ma, and diffuse 50-km lateral flow transports fluids from updip salt domes, resulting in 50-100 g/L brines.

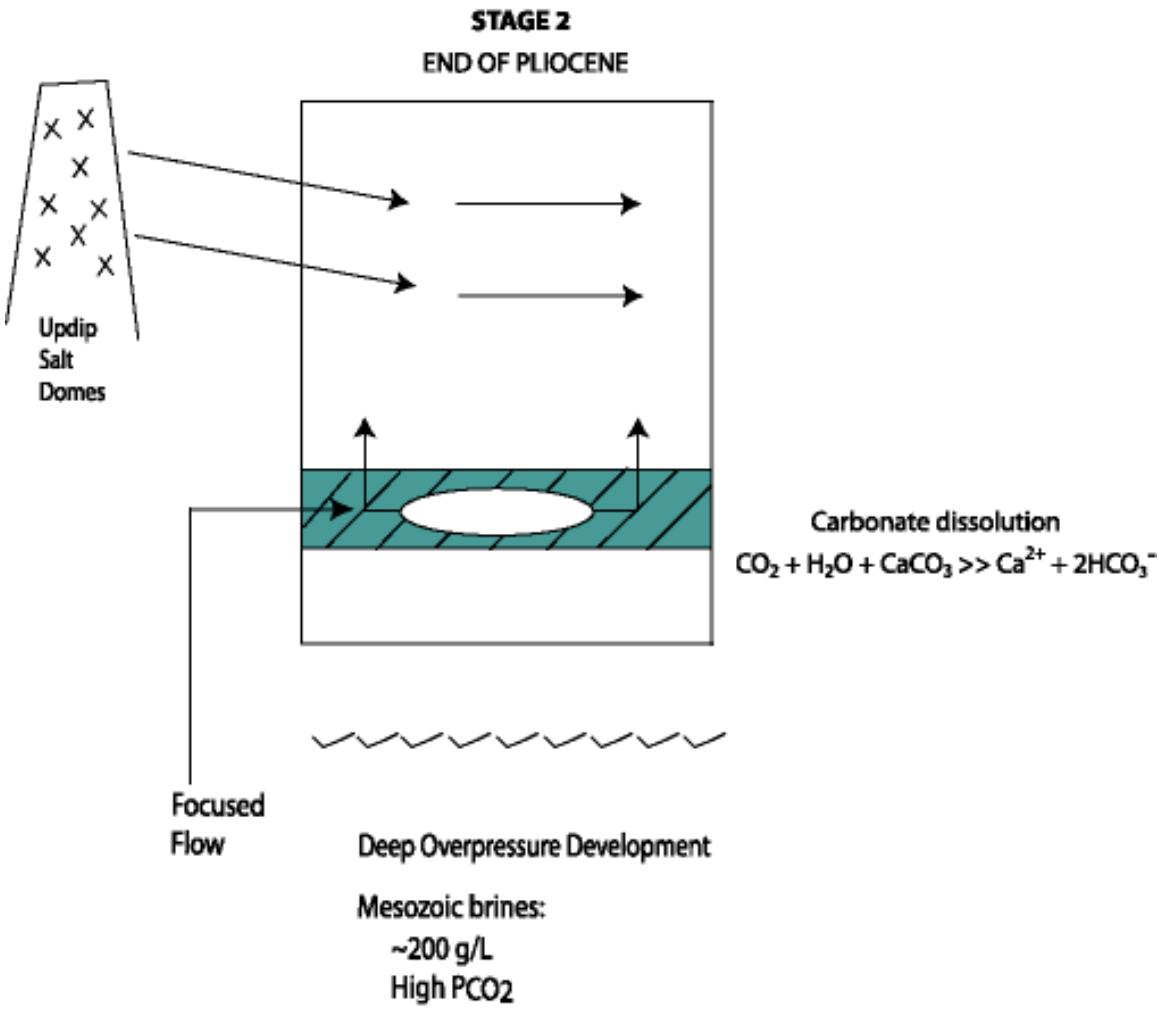

Figure 7.13. Stage 2. By the end of the Pliocene (~2.5 Ma), deep overpressure develops, along with carbonate dissolution, which contributes to generation of secondary porosity, and continued lateral flow from updip salt domes, as well as the onset of focused flow, which is responsible for transporting Mesozoic brines of high Pco_2 and TDS ~200 g/L.

represented by reactions such as: $CO_2 + H_2O + CaCO_3 \rightarrow Ca^{2+} + 2HCO_3^-$, contributes to generation of secondary porosity within the Miocene section during Stage 2.

7.11.3. Stage 3

Mixing of two different types of fluids occurs during Stage 3 (Figure 7.14). The upper fluid of 50-100 g/L TDS, low Ca^{2+}, and high HCO_3^- represents continued lateral flow from updip salt domes, and the lower fluid of ~200 g/L TDS, high Ca^{2+}, and low HCO_3^- represents vertical flow from underlying Mesozoic brine sources. This mixing contributes to calcite precipitation, which is responsible for forming the seal at Matagorda Island 519. Quartz precipitation probably occurred as a result of this type of mixing as well, with quartz enrichment just above the top of overpressured contributing to the effectiveness of the seal. Emplacement of Fe-calcite, ankerite, pyrite, barite, and polycrystalline quartz within the reservoir interval at Matagorda Island 519 may have occurred during or just after Stage 3. Emplacement of these mineral phases must have occurred prior to hydrocarbon generation, because wells in which these minerals are abundant have not produced hydrocarbons. Thus, these diagenetic cements have occluded early calcite dissolution void spaces and prevented generation of secondary porosity in some wells.

7.11.4. Stage 4

Stage 4 of the model represents processes that occurred after the seal was emplaced at Matagorda Island 519 (Figure 7.15). Hydrocarbon generation and overpressuring occurred during Stage 4, represented by reactions such as: Organic Matter $\rightarrow H_2O + CH_4$. During this stage hydrocarbons filled in calcite dissolution voids created from secondary porosity generation. At the end of Stage 4 the requirements for maintaining overpressure were present at Matagorda Island 519: 1) a mechanism to increase fluid pressure (hydrocarbon generation), and 2) a seal to trap excess fluid pressure.

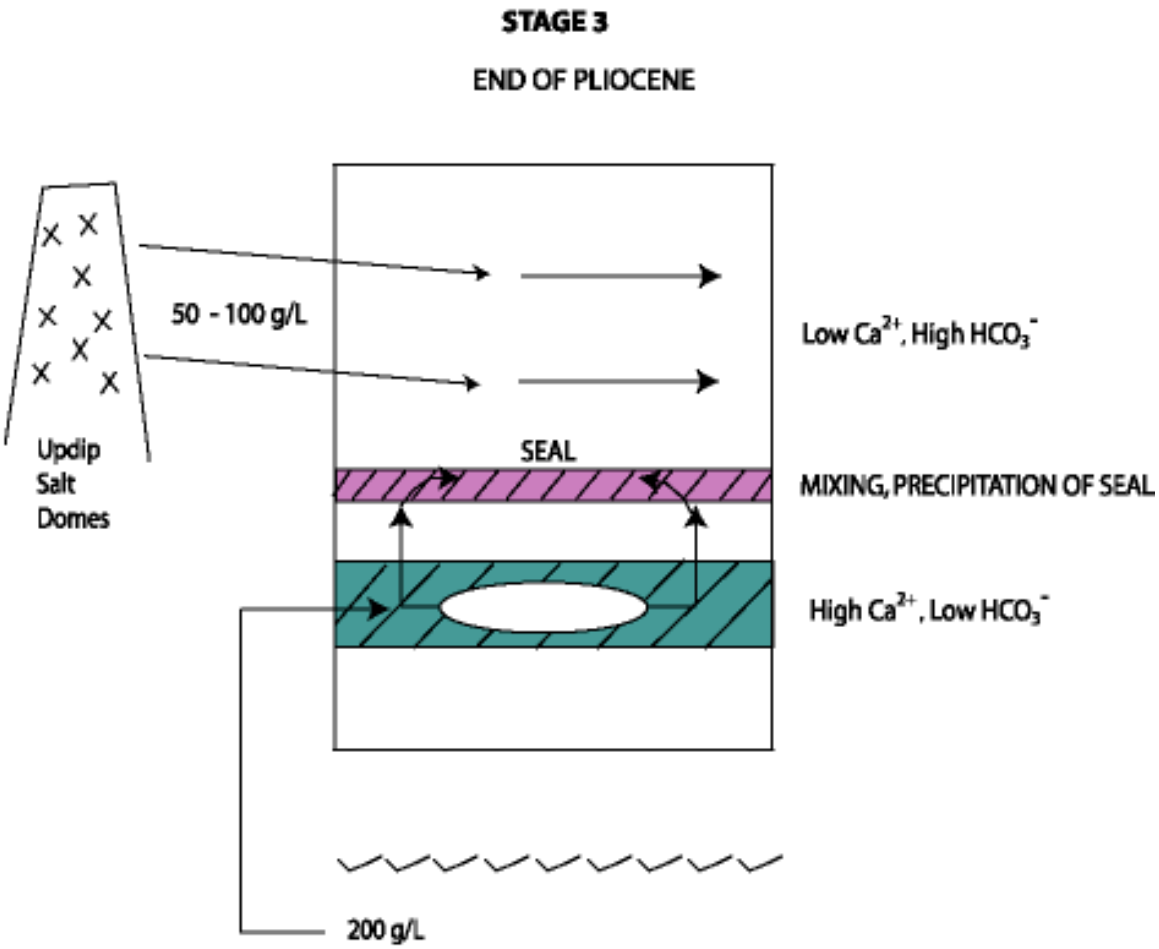

Figure 7.14. Stage 3. Mixing of two different types of fluids occurs, the upper fluid of 50-100 g/L TDS, low Ca^{2+}, and high HCO_3^-, and the lower fluid of ~200 g/L TDS, high Ca^{2+}, and low HCO_3^-. This mixing contributes to the calcite precipitation, which is responsible for forming the seal at Matagorda Island 519.

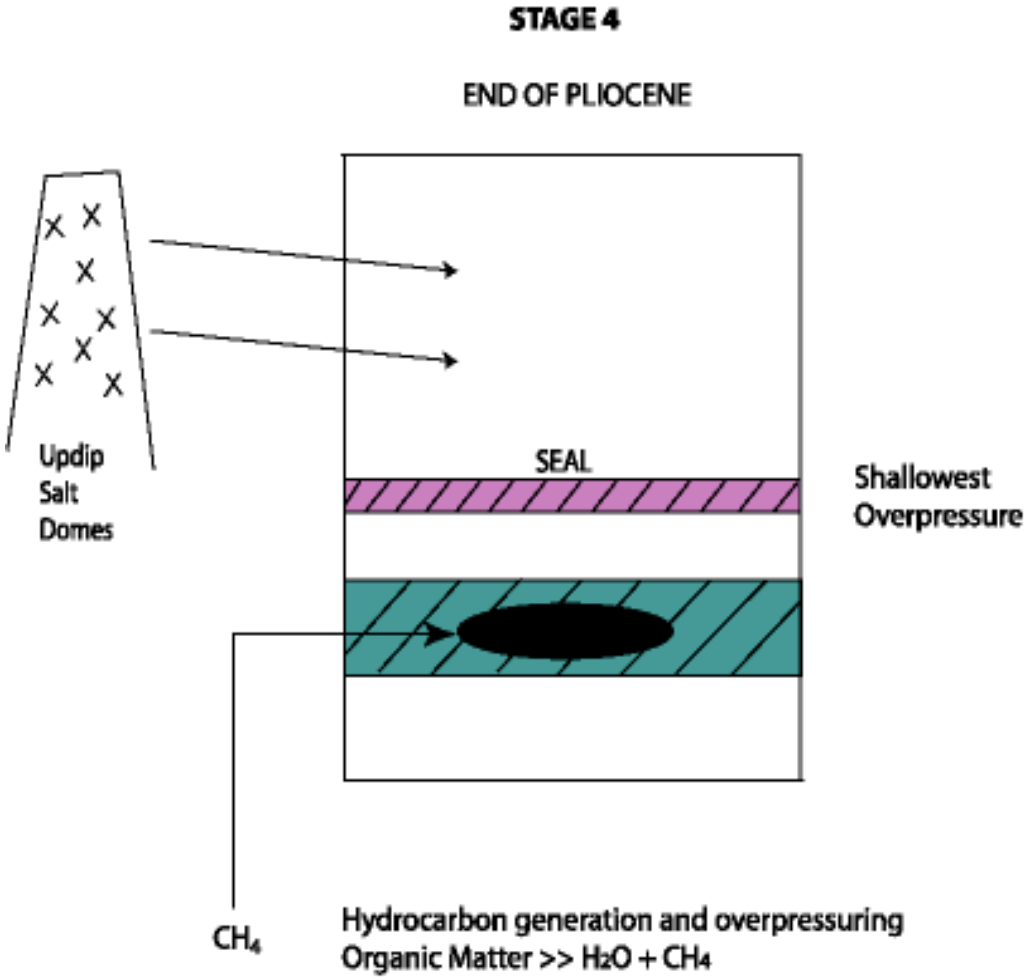

Figure 7.15. Stage 4. Hydrocarbon generation and overpressuring occur, with hydrocarbons filling in calcite dissolution voids created from secondary porosity generation.

7.11.5. Stage 5

Stage 5 involves processes that occur after seal emplacement and at or after hydrocarbon emplacement (Figure 7.16). Overpressuring due to smectite dehydration, represented by the simplistic reaction: Smectite $\rightarrow$ Illite + H_2O, occurs during Stage 5. This process contributes significant volumes of low TDS waters into the overpressured zone, which is reflected in the observed salinity reversal on TDS versus depth plots for this field.

7.11.6. Stage 6

Stage 6 represents processes that have occurred from ~20 ka to the present (Figure 7.17). A freshwater lens moved into the study area at ca. 20 ka, which coincides with a lowering of sea level representing the last glacial maximum during the Pleistocene. The present day TDS versus depth profile is thus complex, representing all stages of development at the Matagorda Island 519 field.

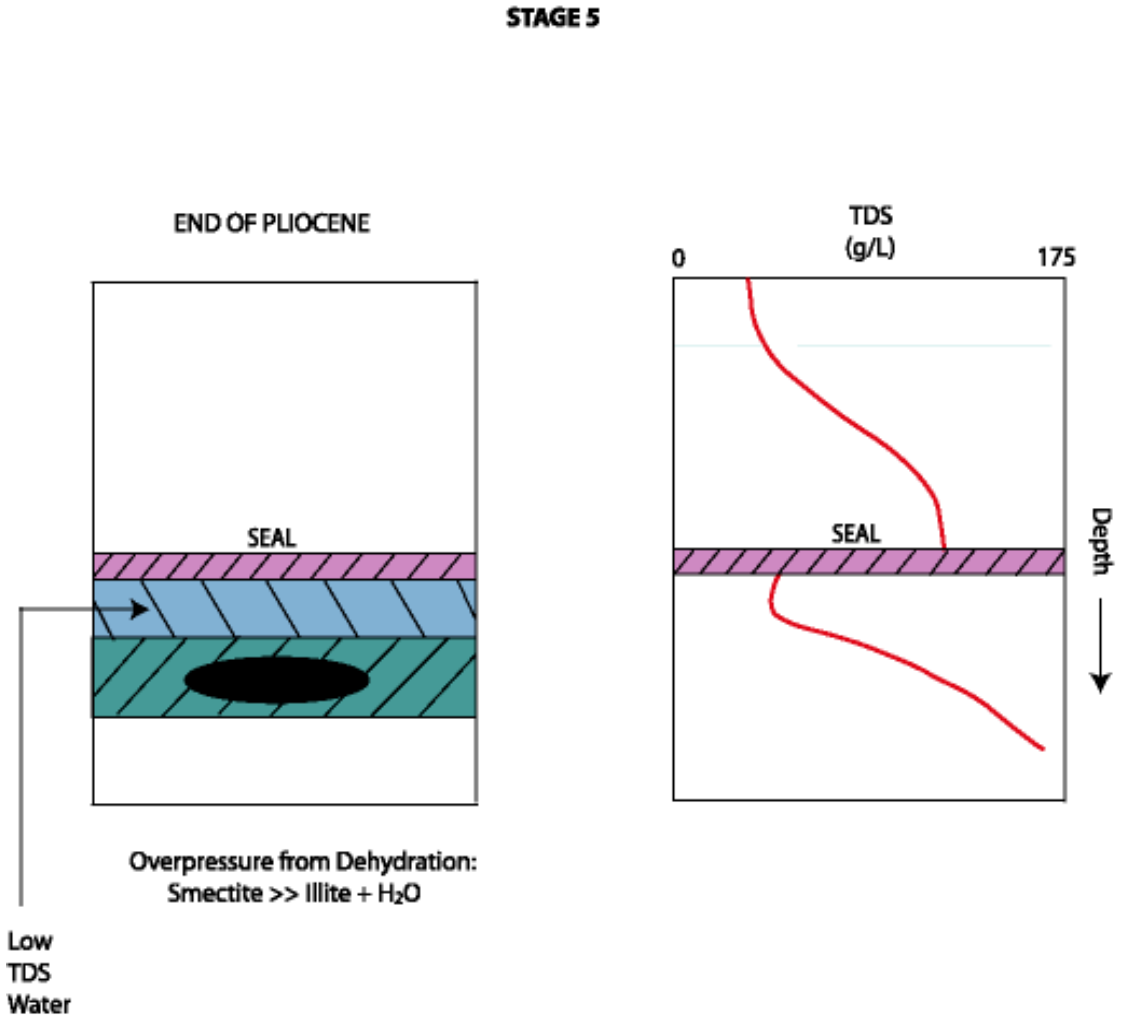

Figure 7.16. Stage 5. Overpressuring due to smectite dehydration occurs. This process contributes significant volumes of low TDS waters into the overpressured zone, which is reflected in the observed salinity reversal on TDS versus depth plots for this field.

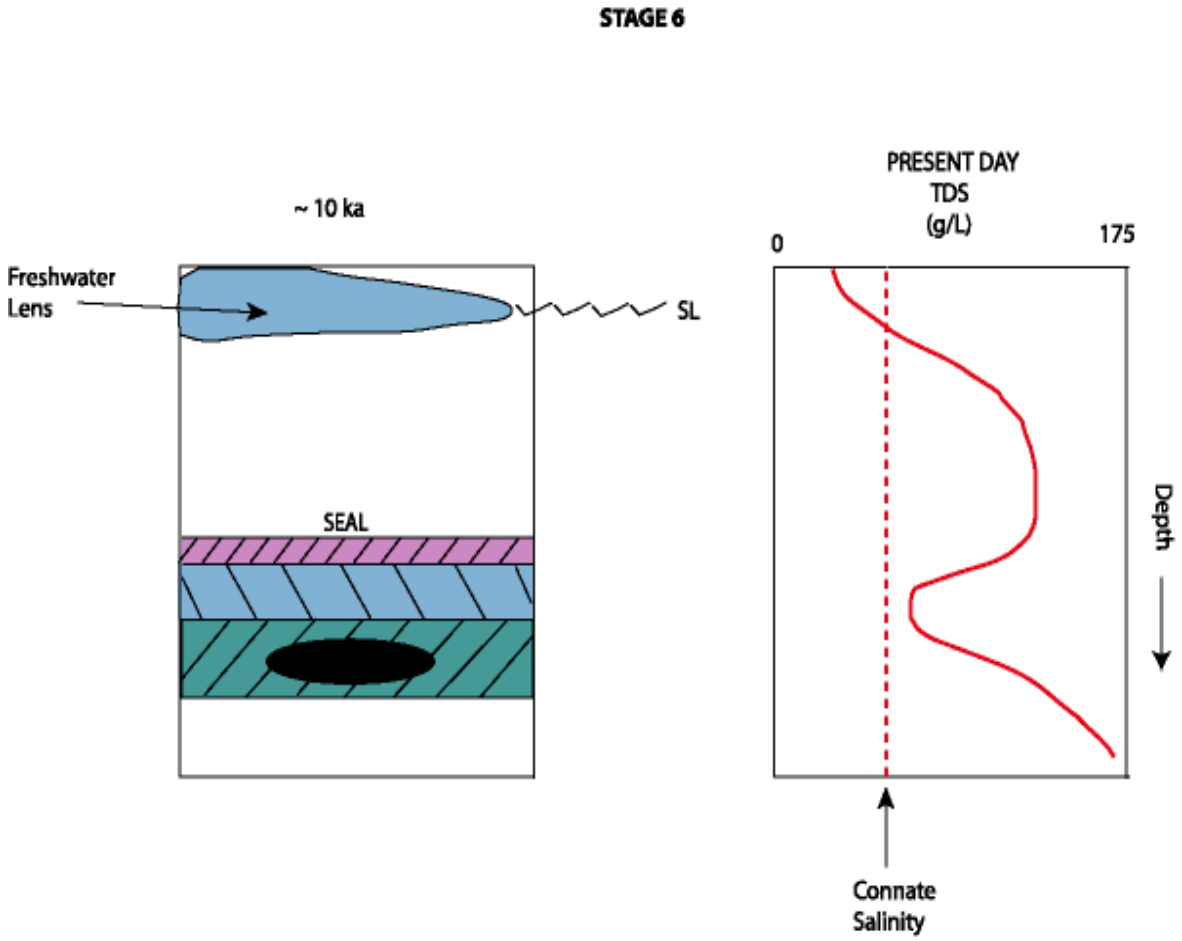

Figure 7.17. Stage 6. A freshwater lens moves into the study area at ca. 10 ka, which coincides with the last glacial maximum during the Pleistocene. The present day TDS versus depth profile represents all stages of development in this study area.

CHAPTER 8. CONCLUSIONS

The relations between overpressuring, diagenesis, and fluid flow at Matagorda Island 519 are complex and multifaceted. The pressure seal at the top of overpressure at this field does not appear to be depositional in nature and is more likely diagenetic in origin. Geochemical, mineralogical, and cuttings information supports the conclusion that the precipitation of diagenetic calcite and possibly quartz cements has been the major factor in development of the seal. The existence of large reservoirs of natural gas below the overpressure transition zone suggests capillary forces could be playing some role in maintaining the seal. Further research is needed, however, to determine if a free gas phase is present within or immediately below the transition zone. Theoretical calculations show that permeabilities at Matagorda Island 519 are sufficient to support the existence of a pressure seal.

If the available fluid pressure data based on shale resistivity response are correct, then there is evidence for at least three vertically-stacked overpressured compartments within the Lower Miocene section at Matagorda Island 519. The upper pressure seal represents the first transition into overpressure and confines the uppermost pressure compartment just below. There appear to be at least two additional deeper overpressured compartments bounded by seals of lesser thickness. It is not known whether the calculated fluid pressures take into account the complex vertical variations in formation water salinity and mudstone mineralogy which have been found to exist at MI 519 during this study. Because salinity and mineralogy are two factors which can affect shale resistivity the hypothesis for the existence of stacked pressure compartments at MI 519 requires further testing. Lateral sealing of the

overpressured section at MI 519 may be provided by faults and diagenetic cements within faults.

Overpressure development at MI 519 does not appear to be due to compaction disequlibrium on the basis of the lack of significant post-Miocene deposition and the lack of a reversal in mudstone porosity below the top of overpressure. This is in marked contrast to many other areas of the Gulf of Mexico basin, including the central Gulf, where compaction disequilibrium associated with rapid more, recent sedimentation has been shown to be the major cause of overpressuring. Aquathermal and osmotic overpressuring are unlikely given the depositional history and salinity structure of the field. The more likely causes of increased fluid pressure at Matatgorda Island 519 are petroleum generation and the presence of a large column of natural gas and clay mineral dewatering.

The spatially complex variations in formation water salinity at MI 519 put important constraints on reconstructing the hydrogeologic history of the field. Most of the salinities are greatly in excess of the original seawater salinity trapped at the time of sediment deposition and represent the outside introduction of dissolved chloride from the dissolution of halite. Large-scale (50-65 km) lateral flow of saline waters from updip salt domes is a likely source for the 50 to 100 g/L waters found above the top of overpressure. As in the nearby Picaroon and Doubloon fields, however, the most saline waters at MI 519 (>100 g/L) may represent focused upward flow of brines sourced from the deep Mesozoic.

Diagenesis and fluid flow are undoubtedly closely related at Matagorda Island 519. The stratigraphic variations in mudstone chemistry support the hypothesis that mudstone diagenesis has been an open-system process at Matagorda Island 519, with significant loss, transport, and enrichment of important diagenetic components, such as Ca, Si, Mg, Fe, and K. The variations in salinity at MI 519 reflect episodes of dynamic fluid flow and the

mixing of fluids of differing composition. Theoretical calculations have shown that it is possible to precipitate large volumes of mineral cements, including calcite and quartz, as a result of fluid mixing, and it is this process which may have resulted in the precipitation of a diagenetic seal at MI 519.

At least six stages of fluid flow and/or diagenetic development have likely occurred at MI 519. The first stage, ~17 Ma, involved haline-driven siliciclastic diagenesis that contributed to early stages of calcite cementation within preferred, permeable intervals. These intervals contained fluids that were transported from updip salt domes over lateral distances of up to 50 km. Deposition and subsidence continued from 17-10 Ma, which contributed to the burial of these Miocene sediments.

The next stages of development occurred at the end of the Pliocene, ~2.5 Ma. Stage 2 involved deep overpressure development, focused flow of underlying Mesozoic brines into the Miocene section, continued flow from updip salt domes, and secondary porosity generated from carbonate dissolution due to the corrosive nature of these Mesozoic brines. In Stage 3 mixing occurred between Miocene fluids, deeply sourced fluids and updip-sourced fluids, thus causing precipitation of the seal. Stage 4 involved hydrocarbon generation and shallow overpressure development, with continued lateral flow from updip sources. This hydrocarbon generation thus filled in the void spaces created from dissolution of calcite during Stage 2, and the hydrocarbons were prevented from flowing upward due to the presence of the seal. Thus, at the end of Stage 4 the requirements for maintaining a pressure seal over time were in place: 1) a mechanism to increase fluid pressure (hydrocarbon generation), and 2) a seal to trap excess fluid pressure.

During Stage 5 “hard” overpressure develops as a result of smectite dehydration, in which low TDS waters are flushed into the zone below the seal and are thus trapped by the

seal. The final stage of development, Stage 6, has occurred from approximately 20 ka to the present. A freshwater lens developed in the shallowest section during the last glacial maximum during the Pleistocene.

The present day salinity profile for Matagorda Island 519 field is complex in nature. The complexity is believed by this author to reflect the various stages of development presented in this study. Thus, detailed analysis of salinity versus depth profiles has lead to the development of a geologic model for the Matagorda Island 519 field. In order to test the hypotheses presented in this study additional data, such as fluid and core samples, will be necessary.

8.1. Future Work

Future research will add to the overall understanding of overpressuring, diagenesis, and fluid flow at the Matagorda Island 519 field. In order to provide a more accurate explanation of how these three geologic processes are potentially related at this field, the scale of investigation must be expanded. The pressure seal and overpressured compartments need to be analyzed within a regional framework. Also, diagenesis observed at Matagorda Island 519 needs to be compared to other research on diagenesis of the Texas Gulf Coast in order to understand the potential regional extent of the diagenetic reactions proposed in this study. Accurate descriptions of fluid flow at Matagorda Island 519 will require analysis of the regional fluid flow regime along the Texas Gulf Coast, both onshore and offshore. In addition to this regional work, it would be useful to perform a petrographic and geochemical study of samples from the overpressure transition zone at Matagorda Island 519 to better constrain the interpretation of how this zone formed.

Petroleum exploration and production is dependent upon the understanding and accurate geologic interpretation of petroleum systems, such as those found at Matagorda

Island 519. Successful exploration and production projects at the Matagorda Island 519 field have proven that this area has future potential for oil and gas prospects, and research projects such as this thesis contribute to the overall understanding of the geologic system, thus aiding in the understanding of the reservoir. In addition, results from this study will have important implications for future hydrogeologic basin modeling in this region of the offshore Texas Gulf of Mexico.

REFERENCES

AL-SHAIEB Z, PUCKETTE J. O., ABDALLA A. A., TIGERT V., and ORTOLEVA P.J. (1994) The banded character of pressure seals. In *Basin Compartments and Seals, AAPG Memoir 61* (ed. P. J. ORTOLEVA), 351-367.

ALTANER S.P. (1983) Zoned K-bentonites, evidence for the effect of solution chemistry on the smectite to illite reaction: Proc. of workshop on smectite alteration (ed. ANDERSON D.M.) Wash. D.C., 19-21.

AWWILLER D. N. (1993) Illite/Smectite formation and potassium mass transfer during burial diagenesis of mudrocks: a study from the Texas gulf coast Paleocene-Eocene. *Journal of Sedimentary Petrology* **63**, 501-512.

BARCLAY S. A. and WORDEN R. H. (2000) Geochemical modelling of diagenetic reactions in a sub-arkosic sandstone. *Clay Minerals* **35**, 57-67.

BARKER C. (1972) Aquathermal pressuring-role of temperature in development of abnormal-pressure zones. *AAPG Bulletin* **56**, 2068-2071.

BARKER C. (1990) Calculated volume and pressure changes during the thermal cracking of oil to gas in reservoirs. *AAPG Bulletin* **74**, 1254-1261.

BATEMAN R. M. (1985) Open-Hole Log Analysis and Formation Evaluation. *International Human Resources Development*, Boston, 647 p.

BATEMAN R. M. and KONEN C. E. (1977) Wellsite log analysis and the programmable pocket calculator. *Trans.-Society of Professional Well Log Analysts Twelfth Annual Logging Symposium* **Paper B**, 1-35.

BATZLE M and WANG Z (1992) Seismic properties of pore fluids. *Geophysics* **57**, 1396-1408.

BENNETT S. C. and HANOR J. S. (1987) Dynamics of subsurface salt dissolution at the Welsh Dome, Louisiana Gulf Coast. In *Dynamic Geology Salt and Related Structures* (eds. LERCHE I. and O'BRIEN J. J.), Academic Press, 653-677.

BETHKE C.M. (1986) Inverse hydrologic analysis of the distribution and origin of Gulf Coast-type geopressured zones. *Journal of Geophysical Research* **91**, 6535-6545.

BLOCH J., HUTCHEON I. E., and DE CARITAT P. (1998) Tertiary volcanic rocks and the potassium content of Gulf Coast shales – The smoking gun. *Geology* **26**, 527-530.

BOLES J. R. and FRANKS S. G. (1979) Clay diagenesis in Wilcox sandstones of Southwest Texas: Implications of smectite diagenesis on sandstone cementation. *Journal of Sedimentary Petrology* **49**, 55-70.

BRADLEY J. S. (1975) Abnormal formation pressure. *AAPG Bulletin* **59**, 957-973.

BRADLEY J. S. and POWLEY D. E. (1994) Pressure compartments in sedimentary basins: a review. In *Basin Compartments and Seals, AAPG Memoir 61* (ed. P. J. ORTOLEVA), 3-26.

BRAY R. B. (1989) Spatial variations in subsurface pore fluid properties in a portion of Southeast Louisiana: Implications for fluid migration and solute transport. *Louisiana State University, M.S. Thesis*. 159 p.

BRAY R.B. and HANOR J.S. (1990) Spatial variations in subsurface pore fluid properties in a portion of Southeast Louisiana; implications for regional fluid flow and solute transport. *Gulf Coast Association of Geological Societies Transactions*, **40**, 53-64.

BREDEHOFT J. D. and HANSHAW B. B. (1968) On the maintenance of anomalous fluid pressures: I. Thick sedimentary sequences. *Geol. Soc. of America Bulletin* **53**, 73-93.

BREDEHOFT J. D., WESLEY J. B., and FOUCH T. D. (1994) Simulations of the origin of fluid pressure, fracture generation, and the movement of fluids in the Uinta Basin, Utah. *AAPG Bulletin* **78**, 1729-1747.

BREWSTER C. (2001) XRF techniques used by Amoco at Matagorda Island 519. *personal communication*.

BREWSTER C. (2000) Matagorda Island 519 field paleontologic and structural data. *unpublished*.

BREWSTER C., SHARPE C., LANDECHE S., HATHON L., and KLEIN B. (1998) A Geological Exploration Model for Offstructure Gas Accumulations in Geopressured Lower Miocene Sandstones, Offshore Texas. *Gulf Coast Ass. of Geological Societies Transactions* **48**, 529-534.

BUFFLER R. T. (1991) Early evolution of the Gulf of Mexico basin. In *Introduction to Central Gulf Coast geology* (ed. GOLDTHWAITE D.), pp. 1-15. New Orleans Geological Society, New Orleans, LA.

CATHLES L. (2001) Capillary Seals as a Cause of Pressure Compartmentation in Sedimentary Basins: *Gulf Coast Section SEPM Foundation, 21st Annual Bob F. Perkins Research Conference Proceedings Volume on CD-ROM*, in press.

CARSLAW H. S. and JAEGER J. C. (1959) *Conduction of heat in solids* (second edition), Oxford University Press, 510 p.

CHAMBERLAIN T. C. (1885) The Requisite and Qualifying Conditions of Artesian Wells. *Fifth Annual Report of the United States Geological Survey*, 131-173.

COHEN D. and WARD C. R. (1991) SEDNORM-A program to calculate a normative mineralogy for sedimentary rocks based on chemical analyses. *Computers & Geosciences* **17**, 1235-1253.

CONYBEARE D. M. and SHAW H. F. (2000) Fracturing, overpressure release and Carbonate cementation in the Everest Complex, North Sea. *Clay Minerals* **35**, 135-149.

DE CARITAT P., BLOCH J., and HUTCHEON I. (1994) LPNORM: A linear programming normative analysis code. *Computers & Geosciences* **20**, 313-347.

DEMING D. (1994) Factors necessary to define a pressure seal. *AAPG Bulletin* **78**, 1005-1009.

DEMING D. (1995) Factors Necessary to Define a Pressure Seal: Reply. *AAPG Bulletin* **79**, 1079-1081.

DEMING D. (2001) *Introduction to Hydrogeology*. McGraw-Hill ISBN, Dubuque, Iowa. 480 p.

DEMING D., CRANGANU C., and LEE, Y. (revised manuscript in review) Self-sealing in sedimentary basins. *Journal of Geophysical Research*.

DURAND C., MATTHEWS J. C., LE GALLO Y., BROSSE E., and SOMMER F. (2000) Illitization and silicification in Greater Alwyn: I. Assessing and synthesizing experimental data. *Clay Minerals* **35**, 211-225.

DUTTON A. R. (1994) Use of aquifer stratigraphy for building numerical models of ground-water flow: case study of the heterogeneous Gulf Coast aquifer in Matagorda and Wharton Counties, Texas. *Gulf Coast Association of Geological Societies Transactions* **44**, 185–192.

DUTTON S. P., WILLIS B. J., WHITE C. D., and BHATTACHARYA J. P. (2000) Outcrop characterization of reservoir quality and interwell-scale cement distribution in a tide-influenced delta, Frontier Formation, Wyoming, USA. *Clay Minerals* **35**, 95-106.

ESLINGER E. and PEVEAR (1988) Clay Minerals for Petroleum Geologists and Engineers. *SEPM Short Course Notes No. 22*, 468 p.

FERTL W. H. and RIEKE H. H. (1980) Gamma ray spectral evaluation techniques identify fractured shale reservoirs and source rock characteristics. *J. Pet. Tech.* November, 2053-2062.

FERTL W. H. (1982) Geopressures; significance and implications to the petroleum industry. In *Society of Exploration Geophysicists 52nd Annual Meeting Abstracts*, 499-501.

FISHER A. T. (1998) Permeability within basaltic oceanic crust. *Reviews of Geophysics* **36**, 143-182.

FISHER A. T. and BECKER K. (2000) Channelized fluid flow in oceanic crust reconciles heat-flow and permeability data. *Nature* **403**, 71-74.

FOSTER J. B. and WHALEN H. E. (1999) Estimation of formation pressures from electrical surveys; offshore Louisiana. In *Pore pressure and fracture gradients* (chairperson A. T. Bourgoyne Jr.), pp. 57-63, Society of Petroleum Engineers of the American Institute of Mining, Metallurgical and Petroleum Engineers (AIME), Richardson, TX.

FUNAYAMA M. (1990) Distribution and migration patterns of subsurface fluids in the Wilcox Group in central Louisiana. *Louisiana State University, M. S. Thesis,* 179 p.

FUNAYAMA M. and HANOR J. S. (1995) Pore fluid salinity as a tool for evaluating reservoir continuity and fluid migration pathways in the Wilcox Group of central Louisiana. *Transactions of the Gulf Coast Association of Geological Societies* **45**, 195-201.

GALLOWAY W. E., GANEY-CURRY P. E., LI X., and BUFFLER, R. T. (2000) Cenozoic depositional history of the Gulf of Mexico basin. *AAPG Bulletin* **84**, 1743-1774.

GEOMAP (1999) Stratigraphic Column for the Texas gulf coast and structural map of Matagorda County, Texas.

GEORGE (1965) Graph for estimating formation pressures from shale resistivity data. *Schlumberger Well Surveying Corp.*, New Orleans, 1 p.

GILES M. R., INDRELID S. L., and JAMES D. M. D. (1998) Compaction – the greast unknown in basin modelling. In *Basin Modelling: Practice and Progress* (eds. DUPPENBECKER S. J. and ILIFFE J. E.), Geological Society of London Special Publications **141**, 15-43.

GROMET L. P., DYMEK R. F., HASKIN L. A., and KOROTEV R. L. (1984) The North American shale composite: its composition, major and trace element characteristics. *Geochimica et Cosmochimica Acta* **48**, 2469-2482.

HAGIWARA T. and JACKSON C. E. (1995) Shale anisotropy; its detection and exploitation by using a 2-MHz LWD resistivity device in high-angle and horizontal wells. *Canadian Well Logging Society Journal* **20**, 50-59.

HANOR J. S. (2002) MUDNORM program to calculate normative mineralogy for sediments from bulk chemistry.

HANOR J. S. (2001) Revised spreadsheet program to calculate apparent formation salinity from SSP log response. w*ritten communication.*

HANOR J. S. (2001) Reactive transport involving rock-buffered fluids of varying salinity. *Geochimica et Cosmochimica Acta* **65**, 3721-3732.

HANOR J. S. (1996) Variations in chloride as a driving force in siliciclastic diagenesis. In *Siliciclastic diagenesis and fluid flow: concepts and applications: SEPM Special Publication No. 55* (eds. CROSSEY, L.J., LOUCKS, R., AND TOTTEN, M.W.), 3-12.

HANOR J. S. (1994) Physical and chemical controls on the composition of waters in sedimentary basins. *Marine and Petroleum Geology* **11**, 31-45.

HANOR J. S. (1994) Origin of saline fluids in sedimentary basins. In *Geofluids: Origin, Migration, and Evolution of Fluids in Sedimentary Basins: GSA Special Publication No. 78* (ed. PARNELL, J.), 151-174.

HANOR J. S. (1987) Origin and migration of subsurface sedimentary brines. *SEPM Short Course No. 21 Lecture Notes.* 247 p.

HANOR J. S. and SASSEN R. (1990) Evidence for large-scale vertical and lateral migration of formation waters, dissolved salt, and crude oil in the Louisiana Gulf Coast. *Gulf Coast Oil and Gases: Their Characteristics, Origin, Distribution, and Exploration and Production Significance:* Proc. 9th Ann. Res. Conf. Gulf Coast Sec. Soc. of Econ. Paleo. Mineral. Foundation, 283-296.

HART B. S., FLEMINGS P. B., and DESHPANDE A. (1995) Porosity and pressure: Role of compaction disequilibrium in the development of geopressures in a Gulf Coast Pleistocene basin. *Geology* **23**, 45-48.

HE Z. and CORRIGAN J. (1995) Factors Necessary to Define a Pressure Seal: Discussion. *AAPG Bulletin* **79**, 1075-1078.

HEARST J. R. and NELSON P. H. (1985) *Well logging for physical properties*. McGraw-Hill Book Company, New York, 571 p.

HOTTMAN and JOHNSON (1999) Estimation of formation pressures from log-derived shale properties. In *Pore pressure and fracture gradients* (chairperson A. T. Bourgoyne Jr.), pp. 7-12, Society of Petroleum Engineers of the American Institute of Mining, Metallurgical and Petroleum Engineers (AIME), Richardson, TX.

HOWER J., ESLINGER E., HOWER M. E., and PERRY E. A. (1976) Mechanism of burial metamorphism of argillaceous sediments: I. Mineralogical and chemical evidence. *GSA Bulletin* **87**, 725-737.

HUENGES E., ERZINGER J., KUCK J., ENGESER B., and KESSELS W. (1997) The permeable crust: geohydraulic properties down to 9101 m depth. *Journal of Geophysical Research* **102**, 18255-18265.

HUNT J. M. (1990) Generation and migration of petroleum from abnormally pressured fluid compartments. *AAPG Bulletin* **72**, 1-12.

INGEBRITSEN S. E. and MANNING C. E. (1999) Geological implications of a Permeability-depth curve for the continental crust. *Geology* **27**, 1107-1110.

JEANS C. V. (2000) Mineral diagenesis and reservoir quality – the way forward: an introduction. *Clay Minerals* **35**, 3-4.

JENNINGS S. and THOMPSON G. R. (1986) Diagenesis of Plio-Pleistocene sediments of the Colorado River delta, Southern California. *Journal of Sedimentary Petrology* **56**, 89-98.

JIANG, PEACOR, and BUSECK (1995) "Chlorite geothermometry"? A discussion on apparent octahedral vacancies in relation to formation temperatures. *Geological Society of China 1995 Annual Meeting, Program and Extended Abstracts.* 274 - 278.

KEHLE R. O. (1971) Geothermal Survey of North America, 1971 Annual Progress Report. *Unpublished duplicate report, Research Comm., AAPG,* 31 p.

KLEIN B., HATHON L., and BREWSTER C. (1998) Petrography and Geochemistry of the Matagorda Island 519 Field, Offshore Texas. *Gulf Coast Ass. of Geological Societies Transactions* **48**, 547-558.

LAND L. S. and MILLIKEN K. L. (2000) Regional loss of SiO_2 and gain of K_2O during burial diagenesis of Gulf Coast mudrocks, USA. *Spec. Publs. Int. Ass. Sediment.* **29**, 183-197.

LAND L. S., MACK L. E., MILLIKEN K. L., and LYNCH F. L. (1997) Burial diagenesis of argillaceous sediment, south Texas Gulf of Mexico sedimentary basin: A reexamination. *Geological Society of America Bulletin* **109**, 2-15.

LI Y., NOWLIN W. D., and REID R. O. (1997) Mean hydrographic fields and their interannual variability over the Texas-Louisiana continental shelf in spring, summer, and fall. *Journal of Geophysical Research* **102**, C1, 1027-1049.

LYNCH F. L. (1996) Mineral/Water Interaction, Fluid Flow, and Frio Sandstone Diagenesis: Evidence from the Rocks. *AAPG Bulletin* **80**, 486-504.

LYNCH F. L. (1997) Frio shale mineralogy and the stoichiometry of the smectite-to-illite reaction: the most important reaction in clastic sedimentary diagenesis. *Clays and Clay Minerals* **45**, 618-631.

LYNCH F. L. and LAND L. S. (1996) Diagenesis of calcite cement in Frio formation Sandstones and its relationship to formation water chemistry. *Journal of Sedimentary Research* **66**, 439-446.

LYNCH F. L., MACK L. E., and LAND L. S. (1997) Burial diagenesis of illite/smectite in shales and the origins of authigenic quartz and secondary porosity in sandstones. *Geochimica et Cosmochimica Acta* **61**, 1995-2006.

LYNCH F. L., MILLIKEN K. L., AWWILLER D. N., MACK L. E., BLOCH J., HUTCHEON I. E., and DE CARITAT P. (1999) Tertiary volcanic rocks and the Potassium content of Gulf Coast shales – The smoking gun: Comment and Reply. *Geology* **27**, 663-665.

McCAIN JR. W. D. (1991) Reservoir fluid property correlations – state of the art. *SPE ReservoirEngineering* **6**, 266-272.

MCMANUS K. (1991) Thermohaline and hydrocarbon related diagenesis of Lower Miocene and Upper Oligocene sediments, West Hackberry Field, Cameron Parish, Louisisana: Implications for mass transport and fluid flow. *Louisiana State University M.S. Thesis,* 269 p.

MACAULY C. I., FALLICK A. E., HASZELDINE R. S., and McAULAY G. E. (2000) Oil migration makes the difference: regional distribution of carbonate cement ^{13}C in northern North Sea Tertiary sandstones. *Clay Minerals* **35**, 69-76.

MARCHAND A. M. E., HASZELDINE R. S., MACAULY C. I., SWENNEN R., and FALLICK A. E. (2000) Quartz cementation inhibited by crestal oil charge: Miller deep water sandstone, UK North Sea. *Clay Minerals* **35**, 201-210.

MIDTB∅ R. E. A., RYKKE J. M., and RAMM M. (2000) Deep burial diagenesis and reservoir quality along the eastern flank of the Viking Graben. Evidence for illitization and quartz cementation after hydrocarbon emplacement. *Clay Minerals* **35**, 227-238.

MINERALS MANAGEMENT SERVICE (2000) Gulf of Mexico Region Paleo for Public Release Report.

MONCURE G. K., LAHANN R. W., and SIEBERT R. M. (1984) Origin of secondary Porosity and cement distribution in a sandstone/shale sequence from the Frio Formation (Oligocene). In *Clastic Diagenesis: AAPG Memoir 37* (eds. MCDONALD D. A. and SURDAM R. C.) Tulsa, Oklahoma, 151-161.

MORTON R. A., JIRIK L. A., and FOOTE R. Q. (1985) *Structural Cross Sections, Miocene Series, Texas Continental Shelf*. Bureau of Economic Geology Publication. The University of Texas at Austin, Austin, Texas. 7 p., 17 plates.

NADEAU P. (2000) The Sleipner Effect: a subtle relationship between the distribution of diagenetic clay, reservoir porosity, permeability, and water saturation. *Clay Minerals* **35**, 185-200.

NEGLIA S. (1979) Migration of fluids in sedimentary basins. *AAPG Bulletin* **63**, 573-579.

NEUZIL C. E. (1995) Abnormal pressures as hydrodynamic phenomena. *Am. J. Sci.* **295**, 742-786.

NIKIEL A. M. (1998) Spatial variations in subsurface pore fluid salinity and physical Properties in South Pelto and South Timbalier OCS areas, offshore Louisiana: implications for regional fluid migration. *Louisiana State University M. S. Thesis*, 104 p.

NIKIEL A. M. and HANOR J. S. (1999) Spatial Variations in Formation Water Salinities, South Pelto and South Timbalier Areas, Eastern Louisiana Continental Shelf. *Gulf Coast Ass. of Geological Societies Transactions* **49**, 396-403.

NIU B. and ISHIDA H. (2000) Different rates of smectite illitization in mudstones and Sandstones from the Niigata Basin, Japan. *Clay Minerals* **35**, 163-174.

NUNN J. A. and SASSEN R. (1986) The framework of hydrocarbon generation and migration, Gulf of Mexico continental slope. *Gulf Coast Ass. of Geological Societies Transactions* **36**, 257-262.

ORTOLEVA P. J. (ed.) (1994) *Basin Compartments and Seals, AAPG Memoir 61*, American Association of Petroleum Geologists, Tulsa, Oklahoma, 477 p.

OSBORNE M. J. and SWARBRICK R. E. (1997) Mechanisms for generating overpressure in sedimentary basins: a reevaluation. *AAPG Bulletin* **81**, 1023-1041.

PAKTUNC A. D. (2001) MODAN – a computer program for estimating mineral quantities based on bulk composition: windows version. *Computers & Geosciences* **27**, 883-886.

PAY M. D., ASTIN T. R., and PARKER A. (2000) Clay mineral distribution in the Devonian-Carboniferous sandstones of the Clair Field, west of Shetland, and its Significance for reservoir quality. *Clay Minerals* **35**, 151-162.

PEARSON M. J. and SMALL J. S. (1988) Illite-smectite diagenesis and paleotemperatures in northern North Sea Quaternary to Mesozoic shale sequences. *Clay Minerals* **23**, 2, 109-132.

POLLASTRO R. M. (1985) Mineralogical and morphological evidence for the formation of illite at the expense of illite/smectite. *Clays and Clay Minerals* **33**, 4, 265-274.

PRENSKY S. (1992) Temperature Measurements in Boreholes: An Overview of Engineering and Scientific Applications. *The Log Analyst* **33**, 313-333.

RAILROAD COMMISSION OF TEXAS (2001) Production Report for Leases 79413 and 88562 at Matagorda Island 519.

REVIL A., CATHLES L. M., LOSH S., and NUNN J. A. (1998) Electrical conductivity in shaly sands with geophysical applications. *Journal of Geophysical Research* **103**, 925-936.

RIDER M. H. (1996) *The Geological Interpretation of Well Logs – Second Edition*. Gulf Publishing Company, United Kingdom, 280 p.

ROSEN R. N., BREARD S. Q., CALLENDER JR. A. D., FLEISHER R. L., LYTTON III R. G., MENCONI L.C., NAULT M. J., ROEDERER R., SHUNICK T. W., and TUTTLE J. L. (1999) *Gulf of Mexico Basin Biostratigraphic Index Microfosssils; A Geoscientist's Guide, Foraminifera and Nannofossils, Oligocene through Pleistocene, Parts I and II*. Gulf Coast Section SEPM Foundation, 215 data sheets, 3 charts.

SALVADOR A. (1991) Chapter 8: Triassic-Jurassic. In *The Geology of North America, The Gulf of Mexico Basin*, pp. 131-180. The Geological Society of America, v. J, Boulder, Colorado.

SCHMIDT G. W. (1973) Interstitial water composition and geochemistry of deep Gulf Coast shales and sandstones. *AAPG Bulletin* **57**, 321-337.

SENI S. J., HENTZ T. F., KAISER W. R., and WERMUND JR. E. G. (1997) *Atlas of Northern Gulf of Mexico Gas and Oil Reservoirs, Volume 1. Miocene and Older Reservoirs.* Bureau of Economic Geology, The University of Texas at Austin, Austin, Texas, 199 p.

SHARP J. M., FENSTEMAKER T. R., SIMMONS C. T., MCKENNA T. E., and DICKINSON J. K. (2001) Potential salinity-driven free convection in a shale-rich sedimentary basin: Example from the Gulf of Mexico basin in south Texas. *AAPG Bulletin* **85**, 2089-2110.

SPEARS R. W. (2000) Relationship between overpressured compartments and pore fluid salinity in sediments of South Marsh Island, OCS 310 offshore Louisiana. *Louisiana State University M. S. Thesis*, 233 p.

STEWART R. N. T., HASZELDINE R. S., FALLICK A. E., WILKINSON M., and MACAULY C. I. (2000) Regional distribution of diagenetic carbonate cement in Paleogene deepwater sandstones: North Sea. *Clay Minerals* **35**, 119-134.

SYROWSKI K. A. (2001) Microtomography of fine-grained Paleogene rocks from the North Sea Central Graben. *Louisiana State University M. S. Thesis*, 199 p.

TAYLOR T. R. (1990) The influence of calcite dissolution on reservoir porosity in Miocene sandstones, Picaroon Field, offshore Texas gulf coast. *Journal of Sedimentary Petrology* **60**, 322-334.

TAYLOR T. R. and LAND L. S. (1996) Association of allochthonous waters and Reservoir enhancement in deeply buried Miocene sandstones: Picaroon Field, Corsair Trend, offshore Texas. *Siliciclastic Diagenesis and Fluid Flow: Concepts and Applications, SEPM Special Publication No. 55*, Society for Sedimentary Geology (SEPM), 37-48.

VOGLER H. A. and ROBISON B. A. (1987) Exploration for Deep Geopressured Gas: Corsair Trend, Offshore Texas. *AAPG Bulletin* **71**, 7, 777-787.

WESSELMAN J. B. and HEATH J. (1977) Computer techniques to aid in the Interpretation of subsurface fluid-pressure gradients. *United States Geological Survey Report PB-268*, Reston, VA. 41 p.

WILCOXIN B. (1989) *Louisiana State University PhD Dissertation*.

WINTSCH R. P. and KVALE C. M. (1994) Differential mobility of elements in burial diagenesis of siliciclastic rocks. *Journal of Sedimentary Research* **A64**, 349-361.

WORDEN R. H., RUFFELL A. H., and CORNFORD C. (2000) Surface temperature, sequence stratigraphy and deep burial diagenesis. *Clay Minerals* **35**, 13-24.

WORRALL D. M. and SNELSON S. (1989) Evolution of the Northern Gulf of Mexico, with emphasis on Cenozoic growth faulting and the role of salt. In *The Geology of North America: an overview* (eds. A. W. BALLY and A. R. PALMER), Boulder, Colorado, The Geological Society of America, **A**, 97-138.

VITA

Kera Gautreau Spears is the eldest daughter of Kirk J. and Lori M. Gautreau, of Gonzales, Louisiana. Kera was born on February 26, 1977, in Baton Rouge, Louisiana, and she has one sister, Amber, one brother, Beau, and one niece, MaKenzie. In May of 1995 Kera graduated with honors from East Ascension High School in Gonzales, Louisiana, and she entered college at Southeastern Louisiana University in Hammond, Louisiana, in the fall of that year. After one year Kera entered Louisiana State University in Baton Rouge, Louisiana, where her interest in geology developed.

As an undergraduate geology major, Kera worked as a research assistant to Dr. Jeff Hanor. It was during this time that she became interested in the Matagorda Island 519 field research project. Kera received her Bachelor of Science degree in geology from Louisiana State University in the summer of 2000, and immediately entered graduate school that fall to work with Dr. Hanor. In July of 2002 Kera began her professional career with ChevronTexaco Exploration and Production in New Orleans, Louisiana.